# Reduced order and sparse representations for patient-specific modeling in computational surgery

Nathan Lauzeral

# THESE DE DOCTORAT

ÉCOLE CENTRALE DE NANTES
COMUE UNIVERSITE BRETAGNE LOIRE

ECOLE DOCTORALE N° 602
Sciences pour l'Ingénieur
Spécialité : Mécanique des solides, des matériaux, des structures et des surfaces

Par
**Nathan LAUZERAL**

## Reduced order and sparse representations for patient-specific modeling in computational surgery

**Thèse présentée et soutenue à Nantes, le 13 décembre 2019**
**Unité de recherche : Institut de Calcul Intensif - EA 7471**

**Rapporteurs avant soutenance** :

| | | |
|---|---|---|
| Stéphane | AVRIL | Professeur, CIS, Ecole nationale supérieure des Mines de Saint-Etienne |
| Céline | GRANDMONT | Directrice de recherche CNRS, Centre de recherche Inria de Paris |

**Composition du Jury :**

Président :

| | | |
|---|---|---|
| Stéphane | AVRIL | Professeur, CIS, Ecole nationale supérieure des Mines de Saint-Etienne |

Examinateurs :

| | | |
|---|---|---|
| Stéphane | AVRIL | Professeur, CIS, Ecole nationale supérieure des Mines de Saint-Etienne |
| Elías | CUETO | Professeur, AMB, Université de Saragosse |
| Céline | GRANDMONT | Directrice de recherche CNRS, Centre de recherche Inria de Paris |
| Alexandre | HOSTETTLER | Docteur - Directeur R&D, IRCAD France |
| Enrique | NADAL | Professeur assistant, CIIM, Université Polytechnique de Valence |

| | | |
|---|---|---|
| Dir. de thèse : | Francisco CHINESTA | Professeur, PIMM, ENSAM ParisTech |
| Co-enc. de thèse : | Domenico BORZACCHIELLO | Docteur, ICI, Ecole Centrale de Nantes |

# Reduced order and sparse representations for patient-specific modeling in computational surgery

Nathan Lauzeral

January 20, 2020

# Abstract

The subject of this thesis is part of the project 3D-Surg. The main goal is to develop three-dimensional (3D) modeling solutions to represent human anatomy with high fidelity using medical imaging techniques. In particular, the aim is to enhance medical images with the relevant biophysics and assist the surgeon or clinician in the process of informed decision making. In the framework of the thesis, the emphasis is on the embedding of interactive biophysical simulation into 3D anatomical modeling of tissues and organs. More specifically, the use of model order reduction (MOR) methods based on sparsity-related techniques is investigated for the development of real-time biophysical modeling. The real-time capacity is at the core of many applications in 3D technologies; it is primarily used to meet the frame rate requirements for real-time visualization and ensure full compatibility between the medical workflow and the simulation runtime. The thesis explores practical solutions and their potential to tackle fundamental bottlenecks that are encountered in MOR applied to the framework of computational surgery. The first part is dedicated to the construction of appropriate anatomical parameterizations through the use of generative statistical shape models based on databases of three-dimensional medical images. Particular attention is put on the compatibility of such parametric representations with MOR techniques, and more specifically with those relying on tensor structures. A successful strategy for sparse sampling in the space of anatomical features is presented within the framework of the sparse subspace learning approach. The second part covers the aspects related to the problem of data completion and image reconstruction from a partial or incomplete dataset using physical priors. The approach that is proposed relies on the knowledge of the physical behavior of the system and uses physical modeling as a way to regularize the reconstruction problem through a restriction of the search space. A semi-intrusive approach is used to introduce hyperreduced models in the formulation of a three-dimensional image registration problem for surgical scene reconstruction. A new hyper-reduction method is proposed, based on a sparsity promoting technique. The results show how a strong identification of the physical model, which would be prone to overfitting errors, is not necessary to obtain acceptable results. Finally, the third part concerns an alternative approach towards the metamodeling of biophysical systems under uncertainty of the underlying parameters. Traditional MOR approaches are not always successful in producing a low dimensional representation of a model. This is the case of electrosurgery simulation, as in many other problems exhibiting moving discontinuities. In these cases, the proposed approach consists in the identification of an appropriate metamodel governing the evolution of the quantities of interest rather than the state variables of the system. The use of sparse regression techniques, that were recently shown to be successful in the identification of deterministic models, was extended to the case of systems with stochastic parameters. For the problem of radiofrequency ablation simulation, results show that under appropriate sampling conditions, sparse regression has the potential to identify a model for the average response of the system.

# Résumé substantiel

Les avancées numériques et technologiques d'aujourd'hui mènent à repenser le bloc opératoire de demain. Des outils d'aide à la prise de décision sont de plus en plus présents lors des opérations qui peuvent s'avérer délicates. Le projet français 3D-Surg, soutenu par la Banque Publique d'Investissement, participe à ces changements et a pour objectif d'accompagner le praticien en développant des modèles et visualisations en trois dimensions (3D) des patients. Les travaux de cette thèse s'inscrivent dans le cadre de ce projet, et se concentrent sur la simulation en temps réel des phénomènes biophysiques appliqués aux tissus et organes du patient. En effet, une compatibilité totale doit être assurée entre le déroulement des opérations médicales et la durée d'exécution de ces simulations, que cela soit dans un souci de visualisation ou de planification des opérations. Pour ce faire, nous explorons la capacité des méthodes de réduction de modèles à accélérer les calculs dans le cadre de la chirurgie computationelle. En particulier, nous exploitons le concept de parcimonie au sein de ces méthodes pour répondre à des contraintes d'intrusivité et de rapidité d'exécution des calculs.

Trois difficultés majeures et essentielles liées à la simulation des phénomènes biophysiques sont identifiées. Pour chacune, différents enjeux dus à la mise en œuvre des méthodes de réduction de modèles sont mis en lumière. La thèse propose alors des solutions pratiques et évalue leurs potentiels pour faire face aux défis rencontrés. Elle est ainsi construite en trois parties, chacune composée de deux ou trois chapitres, chaque partie étant consacrée à la résolution d'un problème identifié.

**Première partie : prise en compte de l'anatomie de l'individu dans la modélisation**

Chaque patient possède une anatomie spécifique qu'il est primordial de prendre en compte dans les simulations numériques. Aujourd'hui, pour chaque nouvel individu, les modèles sont généralement reconstruits à partir de zéro, ce qui peut s'avérer être une tâche fastidieuse. Plus judicieusement, il est possible d'intégrer directement une paramétrisation de la forme des organes au sein du modèle. Le Chapitre 1 présente un état de l'art de ces méthodes, permettant la création de modèles d'organes paramétriques. Ces modèles sont intéressants pour deux raisons. Tout d'abord, ils permettent la prise en compte de la variation de forme des organes au sein d'une population. Dans le cadre de la chirurgie computationnelle, ces modèles paramétriques sont pertinents pour l'automatisation de la segmentation d'images médicales et la création de modèles anatomiques spécifiques. De plus, ils peuvent être intégrés au sein de simulateurs en temps réel, notamment à des fins d'optimisation de formes (e.g. pour la conception de prothèses). Toutefois, après un aperçu des méthodes d'intégration de la forme dans les modèles paramétriques d'organes via les méthodes de réduction de modèles, nous constatons le manque d'approches fondées sur un paramétrage de la forme issu de vraies données médicales. La prise en compte de ces données se révèle être importante si l'on souhaite que le modèle réduit puisse représenter n'importe quelle forme d'organe biologiquement viable. Pour parvenir à ce résultat, une approche statistique est envisageable. Plusieurs méthodologies existent, notamment dans le cadre de la méthode des éléments finis, qui comprennent chacune deux étapes. La première étape consiste en une paramétrisation de la forme via une analyse statistique. La seconde est une étape de "morphing" afin de recréer un maillage volumique à partir de la forme. Afin d'adapter et d'intégrer un tel processus au sein d'un modèle réduit, nous proposons une méthodologie complète dans les Chapitres 2 et 3. Le Chapitre 2 est consacré à la mise en place d'une nouvelle méthode pour la création de la paramétrisation de la forme des modèles éléments finis. Une nouvelle approche pour l'analyse statistique de forme ainsi qu'une technique de morphing innovante sont utilisées pour arriver au résultat. L'efficacité de cette approche est démontrée sur des bases de données comprenant des formes de fémurs ainsi que

des formes de foies. Le Chapitre 3 est dédié à l'intégration de ce modèle paramétrique au sein de la "sparse subspace learning", une méthode de réduction de modèles non intrusive fondée sur un échantillonnage parcimonieux de l'espace des paramètres. Pour ce faire, une stratégie efficace d'échantillonnage dans l'espace des caractéristiques anatomiques est présentée, en mettant l'accent sur la topologie que doit adopter cet espace afin de couvrir la totalité des formes anatomiques existantes. La méthode est testée dans le cadre de la déformation du foie pendant la respiration libre. Un modèle mécanique élastique, homogène, isotrope et linéaire est utilisé. Les résultats montrent l'efficacité de l'approche de réduction de modèles et sa capacité à représenter les déformations subies par le foie lors de la respiration, et ce, notamment pour des formes de foies non présentes dans la base de données. Toutefois, la mauvaise réductibilité de la dimension de l'espace des formes de foies nécessite la prise en compte d'un grand nombre de paramètres (entre 30 et 50). Le modèle réduit étant limité à une quinzaine de paramètres, seule une portion de l'ensemble des formes possibles peut être considérée.

**Deuxième partie : complétion des données grâce à des *a priori* physiques**

Les données médicales sont souvent partielles et contiennent du bruit. Dans le cadre de la chirurgie mini-invasive, le praticien est souvent confronté à des situations où il doit estimer certains paramètres et ne peut se fier qu'à sa propre expérience. Afin de fournir au praticien des informations plus complètes et plus fiables, des modèles mathématiques fondés sur la physique du problème peuvent être intégrés dans la représentation 3D afin de régulariser et étendre les données acquises. L'identification des paramètres des modèles à partir des mesures, connue sous le nom de problème inverse, est introduite dans le Chapitre 4. Les principales méthodes dédiées à la résolution des problèmes inverses y sont présentées et, en particulier, le concept du filtre de Kalman y est détaillé. L'exemple de la chirurgie laparoscopique est ensuite développé ; il explicite et justifie l'utilisation de modèles mathématiques fondés sur la physique pour compléter les données. En effet, en laparoscopie, seules quelques cicatrices sont pratiquées dans la paroi abdominale du patient afin de procéder à l'acte chirurgical. Comme le chirurgien n'a plus d'accès visuel direct, un laparoscope est inséré au sein de l'abdomen afin d'avoir une visualisation via un écran. Cette visualisation ne retourne qu'une image bidimensionnelle (2D) de la surface de la cavité abdominale. Les informations pertinentes pour le chirurgien, telles que la vascularisation des organes ou la position des tumeurs, ne sont plus aisément identifiables. Une représentation 3D en réalité augmentée peut alors être superposée sur ces images intra-opératoires afin d'avoir accès aux données voulues. Toutefois, le modèle 3D utilisé lors de l'augmentation de la scène provient généralement de données préopératoires. Il faut donc prendre en compte les déformations subies par les tissus entre cette acquisition et le moment de l'opération. Pour déformer de manière réaliste cette image des hypothèses sont faites sur le comportement mécanique des tissus. Un problème inverse est ensuite résolu pour recaler la surface du modèle 3D sur l'image 2D retournée par le laparoscope, tout en respectant le comportement mécanique considéré. Cependant, le modèle physique comporte la plupart du temps des paramètres choisis arbitrairement par l'utilisateur. Pour procéder au recalage du modèle tout en estimant la valeur de ces paramètres, nous proposons dans le Chapitre 5 une méthodologie fondée sur un filtre de Kalman étendu. Une approche semi-intrusive est utilisée pour introduire un modèle hyper-réduit dans la formulation du problème afin d'atteindre des performances proches du temps réel dans un cadre non-linéaire. Une nouvelle méthode d'hyper-réduction est introduite via le développement d'un algorithme de régression parcimonieuse assurant la positivité des coefficients. Les résultats prouvent la capacité de cette approche à recaler le modèle 3D à partir de la donnée de lois de comportement hyperélastiques et d'un nuage de points décrivant la surface de la cavité abdominale. On montre aussi qu'il n'est pas nécessaire de précisément identifier les paramètres du modèle physique pour obtenir des résultats acceptables et exploitables.

**Troisième partie : réponse en temps réel de systèmes biophysiques comprenant des incertitudes**

L'ensemble des modèles mathématiques représentant des phénomènes physiques intègrent des paramètres qui déterminent leur comportement. On leur attribue de manière générale une valeur fixe, le modèle est alors dit déterministe. Toutefois, ces paramètres sont la plupart du temps in-

certains. Cela peut être dû à des erreurs de mesure, des variations propres au système physique, etc. Pour prendre en compte ces variations et étudier leur influence sur le résultat des modèles, des méthodes dites de propagation de l'incertitude ont été développées. Ces dernières sont introduites dans le Chapitre 6, en mettant en exergue leur application dans le cadre de simulations en temps réel pour la chirurgie computationnelle. On remarque que ces méthodes impliquent un coût de calcul supplémentaire par rapport à des situations déterministes. Une approche par réduction de modèles peut alors être envisagée pour atteindre ces performances en temps réel. Toutefois, ces approches ne parviennent pas systématiquement à obtenir une représentation de faible rang du modèle, c'est-à-dire à le réduire, et donc à accélérer notablement le temps de calcul. C'est le cas lors de la simulation électro-chirurgicale, ainsi que dans de nombreux autres problèmes présentant des discontinuités en mouvement. C'est pourquoi une approche alternative fondée sur la métamodèlisation est introduite dans le Chapitre 7. Un métamodèle consiste à déterminer les équations régissant l'évolution de quantités d'intérêt plutôt que de se soucier des variables d'état du système. Pour élaborer notre approche, nous nous plaçons dans le cadre de la simulation de l'ablation par radiofréquence. Cette procédure médicale mini-invasive implique l'insertion d'un cathéter dans la zone que l'on désire détruire. Des pulsations électriques sont alors appliquées à la pointe du cathéter afin de provoquer une augmentation de la température, et, par conséquent, la nécrose des tissus. La limite principale de cette approche est l'estimation de la zone nécrosée. En effet, le praticien se base principalement sur son expérience pour estimer le temps nécessaire afin d'obtenir le résultat voulu. En vue de lui fournir un support de décision intra-opératoire, il est possible de simuler les interactions électro-thermo-physiologiques régissant l'évolution de la nécrose. Toutefois, ces simulations sont hautement non linéaires et comportent des couplages forts entre les différentes lois physiques du problème, ce qui requière des moyens de calcul importants. Les méthodes de réduction de modèles classiques sont inefficaces à cause de la présence de discontinuités de certains champs physiques, qui évoluent au cours de l'opération. C'est pourquoi le choix du métamodèle est fait. Dans ce contexte, l'utilisation de techniques de régression parcimonieuse, qui se sont récemment révélées efficaces dans l'identification de modèles déterministes, est étendue au cas des systèmes à paramètres stochastiques. Nous montrons que dans des conditions d'échantillonnage appropriées, une régression parcimonieuse peut permettre d'identifier un modèle pour la réponse moyenne du système. Nous sommes alors capables d'estimer en temps réel et de manière dynamique l'évolution moyenne de la nécrose par rapport à des paramètres matériaux distribués suivant des lois de probabilités connues. Néanmoins, aucune procédure estimant la convergence du métamodèle n'est mise en place. De plus la méthode ne prend en compte que le comportement moyenné et n'est pas capable d'évaluer la variance qui lui est associée. Cela ouvre des perspectives intéressantes pour de futurs développements.

# Remerciements

Je tiens tout d'abord à remercier les personnes sans qui cette thèse n'aurait pas été possible, c'est-à-dire Francisco Chinesta et Domenico Borzacchiello, qui ont été respectivement directeur et encadrant de la thèse. Merci à M. Chinesta pour m'avoir permis de réaliser cette thèse sous sa direction et pour m'avoir offert la possibilité de travailler sur un sujet qui me passionne et me motive. Merci à M. Borzacchiello pour avoir pris le temps de m'encadrer au jour le jour et de m'avoir fait profiter de ses vastes connaissances et capacités pédagogiques, dont, je l'espère, j'ai su m'imprégner.

Ensuite, merci aux membres du jury qui ont accepté d'évaluer mon travail et d'être ainsi les garants de sa qualité de par leur expertise. En premier lieu, je tiens à remercier les rapporteurs, M. Avril et Mme. Grandmont. Un merci en particulier à M. Avril qui a aussi endossé le rôle de président jury. Je remercie aussi bien évidemment M. Cueto et M. Nadal qui ont pu apporter un point de vue critique sur la partie numérique de mon travail, notamment sur les méthodes de réduction de modèles, et M. Hostettler, qui a su mettre en perspective les méthodes développées dans ce manuscrit dans une optique d'application au sein du bloc opératoire.

Cette thèse ayant été financée dans le cadre du projet 3D-Surg, merci à tous les acteurs qui s'engagent pour développer et imaginer la chirurgie de demain. Merci au programme Investissement d'Avenir, à la BPI ainsi qu'à l'IRCAD (Institut de Recherche contre le Cancer de l'Appareil Digestif). En particulier, je remercie les personnes que j'ai pu rencontrer au sein de ce projet et qui m'ont apporté de nombreuses perspectives de développement et d'orientation quant aux méthodes introduites dans ce manuscrit. Merci donc à Yves Rémond, Daniel George et Michael Kugler du laboratoire iCube (Université de Strasbourg) ainsi qu'à Toby Collins et Alexandre Hostettler de l'IRCAD. Un second merci aux membres de l'IRCAD pour les nombreuses données médicales qu'ils nous ont fournies et qui ont été indispensables au bon déroulement de mes travaux.

Un grand merci aux personnes que j'ai côtoyées tous les jours durant ces trois années. Merci notamment aux membres de l'Institut de Calcul Intensif, à sa directrice, Luisa, et à ses membres, qu'ils fassent partie de l'équipe de recherche : Brice, Hugues, Jose, ou bien de l'équipe de gestion du supercalculateur : Pierre-Emmanuel et Richard, ou encore à Florence, gestionnaire du laboratoire. Merci évidemment à tous les doctorants avec qui j'ai passé d'excellents moments et ai bien ri, notamment lors de la pause-café matinale quasi-obligatoire ainsi que durant les nombreuses parties de belotte. Pour les citer dans le désordre mais dans l'ordre alphabétique : Adrien, Alexandre, Amélie, Baptiste, Carlos, Etienne, Gatien, Imad, Julie, Louis, Marie, Nesrine, Nicolas, Thomas B. et Thomas C. Merci aussi à mes colocataires, qui, pour certain.e.s, ont aussi été des collègues de travail, et qui ont rendu ces trois années à Nantes très agréables aussi bien pendant qu'en dehors du travail.

Je remercie bien sûr ma famille qui m'a toujours soutenu dans mes choix et m'a permis de réaliser cette thèse dans les meilleures conditions. Merci en particulier à mon grand-père Henri qui m'a transmis un intérêt pour la recherche bien des années avant cette thèse, ce qui a éveillé ma curiosité et mon goût des sciences. Je suis heureux aujourd'hui de finaliser ce travail que j'envisageais depuis si longtemps. Enfin, merci à Claire, avec qui j'ai passé, je passe et je passerai encore des moments qui me sont chers.

Encore merci à toutes et à tous,
Nathan Lauzeral

# Contents

# List of abbreviations

| | |
|---|---|
| **1D** | One dimension |
| **2D** | Two dimensions |
| **3D** | Three dimensions |
| **AR** | Augmented Reality *or* Aspect Ratio (only in Chapter 2) |
| **CT** | Computed Tomography |
| **EKF** | Extended Kalman Filter |
| **FE** | Finite Element |
| **FEM** | Finite Element Method |
| **FEMWARP** | Finite Element-based Mesh WARPing |
| **FOCUSS** | FOCal Underdetermined System Solver |
| **GOMP** | Greedy Orthogonal Matching Pursuit |
| **GPU** | Graphics Processing Unit |
| **ICP** | Iterative Closest Point |
| **iFEMWARP** | Iterative FEMWARP |
| **IRCAD** | Research Institute against Digestive Cancer |
| **IUQ** | Inverse Uncertainty Quantification |
| **KF** | Kalman Filter |
| **LHS** | Latin Hypercube Sampling |
| **MIS** | Minimally Invasive Surgery |
| **MOR** | Model Order Reduction |
| **MRI** | Magnetic Resonance Image |
| **MSM** | Mass Spring Model |
| **nnFOCUSS** | Non-negative FOCUSS |
| **OR** | Operating Room |
| **PC** | Polynomial Chaos |
| **PCA** | Principal Component Analysis |
| **PDM** | Point Distribution Model |
| **PGD** | Proper Generalized Decomposition |
| **POD** | Proper Orthogonal Decomposition |
| **pROM** | Parametric Reduced Order Model |
| **RB** | Reduced Basis |
| **RBF** | Radial Basis Function |
| **RFA** | Radiofrequency Ablation |
| **RIC** | Relative Information Content |
| **RID** | Reduced Integration Domain |

**ROM** . . . . . Reduced Order Model
**SCM** . . . . . Stochastic Collocation Method
**SINDy** . . . . . Sparse Identification of Nonlinear Dynamics
**SLAM** . . . . . Simultaneous Localization and Mapping
**SSA** . . . . . Statistical Shape Analysis
**SSL** . . . . . Sparse Subspace Learning
**SSM** . . . . . Statistical Shape Model
**SSR** . . . . . Stochastic Sparse Regression
**SVD** . . . . . Singular Value Decomposition
**TPS** . . . . . Thin Plate Spline
**TPS-PR** . . . . . Thin Plate Spline Parametrized Registration
**VOE** . . . . . Volumetric Overlap Error

# List of symbols

*The main symbols are reported for each part in order of appearance. The same symbol may be used in different parts with different meanings.*

## General notations

- The scalars are represented by italic letters such as $x$.
- The vectors are represented by bold italic letters such as $\boldsymbol{x}$.
- The tensors of order 2 or more are represented by capital non-italic bold letters such as $\mathbf{X}$.
- The identity matrix is noted $\mathbf{I}$.
- The $i \times j$ matrix of zeros is noted $\mathbf{0}_{i \times j}$.
- The $i \times j$ matrix of ones is noted $\mathbf{1}_{i \times j}$.
- The transpose of a matrix is noted $\bullet^T$.
- The $\ell^p$-norm is noted $||\cdot||_p$.

## Part I

### Chapter 1

$\boldsymbol{X}$ . . . . . Generic point cloud describing a shape

$(x_i, y_i, z_i)$ . . . . . Position of the $i$-th point in three-dimensions

$\boldsymbol{S}_0$ . . . . . Template shape

$\boldsymbol{T}$, $\boldsymbol{T}_i$ . . . . . ($i$-th) target shape

$N_T$ . . . . . Number of target shapes

$\mathbf{R}_i$ . . . . . Rotation matrix associated to the $i$-th shape

$\boldsymbol{S}$, $\boldsymbol{S}_i$ . . . . . ($i$-th) deformed template shape

$I_f$ . . . . . Bending energy of the thin plate spline method

$I(\bullet)$ . . . . . Functional minimized in the nonrigid registration

$f$ . . . . . Thin plate spline interpolant

$\boldsymbol{s}_i$ . . . . . $i$-th point belonging to a deformed template shape

$\boldsymbol{t}_i$ . . . . . $i$-th point belonging to a target shape

$n_S$ . . . . . Number of points in the template shape

$\gamma_f$ . . . . . Thin plate spline regularization parameter

$\bar{\boldsymbol{S}}$ . . . . . Mean deformed shape

$\boldsymbol{\phi}_i$ . . . . . $i$-th mode of variation of a shape

$\lambda_i$ . . . . . Variance associated to $\phi_i$

$n_p$ . . . . . Number of modes describing a shape

$\tilde{\boldsymbol{S}}$ . . . . . Parametrized shape

$\boldsymbol{\alpha} = (\alpha_1, \cdots, \alpha_{n_p})$ . . . . Vector containing the shape parameters

$h$ . . . . . Threshold for the selection of the number of modes

## Chapter 2

$I_{match}(\boldsymbol{u})$ . . . . . Point matching term of the functional $I(\bullet)$

$I_{tps}(\boldsymbol{u})$ . . . . . Shape bending energy term of the functional $I(\bullet)$

$\boldsymbol{u}$ . . . . . Displacement vector such as $\boldsymbol{S} = \boldsymbol{S}_0 + \boldsymbol{u}$

$\boldsymbol{d}$ . . . . . Distance vector between $\boldsymbol{S}_0$ and $\boldsymbol{T}$

$\boldsymbol{a}$ . . . . . Control points of the regular grid parametrizing the deformation of the template shape

$\mathbf{L}$ . . . . . Biharmonic operator representing the thin plate spline bending energy

$\mathbf{A}$ . . . . . Interpolation operator between $\boldsymbol{u}$ and $\boldsymbol{a}$

$n_b$ . . . . . Discretization of the regular grid containing the control points used in the TPS-PR algorithm

$\gamma$ . . . . . TPS-PR regularization parameter

$\gamma_r$ . . . . . User-defined ratio between the maximum matching and bending energies used to defined $\gamma$ in the TPS-PR algorithm

$\boldsymbol{\phi}_i^b$ . . . . . $i$-th mode of variation of the control points representing a shape

$\tilde{\boldsymbol{a}}$ . . . . . Representation of $\boldsymbol{a}$ in the reduced basis

$\boldsymbol{\Phi}$ . . . . . Matrix containing the modes $\boldsymbol{\phi}_i^b$

## Chapter 3

$n_V$ . . . . . Number of nodes in the template mesh (surface and volume)

$\boldsymbol{u}_d$ . . . . . User-prescribed motion on the surface of the liver to represent the breathing motion

$\boldsymbol{p} = (p_1, \cdots, p_D)$ . . . . . Vector containing the explicit parameters

$D$ . . . . . Number of explicit parameters

$b$ . . . . . Breathing parameter ($b \in [0, 1]$)

$\left(r, \theta_1, \cdots, \theta_{n_p-1}\right)$ . . . . Parametric representation of a shape in the hyper-ellipsoid

$\mathcal{T}$ . . . . . Transformation function such as $\boldsymbol{\alpha} = \mathcal{T}\left(r, \theta_1, \cdots, \theta_{n_p-1}\right)$

$n_c$ . . . . . Number of collocation points at a given hierarchical level of the Smolyak's quadrature rule

$P_j^i$ . . . . . $j$-th point of the set of points defining the Smolyak's quadrature rule at the $i$-th hierarchical level

$\mathcal{P}$, $\mathcal{P}^i$ . . . . . Solution of the SSL (at the $i$-th hierarchical level)

$E_p$ . . . . . Representation error caused by the projection on a reduced basis

$E_{SSL}$ . . . . . Representation error due to the SSL approximation

# Part II

## Chapter 4

| | |
|---|---|
| $\Omega$ | Integration domain |
| $n_q$ | Number of quadrature points |
| $\boldsymbol{a}_i$ | $i$-th quadrature point |
| $c_i$ | $i$-th quadrature weight |
| $g(\boldsymbol{x}_k, \boldsymbol{u}_k)$ | Function actualizing the system's state in the KF |
| $\boldsymbol{x}_k$ | State of the system of the KF at iteration $k$ |
| $\mathbf{G}_k$ | Jacobian of $g(\boldsymbol{x}_k, \boldsymbol{u}_k)$ w.r.t. $\boldsymbol{x}$ |
| $\boldsymbol{u}_k$ | Control vector of the KF at iteration $k$ |
| $\mathbf{O}_k$ | Linear operator modeling the effect of the control vector at iteration $k$ |
| $\boldsymbol{w}_k$ | Process noise of the KF at iteration $k$ |
| $\mathbf{Q}_k$ | Covariance matrix of the process noise of the KF at iteration $k$ |
| $h(\boldsymbol{x}_k)$ | Function mapping the state space into the observed space in the KF |
| $\boldsymbol{y}_k$ | Observation vector of the KF at iteration $k$ |
| $\mathbf{H}_k$ | Jacobian of $h(\boldsymbol{x}_k)$ w.r.t. $\boldsymbol{x}$ |
| $\boldsymbol{v}_k$ | Observation noise of the KF at iteration $k$ |
| $\mathbf{R}_k$ | Covariance matrix of the observation noise of the KF at iteration $k$ |
| $\mathbf{P}_k$ | Covariance estimate matrix of the KF at iteration $k$ |
| $\mathbf{K}_k$ | Kalman gain at iteration $k$ |

## Chapter 5

| | |
|---|---|
| $\Psi$ | Strain energy density |
| $n_v$ | Number of nodes in the mesh |
| $\boldsymbol{X}$ | Position of the deformed mesh |
| $\boldsymbol{X}_0$ | Initial position of the mesh |
| $\boldsymbol{u}$ | Displacement vector such as $\boldsymbol{u} = \boldsymbol{X} - \boldsymbol{X}_0$ |
| $(E, \nu)$ | Young modulus and Poisson ratio characterizing the Saint Venant-Kirchhoff material |
| $(C_1, C_2)$ | Material parameters characterizing the Veronda-Westmann material |
| $\Pi$ | Strain energy |
| $P$ | Pressure |
| $\boldsymbol{\alpha}$ | Reduced degrees of freedom of the displacement in the POD's basis |
| $\lambda_i$ | $i$-th singular value of the SVD |
| $h$ | Threshold for the truncation of the POD |
| $r$ | Truncation order of the POD's basis |
| $\boldsymbol{\Phi}_r$ | Reduced basis containing the modes of deformation |
| $n_{hr}$ | Number of points in the reduced quadrature rule |
| $\boldsymbol{b}_i$ | $i$-th point of the reduced quadrature rule |
| $d_i$ | $i$-th weight of the reduced quadrature rule |

| | |
|---|---|
| $n_e$ | Number of elements in the finite element discretization of the domain |
| $\boldsymbol{q}$ | Input of the sparse approximation |
| $\Theta$ | Dictionary of the sparse approximation |
| $\boldsymbol{\xi}$ | Solution of the sparse regression |
| $p$ | Value of the $\ell^p$-norm employed in the sparse regression |
| $\gamma$ | Regularization parameter of the sparse regression |
| $\Omega_r$ | Reduced integration domain |
| $\mathbf{B}$ | Hessian matrix of $\Pi(\boldsymbol{\alpha})$ w.r.t. $\boldsymbol{\alpha}$ |
| $(h_g, h_s)$ | Thresholds for the convergence of the minimization algorithm |
| $E_a$ | Young modulus of the abdominal cavity |
| $\boldsymbol{t} = (t_x, t_y, t_z)^T$ | Vector of the rigid translation |
| $\boldsymbol{r} = (r_x, r_y, r_z)^T$ | Vector of the rigid rotation |
| $\hat{\boldsymbol{\alpha}}$ | Solution of the strain energy minimization in the reduced basis |
| $\boldsymbol{m}_i = (m_{ix}, m_{iy}, m_{iz})^T$ | Position of the $i$-th measured point |
| $M$ | Number of measured points |
| $\sigma_{mp}$ | Standard deviation of the Gaussian noise associated to the measurement of the points' position |
| $\sigma_P$ | Standard deviation of the Gaussian noise associated to the measurement of the pressure |
| $h_m(\boldsymbol{x})$ | Function mapping the state vector into the space of the measured points $\boldsymbol{m}_i$ |
| $\boldsymbol{d}_b$ | Tumor's barycenter |

# Part III

## Chapter 6

| | |
|---|---|
| $\boldsymbol{X}$ | Random vector of variables |
| $g(\boldsymbol{X})$ | Mathematical function defining a system |
| $\Omega_{\boldsymbol{X}}$ | Sample space of $\boldsymbol{X}$ |
| $\mathcal{F}$ | Set of event of $\boldsymbol{X}$ |
| $P_{\boldsymbol{X}}$ | Probability measure of $\boldsymbol{X}$ |
| $Y$ | Random variable such as $Y = g(\boldsymbol{X})$ |
| $f_{\boldsymbol{X}}, f_Y$ | Density probability of $\boldsymbol{X}$, resp. $Y$ |
| $(\boldsymbol{x}_1, \cdots, \boldsymbol{x}_n)$ | Samples of $\boldsymbol{X}$ in $\mathbb{R}^q$ |
| $(y_1, \cdots, y_n)$ | Samples of $Y$ such as $y_i = g(\boldsymbol{x}_i)$ |
| $\bar{\boldsymbol{x}}, \bar{y}$ | Expectation of $\boldsymbol{X}$, resp. $Y$ |
| $\sigma_{\boldsymbol{X}}, \sigma_Y$ | Standard deviation of $\boldsymbol{X}$, resp. $Y$ |

## Chapter 7

| | |
|---|---|
| $t$ | Time |
| $T$ | Temperature |
| $\phi$ | Electrical potential |

| | |
|---|---|
| $\Omega$ | Thermal damage |
| $DS$ | Degree of vascular stasis (i.e. coagulation) |
| $\sigma(T)$ | Electrical conductivity |
| $\kappa(T)$ | Thermal conductivity |
| $\rho$ | Tissue density |
| $h$ | Enthalpy |
| $T_b$ | Blood temperature |
| $\rho_b$ | Blood density |
| $c_b$ | Specific heat of blood |
| $\omega_b(\Omega)$ | Blood perfusion rate |
| $\sigma_{37}$ | Electrical conductivity at 37°C |
| $\kappa_{37}$ | Thermal conductivity at 37°C |
| $\omega_{b0}$ | Baseline blood perfusion rate |
| $q_h$ | Joule heating term |
| $R$ | Universal gas constant |
| $A$ | Frequency factor |
| $\Delta E$ | Activation energy |
| $\Omega_e$ | Electrode's surface |
| $\Omega_l$ | Liver's surface |
| $Z$ | Impedance |
| $I$ | Pulse's current intensity |
| $h_{elec}$ | Heat transfer coefficient between the electrode and the tissue |
| $T_{elec}$ | Temperature of the electrode |
| $n_s$ | Number of snapshots in the database |
| $\boldsymbol{\alpha}$ | Reduced degrees of freedom in the POD's basis |
| $\boldsymbol{\Phi}$ | Reduced basis containing the modes of the POD |
| $h$ | Threshold for the truncation of the POD |
| $r$ | Truncation order of the POD's basis |
| $x(t)$ | System's state |
| $m$ | Number of temporal time steps |
| $f$ | Dynamic behavior of the system |
| $\boldsymbol{v}(t)$ | Measurements of the system |
| $n_v$ | Number of measured entities |
| $\boldsymbol{V}$ | Measurement matrix |
| $\dot{x}(t)$ | System's state derivative |
| $\Theta$ | Dictionary of the sparse approximation |
| $d$ | Degree of the polynomial candidate functions of the dictionary |
| $n$ | Number of atoms in the dictionary |
| $\boldsymbol{\xi}$ | Solution of the sparse regression |
| $p$ | Value of the $\ell^p$-norm employed in the sparse regression |
| $\gamma$ | Regularization parameter of the sparse regression |
| $\boldsymbol{\theta}$ | Time-independent stochastic parameters |

| | |
|---|---|
| $(h_1, \cdots, h_{n_v+1})$ . . . . . | Bandwidths for the weighted least-squares sparse regression |
| $Q(t)$ . . . . . | Electrical energy |
| $P(t)$ . . . . . | Average power |
| $e$ . . . . . | Error metric for one simulation |
| $E$ . . . . . | Error metric over the left-out set of simulations |
| $d_m$ . . . . . | Euclidean distance from the mean set of parameters |
| $n_t$ . . . . . | Number of sparse regressions for a given value of $p$ |

# Introduction

## General context

The development of computer science in the second part of the 20th century has revolutionized many scientific domains. In particular, it has allowed in the medical field the emergence of the so-called *computational surgery*. The surgical concept has to be understood in a broad sense. It encompasses the surgical act within the operation room, but also the diagnostic, the surgical planning, the patient's recovery, the operation evaluation, and even the prediction of the surgery's outcomes. At each stage, computer science has been used as decision-making support and to alleviate human bias. This support takes many forms. It can be the guiding of robotics systems or the imagery acquisition methods; it is also the modeling of the human organs and their physiological behaviors at different scales, ranging from the musculoskeletal mechanics to the molecular biology along with the hemodynamics or the bioelectricity. Computational surgery is then at the crossroad of many disciplines such as biology, numerical analysis, robotics or data science. It is in this fertile context the thesis takes its roots, in the framework of the project 3D-Surg (see Figure 1). This latter aims at developing the three-dimensional (3D) modeling and visualization of the patient from its medical images combining both real and virtual environments. The 3D modeling of the patient offers many advantages. The most basic application may be the enhancing of the vision during minimally invasive surgery. In such procedures, the surgeon's field of view is often limited because there is no direct visual access to the area of interest. Endoscopes are used to provide minimum visual feedback but an important mental effort is asked to the surgeon for the 3D representation of the scene. Thanks to 3D modeling, a complete representation of the inner structures of the body can be displayed on a TV monitor, augmented reality glasses or directly projected onto the patient's body. Nonetheless, to get a realistic display, the images cannot be solely a static representation of the patient's organs. The biophysical phenomenon of different scales shall be embedded within the model. To do so, an *in silico* replica of the patient must be created. In the literature, many terms are employed to describe this concept. In the case of educational training, the term *virtual patient* is mainly employed, for *in situ* operations the terms *patient avatar* or *patient digital twin* are preferred. They all refer to a digital counterpart of the patient, that can reproduce and adapt its physical state in real-time from external measurements. This digital counterpart ideally contains all the relevant entities composing the biological systems of interest. The behavior of each entity is driven by the physical laws and the medical data, but also by its interaction with the other entities. The result is a complex system, where data integration and physical interaction must be coupled in real-time with high levels of accuracy and reliability. Thanks to such a tool, the intraoperative scene can be enhanced with the visualization of the tissues' deformation, but also with more advanced features concerning the blood flow, the body heat or the propagation of a drug, for example. It permits the clinician to have better control over the operation and to reduce the risk of perioperative morbidity and mortality.

The thesis aims at tackling the subject of the creation of organ digital twins through the prism of model order reduction (MOR) methods. MOR methods are interesting for three reasons. First, their main interest is that they allow accelerating the simulations to reach real-time solving. This condition is essential for visualization as, to get an impression of fluidity, a frame rate of 25 Hz is required. More complex, in haptic applications, it is a 1000 Hz frequency that is needed. Such frequencies are generally incompatible with standard simulations method unless the model is simplified or specific hardware is employed. The remaining interests of the MOR methods are precisely that they do not require any simplification of the model, nor any expensive equipment. They are

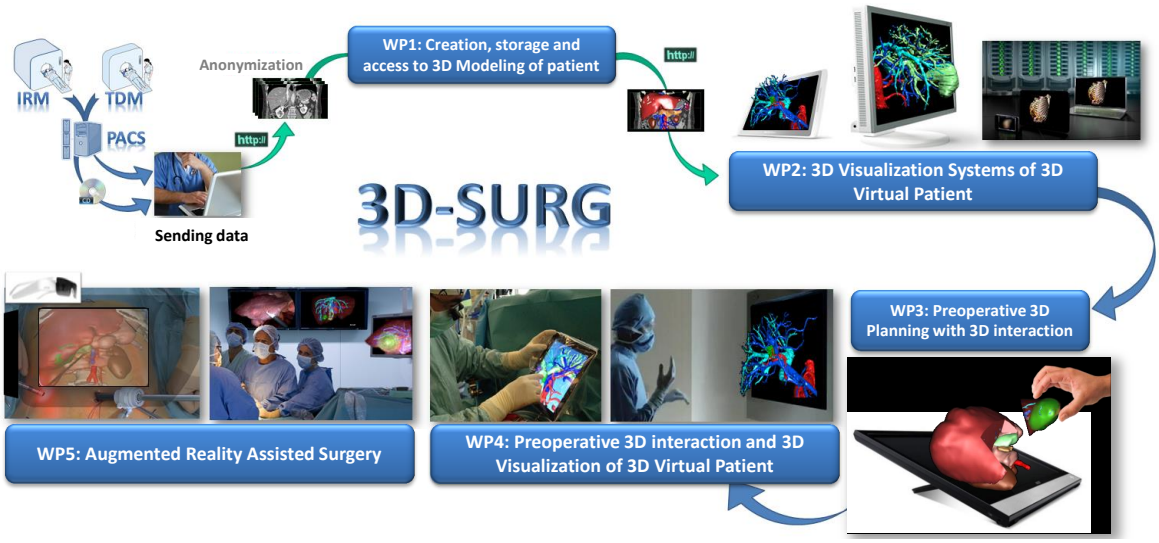


Figure 1: The 3D-Surg project contains five sequential workpackages (WP). They go from the initial data acquisition to the augmented reality setup in the operating room. The thesis is focused on the first workpackage. It consists in creating and stocking the 3D model of the patient. The image comes from http://www.3d-surg.eu/.

conceived to increase the computational speed without simplifying the underlying physics. Moreover, they provide a compact representation of the solution in terms of data size and necessitate very low computational resources to be run. In general, the solution weights only a few megabytes and can be used on smartphones or tablets. Unfortunately, the use of MOR methods in a medical context is not straightforward. We identified three major challenges related to the construction of organ's digital twins based on MOR methods. For each, a new numerical strategy has been proposed involving the use of sparsity-related techniques. Indeed, if the MOR methods are emphasized during this thesis, the notion of sparsity will be the underlying common thread during the manuscript.

The first contribution of this thesis is the integration of the anatomical shape representation within the reduced order model (ROM). A faithful anatomical representation is primordial for the accurate modeling of the patient. Standard approaches tend to recreate the ROM from scratch for each new case. This makes the procedure cumbersome and time-consuming. Ideally, the ROM must be automatically adaptable to the patient's anatomy. Based on statistical shape modeling and a dataset of medical images, we tackle the challenge of embedding the shape variability into the ROM and propose a new methodology to integrate the shape parametrization within the formulation of the ROM. To this end, a new procedure is developed to generate the computational model from the shape parametrization. It combines an original approach for non-rigid registration with a mesh quality-based morphing method. Also, the emphasis is put on the construction of the parametric domain, in particular for methods relying on tensor structures. An efficient sampling strategy is set up in the context of the sparse subspace learning approach for ellipsoid-shaped parametric spaces. The method is successfully applied in the case of the liver deformation during the breathing.

The second contribution of this thesis tackles the issue of the treatment of partial and erroneous medical data. Indeed, in the medical framework, the restrictive conditions lead to an almost systematic lack of knowledge. This is particularly true in minimally invasive procedures. However, these data can be completed thanks to the hypothesis of known physical behavior. By using mathematical models embedding these physical priors, the data can be regularized through a restriction of the search space. Nonetheless, the choice of the model and its parameters is tricky as the quality of the reconstruction depends on them. In this context, we propose a solution for the problem of deformable 3D shape registration based on incomplete image data. A potential application lies in the framework of laparoscopic scene reconstruction, that we use to evaluate our method. We

employ a semi-intrusive approach to introduce hyperreduced models in the computational core of an extended Kalman filter. To this end, a new hyperreduction technique based on a non-negative sparse approximation method is developed. The constitutive behavior of the model is assumed to be known but no a priori is given on its parameters. The results show how a strong identification of the physical model, which would be prone to overfitting errors, is not necessary to obtain acceptable results.

The last contribution of this thesis is the treatment of parameter uncertainty in biophysical systems. These latter are often characterized by moving discontinuities in the spatial domain. MOR methods generally fail in their reduction. To circumvent this issue, the route of metamodeling is preferred. Instead of seeking to represent the state variable of the system in a reduced subspace, metamodels aim to find new governing equations for specific variables of interest. Sparsity promoting techniques have proven to be powerful tools for the representation of the underlying dynamics of deterministic systems. We propose to extend their application in the case of stochastic parameters in the context of radiofrequency ablation. Results show the ability of the method to propagate the uncertainty of the parameters for real-time solutions.

## Structure of the thesis

This thesis is structured in three parts, each one deals with one of the aforementioned challenges. Each part contains an introductory chapter dedicated to the context introduction and the description of the main methods and their application in the concerned framework. It is followed by one or two chapters presenting the solutions we propose, applied to a well-chosen medical procedure. These result chapters are organized as scientific articles, hence, for the sack of completeness, some information may be redundant between some chapters. All parts end with a partial conclusion that comes back to the numerical challenges covered.

Part I is composed of three chapters. Chapter 1 introduces the concept of parametric organ modeling and highlights some contributions in the field of MOR. In Chapter 2 we develop our framework for the creation of parametric organ modeling based on medical images. It is used as a basis for the creation of an anatomy-specific and real-time deformable model of the liver in Chapter 3. Then, Part II contains two chapters. In Chapter 4 the need to introduce physical priors as a means to complete the data is evidenced. The concept of the inverse problem is presented and illustrated in the context of laparoscopic surgery. In Chapter 5, a solution for the problem of deformable 3D shape registration based on incomplete image data is proposed. The ill-posed problem of the static 3D scene reconstruction in laparoscopy is addressed. Next, Part III is divided into two chapters. Chapter 6 is devoted to the introduction of uncertainty propagation and its use for real-time applications. In Chapter 7, a new solution based on metamodeling is proposed in the context of radiofrequency ablation. Finally, the conclusion chapter summarizes the main contributions of the thesis and discusses some possibilities for future development.

## List of publications

These thesis works have generated the following publications:

- N. Lauzeral, D. Borzacchiello, M. Kugler, D. George, Y. Rémond, A. Hostettler, F. Chinesta. Shape parametrization of biomechanical finite element models based on medical images. *Computer Methods in Biomechanics and Biomedical Engineering: Imaging & Visualization*, pages 1-10, 2018.

- N. Lauzeral, D. Borzacchiello, M. Kugler, D. George, Y. Rémond, A. Hostettler, F. Chinesta. A model order reduction approach to create patient-specific mechanical models of human liver in computational medicine applications. *Computer methods and programs in biomedicine*, 170:95-106, 2019.

- N. Lauzeral, D. Borzacchiello. An extended Kalman filter based on hyperreduction for three-dimensional medical image completion embedding physical priors. *In progress.*

- N. Lauzeral, D. Borzacchiello. A metamodeling approach to study radiofrequency ablation outcomes under uncertainty of the model's parameters. *In progress.*

## Collaborations

In the context of the 3D-Surg project, this thesis has been the opportunity to collaborate with:

- The Research Institute against Digestive Cancer (IRCAD), in Strasbourg, France. In particular, with Alexandre Hostettler, thanks to whom we had access to a database of livers' shapes and had the opportunity to gain more insight into the clinical practices by visiting their facilities.
- The ICube laboratory of the University of Strasbourg and, in particular, with Yves Rémond, Daniel George and Michaël Kugler, with whom the initial research focus of this thesis have been determined.

## Software development

Unless stated otherwise, all the simulation results presented in this thesis were generated using proprietary research codes owned by the High Performance Institute. In this sense, this thesis work has been the opportunity to develop several tools that will be useful to the members of the laboratory. The principal contributions are:

- A nonrigid shape registration and morphing library.
- A sampling algorithm for the sparse subspace learning method for hyperellipsoid parametric spaces.
- A library for extended Kalman filtering.
- A coupled nonlinear finite element solver for electrosurgery.
- A toolbox for sparse regression techniques.

All the codes were done in Matlab (The MathWorks, Inc., USA). A part of the simulations were performed using the high-performance computing resources of the Centrale Nantes Supercomputing Centre on the cluster Liger.

# Part I

# Patient-specific anatomical modeling

Chapter 1

# Introduction to parametric organ modeling

**Abstract** Ideally, an organ's digital twin must be automatically adaptable to any new patient. This can be achieved using parametric organ models. After introducing the concept of parametric organ modeling and its use in computational surgery, we show the lack of shape-parametric organ reduced order models based on real medical images in the literature. To introduce the solution we propose in Chapters 2 and 3, the process to create parametric organ models is then introduced from a statistical perspective. First, a short overview of medical image acquisition techniques is done. It is followed by the presentation of the concept of statistical shape analysis which allows parametrizing the organs' shape. Finally, morphing methods to automatically create organs' models from this parametrization are presented.

**Contents**



## 1.1 The importance of accurate organ modeling

A "parametric organ model" refers to the model of an organ that can be automatically generated through a parametrization of its features. These features are most of the time the material parameters and the shape, i.e. the external surface of the model. In this chapter, we consider that the models are used in a finite element (FE) framework. As adapting the material properties in FE models is generally straightforward, the state-of-the-art is focused on the shape representation. A FE model is defined by a geometry, in the case of an organ a three-dimensional (3D) mesh, material properties, and boundary conditions used to represent the constraints applied on the system (loads, imposed displacements, ...).

The first need for parametric models is the coverage of shape variations into a population, e.g. for the design of consumer equipment. From a historical perspective, it has been particularly important in the conception of motor-vehicles and has generated a lot of studies [127]. Indeed, the safety measures are taken accordingly to the results obtained from the models used for the crash

tests or simulations, thus the need to be able to represent the whole population. A simple example of the importance of using different models is, that according to Kent et al. in [139] 1.13-1.32 million fewer car occupant would be injured per year in the United States of America if they had the same physical state than a 20 years old occupant. Consequently, using a unique model for crash simulations is not conceivable. The size and weight of the occupant are also important. Newgard et al. [196] showed that the airbag deployment effectiveness is related to the height and that smaller occupants have higher chances of injuries. Several studies also showed that obese occupants are at higher risk of fatality and injury in frontal crashes [68, 246]. In a study about the effect of age, body mass index and gender on the severity of injuries in motor-vehicles crashes, Carter et al. [50] conclude by stressing out the need for broader computational models to encompass all the variations among the population. Hence, parametric organ models are useful to adapt the simulations that result in the design of many types of equipment. The assessment of shape variation is also pertinent at the individual scale. Indeed, the shape of an organ is never perfectly determined. This can be caused by the image acquisition method but also by the deformation of soft bodies or by biophysiological processes (e.g. tumor growth). In the surgical framework, using several models can help to understand the impact of the shape estimation on values of interest. For example, in [135] the authors show that the destruction of tumors by radiofrequency ablation depends nonlinearly on the size of these latter. This concept, known as uncertainty propagation, is developed in Part III.

More specific to the surgical act, the second need for parametric organ models is to accelerate and personalize further the modeling of the patient for preoperative and intraoperative simulations. As introduced in Section 1.3, preoperative data generally consist in magnetic resonance images (MRIs) or computed tomography (CT) scans. From this data, postprocessing must be done to turn the images into a 3D mesh and to label the area of interest for boundary conditions assignment. The process of extracting a shape from such data is called *segmentation*. In [121] several segmentation methods are compared for CT data. It appears that methods based on statistical shape models (SSMs) perform the best. This statistical approach is the same as the one used to generate the parametrization of organ models, described in Section 1.4. This latter is then used with morphing techniques to generate the parametric organ models (see Section 1.5). Consequently, the use of parametric organ modeling could be used directly to postprocess the medical images and generate the FE model, automatizing the cumbersome stage of mesh generation. It would furthermore relieve the user from defining the boundary conditions, as they can be extrapolated from a *template* mesh, also called *atlas*, to the newly generated models [225].

Finally, to go further into the simulation application, the parametric organ model can be embedded within real-time simulators. Such tools offer many opportunities. For example, they can be used for the shape optimization of prostheses and allow a fast customization [230]. They can also be used for quick diagnostics, especially in the prevention of diseases based on anatomical features [91]. Furthermore, they can - and are already - be used for the preoperative training of the surgeons and as a teaching material for the students to practice on [71]. Finally, in the near future, they will certainly be commonly employed as the simulation cores of patient digital twins to enhance the surgeon's perception within the operating room [25]. To introduce the methods enabling shape parametrized real-time simulations, a short bibliography is presented in the following section. In particular, the emphasis is put on model order reduction (MOR) methods.

## 1.2 Shape-parametric reduced order modeling

In this section, we review some of the methods developed to introduce the shape parametrization into reduced order models (ROMs). Table 1.1 gives an overview of some of these methods applied in the context of computational surgery.

Most of the MOR methods belong to the so-called projection-based methods. In brief, they rely on the projection of the model equations - or the solutions - onto a low dimensional basis, or manifold. The most common ones are the proper orthogonal decomposition (POD) [54], the reduced basis (RB) [229] and the proper generalized decomposition (PGD) [60]. As all MOR methods, they involve a parametric formulation of the problem. In particular, the POD and the

RB belong to the so-called *a posteriori* MOR methods. They require a database of solutions, called the *snapshots*, from which they identify a common lower-dimensional subspace. The search for new solutions is then restricted to this manifold which allows accelerating the computations. The PGD has a similar goal but belongs to the *a priori* methods. It assumes the solution can be written as a separated representation of the input parameters, known as the canonical tensor format. From this assumption and the knowledge of the system's governing equations, it iteratively computes the most compact separated representation that respects the system's equations. Used in their standard form, all these methods require to be affine with respect to the model's parameters, it is referred to as *affine parametric dependence*. To illustrate this statement let consider the weak form of the Poisson equation. We seek the solution $u(\boldsymbol{\mu}) \in \mathbb{V}$ for any parameter $\boldsymbol{\mu}$ such as

$$a(u(\boldsymbol{\mu}), v; \boldsymbol{\mu}) = b(v; \boldsymbol{\mu}) \quad \forall v \in \mathbb{V} \tag{1.1}$$

where

$$a(u(\boldsymbol{\mu}), v; \boldsymbol{\mu}) = \int_\Omega (\boldsymbol{\nabla} u(\boldsymbol{\mu}) \cdot \boldsymbol{\nabla} v) d\omega \,, \quad b(v; \boldsymbol{\mu}) = \int_\Omega f(\boldsymbol{\mu}) v d\omega \,, \tag{1.2}$$

and $\Omega$ is the spatial domain. Note that the Galerkin method is employed as $u$ and $v$ belong to the same space. In the context of a FE, analysis Equation 1.1 can be written as the linear system

$$\mathbf{A}(\boldsymbol{\mu})\boldsymbol{u}(\boldsymbol{\mu}) = \boldsymbol{b}(\boldsymbol{\mu}) \,. \tag{1.3}$$

The affine parametric dependence arises when Equation 1.3 can be written such as

$$\mathbf{A}(\boldsymbol{\mu}) = \sum_{i=1}^{Q_a} \theta_a^i(\boldsymbol{\mu}) \mathbf{A}_i \quad \text{and} \quad \boldsymbol{b}(\boldsymbol{\mu}) = \sum_{i=1}^{Q_b} \theta_b^i(\boldsymbol{\mu}) \boldsymbol{b}_i \tag{1.4}$$

where $\theta_a^i$ and $\theta_b^i$ are two sets of scalar functions and $\mathbf{A}_i$ and $\boldsymbol{b}_i$ are two sets of $\boldsymbol{\mu}$-independent matrices (resp. vectors). In the case of a shape parametrization ($\Omega = \Omega_{\boldsymbol{\mu}}$) nonlinearities can be introduced in the expression of the functions $a$ and $b$ - related to the Jacobian - challenging the affine parametric dependence. Indeed, the FE method requires to perform the integration into a reference domain $\Omega_r$. Consequently, the ability to get an affine expression will depend on the nature of the mapping function $\mathcal{M}(\Omega_{\boldsymbol{\mu}}) = \Omega_r$. The simplest idea is to use a linear mapping $\mathcal{M}$. It is at the root of the RB-based method introduced in [243] by Rozza et al. where a piecewise affine transformation based on subdomain division is used to parametrize the shape. As each spatial subdomain is related to the reference shape by an affine transformation, the affine parametric dependence is preserved. This work is extended to the design of arterial bypass in [242]. Nonetheless, this approach is very restrictive because it imposes to use affine transformations. To be able to deal with non-affine mappings, the empirical interpolation method (EIM) [17] has been extensively used. The EIM allows replacing nonaffine coefficient functions with a collateral reduced-basis expansion which then permits an affine offline-online computational decomposition. Hence, by using a non-affine parametric mapping in conjunction with the EIM, an affine expression of the nonlinear functions can be obtained. Building on this statement, a shape-parametrized MOR method based on the RB and using the free-form deformation (FFD) technique [146, 249] has been developed. It has been introduced in [150] and extended in [172] for the shape optimization of aorto-coronaric bypass anastomoses. The FFD concept is to encapsulate the shape within a cube or another hull object, the shape is then transformed as the hull is deformed. Parametric curves are used to infer the shape's position from that of the hull. FFD suffers from some limitations because the control points cannot be chosen freely and that it is not possible to perform a boundary control. That is why, in [171], Manzoni et al. propose to use radial basis functions (RBFs) to include the shape of blood vessels in the ROM of blood flow simulations. Once again, the ROM is built using the RB method. The RBFs are notably chosen as they allow to reduce the number of control points used to describe a shape while offering the possibility to be posed near to salient features. The selection of the control point has been the subject of a subsequent publication in [93]. Apart from their use in the context of the RB method, the RBFs also have been used in [9] with the POD augmented by a hyperreduction technique [247] for design optimization. For a similar application,

a method based on the PGD is employed in [8] but is restricted to affine mappings (e.g. linear triangle elements).

All the studies previously cited focus on the shape parametrization of ROMs for optimization purposes. They could therefore be used mainly for tasks such as prostheses design (e.g. creating patient-specific stents). From a different standpoint, González et al. propose to create a so-called computational patient avatar for the palpation of the liver in linear elasticity [104] with the goal to provide the surgeon a preoperative training tool. This avatar has real-time abilities allowing haptic response ($\sim 1\,\text{kHz}$ frame rate) and permits to take into account the patient-specific shape. Instead of seeking to parametrize the liver's shape, the authors chose to interpolate the patient-specific anatomy from previously computed *computational vademecums* [61]. A vademecum is defined as a sort of response surface for a parametric model. In this case, each vademecum corresponds to a specific liver shape for which the palpation has been parametrized. To do so, the PGD method is used to compute a ROM for the liver palpation, based on the work from Niroomandi et al. [203]. In other words, the ROM returns the deformation of the liver under a parametrized local load. Note that a shape is not described by a point cloud but by a level-set representation. It means that the space is divided into voxels and each one of them contains the signed distance to the nearest point on the surface of the liver. This choice is justified by the fact that interpolating two shapes does not necessarily return a similar shape. In order to interpolate a new out-of-training shape, the authors propose to use the locally linear embedding method. This latter belongs to the nonlinear dimensionality reduction methods. It is based on the computation of the barycentric coordinates of a point based on its $n_n$ neighbors, where $n_n$ is user-defined. From this computation arises the definition of a weight matrix such that each point is represented by the weighted sum of its $n_n$ nearest neighbors. In this case, a point is the vector of the level-set representing a shape. So, any new shape is going to be represented by a weighted sum of its nearest neighbors. The authors then make an important assumption: the vademecums can be interpolated using the same weights as the shapes. From this point, the real-time computation of the patient-specific avatar is straightforward as it consists in the weighted sum of the solutions returned by the $n_n$ ROM corresponding to the nearest shapes. The method is validated on synthetic data but also on a small database of real geometries.

From this overview, it appears that few studies use databases of real anatomies to build the ROM. Moreover, when the shapes are parametrized it is done by using artificial deformations. This is not satisfactory as the training of the ROMs should be ideally limited to anatomically plausible shapes. Conversely, all possible anatomical shapes must be encompassed in the shape parametrization. To do so, the parametric space of the ROM shall be inferred from an exhaustive shape database. To fill this gap, we propose in the Chapters 2 and 3 a new framework to build shape parametrized ROMs based on databases of real medical images. It relies on the use of a statistical shape analysis (SSA) combined with a morphing procedure to create a shape-parametric organ model. This parametrization is then used to create the ROM thanks to the sparse subspace learning (SSL) method [36]. The SSL is non-intrusive and belongs to the interpolation-based MOR methods. It implies that the affine parametric dependence does not have to be respected any more, making this approach particularly well-suited for the construction of shape-parametric organ ROMs. In order to introduce these chapters, the different stages of the creation of shape-parametric organ models are detailed in the following sections from a statistical perspective. First, the principal medical image acquisition methods are introduced in the next section. Then the SSA is explained in Section 1.4. Finally, the main morphing methods are presented in Section 1.5. To provide the reader with an overview, the workflow of the creation of shape-parametric organ models is provided in Figure 1.1.

## 1.3 Data acquisition

The most common methods to acquire anatomic information are the magnetic resonance (MR) and the computed tomography (CT) imaging. They are at the base of the shape representation for patient-specific modeling. In order to give the reader more insight into the origin of medical data both methods are briefly introduced in this section.

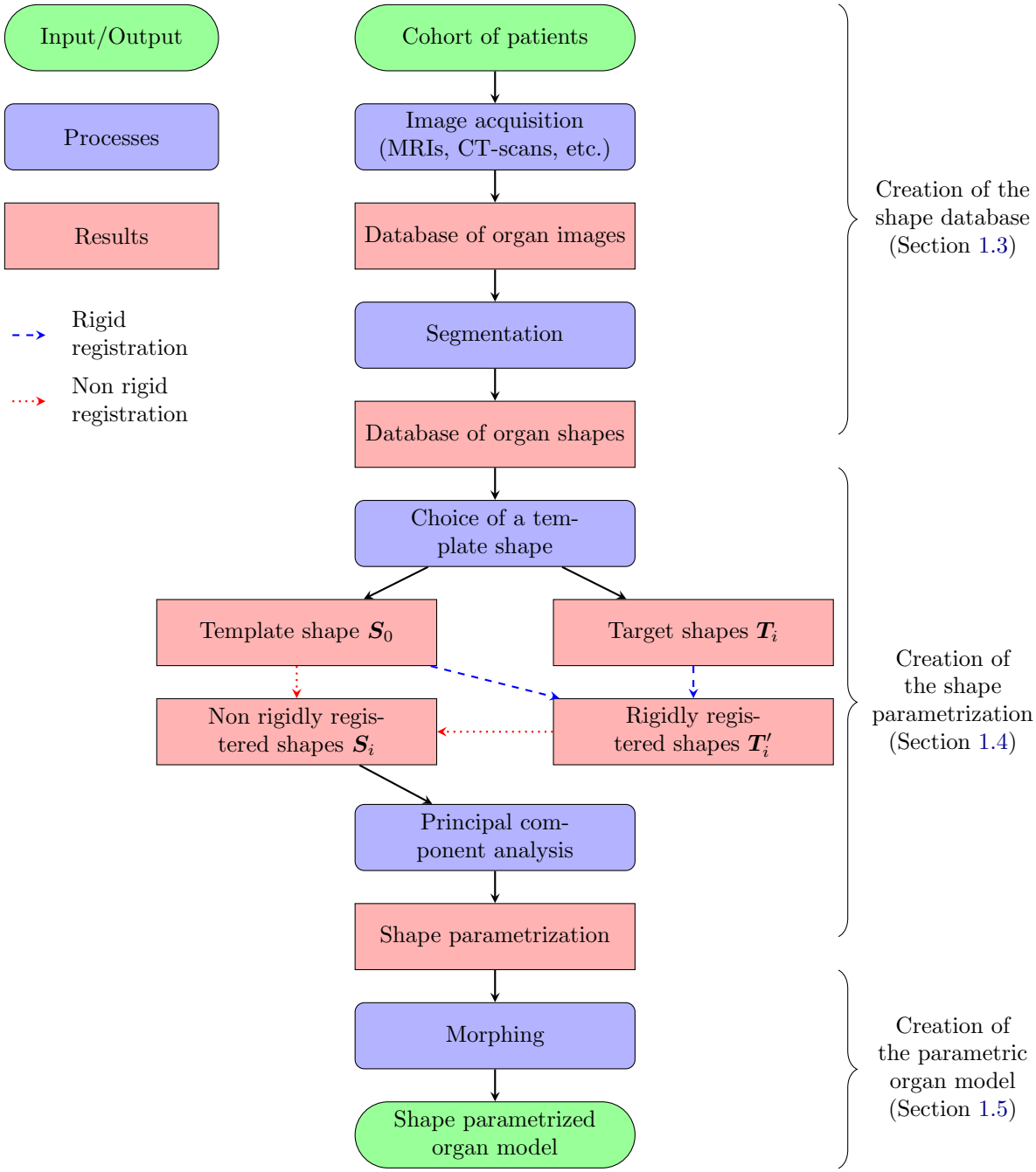


Figure 1.1: Complete flowchart for the construction of shape-parametrized organ models. Each stage is detailed in the corresponding section.

| Reference | [243] | [172] | [171] | [104] |
|---|---|---|---|---|
| Physics | Computational fluid dynamics | Computational fluid dynamics | Computational fluid dynamics | Solid mechanics |
| MOR method | RB | RB | RB | PGD |
| Shape representation | Piecewise affine | Free-form deformation | Radial basis function | Locally Linear Embedding |
| Figure | 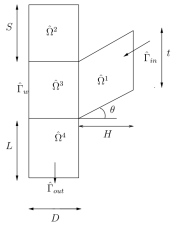 | 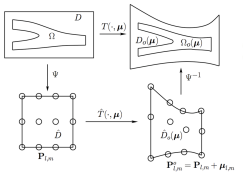 | 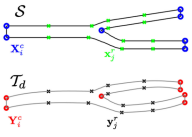 | 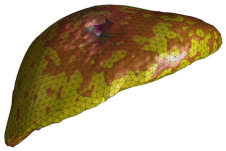 |

Table 1.1: Overview of some shape parametrized ROMs suitable for computational surgery applications. For each application the nature of the physical phenomenon is stated. The first three methods could be used for shape optimization in the context of prostheses design. The last one is a patient-specific real-time haptic simulator for training purposes.

### 1.3.1 Computed tomography imaging

The CT is an X-ray machine coupled to a computer. It provides sliced imaging of different parts of the body and visualizes tissues of different densities such as lungs, bones, soft tissues or blood vessels. It is used for the diagnosis of cancer, trauma, cardiovascular, infectious and osteoarticular diseases. The basic concept of a CT scanner is the following: an X-ray emitter if fixed on a circular structure with a series of receptors diametrically opposed. They are going to measure the radiation going through the body while the couple emitter-receptors rotates around the body, placed inside the circular structure (see Figure 1.2a). As the level of radiation going through the body depends on the density of the tissues, the receptors measure variations of X-ray at each emission. After postprocessing, cross-sectional pictures of the body can be reconstructed, leading to a "sliced" visualization as shown in Figure 1.2b. The CT scanner has the advantage to be very precise, it allows making the distinction between tissues that have a density difference lower than 1%. It can capture pictures of a large range of tissues (bones, cartilage, soft tissues, blood vessels, etc.) in a fast ($\approx 5$ minutes) and non-invasive way. However, as it emits radiations it can damage the body cells, including DNA molecules, and can be the cause of radiation-induced cancers.

### 1.3.2 Magnetic resonance imaging

The MRI scanner uses strong magnetic fields and radio waves to generate an image of the body (see Figure 1.3b). The whole body of the patient is inserted into the scanner which has the shape of a tube (see Figure 1.3a). A primary magnetic field is applied in order the magnetize the tissues. A secondary and weaker oscillating magnetic field, said radiofrequency, is then applied briefly at a specific frequency. This latter corresponds to the resonance frequency of the protons (hydrogen atoms) contained in the water molecules of the tissues. When excited, the hydrogen atoms emit a radiofrequency signal measured by captors placed in the walls of the tube. Depending on the nature of the tissue they are in, the hydrogen atoms do not return to their equilibrium state at the same speed, that allows determining which tissue they belong to. The MRI scanner has the advantage over CT not to use radiations. It is also preferred for soft tissue imaging for its better ability to make the distinction between them, for example between tendons and ligaments. However, the time acquisition is long (from 15 minutes to 2 hours) and the patient can feel anxiety because of the closed space. A MRI is also more expensive than a CT scan.

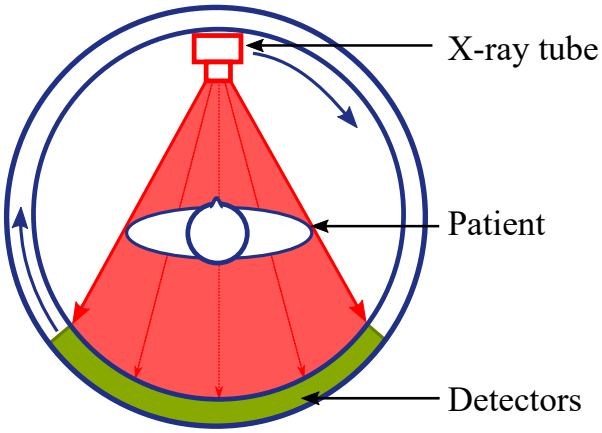


(a) Scheme of a CT scanner.

(b) Reconstructed slice of the abdomen obtained from a CT scan.

Figure 1.2: Presentation of a CT scanner. The CT scan image comes from the IRCAD's open-source database available at https://www.ircad.fr/research/3d-ircadb-01/.

(a) View of a 3 tesla clinical MRI scanner.

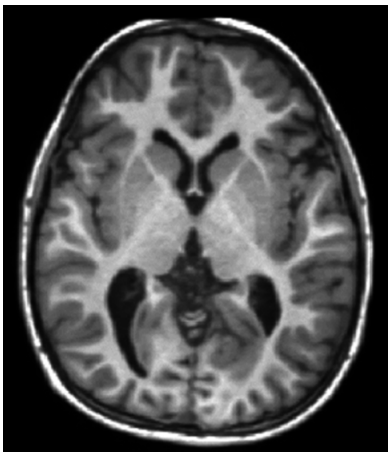

(b) MRI of the head showing a brain section.

Figure 1.3: Presentation of a MRI scanner. The images come from the website page https://en.wikipedia.org/wiki/Magnetic_resonance_imaging.

## 1.4 Statistical shape analysis

### 1.4.1 Overview

A shape is described as the geometric property of an object invariant under rotation, scale and translation. The most generic way to describe a shape is done by using a point cloud belonging to its surface. A 3D shape $\boldsymbol{X}$ described by $n$ points reads

$$\boldsymbol{X} = (x_1, \cdots, x_n, y_1, \cdots, y_n, z_1, \cdots, z_n)^T . \tag{1.5}$$

The SSA aims at extracting a mean shape and its principal modes of variation from a collection of training samples. It has been pioneered by D'Arcy Thompson in On Growth and Form [276], where he explored how the forms of organisms can be explained by geometrical transformations (see Figure 1.4). Because the shape is defined by its invariances, the first step in a SSA is to pose all the shapes in a common reference frame through rotations and translations. If the size of the shapes is not pertinent then a scaling may be applied. This procedure is known as rigid registration or shape alignment. Then, to perform the statistical analysis, a corresponding set of points between all shapes of the dataset must be determined. This set of points is often referred to as landmarks, although it does not correspond to salient features points of the shapes. This step is crucial as wrong corresponding landmarks will lead to introducing noise in the SSMs. Manual correspondence is a tedious task and is not conceivable when dense correspondence is required. Moreover, the results often lake of reproducibility. That is why nonrigid registration methods are employed as they allow automatizing the correspondence. Once the correspondence is done, a dimensionality reduction method is used to get a statistical representation of the data. This is usually accomplished by using the principal component analysis (PCA) [137]. In this section, we give an overview of the SSA method and introduce some of the standard techniques. More insight can be found in [120].

For the sake of brevity, we will focus only on landmarks based SSMs, coined as point distribution models (PDMs) by Cootes et al. [65]. They are the most common SSMs found in the literature.

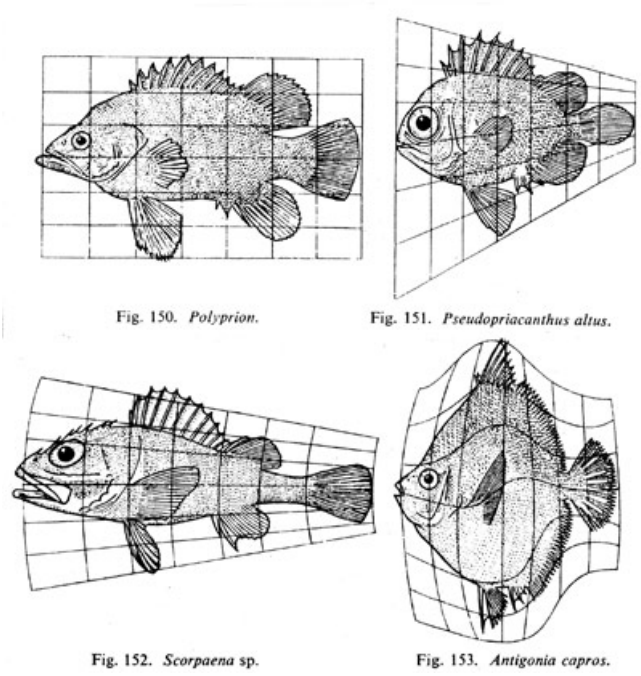


Figure 1.4: Extract from D'Arcy Thompson's book [276]. The shapes of different fishes is related through diffeomorphisms.

### 1.4.2 Rigid registration

The rigid registration is commonly done using a Procrustes analysis, or Procrustes alignment. The standard procedure is based on a reference shape $\boldsymbol{S}_0$, called *template*. All the other shapes from the database are referred to as targets and are noted $\boldsymbol{T}_i$ ($i \in [1, N_T]$). The idea is to align all the targets onto the template through rotation, translation and scaling.

**Translation** The translation is done by removing the mean, or barycenter, of all the shapes so that their new mean lies at the origin of the reference frame. Considering the definition of a shape in Equation 1.5, the mean reads

$$\bar{x} = \frac{\sum_{i=1}^{n} x_i}{n}, \quad \bar{y} = \frac{\sum_{i=1}^{n} y_i}{n}, \quad \bar{z} = \frac{\sum_{i=1}^{n} z_i}{n}\,. \tag{1.6}$$

**Scaling** The scaling is done by computing the mean distance from the barycenter to all the points composing the shapes. This distance reads

$$s = \frac{\sqrt{\sum_{i=1}^{n}(x_i - \bar{x})^2 + \sum_{i=1}^{n}(y_i - \bar{y})^2 + \sum_{i=1}^{n}(z_i - \bar{z})^2}}{n}\,. \tag{1.7}$$

Hence all targets and the template are rescaled by a factor $\frac{1}{s}$ to get a unit scaling.

**Rotation** Once all the shapes lie at the origin, a rotation is applied to each target in order to orient them in the same direction as the template. This is by far the most complex task in Procrustes alignment. It can be solved by a minimization procedure. By noting $\mathbf{R}$ the rotation matrix, we want to solve

$$\mathbf{R}_i = \underset{\mathbf{R}^*}{\arg\min} ||\boldsymbol{S}_0 - \mathbf{R}^* \boldsymbol{T}_i||_F\,, \quad i \in [1, N_T]\,. \tag{1.8}$$

Where $||\bullet||_F$ is the Frobenius norm. This problem is commonly referred to as the orthogonal Procrustes problem [254]. Its solution reads

$$\mathbf{R}_i = \mathbf{U}\mathbf{V}^T \tag{1.9}$$

where $\boldsymbol{S}_0 \boldsymbol{T}_i^T = \mathbf{U}\boldsymbol{\Sigma}\mathbf{V}^T$ is the singular value decomposition (SVD) of $\boldsymbol{S}_0 \boldsymbol{T}_i^T$. The SVD concept is later introduced in Section 1.4.4.

It appears that the rotation and the scaling are independent of the template. Only the rotation requires a reference to align all the shapes. The Generalized Procrustes analysis has been developed to avoid the bias of the template selection. The algorithm works as follows:

1. Choose arbitrarily a template.
2. Perform a standard Procrustes alignment.
3. Compute the mean shape of the current set of superimposed shapes.
4. Compute the distance between the mean shape and the template. If the distance is above a user-defined threshold, choose the mean shape as the new template and go back to step 2.

Note that step 3 requires the knowledge of the correspondence between the landmarks, this problem is addressed in the next section.

**Example 1.1** (*A two-dimensional case: template selection and rigid registration*). To illustrate the statistical shape analysis, an example is given on 2D shapes of human proximal femora. These latter have been obtained on the open-source database [117] and with a post-processing to generate the 2D representation. A reduced dataset of 20 shapes has been used. Some of these shapes can be seen in Figure 1.5. A template is arbitrarily chosen among the set of shapes. As illustrated all the shapes have different positions, orientations, and scales. Note that the shapes are described by a variable number of points.

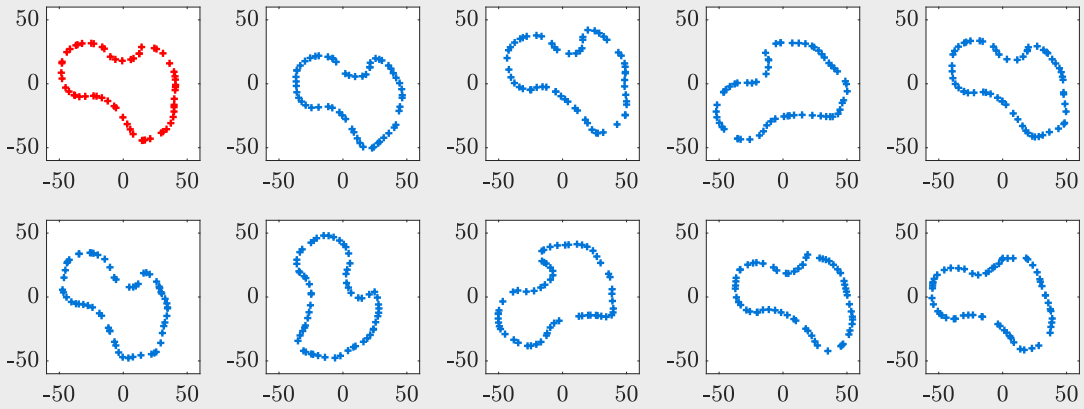


Figure 1.5: Selection of shapes from the femoral head dataset. The template is represented in red (top left) and the targets in blue.

A standard Procrustes alignment is performed. The result is shown in Figure 1.6. All the target shapes are visually positioned, oriented, and scaled as the template.

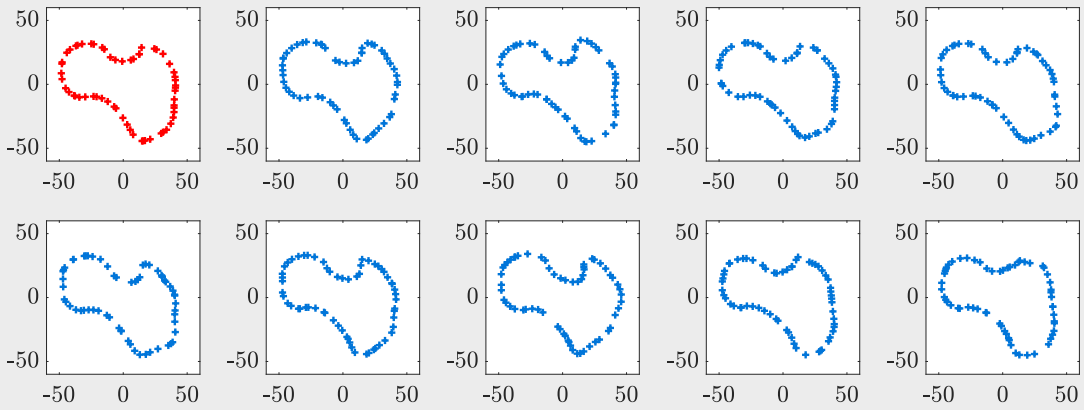


Figure 1.6: Rigid registration of the targets onto the template. The template is represented in red (top left) and the targets in blue.

### 1.4.3 Nonrigid registration

The principle of nonrigid registration is to deform the template shape $\boldsymbol{S}_0$ in order to fit its surface to the surface of each one of the targets $\boldsymbol{T}_i$. It results in a database of deformed shapes $\boldsymbol{S}_i$ which define the correct position of the landmarks. Many methods exist to perform the nonrigid registration. It can be from surface to surface, but also from surface to volume, for the direct segmentation of MRIs or CT scans, or from volume to volume. Once again we refer the reader to [120] for more insight. Here, we illustrate the nonrigid registration with one method: the thin plate spline (TPS). It has been successfully employed in [32] and [22] for image alignment and shape matching and has been found efficient in the context of changes modeling in biological forms [33]. As indicated by its name, the TPS method is a spline-based interpolation method. It also owes its name to

the physical analogy with the bending of a thin sheet of metal. Indeed, the TPS interpolant $f$ is designed to minimize the integrated biharmonic equation

$$I_f = \iiint_\Omega \left( \left( \frac{\partial^2 f}{\partial x^2} \right)^2 + \left( \frac{\partial^2 f}{\partial y^2} \right)^2 + \left( \frac{\partial^2 f}{\partial z^2} \right)^2 + 2 \left( \left( \frac{\partial^2 f}{\partial x \partial y} \right)^2 + \left( \frac{\partial^2 f}{\partial x \partial z} \right)^2 + \left( \frac{\partial^2 f}{\partial y \partial z} \right)^2 \right) \right) dxdydz \,, \tag{1.10}$$

which is the expression of the bending energy of a thin plate [32]. In the TPS method, the TPS interpolant is used to map the reference points $\boldsymbol{s}_i \in \boldsymbol{S}_i$ to their corresponding points $\boldsymbol{t}_i \in \boldsymbol{T}_i$ so as so to minimize the functional $I(f)$, which reads in its regularized form

$$I(f) = \sum_{i=1}^{n_S} ||\boldsymbol{t}_i - f(\boldsymbol{s}_i)||_2 + \gamma_f I_f \,. \tag{1.11}$$

$n_S$ is the number of points in $\boldsymbol{S}_0$ and $\gamma_f \in \mathbb{R}^+$ is a regularization parameter that allows enforcing the smoothness for high values. A natural solution of the interpolant $f$ has the form:

$$f(x,y,z) = a_1 + a_2 x + a_3 y + a_4 z + \sum_{i=1}^{n_S} w_i U(||\boldsymbol{s}_i - (x,y,z)||_2) \tag{1.12}$$

where $U(r) = \text{abs}(r)$ is a radial basis function [48]. In order for $I_f$ to be correctly defined, additional constraints must be added as

$$\sum_{i=1}^{n_S} w_i = 0 \quad \text{and} \quad \sum_{i=1}^{n_S} w_i x_i = \sum_{i=1}^{n_S} w_i y_i = 0 \,. \tag{1.13}$$

With the correspondence condition which reads $\boldsymbol{t}_i = f(\boldsymbol{s}_i)$, Equation 1.11 can be written as

$$\left( \begin{array}{c|c} \mathbf{K} + \gamma_f \mathbf{I} & \mathbf{P} \\ \hline \mathbf{P}^T & \mathbf{0}_{4\times 4} \end{array} \right) \left( \begin{array}{c} \boldsymbol{w} \\ \hline \boldsymbol{a} \end{array} \right) = \left( \begin{array}{c} \mathbf{T}_i \\ \hline \mathbf{0}_{4\times 3} \end{array} \right) \tag{1.14}$$

where $\mathbf{I}$ is the identity matrix, $\mathbf{K}_{ij} = U(||\boldsymbol{s}_i - \boldsymbol{s}_j||_2)$, the $i$-th row of $\mathbf{P}$ contains $(1, \boldsymbol{s}_i^T) = (1, s_{ix}, s_{iy}, s_{iz})$, the $i$-th row of $\mathbf{T}_i$ contains $\boldsymbol{t}_i^T = (t_{ix}, t_{iy}, t_{iz})$, $\boldsymbol{a} = (a_1, a_2, a_3, a_4)^T$ and $\boldsymbol{w} = (w_1, \cdots, w_{n_S})^T$.

Solving the system described in Equation 1.14 requires to find the condition $\boldsymbol{t}_i = f(\boldsymbol{s}_i)$. Hence, the user has to make an initial estimate of the correspondence between the points. As mentioned in [22], this initial estimate is most likely wrong. Thus, an iterative procedure can be set up where each time Equation 1.14 is solved a new set of correspondence is computed.

**Remark 1.1** (*TPS in one and two dimensions*). In 1D and 2D the TPS interpolant has the following forms:

$$f(x) = a_1 + a_2 x + \sum_{i=1}^{n_S} w_i ||s_i - x||_2^3 \tag{1.15}$$

and

$$f(x,y) = a_1 + a_2 x + a_3 y + \sum_{i=1}^{n_S} w_i ||\boldsymbol{s}_i - (x,y)||_2^2 \log(||\boldsymbol{s}_i - (x,y)||_2^2) \,. \tag{1.16}$$

**Example 1.2** (*A two-dimensional case: nonrigid registration and landmarks correspondence*). To illustrate the nonrigid registration with the TPS method, the Example 1.1 is continued. As mentioned in Remark 1.1, in 2D the TPS is applied using Equation 1.16. The template is deformed in order to fit its surface onto each target's surface. The result is shown in Figure 1.7. The TPS performs very well as all the nonrigid registrations outcomes fit the surfaces of the targets.

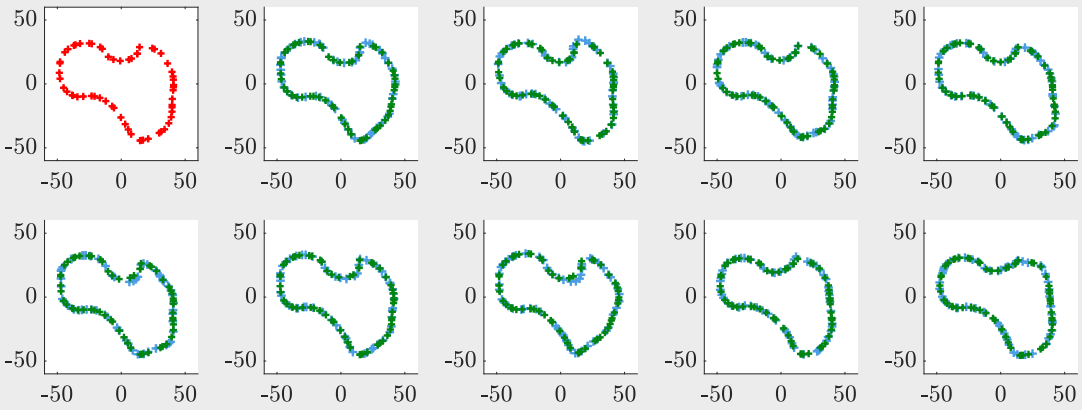

Figure 1.7: Nonrigid registration of the template onto the targets. The template is represented in red, the targets in blue and the deformed templates in green. The shapes are superimposed in order to attest of the good registration.

A more detailed example of a nonrigid registration is given in Figure 1.8. The deformed template points are not exactly superimposed to the target's ones. This is due to the penalization term in Equation 1.11 that is used to smooth the surface. It is also interesting to note that some of the template's points have identical correspondence, hence they try to move toward the same position. The penalization also helps to avoid them to do so. However, it may be not sufficient. In this example, we used the nearest point to establish the correspondence. A good alternative is the robust point matching [99], adapted to the TPS method in [64]. This method allows assigning soft correspondence, meaning a correspondence between two points can be between 0 and 1. This approach is particularly useful for sets of shapes being described by a different number of points.

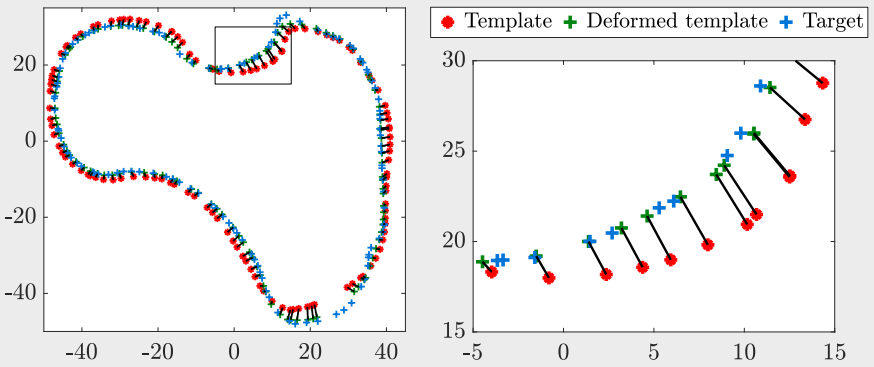


Figure 1.8: Nonrigid registration of the template onto a unique target. The template is represented in red, the target in blue and the deformed template in green. The displacements between the points are shown with black lines. The whole shapes are shown in the left figure. The black box corresponds to the zoomed area shown on the right figure.

Once all the shapes are registered, a new template shape can be used in the case of the generalized Procrustes alignment. The new template corresponds to the mean shape of all the

deformed template shapes, it is shown in Figure 1.9. Here the mean shape is relatively close to the initial template.

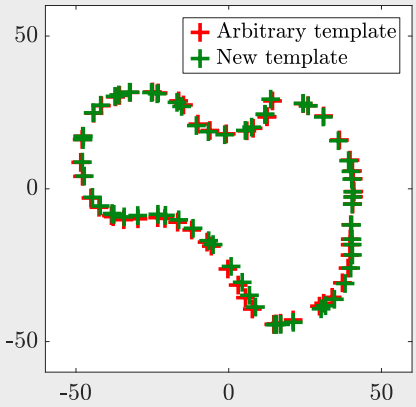


Figure 1.9: Template shape represented with the new mean shape. If the difference between the shapes is greater than a specific threshold, the new shape is used as input for a new iteration of the generalized Procrustes analysis.

### 1.4.4 Dimensionality reduction

Once the landmarks are correctly defined, the PCA [137] is applied in order to find the principal modes of variation describing the shape. First, the mean shape is defined following

$$\bar{\boldsymbol{S}} = \frac{1}{N_T} \sum_{i=1}^{N_T} \boldsymbol{S}_i \,. \tag{1.17}$$

The PCA is based on the eigendecomposition of the covariance matrix associated with the shapes. This latter reads

$$\mathbf{C} = \frac{1}{N_T} \left[ \; \boldsymbol{S}_1 - \bar{\boldsymbol{S}} \,, \quad \cdots \,, \quad \boldsymbol{S}_{N_T} - \bar{\boldsymbol{S}} \; \right] \left[ \; \boldsymbol{S}_1 - \bar{\boldsymbol{S}} \,, \quad \cdots \,, \quad \boldsymbol{S}_{N_T} - \bar{\boldsymbol{S}} \; \right]^T \,. \tag{1.18}$$

Its eigenvectors $\boldsymbol{\phi}_i$ ($i \in [1, 3n_S]$) are associated with eigenvalues $\lambda_i$. Each eigenvalue corresponds to the variability, or variance, of its corresponding eigenvector. By sorting the eigenvalues such as $\lambda_1 \geq \cdots \geq \lambda_{3n_S} \geq 0$, the eigenvectors can be sorted accordingly. The optimal choice to represent the modes of variation of a shape is then the $n_p \in \mathbb{N}^*$ firsts eigenvectors of the covariance matrix. Any new shape $\tilde{\boldsymbol{S}}$ can be written

$$\tilde{\boldsymbol{S}} = \bar{\boldsymbol{S}} + \sum_{i=1}^{n_p} \alpha_i \boldsymbol{\phi}_i \tag{1.19}$$

where $\boldsymbol{\alpha} = (\alpha_1, \cdots, \alpha_{n_p})$ is the vector containing the shape parameters. The choice of this subspace can also be seen as a data compression mean or a way to suppress noise from the data, assuming the noise has a low variance. The choice of the value of $n_p$ is often determined by the formula

$$n_p = \min_{p*} \left( \frac{\sum_{i=1}^{p*} \lambda_i}{\sum_{i=1}^{n} \lambda_i} \right) > h \tag{1.20}$$

where $h \in (0, 1]$ is a user-defined threshold. This ratio allows estimating the percentage of variability encompassed by the truncated representation.

**Remark 1.2** (*Geometrical interpretation of the PCA*). The PCA is often interpreted from a geometrical manner. If $n_p$ eigenvectors are selected to represent the data, then the PCA is equivalent to the fitting of a $n_p$-hyperellipsoid on the data. The semi-axes of the hyperellipsoid are represented by the eigenvectors, also called principal axes, and their lengths by the eigenvalues. The concept is illustrated in Figure 1.10 in two dimensions. Note that the data must be centered on the origin beforehand.

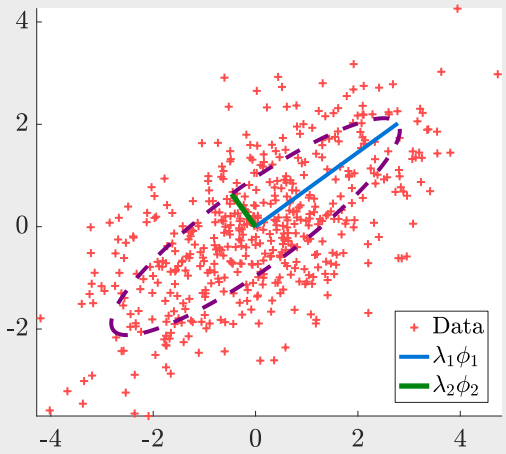


Figure 1.10: Random points are generated following a bivariate normal distribution centered on $(0, 0)$. The principal axes are represented and weighted by their corresponding eigenvalues. They define an ellipse.

The PCA is closely related to another matrix factorization method, the singular value decomposition (SVD). This latter states that any rectangular $n \times m$ matrix $\mathbf{M}$ can be written

$$\mathbf{M} = \mathbf{U}\mathbf{\Sigma}\mathbf{V}^T \tag{1.21}$$

where $\mathbf{\Sigma}$ is a $n \times m$ diagonal matrix containing the so-called singular values and $\mathbf{U}$ (resp. $\mathbf{V}$) is a $n \times n$ (resp. $m \times m$) orthogonal matrix containing the left (resp. right) singular vectors. By choosing the $i$-th column of $\mathbf{M}$ such that $\mathbf{M}_i = \boldsymbol{S}_i - \bar{\boldsymbol{S}}$ it comes

$$\mathbf{C} = \frac{1}{N_T}\mathbf{M}\mathbf{M}^T = \frac{1}{N_T}\mathbf{U}\mathbf{\Sigma}\mathbf{V}^T\mathbf{V}\mathbf{\Sigma}\mathbf{U}^T = \frac{1}{N_T}\mathbf{U}\mathbf{\Sigma}^2\mathbf{U}^T . \tag{1.22}$$

Then, the left singular vectors of the SVD are equivalent to the eigenvectors of the correlation matrix and the squared values of the singular values are equivalent to the eigenvalues. The SVD is often preferred over the PCA for its computational stability and efficiency.

**Example 1.3** (*A two-dimensional case: application of the PCA*). To illustrate the PCA the Example 1.2 is continued. The PCA is applied to the set of deformed template obtained by the nonrigid registration. As explained before, each eigenvalue obtained with the PCA corresponds to the square value of the standard deviation (i.e. the variance) of its corresponding eigenvector. It is common to consider that the shape parameters are not significantly different from the normal distribution. It allows stating that for the $i$-th mode, 95% (resp. 99%) of the shapes are encompassed in the range $[-1.96\sqrt{\lambda_i}, 1.96\sqrt{\lambda_i}]$ (resp. $[-3\sqrt{\lambda_i}, 3\sqrt{\lambda_i}]$). It defines a subspace where the generated shapes are most likely well-defined (i.e. no overlapping) and correspond to plausible forms. The result of the 2D example is given in Figure 1.11 for the first mode. In this case, the shape corresponding to $+3\sqrt{\lambda_1}$ is tangled. Hence taking large boundaries in this application may lead to invalid shapes. The definition of the parameters subspace can be delicate, as discussed in Chapter 3.

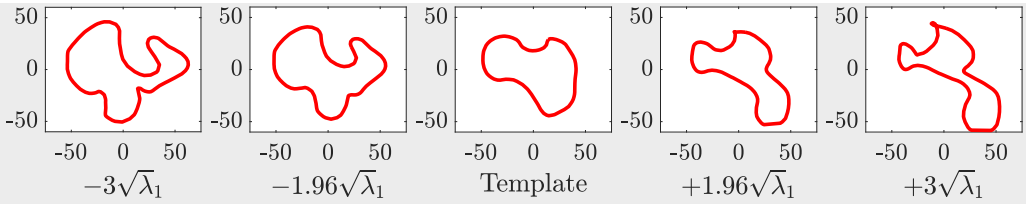


Figure 1.11: First mode of deformation associated with the template. For the sake of clarity, the contour of the point cloud is displayed.

## 1.5 From the shape to the model

The geometry of a FE model is defined by a mesh. A mesh is the subdivision of a continuous geometry into a discrete assembly of topological cells. In FE these cells are often triangles or quadrangles in 2D and tetrahedra or hexahedra in 3D. They are described by their vertices, also called the nodes of the mesh, and their connectivity. The shape of a 3D FE model is therefore the surface mesh of the model. The use of PDMs for shape parametrization is convenient as the point cloud describing a shape can be related to the surface of the FE model. However, there is no consideration about the topology of the latter in a shape parametrization. Hence, two challenges must be addressed to go from the shape parametrization to the parametric model: the preservation of the surface topology and the reconstruction of the inner nodes of the model used to describe its 3D geometry. The concept of adapting a mesh to a given shape is more widely known as *mesh morphing*.

All morphing methods are template-based - also mentioned as atlas-based. It means a model of reference is initially chosen to be deformed and fitted to the target shapes. The former must be particularly well-meshed as it will be the baseline for all the newly generated FE models. RBFs [48] are among the most popular techniques for the creation of parametric organ models. Indeed, they allow to perform the initial nonrigid registration, as seen with the TPS method, but are also defined in the whole spatial domain. Hence they can be used to propagate the surface deformation to the inner nodes of the template model. For example, RBFs have been successfully employed to create parametric ribcage models for thoracic injury risk quantification [292] or to create parametric head models in the context of impact simulations [153, 152]. Furthermore, in order to automatize the postprocessing of medical images, they have been used to generate patient-specific models of the human pelvis directly from CT-scans, bypassing the segmentation step [109, 250]. Empirically, the RBFs allow preserving the topology of the mesh cells. In [109] a smoothing is even done to ensure the quality of the surface mesh. However, in these applications, the quality of the generated FE models is never thoroughly checked. A good surface mesh does not imply good quality volumetric elements. To solve this issue, Bucki et al. [46] used a two-step procedure called mesh-match-and-repair, consisting in a mesh morphing followed by a repair of the mesh. The morphing algorithm is based on the mesh-matching method [272, 72] which involves the construction of an octree around the template model and extrapolates the position of the nodes using spline functions. A so-called elastic registration is then done by minimizing a least-squares criterion involving the distance between the template and the target shapes. The mesh repair step is done by using a Jacobian-based metric to evaluate the goodness of the mesh's elements [47]. Such a procedure is more robust as it ensures the suitability of the mesh to be used for FE computations. Another approach is the use of morphing techniques directly based on the FE method. In [110] an automated hexahedral meshing is presented in the case of hand's bones morphing. The underlying idea is to use Neumann boundary conditions, i.e. loads, to solve a FE problem in linear elasticity. The loads are applied on each node of the template surface mesh and are proportional to their distances to their corresponding landmarks on the target's shape. By iterating the surface correspondence is improved and the FE mesh is deformed. Similarly, in [19] the authors propose to perform the morphing of a left ventricle model using the shape's nonrigid registration as the Dirichlet conditions of a FE problem in linear elasticity. This procedure is a simplified version of the FE mesh warping algorithm - named FEMWARP - based on the weighted

Laplacian smoothing introduced in [257] and later extended in [259]. It is an iterative morphing procedure where the idea is to impose Dirichlet boundary conditions, i.e. displacements, on the surface of the mesh. A linear elastic behavior is still considered but this time the local rigidity of the elements is updated depending on a Jacobian-based mesh quality metric. At each iteration the bad quality elements from the previous increment have their stiffness increased, leading to a smaller quality deterioration. After several iterations the problematic elements have a higher stiffness, hence they are less deformed during the solving of the Dirichlet problem and keep a quality near their initial value. More insight can be found in Chapter 2 Section 2.2.4.2.

To close this section, it is interesting to remind that parametric organ models can also be used to transfer other information than the shape. As mentioned in Section 1.1, a model is defined by a geometry but also by material properties and boundary conditions. The advantage of template-based models is that these characteristics can be transported from the template to the actual model. Moreover, the PCA can be applied to other features than the shape. A good example is the work of Nicolella et al. [199] where a parametric femur model embedding the bone density is created. To do so, a femur template mesh is morphed onto a database of targets for which the bone density has been determined. The PCA is then applied not only to the mesh but also to the field representing the bone's density. It results in statistical shape and density model that allows a direct use in a FE simulation, without the need for parameter assignment. However, note that a SSM of a whole FE mesh may produce tangled meshes.

In the next chapter, a methodology for the generation of shape-parametric organ models is presented. It is based on a novel template-based non-rigid registration coupled with an improved version of the FEMWARP morphing method. The procedure is then adapted to the creation of shape-parametric ROM in Chapter 3.

Chapter 2

# Shape parametrization of biomechanical finite element models based on medical images

**Abstract** The main objective of this chapter is to combine the statistical shape analysis with a morphing procedure in order to generate shape-parametric finite element models of tissues and organs and to explore the reliability and the limitations of this approach when applied to databases of real medical images. As classical statistical shape models are not always adapted to the morphing procedure, a new registration method is developed in order to maximize the morphing efficiency. The method is compared to the traditional iterative thin plate spline method. Two data sets of 33 proximal femora shapes and 385 liver shapes are used for the comparison. The principal component analysis is used to get the principal morphing modes. In terms of anatomical shape reconstruction (evaluated through the criteria of generalization, compactness, and specificity), our approach compares fairly well to the iterative thin plate spline method, while performing remarkably better in terms of mesh quality, since it is less prone to generate invalid meshes in the interior. This is particularly true in the liver case. Such methodology offers a potential application for the generation of automated finite element models from medical images. Parametrized anatomical models can also be used to assess the influence of inter-patient variability on the biomechanical response of the tissues. Indeed, thanks to the shape parametrization the user easily has access to a valid finite element model for any shape belonging to the parameters subspace.

## Contents

## 2.1 Introduction

The finite element (FE) method is widely used to simulate the physical behavior of problems with complex geometries. When the FE model is built upon real images the preprocessing setup can be time-consuming, especially in 3D and when the task has to be repeated several times for similar applications. This step often requires a manual intervention to assign boundary conditions or material properties. A lot of effort has been focused on the development of automated procedures for model generation from real data in order to avoid these overhead costs. A promising technique is the mesh warping [72, 51, 260, 110, 46]. The underlying idea is to define a template mesh that can be morphed in order to fit the target shape while keeping a good mesh quality. The procedure is often applied in a medical framework, the target shapes are then obtained from computed tomography (CT) scans or magnetic resonance images (MRI). A popular way of extracting the shape of the organs from such images is to use statistical shape models (SSMs) [120]. SSMs are statistical representations of the organ shapes built from a training data set. A mesh is chosen as the reference shape and modes of variations of the geometry are associated with it, which allows representing any shape similar to the ones of the training set.

The aim of this study is to fill the existing gap and bridge these two methodologies in order to automatically and quickly build volumetric meshes from SSMs. These latter are used to create a data-based shape parametrization allowing personalizing personalized FE modeling based on medical images. Moreover, shape parametric FE models are useful to quantify the trends of the shapes in the population and assess the influence of anatomy on biomechanical behavior. Indeed, from the parametrization, it is possible to create any FE model of the same family while sharing a unique mesh connectivity and topology. This allows propagating any anatomical landmark from the template to any generated shape. For the study of inter-population mechanical behavior variability, it also allows specifying only once the boundary conditions and material properties and to use them for any shape of generated FE model.

In recent years several studies have focused on the statistical representation of the whole body [127, 305, 20], also using morphing methods to generate complete FE models. In these studies the statistical shape analysis (SSA) is done on specific elements of the skeleton - i.e., the ribs [293, 292] - and particular points on the external body surface. Landmark-based morphing methods are then applied using radial basis functions such as the thin plate spline (TPS). Nonetheless, such kind of morphing has no consideration for the quality of the morphed mesh. To take into account such a factor, the method presented in this chapter works in two steps: a SSA followed by a modified version of the morphing procedure called iFEMWARP [259] (iterative finite element-based mesh warping). In order to maximize the efficiency of the morphing step a new registration procedure, called thin plate spline-parametrized registration, is set up to create the SSMs. This new registration method is compared to the well-known iterative thin plate spline (iTPS) in order to assess its relevance. Although the collection of methods used to create the parametric organ models used in this chapter are quite standard (see Chapter 1 Section 1.4 and 1.5), the originality lies in the gathering of all these methods and in the attention paid in order to create a coherent sequence of operation leading to an optimized, robust and unsupervised procedure. The training sets used for the comparison contain 385 liver shapes and 33 proximal femora shapes. These databases contain 3D geometries of pre-processed medical images, hence the chapter will not deal with image processing or segmentation.

## 2.2 Materials and methods

In this section a shape is described by a cloud of 3D points $(x_i, y_i, z_i) \in \mathbb{R}^3$, with $i = 1, \ldots, n_X$, and will be represented by the vector $\boldsymbol{X} = (x_1, \ldots, x_{n_X}, y_1, \ldots, y_{n_X}, z_1, \ldots, z_{n_X})^T \in \mathbb{R}^{n_X \times 3}$. For the sake of simplicity, the Euclidean distance, or $\ell^2$-norm, will be denoted by $||\bullet||$.

### 2.2.1 Data

The method was applied to two sets of three-dimensional (3D) training shapes provided in *vtk* format. Two distinct organs, the liver and the proximal femora, were chosen to explore the behavior of the proposed method for different kind of tissues and to test its robustness. The main difference between these organs is that the liver is categorized as a soft tissue whereas the femur is a hard tissue. Consequently, the liver shape should present more variability.

In order to create the SSMs, a template shape was chosen for each one of the training sets. A first database of $N_T = 385$ liver shapes was provided by the IRCAD (Institut de recherche contre les cancers de l'appareil digestif, Strasbourg, France). This database contains a large number of liver shapes collected from CT-scans or MRIs over several years, on patients in supine position. The stored meshes quality and precision evolved with the medical image segmentation methods. First, the different organs were identified in every single image independently, leading to discontinuities. This technique was completed with context-based treatment [170] and topological identification [80] which improved greatly the organs consistency and shape. Additional post-treatments [30] were done to guarantee manifoldness and non-overcrossing faces, which are compulsory for 3D-meshing. The integration of additional techniques like context base-voting [59] and region-growing algorithm [94] lead to consequent improvement of the mesh precision, as well as a reduction of the error induced by the segmentation technician. As a result, the liver geometries used present a remarkable diversity in terms of source (male or female, healthy or unhealthy, etc.) or in terms of method used for their generation. They present in particular a strong variation concerning their number of vertices, going from $2,000$ to $150,000$, in order to describe a single liver surface. The liver template surface is described by $1,393$ vertices and $2,782$ triangles (see Figure 2.1a). The volume is meshed with $10,163$ tetrahedra for a total of $2,452$ vertices. Its maximum length is around 260 mm.

The second database contains $N_T = 33$ proximal femora shapes freely provided by [117]. The data were collected on 33 cadavers, 16 males and 17 females, between 61 and 95 years. The proximal femora template surface is described by $1,384$ vertices and $2,764$ triangles (see Figure 2.1b). The volume is meshed with $8,724$ tetrahedra for a total of $2,222$ vertices. Its maximum length is around 90 mm.

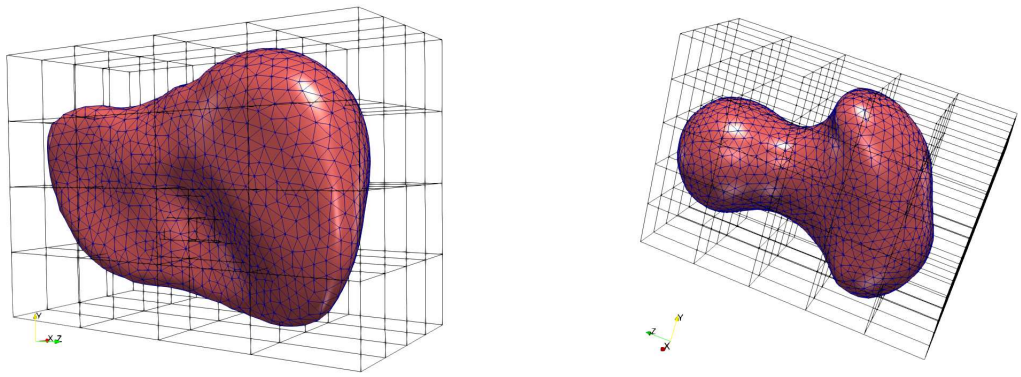

(a) Liver ($n_b = 5$)

(b) Proximal femora ($n_b = 6$)

Figure 2.1: Template meshes with their bounding boxes. The visualization is done on Paraview

### 2.2.2 Creation of the finite element model from statistical shape models

The method presented in this thesis can be split into two parts: an offline stage where the SSMs are built and an online one where the FE model is reconstructed from the shape parametrization.

1. **Offline stage: construction of the SSMs**
   The SSA presented here belongs to the point distribution model (PDM) family. Two major

steps can be identified to build PDMs: the alignment of the shapes and the dimensionality reduction.

a. The alignment step works as follows: a *template* shape $\boldsymbol{S}_0$ - a shape being described by a point cloud - is chosen. Each shape from the training set, subsequently mentioned as *target*, is rigidly registered onto the template. Then, the template is non-rigidly registered onto each target. For each non-rigid registration a deformation field corresponding to the template displacement is associated.

b. A dimensionality reduction method, most of the time the principal component analysis (PCA) [137], is then applied to this deformation database in order to find the principal modes of deformation associated with the template. By selecting the set of modes that best describes the observed variation the user is able to statistically describe any shape with a restricted number of modes. Any new shape $\tilde{\boldsymbol{S}}$ can be written as the sum of the mean shape $\bar{\boldsymbol{S}}$ and a linear combination of the selected principal modes $\boldsymbol{\phi}_i$:

$$\tilde{\boldsymbol{S}} = \bar{\boldsymbol{S}} + \sum_{i=1}^{n_p} \alpha_i \boldsymbol{\phi}_i \tag{2.1}$$

where $\alpha_i$ are the shape parameters and $n_p$ there number. Finally, the subspace containing the shape parameters is defined.

2. **Online stage: reconstruction of the FE model from the SSMs**

a. First, the volumetric mesh of the template shape $\boldsymbol{S}_0$ is computed.

b. For a given new shape the corresponding shape parameters from Equation 2.1 are identified. Consequently, the shape is now described by the same mesh connectivity and topology as the template.

c. As the template volumetric mesh is known the morphing method iFEMWARP can be applied to the new shape in order to create the FE model.

For each new shape the steps b. and c. have to be repeated.

In the remainder of the section, we detail each step of the method.

### 2.2.3 Offline training

#### 2.2.3.1 Template shape

The SSMs are built the first time by arbitrarily choosing a template shape. The mean geometry of all models under consideration is then chosen as the new template shape, i.e. $\boldsymbol{S}_0 = \bar{\boldsymbol{S}}$. Both surface and volume are meshed with gmsh [96] using triangles and tetrahedra, respectively. Special attention is paid to the mesh quality.

#### 2.2.3.2 Rigid registration

All the positions, orientations and sizes between the targets and the template are minimized in order to keep only the shape variation. Two rigid registration methods are used sequentially. A Procrustes superimposition is applied through the principal axis transformation method [6, 179] followed by 30 iterations of the iterative closest point (ICP) [27, 58] using point to point minimization [142]. The ICP alone is not sufficient because it tends to converge to local minima. The principal axis transformation method allows doing a first basic registration taking into account the global shapes.

#### 2.2.3.3 Nonrigid registration

The main idea to perform this registration is to minimize a functional

$$I(\boldsymbol{u}) = I_{match}(\boldsymbol{u}) + I_{tps}(\boldsymbol{u}) \tag{2.2}$$

through the use of a semi-implicit iterative algorithm using gradient descent. The functional is the sum of two terms: a point matching term $I_{match}$ and the shape bending energy $I_{tps}$ through a TPS parametrization. The target shape will be mentioned by $\boldsymbol{T}$ and the corresponding deformed template shape by $\boldsymbol{S}$. The initial template shape stays $\boldsymbol{S}_0$. The non-rigid registration method will be called TPS-parametrized registration (TPS-PR).

**Point matching term** The correspondence is usually performed to associate each node of the template with a pair among the target nodes. In this study a new correspondence method is used taking into account the nearest point in $\boldsymbol{T}$ from each point $\boldsymbol{s}$ in $\boldsymbol{S}$ but also the nearest point in $S$ from each point $\boldsymbol{t}$ in $\boldsymbol{T}$. For each point $\boldsymbol{s}_0$ in $\boldsymbol{S}_0$ and $\boldsymbol{s}$ its position in the deformed state, a displacement vector toward $\boldsymbol{T}$ is defined as

$$Dist(\boldsymbol{s}, \boldsymbol{s}_0, \boldsymbol{T}) = \frac{1}{r+1}\left(d_1(\boldsymbol{s}, \boldsymbol{s}_0, \boldsymbol{T}) + d_2(\boldsymbol{s}, \boldsymbol{s}_0, \boldsymbol{T})\right) \tag{2.3}$$

where $d_1 : (\boldsymbol{s}, \boldsymbol{s}_0, \boldsymbol{T}) \rightarrow \boldsymbol{t} - \boldsymbol{s}_0 \quad / \quad \boldsymbol{t} = \underset{\boldsymbol{t}\in\boldsymbol{T}}{\arg\min}(||\boldsymbol{t} - \boldsymbol{s}||)$

and $d_2 : (\boldsymbol{s}, \boldsymbol{s}_0, \boldsymbol{T}) \rightarrow \sum_{i=1}^{c}(\boldsymbol{t}_i - \boldsymbol{s}_0) \quad / \quad \boldsymbol{t}_i$ has $\boldsymbol{s}$ as closest point

where $c \in \mathbb{N}$ is the number of points $\boldsymbol{t}_i \in \boldsymbol{T}$ having $\boldsymbol{s}$ as the closest point. With this definition of distance between a point and a shape all the points of the target have an influence on the registration. For complete shape registration it allows avoiding having non-registered parts. The point matching term between the template and a target is written

$$I_{match}(\boldsymbol{u}) = \frac{1}{2}||\boldsymbol{u} - \boldsymbol{d}||^2 \tag{2.4}$$

where $\boldsymbol{u}$ is the unknown displacement associated with the template shape and $\boldsymbol{d} = Dist(\boldsymbol{S}, \boldsymbol{S}_0, \boldsymbol{T})$.

**Thin plate spline parametrization** As mentioned in the previous chapter, the TPS is an efficient tool for shape matching and object recognition [22], especially for biological applications [32]. The fundamental idea here is to parametrize the displacement of each point belonging to the template shape using a spline function $f$ so as so

$$\boldsymbol{u}_i = f(x_i, y_i, z_i\,;\,\boldsymbol{a}) \tag{2.5}$$

where the parameters $\boldsymbol{a}$ are associated with the control points of a discrete bounding box as the ones shown in Figures 2.1a and 2.1b. It is conceptually close to the free-form deformation technique mentioned in the previous chapter. Requiring the smoothness of the registration is equivalent to minimize the "bending energy" of this bounding box. This reads as

$$I_f = \iiint_\Omega \left(\left(\frac{\partial^2 f}{\partial x^2}\right)^2 + \left(\frac{\partial^2 f}{\partial y^2}\right)^2 + \left(\frac{\partial^2 f}{\partial z^2}\right)^2 + 2\left(\left(\frac{\partial^2 f}{\partial x \partial y}\right)^2 + \left(\frac{\partial^2 f}{\partial x \partial z}\right)^2 + \left(\frac{\partial^2 f}{\partial y \partial z}\right)^2\right)\right) dxdydz \tag{2.6}$$

where $f$ is called the TPS interpolant. In practice Equations 2.5 and 2.6 can be easily evaluated through a FE approach considering Hermitian shape functions of order 2. In this case, the bending energy is expressed as

$$I_{tps}(\boldsymbol{a}) = \frac{1}{2}\boldsymbol{a}^T\mathbf{L}\boldsymbol{a} \tag{2.7}$$

where $\mathbf{L}$ is the discrete biharmonic operator obtained through traditional FE discretization techniques, while the the displacements of the points are expressed by the linear mapping:

$$\boldsymbol{u} = \mathbf{A}\boldsymbol{a} \tag{2.8}$$

where $\mathbf{A}$ is the interpolation operator. The bounding box is fixed to +5% the size of the template and the number of control points $n_b$ along each dimension can be freely chosen. By introducing Equations 2.4, 2.7 and 2.8 in Equation 2.2 we get the following expression:

$$I(\boldsymbol{a}) = \frac{1}{2}||\mathbf{A}\boldsymbol{a} - \boldsymbol{d}||^2 + \frac{\gamma}{2}\boldsymbol{a}^T\mathbf{L}\boldsymbol{a} \tag{2.9}$$

where $\gamma \in \mathbb{R}$ is a weighting scalar.

**Resolution through gradient descent** As $I_{match}$ non linearly depends on $\boldsymbol{a}$, a nonlinear semi-implicit scheme is used through gradient descent using the golden-section search. As the optimal value for the coefficient $\gamma$ can be hard to find manually, a new factor $\gamma_r$ is introduced as:

$$\gamma = \gamma_r \cdot \frac{\max\limits_{\beta\in[0,1]} I_{match}(\boldsymbol{a})}{\max\limits_{\beta\in[0,1]} I_{tps}(\boldsymbol{a})} \qquad \gamma_r \in \mathbb{R}^+ \tag{2.10}$$

where $\beta \in [0, 1]$ is the golden-section search step. $\gamma_r$ represents the ratio between the maximum matching energy and the maximum bending energy. A high value ($> 1$) means the shape deformation will be highly penalized, a low value ($< 1$) means larger deformations are allowed at each increment. Once $\beta$ is computed, the gradient descent step at iteration $k$ can be written as

$$\boldsymbol{a}^{(k+1)} - \boldsymbol{a}^{(k)} = -\beta\frac{dI}{d\boldsymbol{a}} = -\beta\left[\left(\gamma\mathbf{L} + \mathbf{A}^T\mathbf{A}\right)\boldsymbol{a}^{(k+1)} - \mathbf{A}^T\boldsymbol{d}^{(k)}\right]. \tag{2.11}$$

Each time the golden-section search is run the value of $\gamma$ is actualized. In practice Equation 2.11 is solved iteratively until convergence. Each iteration involves the solution of a $12n_b^3 \times 12n_b^3$ linear system. The factor 12 is coming from each control point having 12 degrees of freedom (three displacements and their three derivatives per axis) and the exponent 3 from the 3D.

#### 2.2.3.4 Principal component analysis

Once all shapes are nonrigidly registered a displacement $\boldsymbol{a}_i$ is associated with each target $i$. The PCA is applied to the matrix $[\boldsymbol{a}_1, \ldots, \boldsymbol{a}_{N_T}]$. The principal modes $\boldsymbol{\phi}_i^b$ of the PCA associated with the $n_p$ largest eigenvalues $\lambda_i$ are chosen to form a reduced basis for $\boldsymbol{a}$. The size $n_p \ll 12n_b^3$ of the basis is chosen depending on the percentage of variability $\lambda_i / \sum_{i=1}^{N_T} \lambda_i$ associated with each deformation mode. The representation of $\boldsymbol{a}$ in the reduced basis reads

$$\tilde{\boldsymbol{a}} = \sum_{i=1}^{n_p} \alpha_i \boldsymbol{\phi}_i^b \tag{2.12}$$

where $\alpha_i$ are the associated shape parameters. Thanks to Equation 2.8 a shape parametrization $\tilde{\boldsymbol{S}}$ can be written as

$$\tilde{\boldsymbol{S}} = \bar{\boldsymbol{S}} + \sum_{i=1}^{n_p} \alpha_i \mathbf{A}\boldsymbol{\phi}_i^b. \tag{2.13}$$

#### 2.2.3.5 Statistical boundary shape models

Each one of the shapes in the database can be described by a linear combination of shape parameters and principal modes (see Equation 2.13). But all combinations of modes cannot be considered as valid shapes. In order to avoid incoherent shapes, shape parameter ranges have to be bounded. The term "$\kappa$-boundary models" was introduced in [160] to define the boundary models which cover

$\kappa\%$ of the overall population along each mode. Various studies on anatomical elements as liver [159, 161], clavicular cortical bone [160] or lunate and scaphoid bones [285] have shown that the shape parameters tend to follow normal distributions over the training data set. Consequently, the shape space $[-3 \times \text{SD}, 3 \times \text{SD}]$ (SD stands for standard distribution) of each mode will define a 99.7%-boundary model. A $q$-hyperrectangle [160] is defined around the mean model, where $q$ is the number of selected modes. It describes a subspace in dimension $q$ where lies the shape parameters able to represent 99.7% of the whole population's shape variation along each dimension. The distribution normality is tested using a Kolmogorov-Smirnov test at the 5% significance level.

**Remark 2.1** (*$\kappa$-boundary models and shape variation coverage*). Note that the $\kappa$-boundary model does not cover $\kappa\%$ of the whole population's shape variation. It only insures this value along each one of the modes of the PCA. Indeed, as discussed in the next chapter, in dimension $q$ the $\kappa$-boundary model covers at maximum $\kappa\%^q$ of the overall variation.

### 2.2.4 Online stage

#### 2.2.4.1 Shape identification from an out-of-sample geometry

Once the offline stage is done, any new shape can be represented by Equation 2.13. The best way to register a new shape is to introduce Equation 2.12 into Equation 2.9 and minimize the function with respect to the shape parameters $\alpha_i$. Indeed, the gradient descent step from Equation 2.11 becomes

$$\boldsymbol{\alpha}^{(k+1)} - \boldsymbol{\alpha}^{(k)} = -\beta \frac{dI}{d\boldsymbol{\alpha}} = -\beta \left[ \left( \gamma \boldsymbol{\Phi}^T \mathbf{L} \boldsymbol{\Phi} + \boldsymbol{\Phi}^T \mathbf{A}^T \mathbf{A} \boldsymbol{\Phi} \right) \boldsymbol{\alpha}^{(k+1)} - \boldsymbol{\Phi}^T \mathbf{A}^T \boldsymbol{d}^{(k)} \right] . \tag{2.14}$$

where $\boldsymbol{\Phi} = \left[ \boldsymbol{\phi}_1^b, \cdots, \boldsymbol{\phi}_{n_p}^b \right]$. The computational cost is now reduced to the solution of a $n_p \times n_p$ system with $n_p \ll 12 n_b^3$. The most time-consuming part is the computation of $\boldsymbol{d}$, the correspondence vector. To simplify the calculations it is possible to take $\gamma$ constant. As the shape already belongs to a predefined subspace it will keep a coherent deformation. Besides, it allows storing the whole matrix $\gamma \boldsymbol{\Phi}^T \mathbf{L} \boldsymbol{\Phi} + \boldsymbol{\Phi}^T \mathbf{A}^T \mathbf{A} \boldsymbol{\Phi}$ for faster computation.

#### 2.2.4.2 Iterative FEMWARP

The iFEMWARP was introduced in [259] and is an extension of the FEMWARP [15, 258] which is a part of the linear weighted Laplacian smoothing framework [257]. For a given mesh in 2D or 3D the FEMWARP assumes that the displacements of the boundary nodes are known. By considering a linear elastic deformation the position of the inner nodes can be easily computed by solving a linear system. Sometimes this procedure is not sufficient to untangle the mesh. A tangled mesh being a mesh where at least one of its elements has a null or negative Jacobian. The process is then iterated. At each iteration, the Jacobians of all the elements are computed and those with a null or negative Jacobian have their rigidity $E$ increased by 50%. The process is iterated until all elements have a strictly positive Jacobian. This method has been proved to be robust [259] and is quite easily implementable. A second parameter $\nu$ corresponding to the Poisson ratio also needs to be defined. To go further, we propose to enhance the method by taking into account the mesh quality. This latter is evaluated through its aspect ratio (AR) defined for a given tetrahedron as three times the quotient of inscribed and circumscribed sphere radii. It reads

$$AR = 3 \frac{IR}{CR} \tag{2.15}$$

where $IR$ (resp. $CR$) is the inscribed (resp. circumscribed) radius. A value of 1 means this is a regular tetrahedron, a value of 0 means the element is flat, also called silver. This metric is commonly used in the literature [5] or in mesh generator software such as gmsh. To run FE computations, it is often advised that the majority of elements has an AR superior to 0.3. However, there is no theoretical back-up proving this threshold value. To improve the iFEMWARP, instead

of only increasing the rigidity of elements with a negative Jacobian, the rigidity of poor quality elements is also increased at each increment following

$$E_e^{i+1} = E_e^i \left(1 + 0.5 \left(1 - \frac{AR^i}{0.3}\right)^2\right) \tag{2.16}$$

where $E_e^i$ is the Young modulus of the $e$-th element at increment $i$ and $AR^i$ its aspect ratio.

In our case, the displacements of the boundary nodes are defined by the shape parametrization. Once the shape parameters are identified the morphing can be directly applied. In this chapter the iFEMWARP is used with $E = 1kPa$ and $\nu = 0.4$. These two parameters are related to the morphing procedure and are called after the elastic constants due to the similarity of the morphing functional with the elastic energy. Nonetheless, these are not related to the tissue's real mechanical properties. All elements start with the same rigidity at the first iteration, after which their relative stiffness is updated. The parameter $\nu$ is chosen so as to limit the compressibility to avoid distorting too much good quality elements during the iterations.

### 2.2.5 Validation

Although the iTPS method has been introduced in the previous chapter, some details are reminded below for completeness. We use it here as a reference to assess the quality of our results.

#### 2.2.5.1 Iterative thin plate spline method

The rigid registration is done using the same method as for the TPS-PR. For the correspondence, landmarks are placed on the template shape by splitting the space into cells forming an equal-sized cubic grid. For each cell containing a surface point, a landmark is created by taking the closest point to the cell's center. Here the space is refined into cells of $7 \times 7 \times 7\,\mathrm{mm}^3$ resulting in around 1300 template landmarks for the proximal femora and the liver. Each landmark is associated with its corresponding point using the "Giessen" approach [286]. This method was proven more efficient than using only the Euclidean distance [161]. Once the initial correspondence is done the registration is computed by minimizing the energy:

$$I(f) = \sum_{i=1}^{n_S} ||\boldsymbol{t}_i - f(\boldsymbol{s}_i)|| + \gamma_f I_f \tag{2.17}$$

where $\boldsymbol{s_i}$ are the template landmarks and $\boldsymbol{t}_i$ their corresponding points on the target. $\gamma_f$ is the regularization parameter and $I_f$ is defined in Equation 2.6. The interpolant $f$ has the form

$$f(x, y, z) = a_1 + a_2 x + a_3 y + a_4 z + \sum_{i=1}^{n_S} w_i U(||\boldsymbol{s}_i - (x, y, z)||) \tag{2.18}$$

where $U(r) = abs(r)$ is a radial basis function.

By iterating the matching and registration processes the final registration is improved. In this chapter $\gamma_f = \delta^2 \gamma_{f0}$ where $\gamma_{f0} = 100$ and $\delta$ is the mean edge length between two points in the set, as recommended in [22]. The maximum number of iterations is fixed to 35.

#### 2.2.5.2 Error metrics

The quality of each registration method is evaluated using three metrics introduced in [76]: the compactness, the generalization, and the specificity. They depend on $n_p$, the number of modes of variation used for the reconstruction. The measure of the compactness is defined by

$$C(n_p) = \sum_{m=1}^{n_p} \lambda_m$$

where $\lambda_m$ is the $m$-th eigenvalue calculated from PCA. A compact model is one with small variance and which requires a small set of parameters to describe the shape. Then, the measure of the generalization is defined by

$$G(n_p) = \frac{1}{N_T} \sum_{i=1}^{N_T} Dist(\boldsymbol{S}_i^0, \boldsymbol{S}_i(n_p))$$

where $N_T$ is the number of shapes of the training set, $\boldsymbol{S}_i^0$ the $i$-th registered shape and $\boldsymbol{S}_i(n_p)$ the corresponding reconstructed shape with $n_p$ modes. The generalization is the ability of the SSMs to represent a shape out of the training set. To evaluate it the SSM is built using $N_T - 1$ shape and the last shape is then reconstructed using $n_p$ modes. The distance between the reconstruction and the ground truth is then evaluated. This leave-one-out test is repeated for all the shapes in the database and then averaged. Finally, the measure of the specificity is defined by

$$S(n_p) = \frac{1}{N} \sum_{i=1}^{N} \min_{\boldsymbol{T}_j \in \mathcal{T}_S} Dist(\boldsymbol{T}_j, \boldsymbol{S}_i(n_p))$$

where $N$ is the number of generated shapes, $\boldsymbol{S}_i$ is a randomly generated shape and $\mathcal{T}_S$ the training set. The specificity is the ability to only represent shapes that are similar to the training set ones. A new set of 1000 uniformly distributed shapes is generated from the SSMs for $n_p$ modes. For each generated shape the distance is computed from its closest shape from the training set. The mean value of the distances is used as the measure of the specificity.

The distance between two shapes is defined in [297] as

$$Dist(\boldsymbol{S}, \boldsymbol{T}) = \frac{1}{2} \left[ \frac{1}{n_S} \sum_{\boldsymbol{s} \in \boldsymbol{S}} \min_{\boldsymbol{t} \in \boldsymbol{T}} ||\boldsymbol{s} - \boldsymbol{t}|| + \frac{1}{n_T} \sum_{\boldsymbol{t} \in \boldsymbol{T}} \min_{\boldsymbol{s} \in \boldsymbol{S}} ||\boldsymbol{s} - \boldsymbol{t}|| \right] \tag{2.19}$$

where $\boldsymbol{s}$ (resp. $\boldsymbol{t}$) are the points belonging to $\boldsymbol{S}$ (resp. $\boldsymbol{T}$) and $N_s$ (resp. $n_T$) their number. The smaller the value, the more similar the shapes. For all of these metrics smaller values mean a better approach. As they depend on the training set, there is no threshold value which allows evaluating the quality of the registration method, that is why we compared the TPS-PR with the iTPS.

To assess the efficiency of the iFEMWARP to describe good volumetric meshes from the SSMs the regularity and quality of the meshes are evaluated. A finite element $e$ is said to be regular if its Jacobian is positive in all of his nodes. For a specified number of mode $n_p$, 1000 instances normally distributed are generated within the boundaries [37] using the SSMs. The iFEMWARP is then applied to reconstruct their volumes. If the morphing does not succeed in untangling the mesh in less than 30 iterations the method is considered as a failure. The percentage of failure defines the regularity error R($n_p$). SSMs built with the iTPS and the TPS-PR are compared. The mesh quality is also evaluated by generating 1000 normally distributed instances, but for the liver only and for a fixed number of mode $n_p = 30$. Only the TPS-PR-built SSMs are considered. For each generated instance the AR of the mesh is evaluated. The normal distribution of the parameters is justified by the fact that the target shape parameters are also normally distributed.

## 2.3 Results

For the liver (resp. the femur) the TPS-PR was run with $n_b = 5$ (resp. $n_b = 6$) (see Figure 2.1a and 2.1b) and $\gamma_r = 0.3$. 35 increments were done for each target.

As mentioned in Paragraph 2.2.3.5 the normality of the shape parameters has to be tested to validate the choice of the boundary shape model. In practice, when using the TPS-PR method only the $15^{th}$ liver mode and the first of the femur did not strictly follow a normal distribution (see Figures 2.2a and 2.2b). The hypothesis of normal distributions is acceptable and the choice of the shape parameter subspace is coherent.

For both the livers and the femurs the TPS-PR models are more compact (Figures 2.3a and 2.4a). This is due to the fact that the evaluation is done on the bounding box degrees of freedom which are fewer than the number of vertices. The generalization is slightly better for the liver

database (Figure 2.3b) and almost equivalent for the femur one (Figure 2.4b). The specificity is worse for the liver but better for the femur (Figures 2.3c and 2.4c). Globally, for this set of parameters both methods behave identically, the compactness put apart.

The error done during the morphing of the liver instances is presented in Figure 2.5. For the femur no tangled meshes are produced with both methods. This is most likely caused by the fact that bones have small shape variations (see Table 2.1). Hence, the mesh is not under large deformations during registration and keeps its integrity. In the case of the liver the TPS-PR produces few tangled meshes starting from $n_p = 16$, but always less than 1% of the generated shapes. On the other hand, the iTPS produces tangled meshes starting from $n_p = 2$ and the percentage of irregular meshes steadily increases until 8% for $n_p = 50$. Globally, the error is bigger in the liver case because the database is larger and there is more variability in its anatomy (see Table 2.2). Moreover, with a large database, the probability to encounter difficult shapes to register increases and poorly meshed surfaces are introduced.

The quality results are presented in Figure 2.6 for $n_p = 30$ in the liver case and for 30 iterations of the iFEMWARP. The SSMs were built using the TPS-PR. In Figure 2.6b the mean AR over 1000 randomly generated shapes is presented in a histogram, showing the efficiency of the enhanced iFEMWARP and the good averaged quality of the morphed meshes. The quality distribution is slightly wider than the template one but stays within an acceptable range. An example of a generated mesh can be seen in Figure 2.6a with the value of its AR represented to testify of the good behavior of the method.

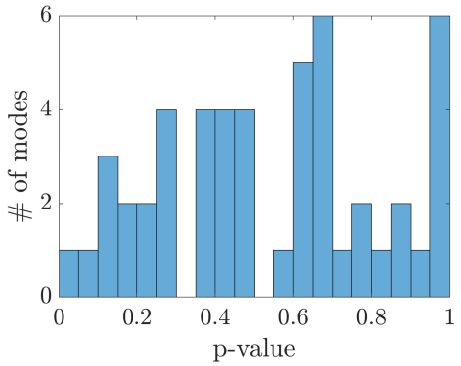


(a) Histogram of the p-values for the liver data, only the 50 first modes are represented.

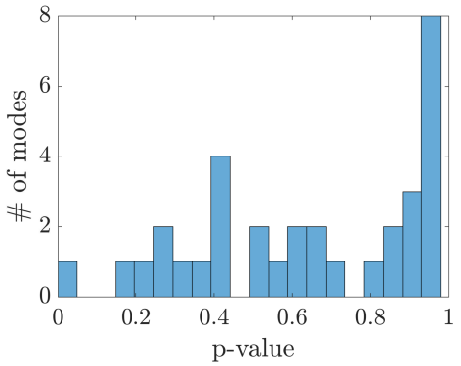


(b) Histogram of the p-values for the femur data, all 33 modes are represented.

Figure 2.2: Kolmogorov-Smirnov test at the 5% significance level applied to the shape parameters of the registered targets obtained with the TPS-PR. A $p$-value superior to 0.05 means the data distribution is not significantly different from the normal distribution.

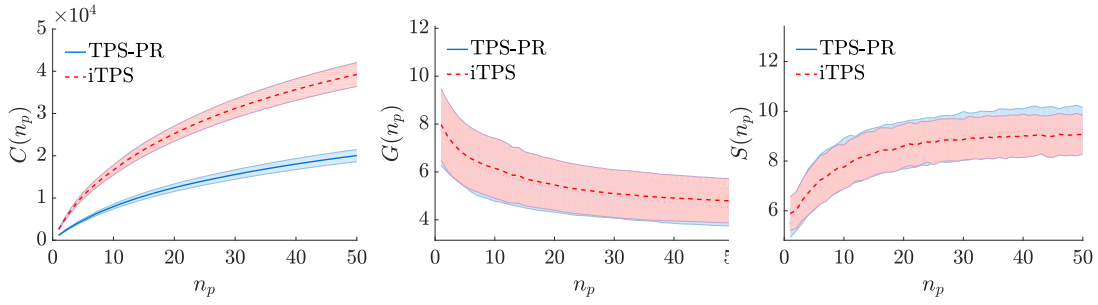


(a) Compactness (b) Generalization (c) Specificity

Figure 2.3: Comparison of the methods for the liver database (compactness, generalization, and specificity). For a given number of modes lower values mean a better method. The shaded area corresponds to one standard deviation.

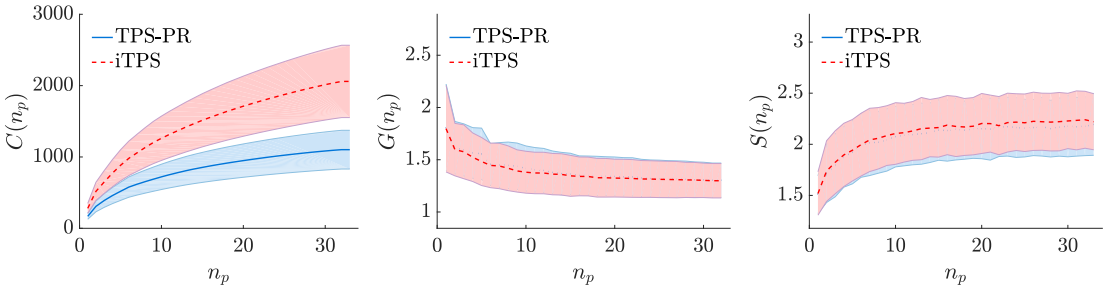


(a) Compactness (b) Generalization (c) Specificity

Figure 2.4: Comparison of the methods for the femur database (compactness, generalization, and specificity). For a given number of modes lower values mean a better method. The shaded area corresponds to one standard deviation.

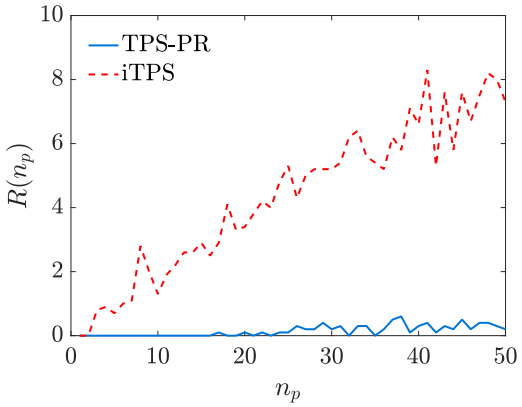


Figure 2.5: Percentage of tangled meshes among the 1000 liver instances generated for each mode $n_p$ after 30 iterations of the iFEMWARP.

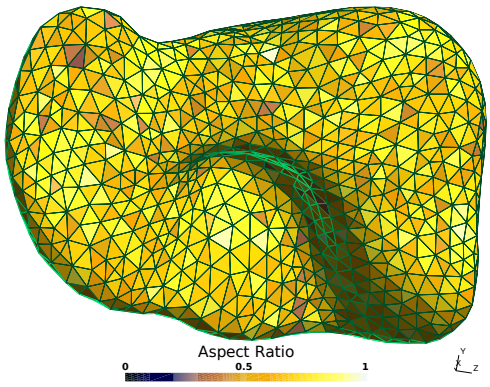


(a) AR map of a randomly generated liver FE model. The visualization is done on gmsh.

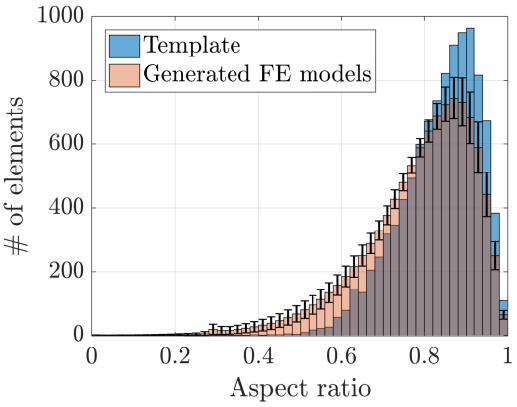


(b) Histogram of the mean AR over 1000 randomly generated shapes. The error bar corresponds to one standard deviation. The template AR histogram is also represented to provide a ground truth.

Figure 2.6: Application of the enhanced iFEMWARP on the liver SSMs for $n_p = 30$. 30 iFEMWARP iterations were done.

Table 2.1: Registration example for five femur shapes. The first row is the target shape from the training set. The second is the shape registered using the TPS-PR and the third with the iTPS method.

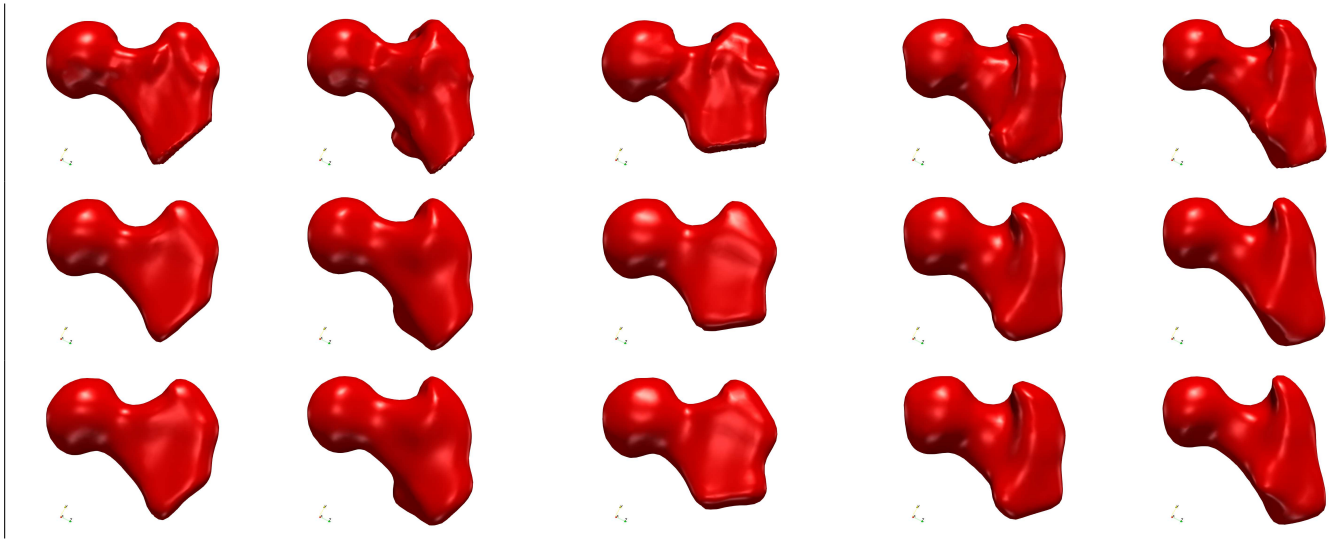


Table 2.2: Registration example for five liver shapes. The first row is the target shape from the training set. The second is the shape registered using the TPS-PR and the third with the iTPS method.

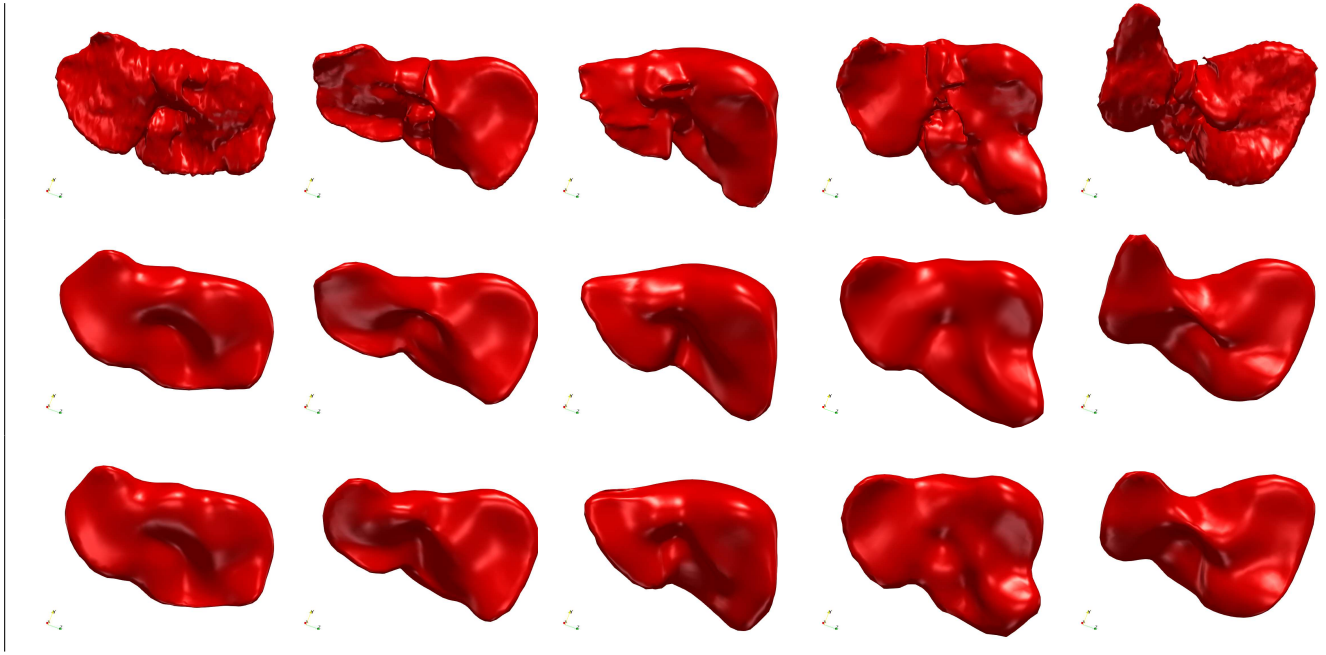

## 2.4 Discussion

This study has been the opportunity to create SSMs from a large database of 385 liver shapes. This is to our knowledge one of the biggest liver training set used in medical SSA coming from real data. With such a large database it is hard to describe the shape with a restricted number of parameters. Visually, at least 30 to 50 modes are required to describe all shapes with fidelity. The tests that have been performed showed how a substantial difference arises when applying the method to real and large data sets and it would be interesting to see how it behaves toward others shapes databases. Indeed, as presented for the femur data set, the method works fine, regardless of the registration method. On the contrary, for the liver, the regularity error is higher but the TPS-PR method succeeds to limit it under 1%. We observed that the true benefits of using the TPS-PR are more evident when larger data sets are used or when the shapes present a greater variability. Concerning the quality of the generated meshes, we showed that they are globally adapted to run FE simulations. However, the AR alone cannot be considered as an insurance of the good mesh quality. Some invalid meshes may still be generated.

The main limitation of the method is that the TPS-PR tends to smooth the target shape. Hence, if small details with strong variations need to be represented the method will probably not be able to fit them. The choice of the parameters has a strong influence on the results and sometimes the best option results from a tradeoff between the quality of surface registration and that of the volume mesh. The parameter $\gamma_r$ is mainly used as a way to penalize the registration and improve the correspondence. Besides, $n_b$ allows fostering either the quality of the registration for high values either the chances of success of the morphing for lower values. A small $n_b$ will smooth the registration and consequently preserve the mesh quality. Smoothing is also necessary in order to eliminate numerical artifacts from the FE solutions, which may arise from the presence of excessively distorted elements or sharp corners. The idea to use a bounding box to penalize the deformation and smooth the surface has already been tackled in [46] to register a generic volumetric mesh onto the patient organ shape, in conjunction with a mesh regularity and quality correction. This correction step presented in [47] could also be used in our case as a backup solution to untangle meshes.

Concerning the computational time, with a Matlab (The MathWorks, Inc. USA) implementation the iFEMWARP takes around 2 seconds per iteration for the proximal femoral and 3 seconds for the liver. Most of the time the convergence is reached in 1 iteration. The most difficult shapes to reconstruct are located on the limits of the boundary model but they also are statistically less likely to be observed. For the registration, an iteration of the TPS-PR takes between 4 and 0.2 seconds depending if the golden-section search is used or not. It is possible to further accelerate the method by not enforcing the golden-section search at each iteration. Indeed, acceptable results can be obtained when the golden-section search is only performed every few iterations. On the other hand, this introduces a significant speed-up since this task is the most time-consuming.

## 2.5 Conclusion

We presented and tested a procedure to automatically generate FE models from medical images by coupling SSMs to a mesh morphing technique. A new registration method has been developed to build the SSMs in order to increase the efficiency of the morphing method. Concerning the quality of the reconstructed shapes, we have shown how the proposed TPS-PR performs equally well as other traditional techniques like iTPS while significantly improving the quality of interior volume meshing. The method can be in principle coupled to other more sophisticated registration techniques (e.g. the SLIDE method [75] which has been proven to be really efficient). However, the choice of the particular approach adopted in this chapter is justified by its flexibility and robustness when applied to a large and rich data set. This approach can be potentially very efficient in automated FE model generation from real data. Indeed, instead of registering a template mesh onto a specific target we create first a shape-parametrized model that allows us to apply a fast morphing algorithm afterward. By doing so the application is faster and enables the creation of shape-realistic FE models.

In the next chapter, this method is used to enable efficient shape parametrization of FE models for parametric model order reduction.

Chapter 3

# A model order reduction approach for anatomy-specific and real-time deformable models of the liver

**Abstract** In this chapter we propose an automated procedure to create mechanical models of the human liver with patient-specific geometry and real-time capabilities. The method hinges on the use of statistical shape analysis to extract the relevant anatomical features from a database of medical images and model order reduction to compute an explicit parametric solution for the mechanical response as a function of such features. The sparse subspace learning, coupled with a finite element solver, is chosen to create low-rank solutions using a non-intrusive sparse sampling of the feature space. In the application presented in the chapter, the statistical shape model is trained on a database of 385 three-dimensional liver shapes, extracted from medical images, in order to create a parametrized representation of the liver anatomy. This parametrization and an additional parameter describing the breathing motion in linear elasticity are then used as input in the reduced order model. Results show a consistent agreement with the high fidelity finite element models built from liver images that were excluded from the training dataset. However, we evidence in the discussion the difficulty of having compact shape parameterizations arising from the extreme variability of the shapes found in the dataset and we propose potential strategies to tackle this issue.

## Contents

## 3.1 Introduction

### 3.1.1 Medical context

Thanks to recent advances in diverse medical technologies, augmented reality (AR) is now on the doorsteps of operating rooms (OR). Such technology opens up many perspectives for various medical applications such as interventional radiology or minimally invasive surgery (MIS) [198, 25]. The main idea is to display virtual information on real images of the patient to see through opaque tissues. In interventional radiology, this augmented representation of the patient is important to visually follow the targeted organs. For example, in radiotherapy such a tool allows following the tumor and predict its displacement during the breathing [126], permitting to minimize the radiated area and consequently the trauma for the patient. Concerning the MIS, the AR is used as a back up for two major drawbacks of the technique: the reduced visibility and in the case of robot-assisted MIS the loss of haptic feedback during the operation [209]. Thanks to AR, it is now possible to provide the surgeon with additional information such as the position of tumors [115, 114] or blood vessels [92, 114]. Modifications in the organ topology due to cuts can even be taken into account [218]. Results on haptic feedback technologies in AR, although not yet robust enough to be used in the ORs, are showing promising results and are currently used as training and learning tools [213, 287]. However, these approaches are often more challenging when applied to soft tissues because of the difficulty of continuously adapting the AR scene to the position of the features of interest. In abdominal surgery, for example, a lot of factors can interact with the organs. They can come from the internal or external environment (surgical tools, insufflation of gas in the peritoneum) or be physiological movements (heart beats, breathing). Hence the necessity to develop robust real-time biomechanical models of the tissues to integrate these movements and reproduce them with fidelity.

### 3.1.2 Scope of the current work

In most computational medicine applications the goal is to create a digital replica of a considered biophysical system that can realistically reproduce the most essential observed features. Two key aspects in this are the possibility to customize the models for specific use cases (accounting for inter-patient and inter-population variabilities) and the real-time interactive response to new assimilated data. This emerging technology, known as the digital twin, merges complex biophysical modeling and advanced real-time simulation techniques with data assimilation and analysis for decision support. Some model and simulation aspects were addressed in the review by [73] in the surgical framework and the use of machine learning is investigated in [176, 158, 177, 178] for parameter identification and mechanical behavior prediction. More specifically, models for visual and haptic feedback applications were developed in [200, 201, 203], where the nonlinearities and load parametrization issues are tackled, and in [202, 231], where the simulation of surgical cutting is dealt with. In this chapter, we build on these works and focus on the aspects related to the integration of medical images in real-time interactive models to personalize the organ anatomy. We propose a numerical framework to personalize biomechanical models interactively using new anatomical data without rebuilding the models from scratch.

The specific anatomy of the patient is generally taken into account case-by-case thanks to pre-operative data such as magnetic resonance images (MRI) or computed tomography (CT) scans. From these inputs, the surface and the volume of the organs of interest can be identified, reconstructed and meshed [121, 18, 306, 149]. This can be a time-consuming and computationally intensive task and needs to be repeated for any new patient, posing severe limitations to the use of such models within interactive simulation environments. Then, to reach real-time performance the models either need to simplify the formulation, e.g. using lumped parameter models, corotational finite element or beam structures [114], or use specific hardware set-up for fast parallel computations [136]. In the first case, oversimplification in the model formulation may lead to incorrect mechanical behavior unless the lumped parameters are accurately tuned to capture the essential features of the equivalent distributed parameters model. In the second one, it involves high-performance computing resources that are rarely available in a clinical environment. In both

cases, computational time will strongly depend on the mesh refinement, limiting the accuracy to the hardware capacity. In this chapter, we follow the route of collocation-based model order reduction (MOR). This approach allows us to simultaneously tackle the specific anatomical representation and the real-time constraint without being limited by the simplification of the physics or the computational cost and bypassing mesh generation and model assembly costs. The reduction of computational costs also enables the use of inexpensive and simple hardware, which could be easily installed in the ORs.

### 3.1.3 Reduced order modeling for organ twins models

MOR methods have seen a growing interest this last decade. They allow reducing the computational complexity in numerical simulations by a parametrization of the solution, enabling real-time *online* computations without simplifying the underlying physics of the model. In return, a computationally intensive *offline* stage must be done beforehand. They are good candidates for the creation of digital twins because they handle data assimilation through their parametric formulation. A distinction can be done between the projection-based and the collocation-based MOR methods. The underlying idea in the former is to seek the solution for the model's governing equations in a lower-dimensional subspace that is specific to the problem at hand. This is accomplished by imposing the orthogonality of the equations' residuals with respect to the new subspace. The resulting system of equations has a considerably reduced computational complexity, while the accuracy of the solutions is preserved. Based on the way the reduced basis is *learned*, projection-based MOR methods are usually divided in two categories: the *a posteriori* methods like the proper orthogonal decomposition [54] or reduced basis method [229], where the reduced order model (ROM) is built from a set of training solutions, available from previous simulations (called snapshots), and the *a priori* methods like the proper generalized decomposition (PGD) [60], in which the parametric solution is assumed to respect the canonical tensor format and is then built from the equations governing the problem. These methods have been used for different applications in relation to the medical framework, and in particular computational surgery [73]. Projection-based ROM including geometrical parameters has been addressed in [172] for optimization purposes and in [104] to synthesize new shapes from manifold interpolation. When using real medical data, the first difficulty to create anatomical models encompassing the shape comes from its parametrization. This latter can be obtained through the use of statistical shape models (SSMs), and, in particular, point distribution models (PDMs) [66]. From a training set of real anatomical shapes the PDMs associate to a template the principal modes of shape variation. This way, the geometry of a specified organ can be statistically described by a limited set of parameters allowing image segmentation [120] or the creation of finite element (FE) shape parametrized models [199, 42].

A key assumption for projection-based ROM is that the problem variational form is affine with respect to the parameters, the so-called affine parametric dependence mentioned in Chapter 1. This guarantees the complexity reduction in the projection step and is therefore fundamental for the performance of the method in terms of execution time. Unfortunately, affine approximations are not always easily recovered. This bottleneck is most likely to be encountered in problems involving a parameterization of the domain geometry, as in our case. To efficiently handle the representation of the shape, we opted for a collocation-based MOR method, the sparse subspace learning (SSL) [36]. On the contrary to projection-based approaches, in collocation-based methods the residual is not constrained to be orthogonal to the solution's subspace but rather enforced to be exactly zero at properly chosen points in the parametric space, called the collocation points. The parametric solution is built by interpolating the solutions of the model at these points, which makes the ROM an a posteriori model. In our case, the main advantage is that the approach is fully data-driven, as it does not require the evaluation of the residual nor its projection onto the lower-dimensional space. Hence, the lack of affinity of the variational form does not affect the performance of the method. As the shape parameterization is based on a PDM which results in the loss of affinity, it motivates our choice of the SSL. This latter is based on the use of hierarchical collocation to build the parametric model, exploiting sparsity and low-rank representation for the solutions. SSL aims for the sparsity of the representation using a sparse grid sampling approach while simultaneously building a reduced order representation of the solution. New out-of-training

solutions can be computed by a hierarchical interpolation of the snapshots coefficients in the reduced basis. Since SSL is only based on the output of a FE solver and does not require any modification of it, it is regarded as a non-intrusive technique. However, the use of hierarchical collocation in the parametric space, in our case hierarchical polynomials, requires a fundamental condition on the regularity of the solution in the parametric space of shape features. To preserve this regularity, we adopt the morphing technique introduced in Chapter 2 to smoothly adapt the FE mesh of the model according to the shape parameters.

### 3.1.4 Overview and chapter organization

This chapter presents a method based on the SSL to create patient-specific mechanical models of the human liver by taking into account their anatomy. To do so, the method developed in the previous chapter (see Chapter 2) based on SSA and a morphing technique is used in order to get the shape parametrization of the human liver. By combining the SSA, the morphing technique, and the SSL, one can solve in real-time a chosen mechanical problem on any shape taken into account by the parametrization. In this chapter, the specific case of the breathing is developed, motivated by previous works from Hostettler et al. [125, 126] where a method to predict the abdominal organs and tumors positions during free breathing was developed. During the breathing, the displacement of the liver's surface can be estimated. From this input the presented method allows reconstructing the organ inner displacements accordingly to the material's constitutive behavior used to represent it, enabling the visualization of tumors or blood vessels positions within the liver. We first present the liver shape database used for the SSA in Section 3.2.1. The mechanical model is introduced in 3.2.2 and the associated breathing simulation is presented in Section 3.2.3. The method to create the parametric reduced order model (pROM) is described in Section 3.3, followed by the process to adapt the model to a new patient in Section 3.3.4. Then, error metrics are defined and generated results are presented and commented in Sections 3.4 and 3.5. Finally, the identified limits of the method are highlighted in the discussion and some potential solutions are suggested.

Data acquisition, processing, and assimilation, as well as more technological aspects, are not covered in this work. More insight can be found in Part II.

## 3.2 Materials and methods

If not specified otherwise, all vectors mentioned by a bold italic letter belong to a three-dimensional space $(x, y, z)$. A shape is described by a point cloud $\boldsymbol{X} \in \mathbb{R}^{n_X \times 3}$ and will correspond to $\boldsymbol{X} = (x_1, \ldots, x_{n_X}, y_1, \ldots, y_{n_X}, z_1, \ldots, z_{n_X})^T$. For the sake of simplicity, the Euclidean distance, or $\ell^2$-norm, will be denoted by $||\bullet||$.

### 3.2.1 Data

The data used in this chapter are the same as in the previous one, described in Section 2.2.1. A set of $N_T = 385$ external surface meshes of livers is considered. They will be referred to as the *target* shapes. The targets have different numbers of vertices (from $2,000$ to $150,000$). Due to the fact that the database has been collected over many years, different qualities of segmentation are included. Some of the shapes are represented in Figure 3.1. A *template* shape close to the average target is chosen as reference (see Figure 3.2) and meshed with gmsh [96]. Its surface is described by $n_S = 1,393$ vertices and $2,782$ triangles. The volume is meshed with $10,163$ tetrahedrons for a total of $n_V = 2,452$ vertices. Its maximum length is $260mm$. Special attention has been paid to the mesh quality using mesh optimization functions implemented in the open software gmsh.

### 3.2.2 Model assumptions

The pROM of the liver is created under the assumption of the quasi-static mechanical equilibrium with a prescribed displacement on the boundaries. The governing equations read

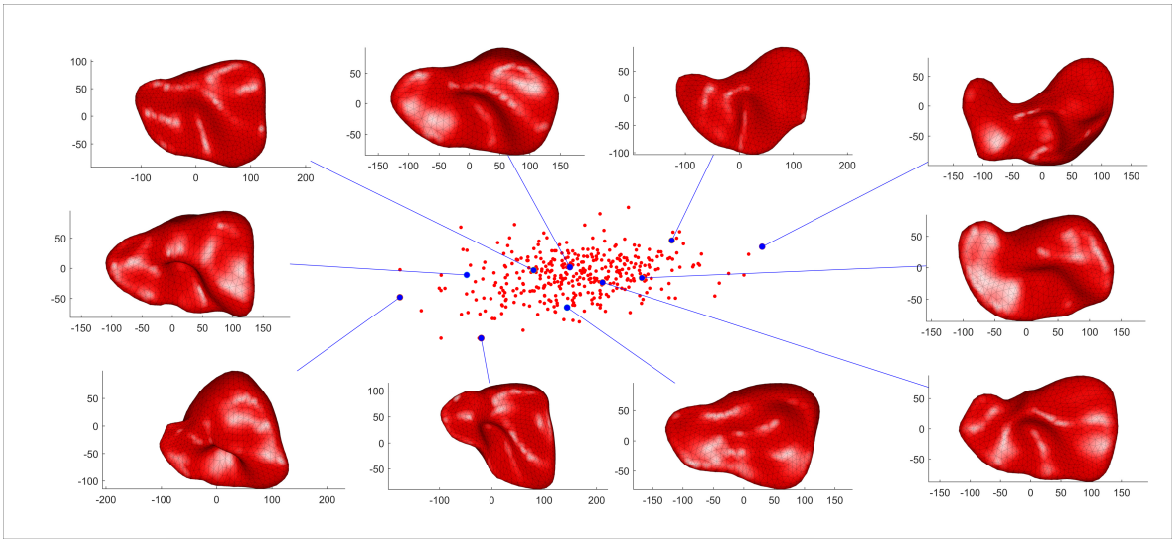

Figure 3.1: 2D mapping of the liver shape population using PCA along the first and second principal axes. Some of the registered target shapes are displayed and linked to their two-dimensional representations. Shapes taken from the dense area are similar, whereas isolated ones are unique. During the construction of the shape parameters boundaries (see Section 3.3.2 and Figure 3.5c) some of these shapes are excluded in order to generate a more precise and compact pROM. The visualization is done on Matlab.

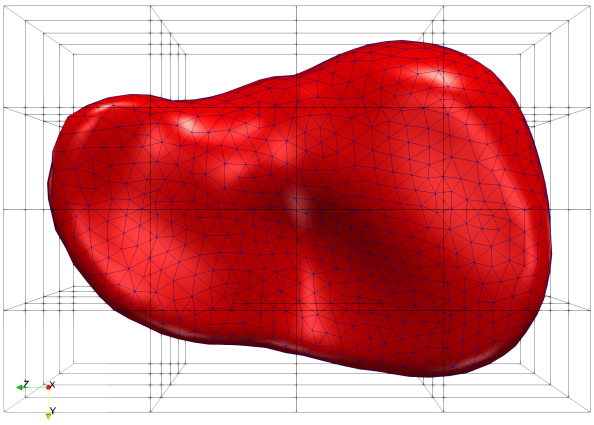

Figure 3.2: Template liver shape. The control points associated with the spline representation used in the non-rigid registration method (see Chapter 2, Section 2.2.3.3) are shown, the discretization used is $n_b = 5$. The mesh has been generated using gmsh and the display is done on Paraview.

$$\begin{cases} \nabla \cdot \sigma & = 0 \quad \text{in the volume} \\ \boldsymbol{u} & = \boldsymbol{u}_d \quad \text{on the boundaries} \end{cases} \tag{3.1}$$

where $\boldsymbol{u}$ is the displacement field and $\sigma$ the Cauchy stress tensor. The user-prescribed motion $\boldsymbol{u}_d$ can be deduced from the position of the abdomen and that of the surrounding organs. For example, for integration in a complete AR tool one could use the work presented in [126] where the position of inner organs is estimated from the abdomen surface motion parametrization under free breathing. The stress-strain relationship is assumed to be linear and the material properties are considered homogeneous and isotropic, although, hyperelastic behavior could also be considered. Figure 3.3 shows an example of geometry in which the vascularization position is updated based on the computed displacement field.

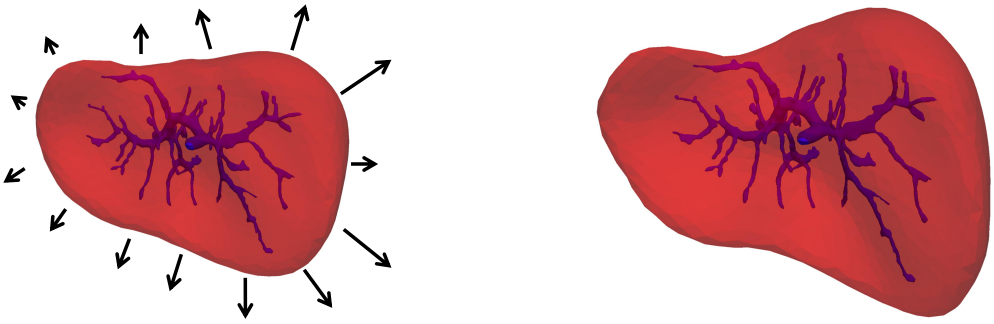

(a) $\boldsymbol{u} = 0$ (b) $\boldsymbol{u} = \boldsymbol{u}_d$ on the boundaries

Figure 3.3: Visualization of the liver (in red) with the representation of the portal vein (in blue) for different values of $\boldsymbol{u}$. The black arrows represent the direction of $\boldsymbol{u}_d$. One of the interests of the procedure is to be able to display internal features to see through the opaque tissues of the liver. The position of the portal vein is deduced from the liver displacement fields computed through the mechanical equilibrium laws (Equation 3.1).

### 3.2.3 Breathing simulation application

The liver is considered as an elastic solid defined by $E = 3kPa$ and $\nu = 0.48$. Its movement during the breathing is modeled by applying fixed Dirichlet boundary conditions to the surface nodes :

$$\boldsymbol{u}(b) = b \times \boldsymbol{u}_d \quad \text{on the boundaries,} \tag{3.2}$$

where $b \in [0, 1]$ is the breathing parameter. The displacement $\boldsymbol{u}_d$ has been computed by taking the extreme positions of a real liver during the breathing *in vivo*, from data provided by the IRCAD. By registering the template shape to the maximum inhalation and exhalation positions using the thin plate spline-parametrized registration (TPS-PR) algorithm (see Chapter 2 Section 2.2.3), the displacement can be directly applied to the template mesh.

**Remark 3.1** (*Breathing modeling*). In this chapter, a single parameter is used to describe the breathing motion. Multiple parameters could be used as well, possibly leading to a more accurate representation. The parametrization could then be obtained by applying a SSA to a database of images corresponding to maximum inhalation and exhalation positions of several patients.

## 3.3 Creation of the parametric reduced order model

### 3.3.1 Overview

In the general case, the offline procedure to build pROM can be separated into two main steps: the parametrization of the problem and the use of a separated variable representation to enable fast computations during the online stage. An illustration of the method is given in Figure 3.4.

**Problem parametrization** To take into account the variability of the model according to the fields of interest, a parametric approach is used. Each field of interest is described by one or several parameters. In this chapter, a distinction is done between the explicit and the implicit parameters (respectively noted $\boldsymbol{p} = (p_1, ..., p_D)$ and $\boldsymbol{\alpha} = (\alpha_1, \cdots, \alpha_{n_p})$). The firsts encompass all kind of parametrization where the parameters are directly deduced from the formulation of the fields of interest. For example, in the case of the material properties, the Young modulus or the Poisson ratio. The same can goes for boundary conditions. In the breathing application presented in this chapter $\boldsymbol{p} = b$ is deduced from Equation 3.2. On the contrary, implicit parameters are "hidden" within the model and must be inferred through methods such as the SSA used to represent the liver's shape. This latter is detailed in Chapter 2 Section 2.2.3. Note that in the current chapter the choice of the parameters subspace boundaries, described hereafter in Section 3.3.2, is different.

**Separated variables representation** Once the model is parametrized, the solution - here the displacement field - is expressed using a separated variables representation. More specifically, the canonical tensor format is used, which allows overcoming the exponential complexity of multi-parametric models. This reads

$$\boldsymbol{u}(\boldsymbol{x}, \boldsymbol{\alpha}, \boldsymbol{p}) = \sum_{i=1}^{d} \delta_i \boldsymbol{B}_0^i(\boldsymbol{x}) \prod_{k=1}^{n_p} B_k^i(\alpha_k) \prod_{l=1}^{D} B_{n_p+l}^i(p_l)\,. \tag{3.3}$$

This formulation expresses the multidimensional field $\boldsymbol{u}$ as the truncated modal expansion in which each mode is the product of lower dimensional functions $B_j^i$ expressing the parameter dependence. $d$ is called the canonical rank of $\boldsymbol{u}$. For the application considered in this chapter, Equation 3.3 becomes

$$\boldsymbol{u}(\boldsymbol{x}, \boldsymbol{\alpha}, b) = \sum_{i=1}^{d} \delta_i \boldsymbol{B}_0^i(\boldsymbol{x}) \prod_{k=1}^{n_p} B_k^i(\alpha_k) B_{n_p+1}^i(b)\,. \tag{3.4}$$

To reach this specific formulation the SSL is used. The method is described below in Section 3.3.3.

### 3.3.2 Shape parametrization

We suppose that the SSA procedure described in Section 2.2.3 in Chapter 2 is done and that any new shape $\tilde{\boldsymbol{S}}$ can be written as

$$\tilde{\boldsymbol{S}} = \bar{\boldsymbol{S}} + \sum_{i=1}^{n_p} \alpha_i \mathbf{A} \boldsymbol{\phi}_i^b \tag{3.5}$$

where $\bar{\boldsymbol{S}}$ is the mean shape, $\alpha_i$ are the shape parameters, $\mathbf{A}$ is the transformation matrix from the control points to the liver's shape and $\boldsymbol{\phi}_i^b$ are the modes of deformation. Once the shape parametrization has been obtained, the subspace where the parameters lie needs to be defined. The definition of this subspace is critical. It must encompass most of the shape variation but must not overpredict the solution. A subspace too large can lead to distorted liver shapes or even tangled meshes. As we aim to use the shape parametrization in conjunction with the iFEMWARP (iterative finite element-based mesh warping) morphing method (see Chapter 2 Section 2.2.4.2), a tangled mesh would lead to the failure of the pROM offline stage. The construction of the subspace is based on the knowledge of the shape parameters associated with the target shapes. Each set of $n_p$ shape parameters defines a shape (Equation 3.5) and a point in dimension $n_p$ (Figures 3.5a and 3.5b). First, a point selection is done to exclude exceptional shapes from the training set.

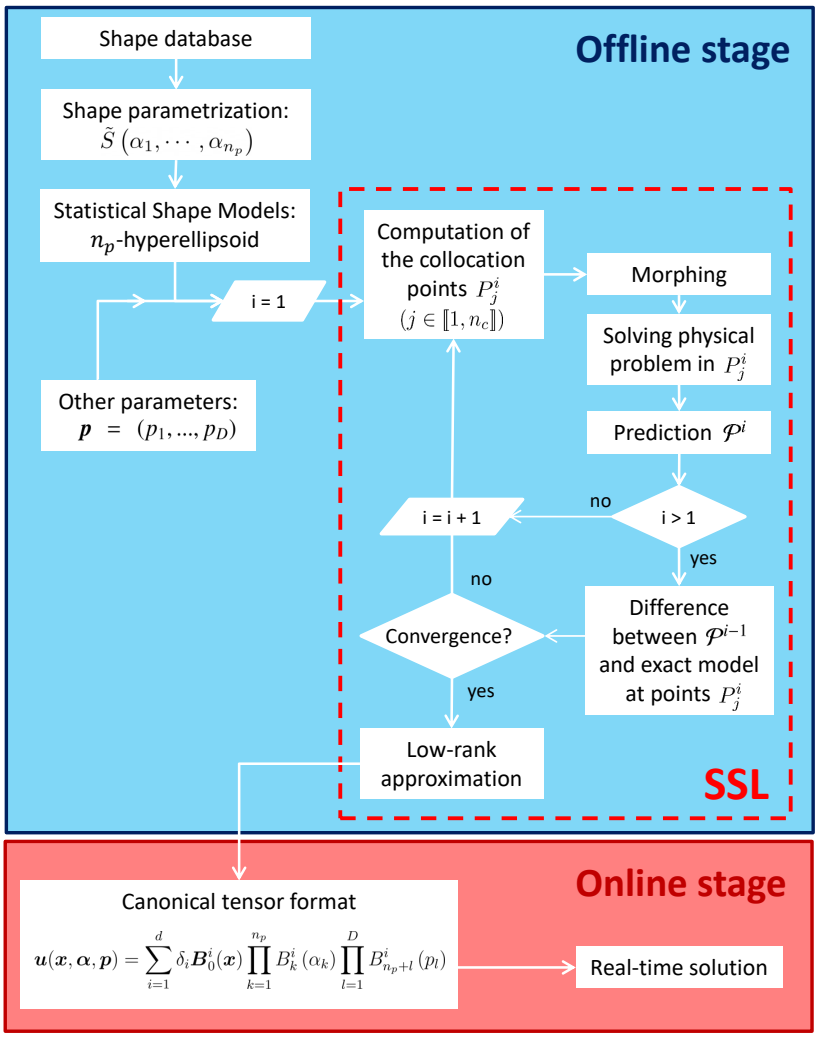


Figure 3.4: Summary of the method to construct the patient-specific pROM. First, an *offline* stage is done where the shape parametrization is built and the SSL is applied. Other parameters $\boldsymbol{p}$ than the shape can be added by the user, in this chapter the breathing motion is added using one parameter such as $\boldsymbol{p} = b$. This step can be computationally intensive but is easily parallelizable. Computational details and notations can be found in Sections 3.3.2 and 3.3.3. Then, for the *online* stage, the solution is written in a compact canonical tensor format (see Equation 3.3) allowing fast computations. This second step enables the real-time visualization of the solutions through the parametric formulation.

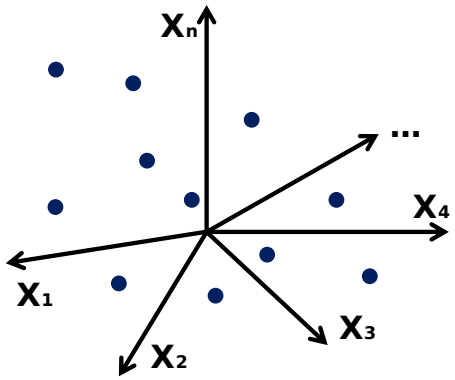


(a) Training data set in initial dimension $n$, where $n$ is the number of degrees of freedom.

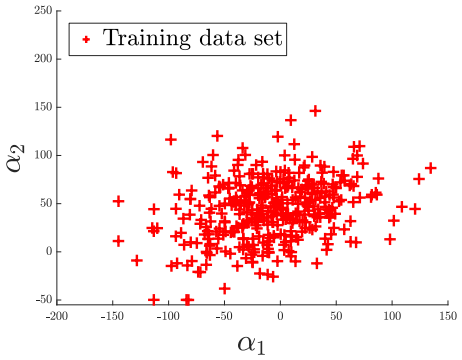


(b) Training data set in dimension $n_p = 2$. A shape is written $\tilde{\boldsymbol{S}}(\alpha_1, \alpha_2)$ (see Equation 3.5).

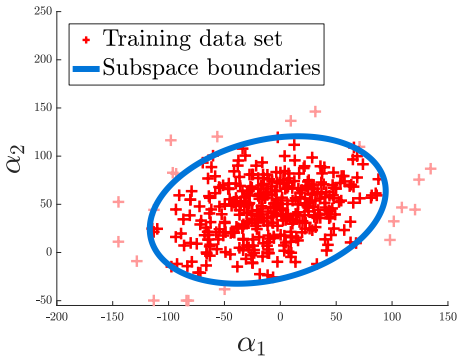


(c) Shape parameters subspace boundaries of the training data set with a 2-hyperellipsoid defined by $\mathcal{T}(r, \theta)$ (see Equation 3.7).

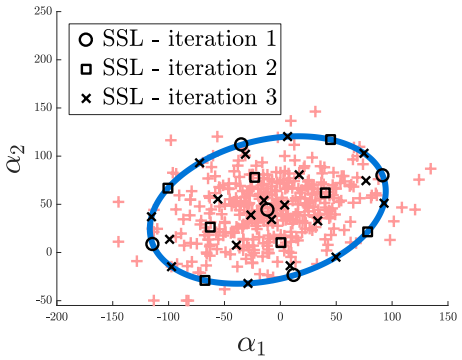


(d) Position of the SSL collocation points in the shape parameters subspace for the three first increments (see Section 3.3.3).

Figure 3.5: Illustration of the pROM construction for a 2D case. The steps are applied sequentially. The creation of the statistical boundary shape model and the SSL collocation points are represented in the shape parameters subspace.

The mean Euclidean distance between each point and its $k$ neighbors is computed. Here $k = 30$ is chosen to get a representative averaged distance from a point to its neighbors while keeping clusters if there are some. A value is considered exceptional if its distance from its neighbors exceeds a given threshold. This latter is empirically fixed to $\bar{d} + 2 \times \text{SD}$, where $\bar{d}$ is the mean distance and SD stands for the standard deviation, in order to keep around 95% of the shapes. Visually, removed points correspond to isolated and peculiar shapes (Figure 3.1), consequently removing them should not have an important impact on new shapes reconstruction. Then, the boundaries of the parameters subspace are defined (Figure 3.5c). To create the more compact subspace as possible, the minimum volume enclosing ellipsoids method [184] is used. The idea is to generate the $n_p$-hyperellipsoid with the smallest volume in which lie all the training shapes not rejected by the point selection. Each hyperellipsoid is defined by its center $\boldsymbol{c} \in \mathbb{R}^{n_p}$, its semi-axes $\boldsymbol{V}_i$ and their associated lengths $l_i$ where $i \in [\![1, n_p]\!]$. As the Euclidean distance between the points depends on the dimension, different training sets will be considered for each $n_p$-hyperellipsoid.

In $n_p$ dimensions the shape parameters $\alpha_i$ are now described by a radius parameter $r \in [0, 1]$ and $n_p - 1$ angle parameters $\theta_i$ such as $\theta_{n_p-1} \in [0, 2\pi]$ and $\theta_i \in [0, \pi]$ when $i < n_p - 1$. In the reference frame $\mathcal{F} = (c; \boldsymbol{V}_1, \cdots, \boldsymbol{V}_{n_p})$ , they are related by

$$\begin{aligned} \alpha_{1,\mathcal{F}} &= r l_1 \cos(\theta_1) \\ \alpha_{k,\mathcal{F}} &= r l_k \prod_{i=1}^{k-1} \sin(\theta_i) \cos(\theta_k) \quad \forall k \in [\![2, n_p - 1]\!] \\ \alpha_{n,\mathcal{F}} &= r l_n \prod_{i=1}^{n_p-1} \sin(\theta_i) \end{aligned} \tag{3.6}$$

As $(\boldsymbol{V}_1, \cdots, \boldsymbol{V}_{n_p})$ defines an orthonormal basis, the shape parameters are written in the initial reference frame thanks to the bijection

$$\begin{aligned} \mathcal{T} : \quad [0, 1] \times [0, \pi]^{n_p-2} \times [0, 2\pi] &\to n_p\text{-hyperellipsoid} \\ (r, \theta_1, \cdots, \theta_{n_p-1}) \qquad &\to \boldsymbol{\alpha} = \mathbf{V}\boldsymbol{\alpha}_{\mathcal{F}} + \boldsymbol{c} \end{aligned} \tag{3.7}$$

where $\mathbf{V} = \left[\boldsymbol{V}_1, \cdots, \boldsymbol{V}_{n_p}\right]$.

### 3.3.3 Sparse subspace learning

The SSL [36] is based on the sparse grid approach [49]. It consists in a sparse and compact representation in tensor format of the space of the solutions. When combined with a dimensionality reduction method - e.g. the PGD - the solution can be written in the canonical tensor format as in Equation 3.3. Such formulation allows storing the data in a compact way and to enable fast computations for real-time applications. A nonlinear greedy algorithm is used to compute a reduced order representation for Equation 3.3 that is one with the smallest possible number of terms $d$.

The method is a constructive and iterative process. We describe it here in a framework where the shape is parametrized (see Equation 3.5) and a set of explicit parameters $\boldsymbol{p}$ are used to define the FE model. First, the subspace where the parameters lie is chosen. It will be the $n_p$-hyperellipsoid created in 3.3.2 for the shape parameters. At each iteration $i$ a point set $P^i = (P^i_1, \cdots, P^i_{n_c})$ is defined following Smolyak's quadrature rule. Note that the value of $n_c$ depends on the iteration $i$. Each point of this set is a combination of $n_p$ shape parameters plus $D$ other ones such as $P^i_j = (\boldsymbol{\alpha}^{P^i_j}, \boldsymbol{p}^{P^i_j})$ $(j \in [\![1, n_c]\!])$. Thanks to the shape parameters $\boldsymbol{\alpha}^{P^i_j}$ the iFEMWARP can be used to get the volumetric meshes for each collocation point. A FE model corresponding to the problem defined by the parameters $\boldsymbol{p}^{P^i_j}$ can then be solved for each $P^i_j$. The computed solutions are interpolated over the whole parameters subspace to get the prediction $\mathcal{P}^i$.

In its initial version, the SSL is defined on hyperrectangular parameter spaces. Here, we adapt it to the case of $n_p$-hyperellipsoids. In this latter, the shape parameters are interpolated over the radius and the angle parameters and Equation 3.7 is used to get their values in the initial reference frame. Let's consider a fixed iteration $i$ and simplified notations. Given $n_c$ data points in the shape

parameters subspace $\left(\boldsymbol{\alpha}^1, \cdots, \boldsymbol{\alpha}^{n_c}\right)$ with all $\boldsymbol{\alpha}^j = \mathcal{T}\left(r^j, \theta_1^j, \cdots, \theta_{n_p-1}^j\right)$ $(j \in [\![1, n_c]\!])$ different and $\left(\boldsymbol{y}^1(\boldsymbol{x}, \boldsymbol{p}), \cdots, \boldsymbol{y}^{n_c}(\boldsymbol{x}, \boldsymbol{p})\right)$ the associated solutions, the radius $r$ is interpolated with the Lagrange polynomials described by

$$L^j(r) = \prod_{k=1, k\neq j}^{n_c} \frac{r - r^k}{r^j - r^k}, \tag{3.8}$$

and the angle $\theta_m$ with the Dirichlet Kernel:

$$\begin{cases} D^j(\theta_m) = \frac{\mathrm{sinc}\left(\frac{1}{2} n_c (\theta_m - \theta_m^j)\right)}{\mathrm{sinc}\left(\frac{1}{2}(\theta_m - \theta_m^j)\right)} \cos\left(\frac{1}{2}(\theta_m - \theta_m^j)\right), & \text{if } n_c \text{ even} \\ D^j(\theta_m) = \frac{\mathrm{sinc}\left(\frac{1}{2} n_c (\theta_m - \theta_m^j)\right)}{\mathrm{sinc}\left(\frac{1}{2}(\theta_m - \theta_m^j)\right)}, & \text{if } n_c \text{ odd} \end{cases} \tag{3.9}$$

which allows writing the predicted solution on the $n_p$-hyperellipsoid as

$$\mathcal{P}(\boldsymbol{x}, r, \theta_1, \cdots, \theta_{n_p-1}, \boldsymbol{p}) = \sum_{j=1}^{n_c} \boldsymbol{y}^j(\boldsymbol{x}, \boldsymbol{p}) L^j(r) \left( \prod_{m=1}^{n_p-1} D^j(\theta_m) \right). \tag{3.10}$$

To ensure the interpolation stability the collocation points along the radius are computed using the Gauss-Chebychev-Lobatto points and the angles are equally spaced. Figure 3.6 illustrates the interpolation functions for the first three increments of the SSL. The interpolation of parameters $\boldsymbol{p} = (p_1, ..., p_D)$ depends on the use case. In this chapter, $\boldsymbol{p} = b$ is interpolated using the Lagrange polynomials from Equation 3.8. Eventually, the solution is written in a compact format using a low-rank approximation as in Equation 3.3. As mentioned in Section 3.1.3 this last step can be done on the fly during the iterations. Here, for the sake of simplicity, it is done only once at the end. Algorithm 1 summarizes the different steps and a graphical representation is given in Figure 3.4.

The non-intrusivity of the method allows using external software to run the computations on the collocation points. Moreover, parallelization can be used as collocation points are independent of one another. Table 3.1 gives an idea of the number of computations required as a function of the number of parameters and the hierarchical level. It must be noticed that interpolating with Lagrangian polynomials and Dirichlet Kernel does not involve the same discretization along the concerned dimensions. The first option will require fewer collocation points, however, the parameters subspace may be overestimated. Whatsoever, for a given number of parameters, the number of hierarchical levels may be guessed by knowing if the expected solution is regular or not in the parameters subspace. As interpolating functions are used to predict the parametric solution, if this latter has a trend similar to a polynomial, for example, then the Lagrange polynomials will be able to quickly recover the pROM. On the contrary, if the solution is expected to vary quickly in the parameters subspace, then the interpolation will be difficult and a high level of iterations will be required. Consequently, the use of the SSL will depend on the smoothness of the solution variations, the number of parameters, the resources needed for a unique computation, and the possibility to use parallelization. Some strategies to avoid the computations of all the collocations points in the SSL can be set up but it will not be detailed in this chapter, more insights can be found in [36].

The PXDMF format [34] is used to visualize the parametric solution in real-time via Paraview. Figure 3.7 gives an example with 3 shape parameters plus the breathing one.

### 3.3.4 Model personalization for patient-specific anatomy

Once the parametric model is built, it can be adapted to a new patient liver anatomy thanks to the shape parametrization. To find the shape parameters associated with a specific anatomy, the idea is to embed the SSMs into the registration technique leading to a reduced complexity formulation. Indeed, as shown in Chapter 2 Section 2.2.4.1, with SSM-based registration a $n_p \times n_p$ system needs to be solved on each iteration, which is done in only a few seconds. Once the shape parameters are estimated, the simulated breathing motion is readily computed as a particularization of Equation

3.4 for the new set of shape parameters. Since the parametric solution has been computed offline the amount of online work to obtain this solution is fairly inexpensive and compatible with real-time constraint. Indeed, this particular solution format allows displaying at a frequency of 25Hz for visualization and up to 1kHz [203].
It must be noticed that a new shape can lie outside of the boundaries of the parameters subspace. In that case, the nearest shape inside of the parameters subspace boundaries - in terms of Euclidean distance - is considered.

**Remark 3.2** (*Real-time FE model generator*). It is interesting to note that if only the shape parameters are used in the parametrization of the ROM, then this latter becomes a way to modify in real-time the shape of the three-dimensional FE model. As shown in Chapter 2 the generated meshes are generally fitted for FE computations. Hence, this approach may be used in simulations where fast remeshing is required.

**Algorithm 1:** Sparse Subspace Learning algorithm

**Inputs :** Shape parametrization $\tilde{\boldsymbol{S}}(\boldsymbol{\alpha})$ (see Equation 3.5),
$n_p$-hyperellipsoid associated with $\boldsymbol{\alpha}$,
Additional parameters $\boldsymbol{p}$,
Convergence tolerance $tol$,
Maximum number of iterations $i_{max}$.
**Output:** Reduced solution $\boldsymbol{u}(\boldsymbol{x}, \boldsymbol{\alpha}, \boldsymbol{p})$

$i = 1$, $cvg = 0$
$U = []$ `// Create empty matrix`
**while** $cvg = 0$ and $i \leq i_{max}$ **do**
  Compute values of the collocation points $P_j^i$ ($j \in [\![1, n_c]\!]$)
  **for** $j = 1$ **to** $n_c$ **do**
    Reconstruct the volumetric mesh of the shape given by $\tilde{\boldsymbol{S}}(\boldsymbol{\alpha}^{P_j^i})$ using the iFEMWARP
    Solve the physical problem associated with the parameters $\boldsymbol{p}^{P_j^i}$ on the volumetric mesh previously computed
    Store the solution - i.e. the snapshot - as $\boldsymbol{u}_j$
  **end**
  Complete the solutions database $U = [U, \boldsymbol{u}_1, \cdots, \boldsymbol{u}_{n_c}]$
  Get the prediction $\mathcal{P}^i(\boldsymbol{x}, \boldsymbol{\alpha}, \boldsymbol{p})$ of the solution over the whole parameters subspace by interpolating the snapshots contained in $U$
  **if** $i > 1$ **then**
    $err = 0$
    **for** $j = 1$ **to** $n_c$ **do**
      $err = \max(err, ||\mathcal{P}^{i-1}(\boldsymbol{x}, \boldsymbol{\alpha}^{P_j^i}, \boldsymbol{p}^{P_j^i}) - \boldsymbol{u}_j||)$
    **end**
    **if** $err < tol$ **then**
      $cvg = 1$
    **end**
  **end**
  $i = i + 1$
**end**
$\boldsymbol{u}(\boldsymbol{x}, \boldsymbol{\alpha}, \boldsymbol{p}) = \mathcal{P}^{i-1}(\boldsymbol{x}, \boldsymbol{\alpha}, \boldsymbol{p})$
Write $\boldsymbol{u}$ in the canonical tensor format (Equation 3.3)
return $\boldsymbol{u}(\boldsymbol{x}, \boldsymbol{\alpha}, \boldsymbol{p})$

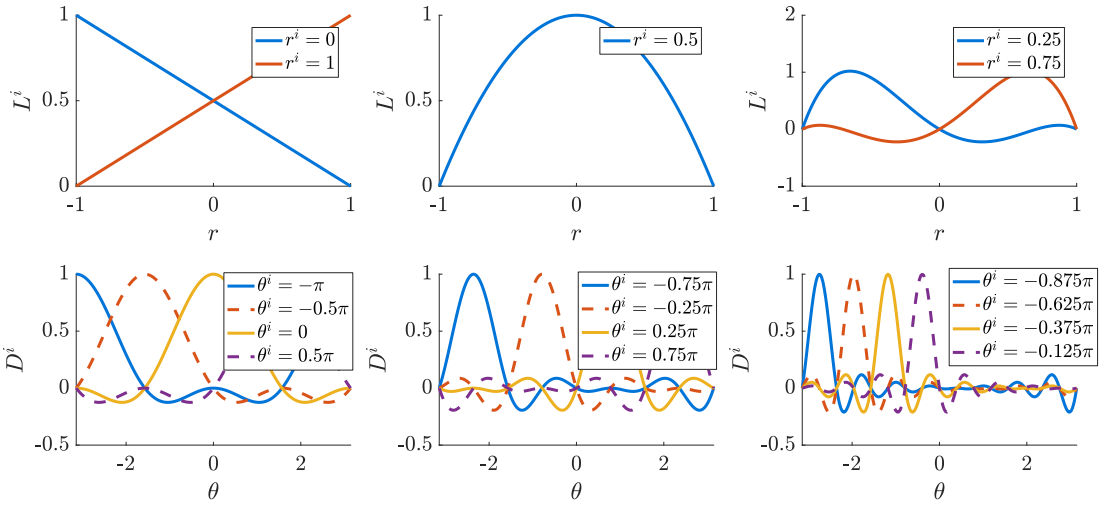


Figure 3.6: Interpolation functions for the radius (on the top) and the angles (on the bottom). The first column corresponds to the first hierarchical level and so on. For the sake of clarity, only half of the angle interpolation functions are represented for the third level.

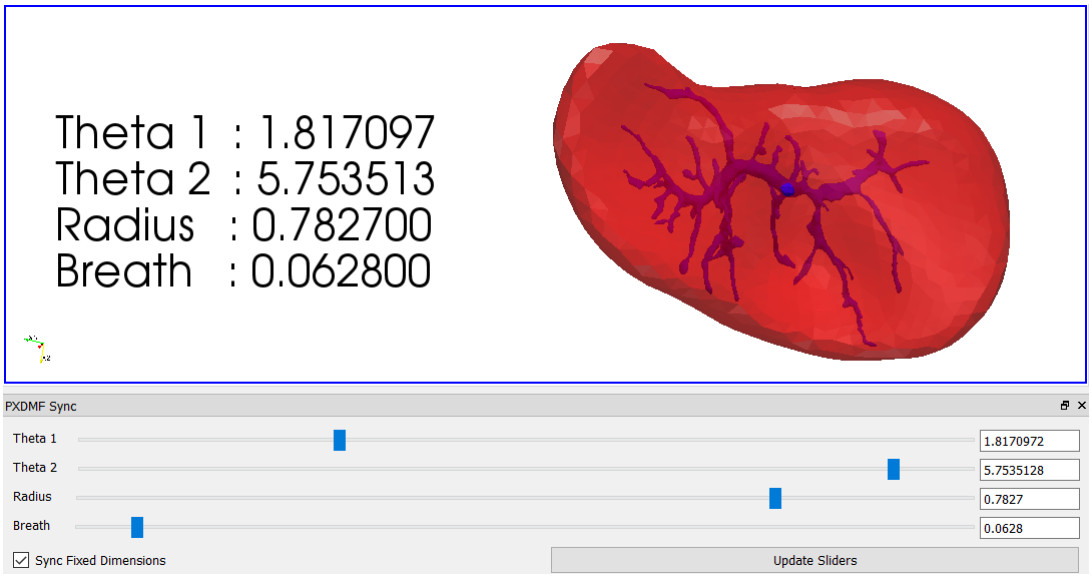


Figure 3.7: PXDMF Paraview plugin to visualize separated variables solutions. A solution with three shape parameters plus the breathing one is represented. The sliders at the bottoms allow visualizing in real-time the result for different sets of parameters within their predefined boundaries. The radius and angles defined in 3.3.2 are used instead of the shapes parameters $\boldsymbol{\alpha}$, which is equivalent as they are linked by Equation 3.7. Here all angles lie in $[0, 2\pi]$ hence some information is redundant.

## 3.4 Validation procedure

For each collocation point of the SSL the rigidity matrix corresponding to the parametrized shape is computed as well as the corresponding displacements of the inner nodes. Considering only the shape, the breathing problem can be seen as adding a shape parameter. The main interest is then to be able to follow the motion of the whole volume when the breathing displacement is applied to a given shape. In a nutshell, without the SSL the following steps need to be applied for each new shape:

1. Find the shape parameters.
2. Reconstruct the interior of the mesh with the iFEMWARP.
3. Compute the rigidity matrix corresponding to the FE model.
4. Solve the FE boundary conditions problem for a given value of the breathing parameter.

With the SSL once the shape parameters are found the solution for any breathing parameter is given by Equation 3.4. The reconstruction with the iFEMWARP, the rigidity matrix computation and the solving are bypassed. This means that the SSL error comes from the "simplification" of these steps. Consequently, its error lies in the reconstruction of the interior, either from the iFEMWARP or from the solving of the FE breathing problem. To assess the accuracy of the SSL "leave-one-out" tests are performed. To this end, the ROM is built using $N_T - 1$ liver shapes. The last shape is then reconstructed with $n_p$ modes and the error between the ROM reconstruction and the complete model - i.e. the one built following the 4 steps - is evaluated. Several sources of error are identified:

1. The initial non-rigid registration onto the target shapes. This error is hard to quantify as the correspondence between vertices is not known. That is why the nonrigidly registered template is considered as the ground truth afterward in order to be able to compare the vertices position in surface and volume. To estimate the registration accuracy the volumetric overlap error $\text{VOE}(S, S') = 100 \times (1 - |S \cap S'|/|S \cup S'|)$ is evaluated [121], where $S$ and $S'$ represent the compared shapes. An error of 100% means the shapes are completely dissociated, an error of 0% means they perfectly overlap.

2. The projection of the shape on a partial set of principal axis obtained with the SSA. Knowing the solution with the whole set of modes it is possible to compute the error as the distance between corresponding vertices as: $E_p(n_p) = \frac{1}{n_V} \sum_{\mathbf{s} \in \Omega} ||\mathbf{s} - \mathbf{s}'||$ where $\Omega$ represents the whole set of nodes, $\mathbf{s}$ the points of the projected shape and $\mathbf{s}'$ the corresponding points of the ground truth shape. The volume of both shapes is reconstructed with 30 iFEMWARP iterations.

3. The interpolation done by the SSL approximation of the model. This error can be measured by comparing the results from the iFEMWARP plus the FE problem on one hand and the SSL on the other hand. This error reads: $E_{SSL}(n_p) = \frac{1}{n_V} \sum_{\mathbf{s} \in \Omega} ||\mathbf{s} - \mathbf{s}'||$ where $\Omega$ represents the whole set of nodes, $\mathbf{s}$ the points of the SSL rebuilt volumetric mesh and $\mathbf{s}'$ the corresponding points of the FE computed solution done on the iFEMWARP reconstructed model. A distinction is done between $b = 0$, where no FE solution is computed but only the iFEMWARP, and $b = 1$ where both are.

The maximum global error is the sum of all these independent errors. The tests are done on 20 randomly chosen shapes from the database. The values of $E_p$ and $E_{SSL}$ are then averaged.

## 3.5 Results

To perform the SSA, the TPS-PR was run with $n_b = 5$ and $\gamma_r = 0.5$ (see Chapter 2 for parameters description). 35 increments were done for each registration. To create the pROM, the SSL was

limited to the third hierarchical level to stay within a reasonable number of collocation points (see Table 3.1). With a Matlab (The MathWorks, Inc., USA) implementation a computation in a collocation point - i.e. running the iFEMWARP and solving the FE problem - took between 2 and 30s on an Intel Xeon E5-2680v3 2.5Ghz processor. We used the Parallel Toolbox on 24 cores to drastically reduce the computational time since all computations are independent and can be trivially parallelized.

| $i$ \ $n_p$ | 1 | 2 | 3 | 4 | 5 | 6 | 7 | 8 | 9 | 10 |
|---|---|---|---|---|---|---|---|---|---|---|
| 1 | 4 | 10 | 14 | 18 | 22 | 26 | 30 | 34 | 38 | 42 |
| 2 | 4 | 21 | 43 | 73 | 111 | 157 | 211 | 273 | 343 | 421 |
| 3 | 9 | 58 | 144 | 290 | 512 | 826 | 1,248 | 1,794 | 2,480 | 3,322 |
| 4 | 20 | 152 | 440 | 1,020 | 2,044 | 3,696 | 6,192 | 9,780 | 14,740 | 21,384 |
| 5 | 44 | 384 | 1,264 | 3,304 | 7,392 | 14,784 | 27,168 | 46,728 | 76,208 | 118,976 |

Table 3.1: Number of collocation points, i.e. computations, per number of shape parameters $n_p$ as a function of the SSL hierarchical level $i$. One mode being used for the breathing the total number of parameters is $n_p + 1$. The level $i$ is limited to 3 in order to stay within a reasonable number of computations to do for $n_p = 10$ shape parameters. These values could be increased with more computational resources. Adding a hierarchical level would increase the accuracy of the SSL and adding a shape parameter would improve the shape representation.

First, the non-rigid registration VOE is presented in a histogram in Figure 3.8. Globally the shapes are well-registered, the error mainly comes from the smoothing of the surfaces by the TPS-PR method which does not particularly deteriorate the shapes representations.

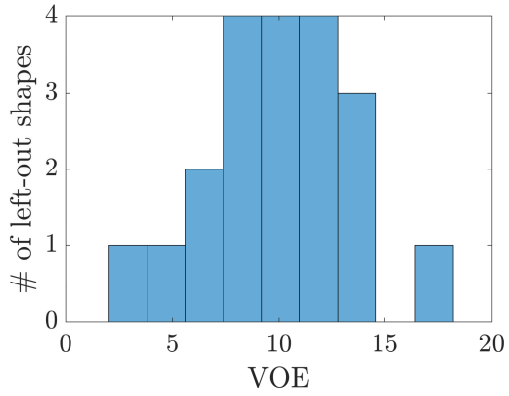


Figure 3.8: Histogram of the volumetric overlap error. This error quantifies the goodness of the registration between two closed surfaces by evaluating the percentage of volume not superimposed. A value of 100 means the shapes are dissociated and a value of 0 means they are perfectly superimposed. Here the mean value is around 10% and the standard deviation around 3.5%. Knowing the quality of the shapes from the database these values can be considered as good ones. The error mostly comes from the smoothing of the surfaces.

Then, the mean error done by the sole reconstruction is presented in Figure 3.9 for $n_p = 1, \cdots, 100$ shape modes. An example is provided in Figure 3.12a. The median value is also represented. It is shown that its value is always lower than the mean. This is due to the fact that some of the shapes are very peculiar and consequently require a high number of modes to be represented. That was expected considering that the database contains a large variety of livers, a lot of them belonging to ill patients. Because of the large variability of the database both measures of error are quite important. 50 modes are required to get a median error lower than 4 mm, this value is given in [125] as the threshold where protocol in radiotherapy could be significantly improved by such a tool. Seeking to reach such accuracy can be debated, though. Indeed, there is an initial error in our

source data, resulting from image segmentation and non-rigid registration. Therefore, although the additional computational effort would improve the model precision, it would not increase its accuracy.

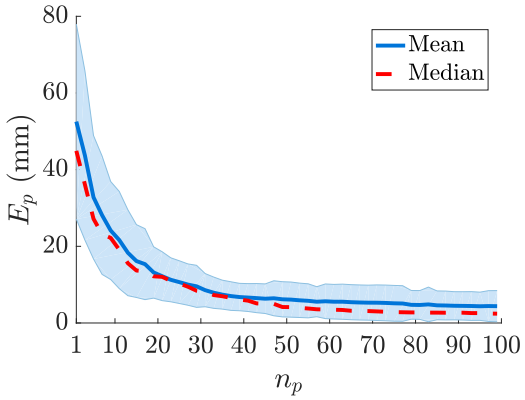


Figure 3.9: Error made by the projection on the first $n_p$ modes. The shaded area corresponds to one standard deviation. This error shows that a relatively high number of modes ($> 50$) is required to have a good median reconstruction ($< 4\,\text{mm}$). Some of the database's liver shapes represented in Figure 3.1 testify of the shape variability of our database and consequently justify the high number of modes required to have a good representation.

Next, the suitability of the parameters subspace is evaluated. Figure 3.10 summarizes how many shapes are removed from the training set to build the $n_p$-hyperellipsoid (see the method in Section 3.3.2) and how many reconstructed shapes among the "leave-one-out" tests are outliers, i.e. they are located out of the parameters subspace boundaries. It appears that the number of shapes excluded from the training set varies around 20 and does not seem to depend directly on the number of modes. On the contrary, the number of outliers increases with the number of modes. Such sets of parameters are exceptional and automatically introduce an error as they do not belong to the pre-computed solution and need to be projected onto the $n_p$-hyperellipsoid. For a standard use they should not be considered, that is why a distinction is made afterward between them and the inliers, i.e. the shapes located inside the parameters subspace boundaries.

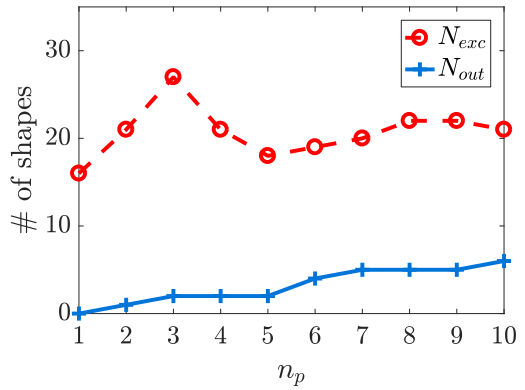


Figure 3.10: $N_{exc}$: number of shapes excluded from the parameters subspace by the point selection. $N_{out}$: number of sets of parameters taken out of the parameters subspace in the leave-one-out tests. These values depend on the considered number of modes $n_p$. $N_{exc}$ is approximately constant and represents around 5% of the number of shapes in the database. On the other hand, $N_{out}$ steadily increases with $n_p$, meaning that the chance of having a new shape out of the pre-computed solution increases with the dimensionality.

Eventually, the error between the FE solution and the SSL prediction is shown in Figures 3.11a and 3.11b. As mentioned before a distinction is made between inliers and outliers. Moreover, the error is computed for $b = 0$ and $b = 1$ to assess the impact of the breathing parametrization on the error. The breathing approximation has a low impact on the error, around $0.1\,\mu$m. On the contrary, taking shapes out of the parameters subspace introduces a bigger error. With inliers only the maximum error is around $1\,\mu$m against 1 mm when all shapes are taken into account. In both cases the error increases with the number of modes, showing that the convergence is more difficult for higher dimensions. A visual representation of this error is provided in Figure 3.12b for $b = 1$.

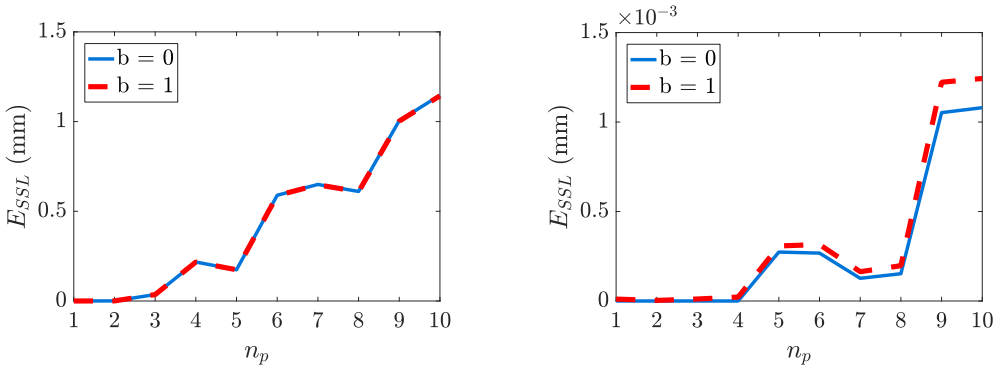


(a) $E_{SSL}$ over the whole left-out training data set.

(b) $E_{SSL}$ over the inliers.

Figure 3.11: Representation of the error made by the SSL. The value is averaged over the respective training data sets. Two data sets are compared by distinguishing inliers and outliers. The error is also represented for two extreme values of the breathing parameters $b$. For inliers only the error is very low ($< 1.5\,\mu$m). When outliers are taken into account it increases up to 1 mm for $n_p = 10$ modes, which is still suitable for AR applications. In both cases the parameter $b$ adds an insignificant error ($< 0.1\,\mu$m).

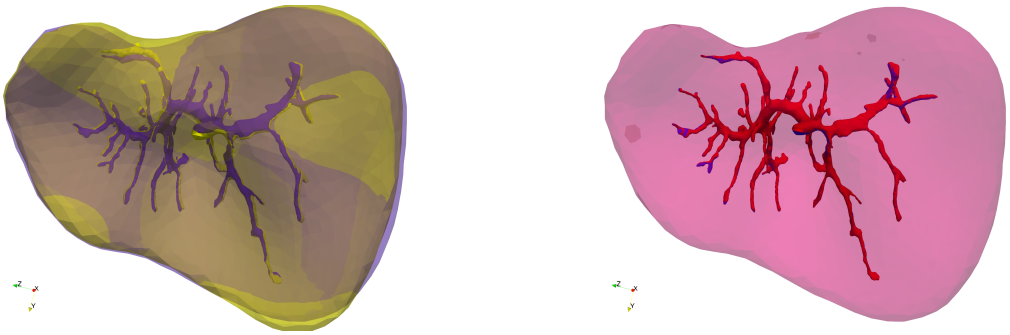

(a) Ground truth shape (in yellow) versus its projection on the principal axis (in blue).

(b) Projection on the principal axis (in blue) versus the ROM shape (in red).

Figure 3.12: Comparison of the shape and the portal vein representations produced by the different steps (the portal vein allows to visually assess the accuracy of the volume reconstruction). The ground truth shape is chosen randomly among the database. The red and blue shapes are reconstructed with $n_p = 10$ shape modes. The breathing parameter is fixed to $b = 1$. The projection on a partial set of principal axis provokes a degradation of the representation as evidenced by the slight shift between the yellow and blue shapes. However, the SSL replicates almost perfectly the projection and the difference is not discernible at naked eye.

## 3.6 Discussion

Globally, the error done in the leave-one-out tests comes from the reconstruction from a limited number of modes. This error could be decreased by using more modes to represent the shape. However, more modes means more computations for the SSL and a more difficult convergence. Here it is difficult to go further than 10 shape modes for the SSL without reaching high computational times. Concerning the SSL error, the main flaw lies in the choice of the parameters subspace. As shown in the previous section the SSL error mainly comes from reconstructed shapes taken out of the parameters subspace, and their number increases with the number of modes. Nonetheless, this error stays within an acceptable range and for shapes taken inside the parameters subspace a really high fidelity reconstruction is done. Moreover, a consequent speedup is achieved. As noticed in Section 3.5 this initial model is already computed relatively fast, and with an implementation in a low-level programming language and more powerful hardware, a computation could certainly be done in near real-time ($\sim$ 1s), which would be sufficient for breathing applications and would question the use of a pROM. As mentioned before the use case presented in this chapter is a simple example to illustrate the method and more complex situations involving nonlinear behaviors should be tested. Anyhow, the pROM approach still has the advantage of requiring simple computational means, which is important to compensate for the lack of advanced hardware in clinical environments.

The first point to tackle to improve the method would be to reduce the number of modes necessary to represent the shape. As the model is based on a large liver shape database coming from medical data, there is an important shape variability. An idea to reduce this variability would be to cluster the data beforehand. By sorting similar shapes into clusters the variability would be reduced inside each of them [105]. A specific ROM would be then created for each cluster. When a new shape would be introduced, an additional step consisting in finding in which cluster it lies would be done.

The next difficulty to deal with would be the parameters subspace choice. It needs to be a compromise between completeness and efficiency of the SSL while keeping a simple and parametrizable topology. On the contrary to the subspace taken in the previous chapter, we did not choose a $\kappa$%-boundary model [160]. Such subspace considers a normal distribution of the data along each dimension and fixes the boundaries separately depending on their standard deviation. Consequently, if one wants to cover 95% of the variability along each dimension, it does not mean that 95% of the whole variation will be covered. In fact, the variation covered lies in $([0.95^{n_p}, 0.95] \times 100)$% where $n_p$ is the number of modes - i.e. the dimension. Hence, for an increasing number of modes there is a possible decrease in the variation coverage. That is why the method is not used here and that we use a non-statistical determination of the subspace. Nonetheless, the hyperellipsoidal shape of the parameters subspace can be seen as the space covering $\kappa$% of the variation under the assumption of a multivariate distribution of the shape parameters. Here, for a number of modes superior to 2 the data do not follow such distribution according to the Henze-Zirkler test [122]. But, if the data could be clustered with a multivariate Gaussian mixture model as proposed before, such choice for the parameters subspace boundaries would be natural and would allow to strictly cover $\kappa$% of the variation.

## 3.7 Conclusion

A data-based pROM has been developed. This ROM allows us to take into account the patient-specific shape and to model the mechanical deformations caused by the breathing motion. The procedure relies on a SSA in conjunction with the SSL. We used the TPS-PR registration method introduced in the previous chapter to increase its efficiency. The principal novelty of this approach, when compared to literature, is the use of medical data for the shape parametrization of the ROM. A first application to simulate the breathing was done on a simple elastic case, but other applications are envisaged. We showed that, because of the large size of our database, the main limitation is the ability to statistically represent the initial liver shape with a small number of modes. Some leads are suggested to solve this issue, in particular, the data clusterization. The

whole process works smoothly and provides an efficient way to address the initial matters of patient-specific shape representation within interactive simulation environments, contributing to open the way to the creation of MOR-based tools for anatomy-specific real-time simulations.

# Part I: partial conclusion

This part has been dedicated to the construction of a shape-parametric reduced order model based on medical data for the patient-specific anatomical representation. To this end, we have developed a new methodology for shape-parametric organ modeling based on an unsupervised shape registration method coupled with an enhanced version of the finite element-based mesh warping algorithm. The reduced order model (ROM) has then been built using the sparse subspace learning (SSL) method, a non-intrusive approach for model order reduction (MOR). It has been the opportunity to discuss the topology of the parametric space. Indeed, MOR techniques such as the SSL or the proper generalized decomposition rely on the tensorial structure of the parameters. Here, we based the construction of the parametric space on a statistical approach. As a matter of fact, it is possible to determine the probability density function associated with the shape parameters distribution. Based on this distribution, a bounded subspace containing only plausible shapes can be defined. Under the assumption of a multivariate normal distribution of the parameters, the optimal shape of this subspace is a hyperellipsoid. To express the parametrization of this new parametric space in a tensorial form, a non-affine transformation is required. This latter has the particularity to involve a periodicity of the parametric space. To adapt the SSL to this specificity, an adequate sampling procedure has been developed along with the use of adapted trigonometric functions for the construction of the parametric basis. It revealed to be an efficient strategy, even though it is limited by the potential high dimensionality of the organ's shape representation.

This limit is in itself an interesting result. It opens many research perspectives to improve the method. Apart from the natural shape variability of the organs, several sources of approximation can artificially increase the dimensionality of the problem. The first is the image segmentation. The noise from these data can introduce some shape variability that should not be taken into account. The registration process we propose tends to regularize this noise thanks to a physics-based approach. Then, the correspondence stage between the shapes can introduce variability in the model. As in our methodology the shapes are registered individually, the points correspondence do not take into account the global variability of the modes of deformation. Consequently, some strategies to perform simultaneously the correspondence between all the shapes could be envisaged. A metric based on the shape's variability could be used to control the algorithm. If such an approach does not succeed to reduce the shape dimensionality, the shape's clusterization could be an efficient strategy. By sorting the shapes accordingly to their similarity into clusters, dimensionality reduction should perform better at a local level. A ROM would then be built for each cluster. Any new shape would be attributed to a cluster and reconstructed accordingly. Last but not least, the modeling of the whole shape may be not necessary. We could think to only represent a portion of interest of the organ. It would automatically be subject to less variation. However, the mechanical problem should be adapted as specific boundary conditions would be necessary. If none of these propositions is efficient enough, the effort could be concentrated on improving the SSL. Approaches performing anisotropic or adaptive sampling could be employed to reduce the computational cost and include more modes. Alternatively, a projection-based MOR method in conjunction with a hyperreduction technique could be embedded within the sampling strategy (see Chapter 4 Section 4.2 for an introduction to hyperreduction). The SSL would not be non-intrusive anymore but the projection-based ROM constructed on the fly could be used to accelerate the computations at the collocation points. The interest of the SSL will then lie in the fast generation of the results, that do not require to solve the governing equations as in the projection-based MOR methods.

Finally, the interest in creating a ROM able to cover any anatomy can also be questioned. We have seen that many obstacles prevent their use for short-term applications. On the other hand, building the ROM from scratch for each patient is conceivable thanks to the non-intrusivity of the

SSL and the use of parametric-organ models. These latter are not limited by the number of modes and allow to generate FE models in seconds. From this result, the model could be enhanced with the patient-specific features (material properties, vascularization, tumor, etc.) and used in the framework of the SSL to generate a ROM tailored to the patient. The non-intrusivity enables the use of standard modeling software, hence it would not disturb the standard medical workflow nor require specific competencies from the persons in charge of the simulations. The use of MOR into the medical framework could benefit from simpler approaches such as this one. Indeed, there is no in situ use of ROMs to drive the real-time computations for surgical simulators. The publication of a first study involving MOR as the computational core of a surgical simulator during a real operation would attest to the sustainability of the approach.

# Part II

# Completing medical data using physical priors based on model order reduction

Chapter 4

# The mathematical model as a means to complete the data

**Abstract** This chapter introduces the concept of data completion based on physical priors in the framework of computational surgery. We focus the discussion on the lack of comprehensive data in the context of minimally invasive surgery. To alleviate this issue, the emphasis is put on the use of mathematical models to complete medical data and the capacity of model order reduction methods to accelerate the computations, even in nonlinear models. To explain the data assimilation procedure, a brief overview of the inverse uncertainty quantification methods is provided. In particular, we highlight the Kalman filter approach which is widely used for data completion and parameter identification in engineering. To give more insight, the example of the three-dimensional scene reconstruction in augmented reality for laparoscopy is detailed. The different stages of the numerical procedure required for data completion along with the embedding of the physical priors are presented.

## Contents



## 4.1 A short introduction to the role of simulation in minimally invasive surgery

In their most simple form, surgical operations are performed using open surgery. The procedure involves incisions ranging from a few centimeters to tens of centimeters, depending on the type of operation. Open surgery is convenient as it is a simple way to provide the surgeons with visual and haptic access to the targeted organs. Moreover, they can perform techniques such as palpation with their own hands, and easily collect information such as the difference of rigidity between the tissues (e.g. to locate fibrosis) or feel the blood pulse (e.g. to detect blood vessels). However, resorting to open surgery has serious drawbacks as it implies an important trauma for the patient. Large incisions take more time to heal, can be infected - causing postoperative morbidity - and create large scars that can be psychologically difficult to bear.

To alleviate the costs of open surgery, the development of medical technologies has allowed the creation of minimally invasive surgery (MIS). This term encompasses techniques that minimize

the size of the incisions, and, consequently, reduce the invasiveness. Usually, the operations are image-guided. The images can come from non-invasive techniques such as magnetic resonance or computed tomography imaging, or from tools such as endoscopes which are directly inserted into the body. In the latter case, the images are captured either with monocular cameras that provide two-dimensional (2D) images or, more rarely, with stereoscopic cameras that allow simulating human binocular vision. Concerning the sense of touch, the minimally invasive instruments generally only return force feedback, which is inadequate to perform precise action such as palpation. Anyhow, in all configurations the surgeons suffer from a loss of information that generally requires them specific training and additional efforts during the operation.

In order to give back the surgeons their senses of vision and touch and alleviate the constraints imposed by the MIS, an interesting perspective consists in providing them computer guiding software. They enable three-dimensional (3D) segmentation of the preoperative images and therefore 3D patient modeling. These data can be used for diagnosis and surgery planning but also for intraoperative guidance in augmented reality (AR) [198, 25, 288]. For instance, in [168] the authors review the use of computer vision and augmented reality in gastrointestinal endoscopy. The emphasis is put on polyp detection. In standard procedures, the operator explores the area of interest with an endoscope and removes harmful polyps. But, it is common for some to be missed. Hence, the guiding software can help the clinicians by detecting in real-time the polyps from the endoscopic images and by superimposing their contours on the camera display. Moreover, it may help the clinician to make the distinction between harmful and harmless polyps by attributing them a grade, which allows minimizing unnecessary polyp resection. Furthermore, based on [129], the authors propose to enhance the 2D images obtained during endoscopic ultrasound with the preoperative 3D representation of the organs in order to simplify targeting for needle biopsies or cyst drainage. To do so, the preoperative 3D images must be registered onto intraoperative data. But, both sets of data generally do not match. Indeed, the organs undergo some deformations between the initial data acquisition and the operation but also intraoperatively due to physiological motions and to the interaction of the surgical tools with the tissues. Moreover, the data acquired during the operation are generally incomplete and noisy [233, 303]. Hence, to infer the displacement of hidden structures from the available data the 3D model must encompass physical priors on the behavior of the organ. It allows regularizing the noise and propagating the partial information to features not represented by the images. This is also convenient to return realistic haptic feedback if necessary.

To incorporate physical knowledge into the models, several hypotheses are generally set. First, the governing equations and the numerical method to solve them have to be chosen. Most of the time, several approaches exist to represent the same physical phenomenon and the choice of the numerical method is often a compromise between two antithetical considerations: the computational speed and the level of accuracy. On the one hand, speed is important because the output frequency must satisfy the visualization or haptic frame rate. On the other hand, without accurate and complex models some physical behavior cannot be represented. In this context, the route of model order reduction (MOR) is interesting as it allows reducing the computational complexity while preserving the underlying physics of the system. Then, the model parameters must be tuned. By parameters we encompass the material properties and the boundary conditions. A model is never more than an approximation of reality. Hence, to be the closest to the truth than possible it is mandatory to impose the right set of parameters. Nonetheless, when using an approximated model to fit medical data, there never is a perfect correspondence between the "real" and the synthetic data. It is possible for distinct temporal or spatial acquisitions on the same system to correspond to different sets of parameters on the model. It can be caused by the inexact model's parameters but also by the measurement errors. For this reason, if the measured data are not extensive enough a strong identification of the model's parameters can be in fact detrimental to the accuracy of the numerical reconstruction. The model is then said to be *overfitted*. Once again, the choice of MOR methods is convenient as it is based on a parametrization of the system. Hence, reduced order models (ROMs) are naturally suited to the exploration of the parametric space of the model and allow adapting it with a low amount of computations. We propose in Section 4.2 a short digression on MOR approach for nonlinear systems. Then, in Section 4.3, the methods used for parameter identification and model fitting from partial, noisy, and dynamic data are introduced. Their

application is illustrated in Section 4.4, in the context of AR in laparoscopy. We show that few studies tackled the problem of automatic static registration. That is why we propose in the next chapter a new solution for the use of physical priors in image completion in the framework of AR in laparoscopy, based on a nonlinear ROM. We prove on synthetic data that the initial registration of the AR scene onto the real data can be done in an unsupervised manner. The automation is important to avoid introducing human bias into the AR scene and to reduce the workload of the surgeons.

Note that this chapter is particularly focused on AR for surgery, but methods for data assimilation based on physical priors are also commonly used in other applications, notably in cardiovascular (e.g. see [228, 214, 90]) or respiratory (e.g. see [207, 227]) system modeling .

## 4.2 Reduced order modeling for nonlinear systems

As introduced in the previous section, the use of MOR methods is well-suited for data completion based on physical priors for three reasons:

- ROMs respect the physics of the system,
- ROMs allow accelerating the computations,
- ROMs have a parametric structure that allows easy exploration of the system's parametric space.

Consequently, for a given set of observations (e.g. medical images), the solution of the physical model can be rapidly evaluated for many sets of inputs and permits greater flexibility than with standard high fidelity numerical methods. The standard MOR methods are the proper orthogonal decomposition (POD) [54], the reduced basis (RB) [229] and the proper generalized decomposition (PGD) [60]. They rely on the projection of the governing equations and of the solutions onto a lower-dimensional subspace, or manifold, which allows reducing the number of degrees of freedom. Among the projection-based MOR methods, a distinction is done between the *a priori* methods (the POD and RB) and the *a posteriori* ones (the PGD). Here we focus on the former. MOR methods are divided into a computationally expensive *offline* stage, where the parametric representation is built, and an inexpensive *online* stage, during which the model is evaluated for specific sets of parameters. In a priori methods, the offline stage consists in creating a database of high fidelity solutions, called *snapshots*. These snapshots depend on parameters and must be representative of the solution space spanned by the parametric space. MOR approaches then consist in finding the lowest dimensional subspace able to span the snapshot database. In the online stage, for each new set of parameters belonging to the given parametric space, any new solution will be considered to belong to this reduced dimensional subspace. It permits to drastically reduce the number of degrees of freedom and accelerate the computations. Nonetheless, as mentioned in the previous section, complex models are necessary to represent faithfully most of the biophysical behaviors. By complex we imply that it involves nonlinearities. Unfortunately, in their standard formulation MOR methods face a major difficulty in such cases. Indeed, in nonlinear problems, iterative methods such as the Newton-Raphson procedure are used to determine the solution of the governing equations. At each iteration, the nonlinear terms must be evaluated and projected onto the lower-dimensional subspace computed during the offline stage. This makes the online stage particularly inefficient and restrains the interest of MOR.

That is why, since the 2000s, many studies have addressed the issue of nonlinear a posteriori ROM. Most of the approaches propose building a secondary low-dimensional subspace, other than the solution's subspace, in order to approximate the nonlinear term. Then, the empirical interpolation method (EIM) [17, 165], as well as its discrete counterpart (DEIM) [55], can be used to give interpolation properties to the nonlinear term's subspace. As opposed to projection, interpolation allows approximating the nonlinear term by evaluating only a few points, which can be done inexpensively during the online stage. A number of variants have been proposed, such as the unassembled DEIM [279], which is specifically tailored for finite element computations, and the localized DEIM [220], that proposes to switch between local subspaces in order to capture

different regimes of the system, using clustering and supervised learning techniques. Interpolation-based techniques were described in [52] as approximate-then-project approaches. Alternatively, project-then-approximate approaches, for which Ryckelynck coined the term *hyperreduction* [247], propose roughly to approximate the projection of the nonlinear term directly. The idea of this approach relies on the fact that the terms we want to approximate come from the evaluation of integrals. In numerical integration, or numerical quadrature, one can approximate the integrals as a weighted sum of the integrand evaluated in a few optimal points of the domain, also called quadrature points. When considering a function $f$, it reads in its simplest expression

$$\int_\Omega f d\Omega = \sum_{i=1}^{n_q} c_i f(\boldsymbol{a}_i) \tag{4.1}$$

where $\Omega$ is the integration domain, $\boldsymbol{a}_i \in \Omega$ are the quadrature points, $c_i$ their associated quadrature weights and $n_q \in \mathbb{N}^*$ their number. The idea is to minimize the value of $n_q$ to reduce the number of times the function $f$ must be evaluated. To this end, sparsity promoting techniques are used. In practice, the goal is to minimize the $\ell^0$-norm of $\boldsymbol{c} = (c_1, \cdots, c_{n_q})$ but, as this is an NP-hard problem, several methods have been developed to relax it. The first scheme of this kind is based on the greedy orthogonal matching pursuit (GOMP) algorithm [216, 77]. It has been firstly applied in the context of computer graphics by An. et al. (2009) [10] and then involved in computational mechanics application by Farhat and co-workers [87, 88]. While the GOMP algorithm involves the use of the least-squares method in its iterations, its adaptation as hyperreduction technique makes use of the non-negative least squares (NNLS) algorithm. The NNLS is fundamental because it ensures the stability of the method preserving the spectral properties of the nonlinear term, i.e. the positivity of the weights $c_i$. This aspect has been pointed by Farhat highlighting the fact that the interpolation-based techniques are not suitable in some applications due to the instability they naturally carry. The NNLS algorithm requires more operations than the least-squares one. For this reason, Hernández et al. [123] use the NNLS only when the simple least-squares fails in returning a solution vector with positive coefficients. Recently, another type of method for the hyper-reduction has been proposed in [215, 298]. This technique is based on a sparsity promoting approach. It relies on the minimization of the $\ell^1$-norm of an objective function with the constraint that an underdetermined system has to be satisfied, the minimization can be cast as a linear programming problem and solved through the simplex algorithm. Nonetheless, the use of the $\ell^1$-norm to find a reduced quadrature rule is not optimal. By considering the constant function in Equation 4.1 and positive quadrature weights it arises

$$\int_\Omega 1 d\Omega = \sum_{i=1}^{n_q} c_i = ||\boldsymbol{c}||_1 = |\Omega|, \quad \forall\, i \quad c_i \geq 0\,. \tag{4.2}$$

Hence, the $\ell^1$-norm of the quadrature weights must be equal to the measure of the domain. Consequently, minimizing the $\ell^1$-norm to perform the sparse approximation is conceptually a nonsense as Equation 4.2 must be respected. We propose in Chapter 5 a new approach based on the $\ell^p$-norm minimization, with $p < 1$, to perform the sparse approximation. Note that for $p < 1$, the $\ell^p$-norm is not a real norm as it does not respect the triangle inequality. We employ the word norm for the sack of simplicity. More rigorously, the term diversity measure has been employed in the literature [236].

## 4.3 Integrating the data in the simulation and vice versa

We have seen the interest of using physical priors to complete the data and explained why and how MOR is adapted to this task. We now give an overview of the methods to perform data integration into the model and focus in particular on the Kalman filter approach.

### 4.3.1 The inverse problem

The *inverse problem* - or inverse uncertainty quantification (IUQ) - is the determination of the unknown factors influencing measured variables. In other words, IUQ is the science of computing

the causes of observable effects. It is the reverse concept of forward uncertainty propagation later introduced in Chapter 6. The range of application of inverse problems is broad as many systems are based on measurements to produce outputs. Since a measure on real data is always subject to noise and error, the mathematical relation between the unknown inputs - i.e. the model's parameters - and the measured outputs is rarely bijective. Moreover, the mathematical model itself is only a mere approximation of reality. Hence, the inverse problem is typically *ill-posed*. A well-posed problem (in the sense defined by J. Hadamard) must respect existence, uniqueness, and stability conditions. In IUQ the stability and uniqueness are generally not respected. For example, considering the heat equation with fixed Dirichlet conditions, any initialization will lead to the same solution for a sufficiently long time. It violates the uniqueness condition of the inverse problem. According to P. Argoul [12], the methods to solve the inverse problems can be divided into three main categories:

- The first one is the **the functional analysis**. The ill-posed problem is transformed into a well-pose problem thanks to the restriction of the mathematical model's variables to a specific space. This latter is often determined thanks to physical considerations. Numerically it is translated through a set of global constraints on the set of solutions.

- Then, a popular non-statistical approach is the **regularization of ill-posed problems**. In this kind of method, an a priori information is added to the mathematical formulation of the problem in order to stabilize the solution while taking into account the measurement errors. The priors are often inspired by physical considerations. For example, the thin plate spline registration method introduced in Chapter 1 is a good example of regularization, where the penalization term is inspired by the analogy with the bending of thin sheets of metal. The probably most well-known regularization technique is the Tikhonov's one [278] where a non-negative stabilizing functional is added to the mathematical expression of the solution. As shown in Chapter 2 Section 2.2.4.1, MOR can easily be used to reduce the number of degrees of freedom and to accelerate the regularization - considering that the principal component analysis is a form of MOR. Other MOR methods also have been used in this context, such as in [189] where the PGD is employed for the real-time control of industrial processes.

- The last kind of method is the statistical approach of IUQ, the so-called **stochastic or Bayesian inversion methods**. In this framework, the uncertain variables are not deterministic but are described by probability density functions. The values of interest are not anymore the variables themselves but the descriptors of the probability density functions: the average, the standard deviation, the maximum probability, etc. These methods are based on Baye's theorem that reads

$$P(A|B) = \frac{P(B|A)P(A)}{P(B)} \tag{4.3}$$

  where $A$ and $B$ are events and $P(B) \neq 0$, with $P(A)$ (resp $P(B)$) the probability of $A$ (resp $B$). In inverse problems, we seek to determine the probability of having $A$ knowing $B$, i.e. the posterior probability $P(A|B)$. The prior probability $P(A)$ is initially assumed to be known or approximately guessed. The measured probability $P(B)$ can be considered fix or known. The term $P(B|A)$ is named the likelihood function, it is the probability of having $B$ knowing $A$. The mathematical model is used to estimate the likelihood function, and, ultimately solve Equation 4.3. Often, the process is iterated in order to update the prior probability and have a better initial guess. As it requires a certain amount of computations, the MOR approach can be employed to reach reasonable computational costs. For instance, in [244], a framework for model updating based on the PGD is developed.

The Bayesian inference is a natural regularization approach and, in the specific case where all uncertainties are Gaussian, can be proved to be similar to a weighted Tikhonov regularization [274]. Always in this peculiar configuration and with linear systems, the solution of the Bayesian inverse problem can be provided by a Kalman filter [84]. This method is detailed in the next section.

### 4.3.2 The Kalman filter

The Kalman filter (KF) [294] is a widely used method for state estimation in partial, noisy, and dynamic systems and for parameters estimation in inverse problems. The basic KF is restricted to linear models and considers Gaussian noises, estimates and errors. Its framework has been extended to nonlinear models with the unscented Kalman filter [138], the ensemble Kalman filter [85] or the extended Kalman filter (EKF) [237], this latter is developed in Chapter 5. MOR methods have been successfully employed in the context of linear KF [89] but also in nonlinear cases, in particular in the PGD framework for the unscented Kalman filter [173] and the EKF [103]. In this section, we introduce the standard KF to give the reader an insight into this common procedure used in the context of inverse problems. Note that the KF and its nonlinear extensions do not strictly belong to the Bayesian inversion methods as they assume Gaussian probability distributions [84].

The KF estimates the current state of a system from the knowledge of a sequence of noisy observations. By considering the discrete time step $k$, the KF assumes that the true state of the system is expressed as a function of the previous state $k-1$ such as

$$\boldsymbol{x}_k = g(\boldsymbol{x}_{k-1}, \boldsymbol{u}_k) + \boldsymbol{w}_k = \mathbf{G}_k \boldsymbol{x}_{k-1} + \mathbf{O}_k \boldsymbol{u}_k + \boldsymbol{w}_k \tag{4.4}$$

where

- $g$ the function actualizing the system's state, it is assumed to be linear in the case of the standard KF,
- $\boldsymbol{x}_k$ is the new state of the system,
- $\boldsymbol{x}_{k-1}$ is the previous state of the system,
- $\mathbf{G}_k$ is the linear operator modeling the state transition,
- $\mathbf{O}_k$ is the linear operator modeling the effect of the control vector $\boldsymbol{u}_k$,
- $\boldsymbol{w}_k$ is the process noise assumed to be drawn from a zero multivariate normal distribution with covariance $\mathbf{Q}_k$, i.e. $\boldsymbol{w}_k \in \mathcal{N}(\mathbf{0}, \mathbf{Q}_k)$.

The observation is deduced from the system's state following

$$\boldsymbol{y}_k = h(\boldsymbol{x}_k) + \boldsymbol{v}_k = \mathbf{H}_k \boldsymbol{x}_k + \boldsymbol{v}_k \tag{4.5}$$

where

- $h$ is the function mapping the state space into the observed space, it is assumed to be linear in the case of the standard KF,
- $\boldsymbol{y}_k$ is the observation vector at the current time step,
- $\mathbf{H}_k$ is the linear operator that maps the state space into the observed space,
- $\boldsymbol{v}_k$ is the observation noise assumed to be drawn from a zero multivariate normal distribution with covariance $\mathbf{R}_k$, i.e. $\boldsymbol{v}_k \in \mathcal{N}(\mathbf{0}, \mathbf{R}_k)$.

The KF then recursively updates its estimation of the system's state by introducing the observed information. To do so, the procedure is often described as a two-stage process: the *predict* stage and the *update* stage. In the first one, the new state of the system at time $k$ is updated from the knowledge of the previously estimated state at time $k-1$. The system's state is then commonly noted $\hat{\boldsymbol{x}}_{k|k-1}$ and its a posteriori error covariance matrix $\mathbf{P}_{k|k-1}$ is introduced (it measures the estimated accuracy of the state estimate). In the second stage, the observed information is introduced and combined with the current state estimate to refine its evaluation. The new state estimate, termed as the *a posteriori* estimate, is noted $\hat{\boldsymbol{x}}_{k|k}$. The two stages are normally performed alternatively but if observations are not available several predictions can be done sequentially. Mathematically it reads

**Predict stage**

$$\begin{aligned}\hat{\boldsymbol{x}}_{k|k-1} &= \mathbf{G}_k \hat{\boldsymbol{x}}_{k-1|k-1} + \mathbf{O}_k \boldsymbol{u}_k \\ \mathbf{P}_{k|k-1} &= \mathbf{G}_k \mathbf{P}_{k-1|k-1} \mathbf{G}_k^T + \mathbf{Q}_k\end{aligned} \tag{4.6}$$

**Update stage**

$$\begin{aligned}\mathbf{K}_k &= \mathbf{P}_{k|k-1}\mathbf{H}_k^T \left(\mathbf{H}_k \mathbf{P}_{k|k-1} \mathbf{H}_k^T + \mathbf{R}_k\right)^{-1} \\ \hat{\boldsymbol{x}}_{k|k} &= \hat{\boldsymbol{x}}_{k|k-1} + \mathbf{K}_k \left(\boldsymbol{y}_k - \mathbf{H}_k \hat{\boldsymbol{x}}_{k|k-1}\right) \\ \mathbf{P}_{k|k} &= \left(\mathbf{I} - \mathbf{K}_k \mathbf{H}_k\right) \mathbf{P}_{k|k-1} \,.\end{aligned} \tag{4.7}$$

**Example 4.1** (*Illustration of the Kalman filter on a 1D case*). Let's consider the Kalman filter is used to localize a car in one dimension (1D). The mathematical model returns the car position $x$ from the knowledge of its initial position and the throttle input. However, the car is subject to the road defects and the wind, consequently, the model accumulates the error over time. To compensate for this error, GPS data $y$ are available but are only precise to a certain extent. To model these uncertainties, both the model and the measure are represented as Gaussian distributions with standard deviations $p$ and $r$, respectively. As shown in Figure 4.1 the Kalman filter is going to take both inputs with their uncertainty and estimate an optimal state with a new uncertainty $p$. If the uncertainty on the prediction is higher than the uncertainty on the measure, then the updated value is going to be more similar to the measure and vice versa. Hence, if a long distance is covered between two consecutive time steps $k-1$ and $k$ the mathematical model will tend to accumulate error, its associated standard deviation is going to increase and the filter is going to put more confidence on the GPS data. On the contrary, for short distances, the model will be more precise than the GPS and the filter will put more trust in the former.

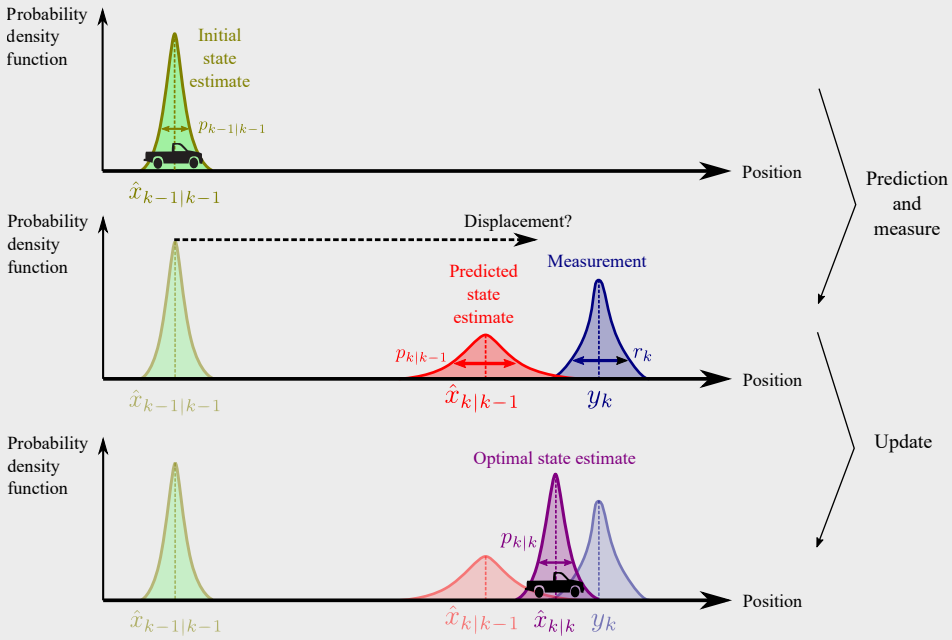


Figure 4.1: Illustration of the Kalman filter on a 1D example. The position of a car is estimated at each time step $k$. The three consecutive stages of the Kalman filter are represented. First, an initial position is given (top figure). Then, the mathematical model is used to predict the new state and some measurements are acquired (middle figure). Finally, from this knowledge, the Kalman filter infers the updated position of the car (bottom figure).

The predict stage is solely the application of Equation 4.4. The solution is based on the mathematical model. The interest of the KF is obviously the update stage where the observations are used to correct the model. The matrix $\mathbf{K}_k$ is referred to as the Kalman gain. It allows updating the a posteriori state estimate and covariance from the knowledge of the discrepancy between the observed state and the a priori estimation. The main difficulty in the practical implementation of the KF is the estimation of the noise covariances $\mathbf{Q}_k$ and $\mathbf{R}_k$. Many approaches have been developed to solve this issue, for example, the autocovariance least-squares [208]. The structure of nonlinear KFs still follows this two-stage structure but adapt the Equations 4.4 and 4.5 to nonlinear functions $g$ and $h$.

## 4.4 Data completion in augmented reality for laparoscopy

We have seen in the previous sections how we can fit a numerical model onto medical data. In this section, we provide an example of application with the augmented reality in laparoscopy. The laparoscopic surgery is first introduced, followed by the modeling of the physical priors and the integration of the medical data into this model.

### 4.4.1 The laparoscopic surgery

The laparoscopy refers to minimally invasive procedures performed at the level of the abdomen. The surgeon uses small incisions in the abdominal wall to insert the surgical and optic instruments. Usually, gas is insufflated within the abdomen, in the peritoneal cavity (pneumoperitoneum). This elevates the abdominal wall above the internal organs to create a working and viewing space. The laparoscopic operation is considered as one of the most complex to integrate within an AR framework (see Figure 4.2). Indeed, on the contrary to neurosurgery where the brain's motion is limited by the skull and can be considered as null, the laparoscopy implies large deformations as it mainly involves soft tissues. These deformations come from the pneumoperitoneum [251], but also from physiological motions such as the breathing or the heart beats and, during the operation, from the interaction between the surgical tools and the tissue. According to Bernhardt et al. [25], two distinct parts must be considered for AR in laparoscopy: the initial static registration of the augmented scene and a tracking procedure during the operation, to assess the different interaction between the surgical tools and the tissues. For both, several sources of data are available.

First, 3D preoperative images are acquired using computed tomography (CT) scans or Magnetic resonance images (MRIs). Since these data are obtained a few hours or days before the operation, they can be postprocessed and are generally of good quality. However, this delay between the acquisition and the surgery makes them "outdated". During the operation, the organs are in different positions because of potential physiological changes and more simply because the patient will not be exactly positioned similarly. Moreover, the organs are compressed due to pneumoperitoneum. To alleviate this problem, non-invasive methods can be used to get intraoperative images such as flat-panel cone-beam CT or open MR scanners. They provide 2D slices of the patient and have the advantage to be up-to-date. However, these data are often of poor quality because the measurement instruments must fit within the operating room and are consequently simplified. The data can also be acquired more directly through the use of an endoscope inserted in the abdomen. These images are most of the time 2D but can be stereoscopic in order to reproduce the human binocular vision. They are of good quality but can only capture the directly visible surface of the abdominal cavity. Hence, they do not provide information on the inner structures of the body. Finally, interventional measurements can be used to predict cyclic perturbations such as the breathing or the heart beats.

Thus, during a laparoscopy, the shape and structure of the organs are known thanks to preoperative images and an augmented representation of the features of interest can be computed from these data. Unfortunately, it does not match the intraoperative scene because of several sources of deformation of the soft tissues. Consequently, several sources of information must be used to adapt the initial 3D model to the current state. All this information is partial, can be noisy, and is not generally available at the same time. To address this challenge, a solution is to assign to the model

a behavior inspired by the physics, referred to as physical prior. In the case of deformable models, we suppose the deformation must respect mechanical laws that regularize their displacement. By doing so, we ensure that incorrect measurements will not cause unrealistic deformations and ensure a coherent display. It also allows inferring from partial data the position of structures of interest hidden to the image acquisition devices. To perform this deduction, an inverse problem must be solved

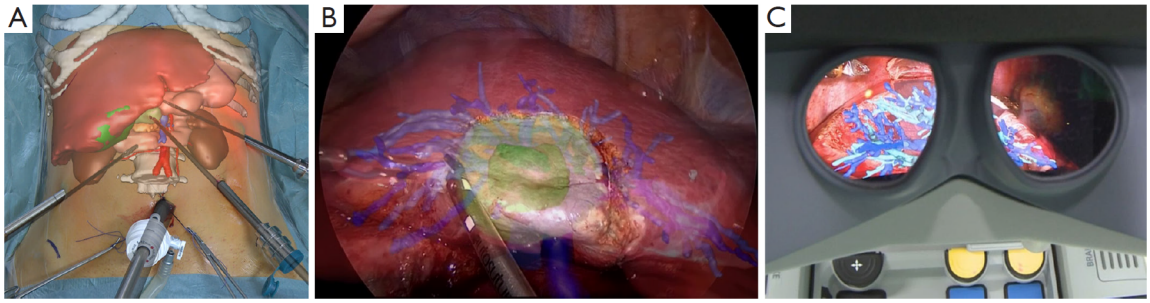


Figure 4.2: Illustration of an augmented reality scene in liver resection surgery (from [265]). The operation is performed on the Da Vinci robot providing an AR view via a direct display on the patient (A) or through AR glasses (C). The method used for the AR scene registration is based on a user-dependent interaction. Consequently, the authors concede that without integrating real-time deformable models the method will remain limited.

### 4.4.2 Deformable models

Many kinds of deformable models have been used in the context of surgical simulation [304]. The standard methods can be sorted into two categories: the heuristic-based and the continuum-mechanics-based methods (see Table 4.1). In the former, the deformation is generally driven by a coarse approximation of the constitutive laws governing the mechanical behavior. Two popular methods are the mass-spring model (MSM) [102] and the ChainMail algorithm [98]. In the MSM the mechanical system is represented by a dynamical network of lumped masses interconnected by elastic springs. Thanks to many developments, soft tissue mechanical properties such as near incompressibility, heterogeneity, and time-dependent viscoelasticity can be integrated. The MSM systems are simple to implement and have low computational complexity. However, the mass-spring structure can influence the deformation and may introduce artificial anisotropy. Moreover, to fit a MSM model to real data, each mass and spring stiffness must be tuned. It can become a cumbersome task and limit the model validity for out-of-the-training situations. The ChainMail algorithm is an even more simplified approach based on motion constraints. It uses the geometric limits of a mass point, or chain, to control the movement of its neighbors. A set of conditions is defined to adjust the amplitude of a chain's movement depending on the position of the surrounding chains. The position of the entire chainmail is computed by minimizing the global potential energy of the system. The ChainMail algorithm has the main advantage to be even faster than the MSM method, despite a lower mechanical accuracy. Hence, heuristic-based methods have the principal advantage to be computationally efficient while returning an approximation of the mechanical behavior. They have been extensively used in the early 2000s and are good candidates when high frame rates are required, as in haptic applications including topological changes [28].

Nowadays, the research effort is mainly focused on continuum-mechanics-based models. Here again, the methods can be sorted into two main categories: the mesh-based and the mesh-free methods. The first is typically illustrated with the finite element method [307] (FEM). Such a method implies a discretization of the space into reference elements. The constitutive laws are then enforced at the element level. The overall contribution of the elements is evaluated by assembling the solution over the entire model. The FEM is a common approach to reach high accuracy in biomechanical simulations [83]. However, it comes at the price of high computational costs. To meet the real-time visualization constraint, several methods have been employed to speed-

up the computations. Among them are the total Lagrangian formulation or the MOR approach. However, a main critic can be addressed to the mesh-based method: the mesh itself is a burden to the computation. As mentioned in Part I of this thesis, the creation of the mesh can be time-consuming as several quality criteria must be respected. Moreover, when the deformation implies very large strain, the distortion of the elements can lead to the failure of the method because of null or negative Jacobians. That is why meshless-based methods can be preferred [21]. These approaches do not require any explicit topological structure. They employ a set of arbitrarily positioned nodes in the problem's domain and interpolate the state variables in each node by considering the neighbors. As in the mesh-based methods, computations can be time-consuming. Similarly, they can be accelerated thanks to methods such as MOR. Nonetheless, the physical accuracy of meshless methods heavily depends on the placement of the nodes and sparse regions are poorly handled.

To conclude, we have shown that various kinds of deformable models exist. Heuristic methods are simple to use and provide very fast computations, satisfying the real-time for visualization (25 Hz) and even haptic feedback (1 kHz). Nonetheless, they are physically inaccurate as they do not respect the equations governing the mechanics of the system. On the other hand, continuum-mechanics-based methods respect these equations but are more complex to use. Moreover, they are generally not fast enough for real-time. Hence, strategies such as MOR must be set up to speed up the computations, requiring an additional effort for the implementation.

| Category | Heuristic | | Continuum-mechanics-based | |
|---|---|---|---|---|
| Method | Mass-Spring model | ChainMail | Mesh-based | Mesh-free |
| Figure | 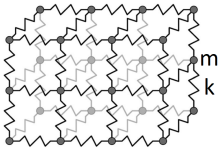 | 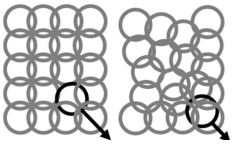 | 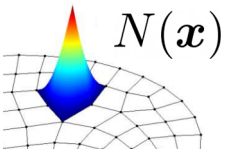 | 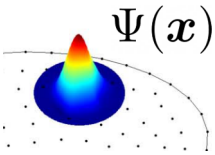 |
| Figure reference | [304] | [304] | [56] | [56] |

Table 4.1: Overview of the deformable models introduced in this chapter. The heuristic methods are illustrated on the left. In the mass-spring method, the system is composed of lumped masses $m$ linked by springs of rigidity $k$. The ChainMail figure shows two steps of the deformation. First, the chainmail is in its initial position and a displacement is imposed on a chain. Then, the motion of the chain induces the displacement of its neighbors and of the whole chainmail. The continuum-mechanics-based methods are represented on the right. For mesh-based methods, the domain is decomposed into cells. The value inside each cell is interpolated using the value at its nodes using shape functions $N(\boldsymbol{x})$. For mesh-free methods, nodes are scattered inside the domain and identical shape functions $\Psi(\boldsymbol{x})$ are used for all of them in order to interpolate the solution over the whole domain.

### 4.4.3 Data integration for image registration

Once a deformable model is chosen as a physical prior, it remains the question of the data acquisition and of the registration between them and the model. In [25], the authors review the AR registration methods in laparoscopy (see Figure 4.3) and sort them into four categories. The first category is the interactive approach. It mostly relies on manual inputs by an expert to perform the registration (task 0). These inputs are most of the time fiducial markers positioned on the medical images and on the augmented vision such as the correspondence is known. The second approach is similar to the first one and is named point-based approach (task 0). This time the markers are automatically detected, they can be artificial or natural. The third approach is the surface-based approach. The whole surface of the laparoscopic scene is reconstructed (task 1). It provides more information than the point-based approach and can incorporate fiducial markers. The augmented scene is then rigidly or non-rigidly registered (task 2). The last approach is the volume-based approach. Thanks to previously mentioned instruments, 3D information of the patient can be acquired intraoperatively. They are used to get deeper information than the sole surface of the organs. It enables the registration of new features, as the inner vessels (task 3). In this last case, the images from the different imaging modalities must also be inter-registered (task 4). The first and second categories of methods are not very interesting as they provide little information. In general, it only allows a rigid registration the AR scene, which does not require a physical prior. The fourth category involves expensive devices that are not always available. Hence, we focus on the surface-based methods that only require standard equipment.

As shown in Figure 4.3, two steps are required to register the 3D preoperative data onto the laparoscopic images. The first one is the reconstruction of the inner surface and the second one is the registration of the 3D model onto this surface. They are often treated sequentially and, they both consist in solving an inverse problem. The challenge in surface reconstruction is to be able to reconstruct a 3D view from 2D images. For the initial static registration, the scene can be considered rigid. But, for the representation of intraoperative deformations, the algorithm must be able to represent dynamically the topological changes. In the case of the initial static registration, the camera can be considered either static or moving. In [155] the authors propose a classification of the different methods. Three main techniques arise for the construction of the 3D surface from a static image. The first involves the use of stereo laparoscopes. These methods are often based on feature detection. This latter can be challenging when the surface has a homogeneous texture as in the case of the liver. To overcome this issue, active methods are proposed. They involve the projection of a specific pattern onto the surface of the organs, using laser stripes or structured light. The depth can then be evaluated from the deformation of the projected shapes. To avoid using additional hardware, the most simple method stays the shape-from-shading. It bases the reconstruction of the 3D scene on the shades created by the light of the laparoscope. If the camera is moving, other methods can be considered. A popular framework is the visual simultaneous localization and mapping (SLAM). The procedure is popular in robotics to simultaneously build a 3D map of the scene and track the camera position. Its first successful application in real-time with a monocular camera has been achieved in the early 2000s based on the EKF [78]. From this seminal work, several studies improved the method and adapted it to surgical procedures [185, 108, 107]. New visual SLAM approaches have also been proposed such as the parallel tracking and mapping algorithm [144] or the ORB-SLAM [187] method, and applied successfully in the laparoscopic context [154, 166]. The visual SLAM framework has also been used in the case of dynamic scene registration, in the so-called non-rigid structure from motion framework. For example, in the work of Agudo et al. [3, 4], the authors proposed a method based on the EKF-SLAM and a finite element (FE) formulation to encompass the structure deformation. The surface is considered as an elastic thin-plate solid. Thanks to this physical prior, a millimeter precision is reached.

Once the target surface is identified in the augmented scene, the preoperative 3D model must be registered to it. The standard approach is to use salient features to make the correspondence between specific regions of the images and the 3D model. It can be manually or automatically positioned landmarks [224] and/or contours [116, 2, 145]. A marker-less approach has also been proposed in [82]. More originally, in [271] the authors propose to consider the surfaces as electrically charged and to register them by solving a FE problem while taking into account the deformation of

the mechanical model. For most of the methods, once the correspondence is found, the 3D model is deformed using the pairs of matching points as boundary conditions. The standard procedure is to minimize a functional composed of a distance term, representing the distance between the two surfaces we want to register, plus a regularization term representing the mechanical energy of the system. In recent studies, FE is the method of choice to simulate the model's deformations. Thanks to computationally efficient approaches such as the corotational FE [193], real-time visualization is accessible. Moreover, the FE method makes it easy to integrate advanced features such as the internal structures (e.g. the tumor or the vascularization [114, 226]) or specific boundary conditions, such as the effect of gravity [212]. Nonetheless, this approach also involves a parametrization of the constitutive equations describing the mechanical behavior (e.g. the Young modulus and the Poisson ration in the elastic case). These parameters are often chosen arbitrarily, leading to a possibility inaccurate estimation of the deformation. In [124], Hoshi et al. propose to infer directly their values from medical images using an EKF. However, the study is restrained to a simple homogeneous isotropic linear elastic material and the setup is very basic. We propose in the next chapter to tackle both the registration and the parameter identification problem simultaneously in a nonlinear context. To this end, an EKF based on a MOR method is employed. Even though only synthetic data are used, an effort is put on the reproduction of realistic laparoscopic conditions.

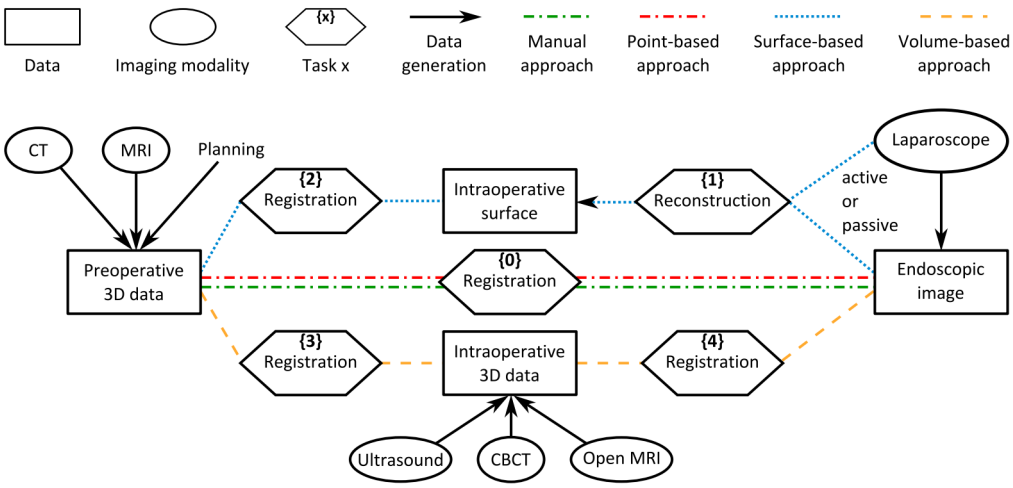


Figure 4.3: Current approaches for registration in laparoscopic AR as presented in [25]. They are related to the four categories of registration methods.

Chapter 5

# An extended Kalman filter based on hyperreduction for three-dimensional medical image completion embedding physical priors

**Abstract** In this chapter, a new approach for the initial static registration of the augmented scene in laparoscopy is presented. This problem is chosen as it contains a lack of information, requiring the use of physical priors to complete the data. First, the available 3D model acquired preoperatively is not representative of the reality as it is not submitted to the artificial pneumoperitoneum pressure. Then, the monocular laparoscopes usually employed in this kind of operation only return two-dimensional images of a partial surface of the organs. To solve this ill-posed problem, we propose an automatic registration procedure based on an extended Kalman filter. We assume the surface reconstruction of the abdominal cavity is provided by a simultaneous localization and mapping procedure. To account for the near real-time constraint of surgery, a semi-intrusive hyperreduced order model, based on a sparsity promoting technique, is developed. Hyperelastic materials are considered for the soft tissues, and no a priori is given on their parametrization. Results on synthetic data show that the registration can be performed in a few seconds and that a weak identification of the material parameters is not harmful to the accuracy of the procedure.

## Contents

## 5.1 Introduction

### 5.1.1 Motivation

The *accurate* and *real-time* simulation of biological soft tissues was foreseen twenty years ago as the operating rooms' (OR) next revolution, in particular for augmented reality (AR) applications in hepatic surgery [175]. Such a feature would allow revealing hidden structures from the surgeon's eyes such as organ vessels and tumors. Since then, several approaches were explored to find a balance between accuracy and computational efficiency. Indeed, an accurate representation of biological soft tissues implies heavy-computations as they have complex topologies and nonlinear behaviors. On the other hand, real-time encompasses computation frequencies ranging from 1Hz, for the tracking of slow movements such as the breathing, to 1kHz, in the particular case of haptic feedback. Many studies have tried to find a compromise between these two conflicting goals, in particular, to represent the organ deformation for interactive surgical simulations [304].

The first challenge that should be tackled in the context of augmented-reality surgery, and more specifically in laparoscopy, is the initial pose of the model within the augmented environment. The latter is often considered to be done manually, even though it reveals to be particularly complex. Indeed, laparoscopic surgery involves gas insufflation into the abdominal cavity (pneumoperitoneum) which induces a displacement and a deformation of the organs of interest [16]. In basic surgical AR procedures, the shape of the organs is acquired preoperatively and is then registered at the beginning of the operation to their real counterparts. Here, these latter do not match the preoperative data anymore. Hence, to be able to represent the deformed organs the information must be taken directly from the intraoperative scene. Some methods were proposed to exploit intraoperative data from computed tomography (CT) scans [210] or ultrasound probes [74, 266]. However, these devices are not always available in the OR and can be cumbersome. The most basic tool the surgeon always have at his disposition is a camera embedded in a laparoscope, used to explore the environment. The camera can only capture two-dimensional information on the visible surface of the organs. Hence, to recreate the three-dimensional (3D) scene, the deformable model must be adapted on the base of partial surface information leading to an ill-posed problem. Several methods employ stereo laparoscopes in order to recreate a depth perception and perform the preoperative liver registration [224, 116, 240, 181]. In [212], a method is even proposed using solely a single monocular laparoscopy image. Whatsoever, all the previously mentioned techniques are based on contour or landmarks detection. Most of the time it requires a manual intervention forbidding the full automation of the method. Automatic contour detection methods exist but they are prone to failure in case of textureless tissues. An alternative to feature detection is the reconstruction of the whole AR scene using dense 3D point clouds. In the last decade, SLAM (simultaneous localization and mapping) systems have emerged as a reliable approach to build such an environment, in particular in the case of laparoscopy with hand-held monocular endoscopes [107]. In the continuity of this work, Mahmoud et al. proposed in [167] a method that robustly

densifies a sparse SLAM for the reconstruction of laparoscopic scenes. Under the assumption that the surgeon does not manipulate the environment, the scene is considered rigid. In this chapter, we propose to build on this work and to develop an unsupervised algorithm able to perform the initial static registration of the AR laparoscopic scene from the knowledge of a rigid 3D point cloud.

### 5.1.2 Simulation context

As mentioned before, the problem of the registration is ill-posed. This is due to a lack of information either caused by the measurement techniques or by the model used to approximate the solution. To solve this kind of problem, inverse uncertainty quantification methods are used. They estimate the discrepancy between the measurements and the mathematical model and return the best model's parameters which allow representing the measurements. The Kalman filter (KF), and its extensions for nonlinear behaviors the extended Kalman filter (EKF) and unscented Kalman filter are commonly used methods to perform inverse uncertainty quantification. The KF can be presented as one of the simplest dynamic Bayesian networks. It is a two-step process: the first step is to predict the state of the system thanks to the mathematical model and the second step uses the noisy measurements to refine the estimate of the state of the system. In the context of AR for the representation of mechanical deformation, the KF can be used to mitigate the measurement errors - such as data occlusion - thanks to physical-based priors. On the inverse, they can be used for parameter identification [190, 14]. The real bottleneck of such methods is that they require a real-time and accurate mathematical model to be used as a prediction. Model order reduction (MOR) methods are good candidates for such an application as they allow to decrease the mathematical complexity of a model without simplifying the underlying physics. In [103] a framework using the proper generalized decomposition method within the EKF is established, with a focus on nonlinear mechanics applications. It is used for physically-based augmented reality in [14]. This framework is extended to more general Bayesian inference in [244]. To build on this works, we take the route of MOR coupled with an EKF to tackle the problem of deformable 3D shape registration based on incomplete image data.

### 5.1.3 Overview

In this chapter, we propose an unsupervised method for fast static registration of the organs, and especially of the liver, in the context of augmented laparoscopy. To be able to register the data in quasi real-time and to take into account the uncertainty of the parameters of the mathematical model, an EKF is used. The mathematical model used in the filter hinges on an innovative MOR method integrating a novel hyperreduction approach, relying upon spare approximation theory. The reduced order model (ROM) is based on the mechanical energy minimization of the system and can be performed with standard optimization solvers. Moreover, the training data required to build the ROM are obtained using an external finite element (FE) solver. As an implementation effort is still required for the formulation of the system's mechanical energy, the method is coined as "semi-intrusive". In this work, only synthetic data are used to validate the EKF. The inputs are considered to be the intra-abdominal pressure and the position of a point cloud describing the abdominal surface, acquired thank the SLAM method. Hence, only the challenge of the static registration from partial measures and inaccurate preoperative data is tackled. The measures themselves are considered to be provided by an external preprocessing stage. As no landmark or contour detection is considered, the registration is considered as unsupervised.

### 5.1.4 Chapter organization

The chapter is organized into seven sections. In Section 5.2 the model is introduced. Its geometry is first described, followed by the soft tissue modeling, the boundary conditions, and the constitutive equation. The MOR strategy is defined in Section 5.3 and the EKF formulation is detailed in Section 5.4. The validation setup is then introduced in Section 5.5 before the results in Section 5.6. Finally, the discussion and the conclusion are done in Section 5.7 and 5.8, respectively.

## 5.2 Model of the abdominal cavity

### 5.2.1 Geometry

The model's geometry encompasses not only the liver but also a portion of the abdominal cavity. It allows using simple boundary conditions, presented in Section 5.2.4. The model contains a liver mesh embedded within a dummy mesh used to represent the rest of the abdominal cavity (stomach, viscera, ...). A spherical tumor of 16 mm radius is inserted inside the liver. Only tetrahedral elements are used. All the operations on the meshes were done using the open-source software PyMesh, for the boolean operation on the surface meshes, Meshlab, for the cleaning of these latter, and gmsh, for the creation of the 3D mesh from the surfaces. The liver's mesh contains $6,784$ elements for $1,632$ nodes, the tumor 605 elements for 190 nodes and the remain $24,032$ elements for $5,071$ nodes. The total number of nodes is $n_v = 6,893$. The maximal dimensions of the assembly are 182 mm long (craniocaudal axis), 223 mm wide (left-right axis) and 129 mm in high (dorsoventral axis). The different parts composing the mesh are shown in Figures 5.1 and 5.2a and the final mesh is shown in Figure 5.2b.

### 5.2.2 Soft tissue modeling

Hyperelastic constitutive behaviors are commonly used for soft tissue modeling. Their stress-strain relationship derives from a strain energy density function $\Psi$. Hyperelastic materials have the characteristic not to dissipate the strain energy, hence, the energy stored when undergoing deformation is not dependent on the history. In the model, two kinds of hyperelastic isotropic homogeneous material laws are used. The Saint Venant-Kirchhoff law for the tumor and the abdominal cavity and the Veronda-Westmann law for the liver.

**Saint Venant-Kirchhoff formulation** The tumor and the simplified abdominal cavity behaviors are described by a Saint Venant-Kirchhoff law. This latter is considered as the most basic hyperelastic material as it is a mere extension of the classical linear elastic material in large deformation. Many studies from the literature used similar behaviors in the case of the tumors [282]. The choice of such behavior for the abdominal cavity is arbitrary as no data was found in the literature on a homogenization of this latter. Homogenization is in itself an important simplification but it would not have been pertinent for the application presented in this thesis to go more into details. The St Venant-Kirchhoff strain energy density function reads

$$\Psi = \frac{1}{2}\lambda(\operatorname{tr}\mathbf{E})^2 + \mu\mathbf{E}:\mathbf{E} \tag{5.1}$$

where $\mathbf{E} = \frac{1}{2}(\mathbf{C} - \mathbf{I})$ is the Green-Lagrangian strain tensor and $\mathbf{C}$ is the right Cauchy–Green deformation tensor. This latter can be detailed as

$$\mathbf{C} = \mathbf{F}^T\mathbf{F} \tag{5.2}$$

where

$$\mathbf{F} = \frac{\partial \boldsymbol{X}}{\partial \boldsymbol{X}_0} = \frac{\partial \boldsymbol{u}}{\partial \boldsymbol{X}_0} + \mathbf{I}\,. \tag{5.3}$$

where $\boldsymbol{u} = \boldsymbol{X} - \boldsymbol{X}_0$ is the displacement between the current and the initial position, respectively $\boldsymbol{X}$ and $\boldsymbol{X}_0$. $\mathbf{I}$ is the identity matrix. The so-called Lame parameters $\lambda$ and $\nu$ are related to the Young Modulus $E$ and the Poisson ratio $\nu$ with

$$\lambda = \frac{E\nu}{(1+\nu)(1-2\nu)}$$
$$\mu = \frac{E}{2(1+\nu)}\,.$$

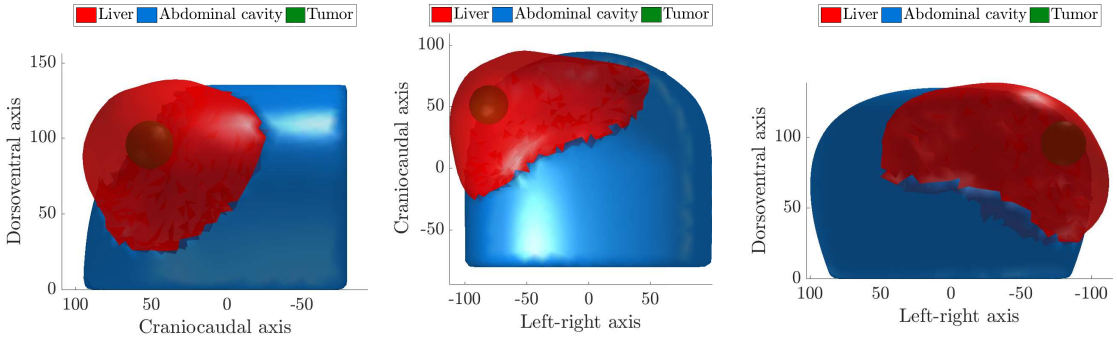


(a) View from left-right axis. (b) View from dorsoventral axis. (c) View from craniocaudal axis.

Figure 5.1: The model's geometry is shown, with its several parts dissociated, from different angles of view. The liver is represented in red, the tumor in green and the abdominal cavity in blue.

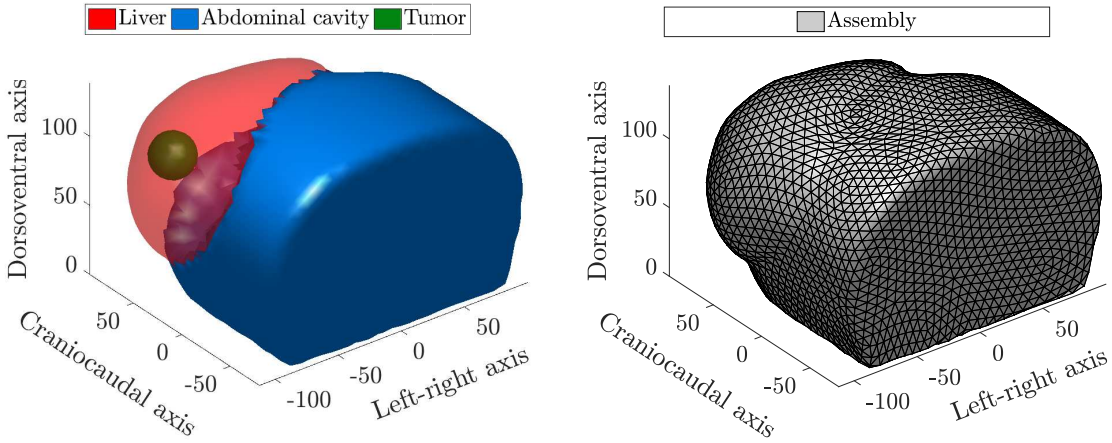


(a) Geometrical assembly of the several parts. Only the surfaces are represented.

(b) Mesh preview of the geometrical assembly.

Figure 5.2: The model's geometry is shown with its several parts dissociated (on the left) and on its meshed version (on the right). The liver is represented in red, the tumor in green and the abdominal cavity in blue.

**Veronda-Westmann formulation** Several laws have been used to represent the liver's behavior [174]. Here the liver is modeled by a Veronda-Westmann [289] formulation, successfully used in [299] to represent the liver's deformations. Its strain energy density function reads

$$\Psi = \underbrace{C_1 \left[ e^{\left(C_2(\tilde{I}_1 - 3)\right)} - 1 \right] - \frac{C_1 C_2}{2} \left( \tilde{I}_2 - 3 \right)}_{\tilde{\Psi}(\tilde{\mathbf{C}})} + U(J) \tag{5.4}$$

where $\tilde{\Psi}(\tilde{\mathbf{C}})$ is the deviatoric part, $U(J) = \frac{1}{2}K(\ln J)^2$ is the dilation term and

$$\begin{aligned} \tilde{I}_1 &= \mathrm{Tr}(\tilde{\mathbf{C}}) \\ \tilde{I}_2 &= \frac{1}{2}\left( \mathrm{Tr}(\tilde{\mathbf{C}})^2 - \mathrm{Tr}(\tilde{\mathbf{C}}^2) \right) \\ J &= \det \mathbf{F} \\ \tilde{\mathbf{C}} &= \tilde{\mathbf{F}}^T \tilde{\mathbf{F}} \\ \tilde{\mathbf{F}} &= J^{-\frac{1}{3}} \mathbf{F} \,. \end{aligned} \tag{5.5}$$

The material is considered quasi-incompressible, hence, to enforce $J \approx 1$, the penalization term $K$ is chosen to be equal to $10^7$.

### 5.2.3 Governing equation

For a given quasi-static hyperelastic mechanical system, a total potential energy functional can be defined as

$$\Pi(\boldsymbol{u}) = \int_\Omega \Psi(\boldsymbol{u})\, d\Omega - \int_\Omega \boldsymbol{f}_0 \cdot \boldsymbol{u}\, d\Omega - \int_{\partial\Omega} \boldsymbol{t}_0 \cdot \boldsymbol{u}\, d\partial\Omega \tag{5.6}$$

where $\boldsymbol{u}$ is the displacement between the initial and current position, $\boldsymbol{f}_0$ are the body forces, $\boldsymbol{t}_0$ are the traction forces, $\Omega$ is the integration domain and $\partial\Omega$ is the boundary of this latter. The equilibrium equation for continuum systems, developed in the framework of virtual works, leads to the assertion: *the minimum of the potential energy* $\Pi$ *with respect to the displacement* $\boldsymbol{u}$ *is the solution of the mechanical equilibrium equation* (see for example [31]). Hence the solution of the equilibrium can be written

$$\hat{\boldsymbol{u}} = \arg\min_{\boldsymbol{u}} \Pi(\boldsymbol{u}) \,. \tag{5.7}$$

### 5.2.4 Boundary conditions

The geometrical model used in this chapter is quite simplified, e.g. the abdominal wall is not represented and no contact is modeled, thus the boundary conditions are adapted. They are illustrated in Figure 5.3. As during laparoscopy the patient lies on its back, the rear part of the abdomen is pinned and no movement is allowed. Furthermore, the inferior part of the abdomen is not taken into account in the geometry. Hence, the lower section of the model has its movement forbidden in the craniocaudal axis to simulate the presence of non-represented organs. Laparoscopic surgery involves the insufflation of gas into the peritoneal cavity. The intra-abdominal pressure is maintained around 10-20 mm Hg (i.e. $\approx$ 1.3-2.7 kPa). This translates in Equation 5.6 by $\boldsymbol{f}_0 = 0$ and $\boldsymbol{t}_0 = -P\boldsymbol{n}$ where $\boldsymbol{n}$ is the outward normal pointing vector of the domain $\partial\Omega$ and $P \in \mathbb{R}^+$ is the pressure. This pressure is only applied to the nodes having a height superior to 50 mm, as shown in Figure 5.3. In this configuration, the pressure is applied to 30% of the whole liver surface and to 19% of the whole abdominal cavity one.

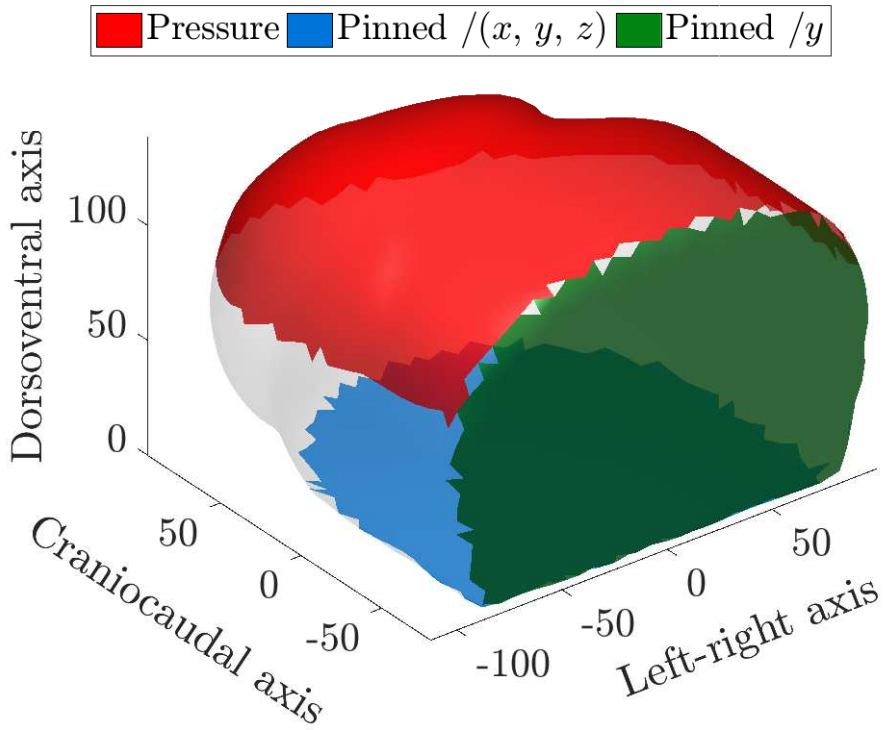


Figure 5.3: Geometry of the model with the boundary conditions. The axes $(x, y, z)$ correspond to the left-right, craniocaudal and dorsoventral axes, respectively. The blue surface is pinned in all directions and represents the back. The green surface is pinned in the craniocaudal direction to represent the remaining organs of the abdomen. The red surface is where the pressure is applied. The latter surface represents 30% of the liver surface and 19% of the abdominal cavity one.

## 5.3 Construction of the reduced order model

### 5.3.1 Overview

The final goal is to solve Equation 5.7. As the displacement $\boldsymbol{u}$ can contain thousands of degrees of freedom, minimization strategies are set up such as the Newton-Raphson method. It involves to compute the derivative of $\Pi(\boldsymbol{u})$ and, consequently, implies some implementation effort and the cost of the matrix assembly during the computations. We propose a new approach where the number of degrees of freedom is lowered to a few tens thanks to the proper orthogonal decomposition (POD) and the integration domain is reduced through a hyperreduction technique. It allows us to use directly a standard optimization solver to minimize Equation 5.7 as the value of $\Pi$ will now depend on a restrained number of parameters.

### 5.3.2 Proper orthogonal decomposition

The POD is a concept very similar to the principal component analysis, the Karhunen-Loéve decomposition or the singular value decomposition (SVD). An introduction can be found in [54]. Let's consider the SVD and explain how it can be used for model reduction in the current context. First, a database $\mathbf{U} = [\boldsymbol{u}_1, \cdots, \boldsymbol{u}_{n_s}]$ must be created. Each $\boldsymbol{u}_i \in \mathbb{R}^{3n_v}$ is the solution, also called *snapshot*, of Equation 5.7 under a specific initialization (material parameters and boundary conditions). The SVD allows writing $\mathbf{U}$ such as

$$\mathbf{U} = \boldsymbol{\Phi}\mathbf{A} \tag{5.8}$$

where $\boldsymbol{\Phi} = [\boldsymbol{\phi}_1, \cdots, \boldsymbol{\phi}_{3n_v}]$ is an orthonormal basis and $\mathbf{A} = [\boldsymbol{\alpha}_1, \cdots, \boldsymbol{\alpha}_{n_s}]$ contains the vectors such as $\boldsymbol{u}_i = \boldsymbol{\Phi}\boldsymbol{\alpha}_i$. A singular value $\lambda_i$ is associated with each singular vector, or *mode*, $\boldsymbol{\phi}_i$. These former are naturally sorted by the SVD so as so $\lambda_1 \geq \cdots \geq \lambda_{3n_v} \geq 0$. In practice, the underlying dimension of $\mathbf{U}$ is generally lower than $3n_v$. This lower dimensionality is observable by a consequent drop in the value of the singular values. Saying $r < 3n_v$ is the rank of $\mathbf{U}$, it follows $\lambda_r \gg \lambda_{r+1}$. It has been shown that the best rank-$r$ approximation of $\mathbf{U}$ - based on its Frobenius norm minimization - can be achieved by keeping the $r$ largest singular values such as

$$\mathbf{U} \approx \boldsymbol{\Phi}_r \mathbf{A}_r \tag{5.9}$$

where $\boldsymbol{\Phi}_r = [\boldsymbol{\phi}_1, \cdots, \boldsymbol{\phi}_r]$ and $\mathbf{A}_r = [\boldsymbol{\alpha}_1^r, \cdots, \boldsymbol{\alpha}_{n_s}^r]$. The POD uses this low-rank representation of $\mathbf{U}$ to assume that each new solution $\tilde{\boldsymbol{u}}$, similar to the ones from the database, can be written as

$$\tilde{\boldsymbol{u}} = \sum_{i=1}^{r} \boldsymbol{\phi}_i \tilde{\alpha}_i = \boldsymbol{\Phi}_r \tilde{\boldsymbol{\alpha}} \tag{5.10}$$

where $\tilde{\boldsymbol{\alpha}} = (\tilde{\alpha}_1, \cdots, \tilde{\alpha}_r)^T \in \mathbb{R}^r$ are the reduced degrees of freedom of the solution. The selection of the truncation order $r$ is usually done in order to maximize the *relative information content* (RIC) while minimizing $r$. The RIC is defined relatively to the singular values, the selection of the best truncation order $\hat{r}$ then reads

$$\hat{r} = \underset{r \in \mathbb{R}_*^+}{\arg\min} \left( \frac{\sum_{i=1}^{r} \lambda_i}{\sum_{j=1}^{3n_v} \lambda_j} > h \right) \tag{5.11}$$

where $h \in (0, 1]$ is a threshold defining the percentage of variability the ROM must encompass.

The notion of model reduction takes here its meaning because instead of having $3n_v$ degrees of freedom, the solution $\tilde{\boldsymbol{u}}$ depends now on only $\hat{r} \ll 3n_v$ parameters (often $\hat{r}$ is around a few tens). The minimization of Equation 5.7 is now manageable with standard optimization solvers without requiring a full FE solver. Nonetheless, when the models involve non-linear terms the POD is insufficient to accelerate significantly the computations. The evaluation of non-linearities and the resulting matrix assembly involve an important computational overhead. That is why hyperreduction techniques have been developed.

### 5.3.3 Hyperreduction

The hyperreduction has been introduced by Ryckelynck [247, 248]. It is a way to find reduced integration domains (RIDs) that allows doing fast numerical integrations. This approach is commonly used in conjunction with the POD in nonlinear problems. A brief reminder of the quadrature principle in the FE framework is first presented, followed by the description of the hyperreduction method we developed.

#### 5.3.3.1 Quadrature in finite element analysis

The basic problem in numerical integration is to compute an approximate solution to a definite integral of a function $f$ over a domain $\Omega$. To this end, $n_q \in \mathbb{N}^*$ quadrature points $\boldsymbol{a}_i \in \Omega$ associated with weights $c_i$ are defined such as

$$\int_\Omega f(\boldsymbol{a})\, d\boldsymbol{a} = \sum_{i=1}^{n_q} f(\boldsymbol{a}_i) \times c_i \,. \tag{5.12}$$

In FE methods, the domain is partitioned in reference elements with specific shapes (triangles, quadrilaterals, tetrahedra, hexahedra, ...). The fields of interest are computed exactly at the nodes (or vertices) of each element. To know the value of a field over the whole domain piecewise polynomial functions are used to interpolate the value at the nodes. The FE method is formulated such as the integral of specific functions must be computed over the elements' domain. Consequently, considering a mesh with $n_e$ elements, each one containing $n_q^e$ quadrature points, then the function of interest $f(\boldsymbol{x})$ must be evaluated $n_q = n_e \times n_q^e$ times to compute the integral over the whole domain. What we seek with hyperreduction is to find a RID for the problem at hand, using data from high fidelity simulations, such as

$$I = \int_\Omega f(\boldsymbol{a}) d\boldsymbol{a} = \sum_{j=1}^{n_e} \sum_{i=1}^{n_q^e} f(\boldsymbol{a}_i^j) \times c_i^j \approx \sum_{i=1}^{n_{hr}} f(\boldsymbol{b}_i) \times d_i \tag{5.13}$$

where $\Omega \subset \mathbb{R}^D$ is the spatial domain in dimension $D$, $\boldsymbol{a} \in \Omega$ the position of a point in this latter, $\boldsymbol{a}_i^j$ the position of the $i$-th quadrature points in the $j$-th finite element with $c_i^j$ the corresponding weight, $\boldsymbol{b}_i$ the points from the reduced quadrature rule with $d_i$ the corresponding weights and $n_{hr} \ll n_e \times n_q^e$ their number. This approach enables a consequent speed-up of the computations as $f$ is only evaluated only $n_{hr}$ times instead of $n_e \times n_q^e$, which allows simplifying the subsequent matrix assemblies.

#### 5.3.3.2 Hyperreduction method

**Sparse approximation** The sparse approximation (SA), is a method aiming at finding a sparse representation $\hat{\boldsymbol{\xi}}$ of an input data $\boldsymbol{q}$. This latter is a linear combination of *atoms* $\boldsymbol{\theta}_i \in \mathbb{R}^N$ ($i \in [\![1, K]\!]$) composing the columns of the *dictionary* $\Theta$. The problem reads

$$\begin{array}{c} \min_{\boldsymbol{\xi} \in \mathbb{R}^K} \|\boldsymbol{\xi}\|_p \\ \text{subject to } \boldsymbol{q} = \Theta\boldsymbol{\xi} \end{array} , \quad p \leq 1 \tag{5.14}$$

where $||\cdot||_p$ is the classical $\ell^p$-norm associated with vectors. The size of the dictionary $\Theta$ is $N \times K$ where $K > N$, the dictionary is then said to be *overcomplete*. The problem is generally written using the Lagrangian formulation as

$$\hat{\boldsymbol{\xi}} = \arg\min_{\boldsymbol{\xi}} ||\boldsymbol{\xi}||_p + \gamma ||\boldsymbol{q} - \Theta\boldsymbol{\xi}||_2^2 \,, \quad p \leq 1 \tag{5.15}$$

where the weighting scalar $\gamma \in \mathbb{R}_*^+$ allows to foster either the sparsity or the quality of the approximation. Indeed, $||\boldsymbol{q} - \Theta\boldsymbol{\xi}||_2^2$ corresponds to the representation error and $||\boldsymbol{\xi}||_p$ is an evaluation of the vector's sparsity. The value $p$ depends on the algorithm, $p = 0$ is equivalent to count the number of non-zero elements in $\boldsymbol{\xi}$, but the problem is easier to solve with ($p \leq 1, p \neq 0$) and reaches the

same goal. A stopping criterion must be given, it can be set on the sparsity of $\boldsymbol{\xi}$, i.e. the sparsity measured with the $\ell^p$-norm, or on the representation error.

**Reduced quadrature rule** If we have a collection of measures $\mathcal{I} = \{I_1, \cdots, I_N\}$ ($N \in \mathbb{N}^*$) for different configurations (for example $\Omega$ can change, or a parameter in the integrated function), thanks to Equation 5.13 we can write

$$\underbrace{\begin{bmatrix} I_1 \\ I_2 \\ \vdots \\ I_N \end{bmatrix}}_{\boldsymbol{q}} = \underbrace{\begin{bmatrix} f_1(\boldsymbol{a}_1) & f_1(\boldsymbol{a}_2) & \cdots & f_1(\boldsymbol{a}_{n_q}) \\ f_2(\boldsymbol{a}_1) & f_2(\boldsymbol{a}_2) & \cdots & f_2(\boldsymbol{a}_{n_q}) \\ \vdots & \vdots & \ddots & \vdots \\ f_N(\boldsymbol{a}_1) & f_N(\boldsymbol{a}_2) & \cdots & f_N(\boldsymbol{a}_{n_q}) \end{bmatrix}}_{\Theta} \underbrace{\begin{bmatrix} c_1 \\ c_2 \\ \vdots \\ c_{n_q} \end{bmatrix}}_{\boldsymbol{c} \Leftrightarrow \boldsymbol{\xi}} \tag{5.16}$$

where $f_i$ are the function $f$ evaluated on the different configurations. A SA is used to find a sparse representation of $\boldsymbol{c}$. This way we can define a sparse vector $\boldsymbol{c}' = (c'_1, \cdots, c'_{n_q})^T$ such that $\boldsymbol{q} \approx \Theta \boldsymbol{c}'$ and where most of the $c'_i$ are zeros. By noting $(d_1, \cdots, d_{n_{hr}})$ (where $n_{hr} \ll n_q$) the subset of $(c_1, \cdots, c_{n_q})$ corresponding to the non-zeros values and $(\boldsymbol{b}_1, \cdots, \boldsymbol{b}_{n_{hr}})$ the positions of the corresponding quadrature points, Equation 5.16 reads

$$\begin{bmatrix} I_1 \\ I_2 \\ \vdots \\ I_N \end{bmatrix} \approx \begin{bmatrix} f_1(\boldsymbol{b}_1) & f_1(\boldsymbol{b}_2) & \cdots & f_1(\boldsymbol{b}_{n_{hr}}) \\ f_2(\boldsymbol{b}_1) & f_2(\boldsymbol{b}_2) & \cdots & f_2(\boldsymbol{b}_{n_{hr}}) \\ \vdots & \vdots & \ddots & \vdots \\ f_N(\boldsymbol{b}_1) & f_N(\boldsymbol{b}_2) & \cdots & f_N(\boldsymbol{b}_{n_{hr}}) \end{bmatrix} \begin{bmatrix} d_1 \\ d_2 \\ \vdots \\ d_{n_{hr}} \end{bmatrix} \tag{5.17}$$

which corresponds to Equation 5.13 for all elements of $\mathcal{I}$. An important point in numerical integration is that all quadrature weights must be positive and that $\sum_{i=1}^{n_q} c_i = \sum_{i=1}^{n_{hr}} d_i = \int_\Omega 1 d\Omega = |\Omega|$. To respect these conditions, we developed a modified version of the sparse approximation algorithm called focal underdetermined system solver (FOCUSS) [106].

**Remark 5.1** (*Size of the dictionary* $\Theta$). In the hyperreduction approach, the value $N$ corresponds to the number of simulations and $K = n_q$ to the number of quadrature points. Consequently, the condition $K > N$ on the dictionary size is quasi-systematically respected. If that is not the case, one can refer to Chapter 7 Section 7.4.2 where the use of the FOCUSS algorithm for large atoms is discussed.

#### 5.3.3.3 The non-negative FOCUSS algorithm

**The method** The original FOCUSS algorithm has been introduced in [106]. It solves the sparsity constraint by iteratively computing $\boldsymbol{\xi}$. At iteration $k$ it reads

$$\boldsymbol{\xi}_{k+1} = \mathbf{W}_{k+1}(\Theta \mathbf{W}_{k+1})^+ \boldsymbol{q} \tag{5.18}$$

where $\mathbf{W}_{k+1} = \text{diag}(|\boldsymbol{\xi}_k|^{(1-\frac{p}{2})})$, diag is the diagonalization operator and $\mathbf{M}^+$ denotes the Moore-Penrose inverse of $\mathbf{M}$ such as $\mathbf{M}^+ = \mathbf{M}^T(\mathbf{M}\mathbf{M}^T)^{-1}$. As noise can be present in the data, a regularized version of the method has been developed in [235]. The problem is then reformulated as in Equation 5.15 and Equation 5.18 becomes:

$$\boldsymbol{\xi}_{k+1} = \mathbf{W}_{k+1}\Theta_{k+1}^T(\Theta_{k+1}\Theta_{k+1}^T + \gamma \mathbf{I})^{-1}\boldsymbol{q} \tag{5.19}$$

where $\Theta_{k+1} = \Theta \mathbf{W}_{k+1}$ and $\mathbf{I}$ is the identity matrix. Hereafter, the elements of $\boldsymbol{\xi}$ will be referred to as the weights associated with the atoms. In our non-negative version of the FOCUSS algorithm, called nnFOCUSS, the positivity of the entries of $\boldsymbol{\xi}_k$ - i.e. the weights - is enforced in two stages. The first step is to choose an initialization $\boldsymbol{\xi}_0$ containing only positive values. Then, at each iteration, the positivity constraint is applied using Algorithm 2. Besides, the condition on the measure of the domain $\sum_{i=1}^{K} \xi_{k,i} = |\Omega|$ is enforced by adding the uniform vector as a row of the dictionary. As we seek for the sparsest solution, the algorithm is considered to reach convergence when $||\boldsymbol{\xi}_{k+1} - \boldsymbol{\xi}_k||_2 / ||\boldsymbol{\xi}_k||_2 < \epsilon$, where $\epsilon$ is a user-defined tolerance.

**Algorithm 2:** Non-negative FOCUSS algorithm

**Inputs :** $\Theta$,$\boldsymbol{q}$,$\boldsymbol{\xi}_k$,$\gamma$,$p$

**Output:** $\boldsymbol{\xi}_{k+1}$

Compute $\boldsymbol{\xi}_{k+1}$ using Equation 5.19
**if** any$(\boldsymbol{\xi}_{k+1} < 0)$ **then**
  $i \leftarrow$ index of min $(\boldsymbol{\xi}_{k+1})$
  $\boldsymbol{\delta} = \boldsymbol{\xi}_{k+1} - \boldsymbol{\xi}_k$
  $\alpha = -\boldsymbol{\xi}_k[i]/\boldsymbol{\delta}[i]$
  $\boldsymbol{\xi}_{k+1} = \boldsymbol{\xi}_k + \alpha\boldsymbol{\delta}$
**end**
Return $\boldsymbol{\xi}_{k+1}$

**Scaling and initialization** It is interesting to note that if two atoms $\boldsymbol{\theta}_1$ and $\boldsymbol{\theta}_2$ are linearly dependent such as $\boldsymbol{\theta}_1 = \kappa\boldsymbol{\theta}_2$ with $\kappa \gg 1$, then for a uniform initialization of $\boldsymbol{\xi}_0$ the weight associated with the atom $\boldsymbol{\theta}_2$ will have more probability to be null as its initial value is closer to 0. Therefore, to avoid giving any preference to any column, it may be pertinent to normalize them. This way, for a uniform initialization no atom would be preferred. Note that scaling the dictionary and using as initialization the norm of the atoms is equivalent to not do the scaling.

To evaluate the interest of scaling the dictionary, a simple test case is used. We consider a set of polynomial functions $\mathcal{P}$ of degree $d$ defined over the domain $[-1, 1]$. According to the Gauss-Legendre quadrature rule, each function in $\mathcal{P}$ can be exactly integrated with $q_{GL}$ quadrature points under the constraint that $d \leq 2q_{GL} - 1$. To test the nnFOCUSS' ability to find the sparsest quadrature rule, we create a database of polynomial functions of degrees $d$ evaluated in $q_T \gg q_{GL}$ points, among which are the Gauss-Legendre quadrature points. The test is done with $q_{GL} = 10$, $d = 19$, $q_T = 2000$ and 101 polynomial functions with random coefficients taken from the normal distribution. The results are shown in Figure 5.4 with and without scaling of the dictionary.

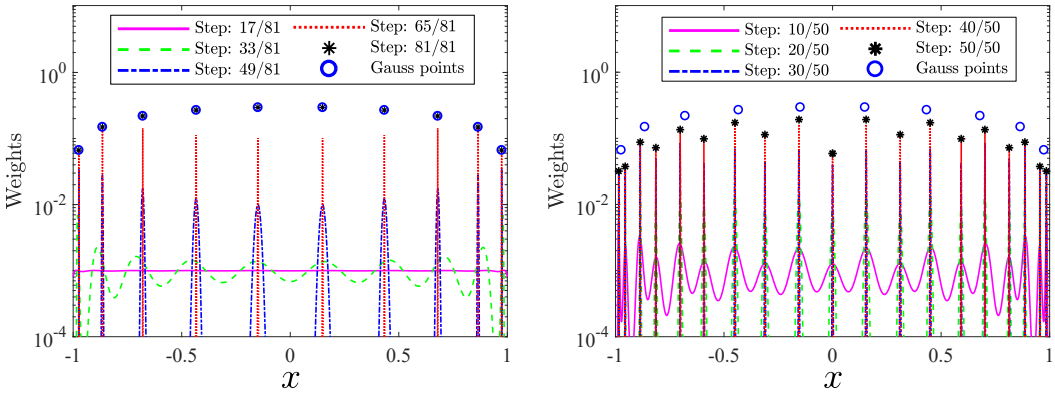


(a) No scaling (b) With scaling

Figure 5.4: Evolution of the weights of the atoms during the non-negative FOCUSS. Two cases are considered, with and without scaling of the dictionary. The initialization is done with a uniform vector. It appears that in both cases a sparse solution is found but the Gauss-Legendre quadrature is only found without scaling.

The results show that the scaling is not necessarily beneficial to find the sparsest solution. This is in fact due to the effect of the so-called basins of attraction. As said before, computing the solution with a uniform initialization but without the scaling is equivalent to scale the dictionary and using a non-uniform initialization. As the system in Equation 5.14 is underdetermined, multiple solutions exist. When using a random initialization, the solution is going to be attracted to a specific basin of attraction. Each basin is a local minimum and returns a different solution. That is why, when there is no a priori on the topology of these basins, using several random initializations

and comparing the results can be the more efficient approach. In the test case, it appears that the uniform initialization and scaling the dictionary converges to a non-optimal basin of attraction. However, initializing with the norm of the atoms and scaling the dictionary leads to the Gauss-Legendre quadrature points. More discussion on the basin of attraction can be found in [106].

**Comparison with other methods** We compare the ability of the nnFOCUSS to find the Gauss-Legendre quadrature with the algorithms used in the literature. The dictionary is not scaled. We consider the empirical interpolation method (EIM) [17], the heuristic method described in [123] and the dual simplex method [215]. The results are shown in Figure 5.5. It appears that the sole algorithm able to find the Gauss-Legendre quadrature rule is the nnFOCUSS. Moreover, as discussed in Chapter 4 Section 4.2, the approach based on the EIM is not suited as negative weights are returned. Consequently, from this test case, we can assume that the nnFOCUSS algorithm is well-suited to find reduced quadrature rules and we use it afterward to find RIDs.

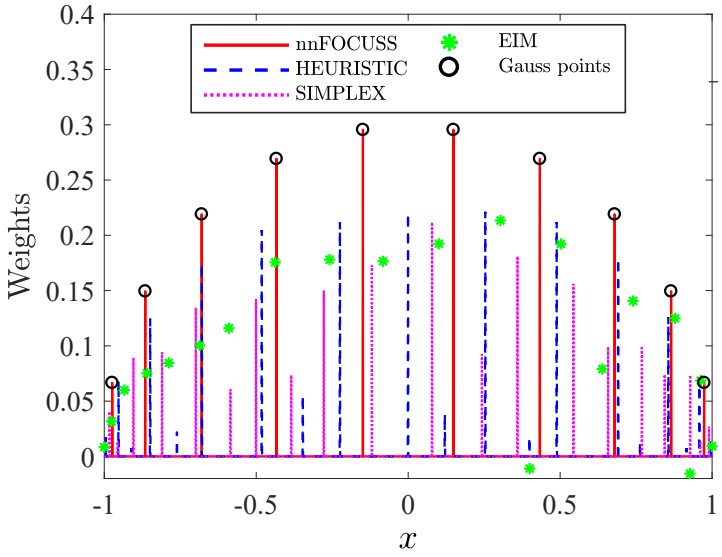


Figure 5.5: Sparse quadrature rule obtained with the nnFOCUSS, heuristic, simplex, and EIM algorithms. Only the nnFOCUSS is able to recover the Gauss-Legendre quadrature rule. Also, as discussed in Chapter 4 Section 4.2, the EIM returns negative values, hence it does not respect the positivity condition.

### 5.3.4 Energy minimization procedure

**Application of the POD** As said in Section 5.2.3, the solution of the mechanical equilibrium equation for hyperelastic materials is the stationary point of Equation 5.6 with respect to the displacement $\boldsymbol{u}$. Thanks to Equation 5.10, this assertion can be written as

$$\hat{\boldsymbol{u}} = \boldsymbol{\Phi}_r \times \arg\min_{\boldsymbol{\alpha}} \Pi(\boldsymbol{\alpha}) \,. \tag{5.20}$$

The minimization of the strain energy $\Pi$ is now done with respect to the parameters $\alpha_i$. The minimization method is accelerated further using hyperreduction, as detailed below.

**Application of the hyperreduction** Equations 5.1, 5.2, 5.3, 5.4 and 5.5 are used to compute the value of the strain energy density $\Psi$ from the knowledge of the vector $\boldsymbol{\alpha}$. As only a pressure $P$ is considered the total potential energy expression (see Equation 5.6) reads

$$\Pi = \int_{\Omega} \Psi(\boldsymbol{u})\, d\Omega + \int_{\partial\Omega} P\boldsymbol{n} \cdot \boldsymbol{u}\, d\partial\Omega \tag{5.21}$$

Moreover, as linear tetrahedron elements are used the strain energy density is constant per element and one gauss point is used per tetrahedron. The discrete version of Equation 5.21 is:

$$\Pi = \sum_{e=1}^{n_e} \Psi_e V_e + P \sum_{e=1}^{n'_e} \boldsymbol{n}_e \cdot \boldsymbol{u}_e \,, \tag{5.22}$$

where $\Psi_e$ is the strain energy density of the $e$-th element, $V_e$ its volume, and $n_e$ is the number of tetrahedra. $n'_e$ is the number of quadrature points belonging to the surface where the pressure is applied and $\boldsymbol{n}_e$ (resp. $\boldsymbol{u}_e$) is the normal (resp. displacement) in these points. Three Gauss points are used per triangle. The hyperreduction is then used to find a new RID $\Omega_r \subset \Omega$. That means that a subset of quadrature points where the strain energy and the pressure work need to be computed is selected and associated with new weights such that

$$\Pi = \sum_{e=1}^{n_1^{hr}} \Psi_e d_1^e + P \sum_{e=1}^{n_2^{hr}} \boldsymbol{n}_e \cdot \boldsymbol{u}_e d_2^e \tag{5.23}$$

where $n_{hr} = n_1^{hr} + n_2^{hr} \ll n_e + n'_e$ is the number of integration points and $(d_1^e, d_2^e) \in (\mathbb{R}_*^+)^2$ are the new weights.

The minimization is now done with respect to only $r$ parameters and the computations are accelerated further using only $n_{hr}$ integration points. Any optimization solver can be used to solve the problem.

**Remark 5.2** (*Computation of the domain* $\Omega_r$). The computation of the domain $\Omega_r$ is not straightforward as there is no constraint on the choice of the position of the quadrature points. In the case of imposed boundary conditions, such as the pressure or a displacement, it is necessary to take into account the nodes where the constraint is imposed. If none of the elements belonging to the RID contains one of these nodes the boundary conditions will not "be seen" by the strain energy and the trivial solution will be $\boldsymbol{u} = \boldsymbol{0}$. That is why two integration domains are defined. The first, $\Omega^b$, contains all the elements that have a least one of their nodes belonging to the boundary conditions. In the case of a pressure, it will be the surface elements. In the case of Dirichlet conditions, it will be volumetric elements. The other domain is defined by $\Omega^o = \Omega \cap \overline{\Omega^b}$. Hyperreduction is done on each domain separately to find the local RIDs $\Omega_r^b$ and $\Omega_r^o$. The whole RID is then defined as $\Omega_r = \Omega_r^b \cup \Omega_r^o$

**Minimization method** A thorough review of numerical optimization methods can be found in [205]. In this thesis, a quasi-Newton algorithm is used. The algorithm is available on Matlab with the function fminunc. This is an iterative method used to find zeros or local extrema when the Jacobian or Hessian is unavailable or difficult to compute. Here the Jacobian is provided to increase the computational speed. Finding the minimum of the strain energy function $\Pi$ comes to find the zero of its derivative. As in Newton's method, at iteration $k$ the second-order approximation of the function at the point $\boldsymbol{\alpha}_k$ is evaluated. Using the Taylor expansion it reads

$$\Pi\left(\boldsymbol{\alpha}_{k+1}\right) \approx \Pi\left(\boldsymbol{\alpha}_k\right) + \boldsymbol{\nabla}\Pi\left(\boldsymbol{\alpha}_k\right)^T \Delta\boldsymbol{\alpha}_k + \frac{1}{2}\Delta\boldsymbol{\alpha}_k^T \mathbf{B}_k \Delta\boldsymbol{\alpha}_k \,, \tag{5.24}$$

where $\mathbf{B}_k$ is the hessian matrix and $\Delta\boldsymbol{\alpha}_k = \boldsymbol{\alpha}_{k+1} - \boldsymbol{\alpha}_k$. The gradient of the function is then written

$$\boldsymbol{\nabla}\Pi\left(\boldsymbol{\alpha}_{k+1}\right) \approx \boldsymbol{\nabla}\Pi\left(\boldsymbol{\alpha}_k\right) + \mathbf{B}_k \Delta\boldsymbol{\alpha}_k \,. \tag{5.25}$$

Assuming the nullity of the gradient in $\boldsymbol{\alpha}_{k+1}$ leads to

$$\boldsymbol{\alpha}_{k+1} = \boldsymbol{\alpha}_k \underbrace{-\mathbf{B}_k^{-1} \boldsymbol{\nabla}\Pi\left(\boldsymbol{\alpha}_k\right)}_{\boldsymbol{p}_k} , \tag{5.26}$$

$\boldsymbol{p}_k$ is called the descent direction. Solving Equation 5.26 requires to compute the inverse of the Hessian. In the quasi-Newton algorithm this value is approximated under the assumption

that Equation 5.25 is a strict equality, which is called the *secant equation* (this is the first-order Taylor expansion of the gradient). Several methods exist to compute this value, here the Broyden–Fletcher–Goldfarb–Shanno (BFGS) algorithm is used. This method offers the advantage to produce positive definite Hessian approximation if the initial guess is positive definite. By introducing $\boldsymbol{\delta}_k = \boldsymbol{\nabla}\Pi\left(\boldsymbol{\alpha}_{k+1}\right) - \boldsymbol{\nabla}\Pi\left(\boldsymbol{\alpha}_k\right)$, at each iteration of the quasi-Newton algorithm the Hessian is updated following

$$\mathbf{B}_{k+1} = \mathbf{B}_k + \frac{\boldsymbol{\delta}_k \boldsymbol{\delta}_k^T}{\boldsymbol{\delta}_k^T \Delta\boldsymbol{\alpha}_k} - \frac{\mathbf{B}_k \Delta\boldsymbol{\alpha}_k \left(\mathbf{B}_k \Delta\boldsymbol{\alpha}_k\right)^T}{\Delta\boldsymbol{\alpha}_k^T \mathbf{B}_k \Delta\boldsymbol{\alpha}_k} \,. \tag{5.27}$$

Using the Sherman-Morison formula the inverse can be directly computed as

$$\mathbf{B}_{k+1}^{-1} = \left(\mathbf{I} - \frac{\Delta\boldsymbol{\alpha}_k \boldsymbol{\delta}_k^T}{\boldsymbol{\delta}_k^T \Delta\boldsymbol{\alpha}_k}\right) \mathbf{B}_k^{-1} \left(\mathbf{I} - \frac{\boldsymbol{\delta}_k \Delta\boldsymbol{\alpha}_k^T}{\boldsymbol{\delta}_k^T \Delta\boldsymbol{\alpha}_k}\right) + \frac{\Delta\boldsymbol{\alpha}_k \Delta\boldsymbol{\alpha}_k^T}{\boldsymbol{\delta}_k^T \Delta\boldsymbol{\alpha}_k} \,. \tag{5.28}$$

**Remark 5.3** (*Line search*). In general, Equation 5.26 is written

$$\boldsymbol{\alpha}_{k+1} = \boldsymbol{\alpha}_k + \beta_k \boldsymbol{p}_k \,, \tag{5.29}$$

where $\beta_k \in \mathbb{R}^+$ is the line search step. It determines how far $\boldsymbol{\alpha}$ should move along the descent direction. It is chosen so as so "loosely" minimizing $\Pi(\boldsymbol{\alpha}_k + \beta_k \boldsymbol{p}_k)$. Several methods exist, for example, in this thesis the Golden section search is employed in Chapter 2.

The convergence is considered to be reached when $||\boldsymbol{\nabla}\Pi\left(\boldsymbol{\alpha}_{k+1}\right)||_\infty < h_g$ and $|\boldsymbol{\alpha}_{k+1} - \boldsymbol{\alpha}_k| < h_s(1 + |\boldsymbol{\alpha}_k|)$ where $h_g$ and $h_s$ are thresholds defined by the user. The first inequality corresponds to the fact that the gradient must be null at a minimum point. The second one ensures that the variations of the parameters are small between two consecutive steps.

## 5.4 Extended Kalman filter

We have shown how the mathematical model can be accelerated thanks to MOR. To adapt it to the measurements we integrate the ROM within an EKF. The KF is a common way to solve inverse problems [294]. In its original form, it is suited to solve linear problems with stochastic parameters belonging to normal distributions. It has been developed to solve nonlinear problems with its extended and unscented versions. Here we focus on the extended version for discrete-time measurements (an introduction of the KF and EKF can be found in [237]). In this section, the pieces of advice from [253] are followed in order to increase the filter's stability. An overview of the method is provided in Figure 5.6.

### 5.4.1 General formulation

Let $k$ denote the $k$-th temporal measure. The initial assumption is that the process $\boldsymbol{x} \in \mathbb{R}^n$ is described by a nonlinear stochastic equation involving the differentiable function $g$ so as so

$$\boldsymbol{x}_{k+1} = g(\boldsymbol{x}_k, \boldsymbol{u}_k) + \boldsymbol{w}_k \tag{5.30}$$

with a measurement $\boldsymbol{y} \in \mathbb{R}^r$ that is also described by a nonlinear stochastic equation involving the differentiable function $h$ that reads

$$\boldsymbol{y}_{k+1} = h(\boldsymbol{x}_k) + \boldsymbol{v}_k \tag{5.31}$$

where $\boldsymbol{u}$ is an optional control input and the random variables $\boldsymbol{w} \in \mathbb{R}^n$ and $\boldsymbol{v} \in \mathbb{R}^r$ represent the process and measurement noises such as

$$\begin{aligned} \boldsymbol{w}_k &\sim \mathcal{N}(\mathbf{0}, \mathbf{Q}_k) \\ \boldsymbol{v}_k &\sim \mathcal{N}(\mathbf{0}, \mathbf{R}_k) \,. \end{aligned}$$

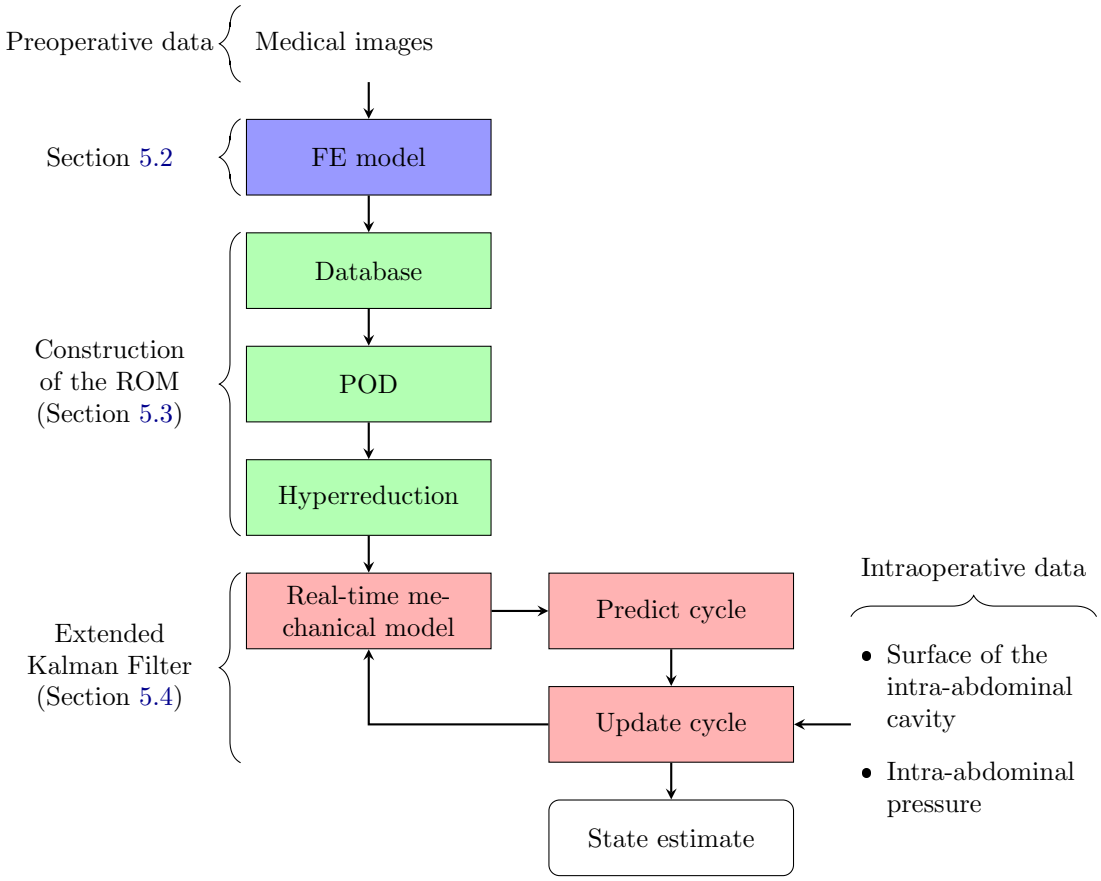


Figure 5.6: Flowchart of the EKF (in red) with the detail of the construction of the ROM (in green). Each stage is detailed in the corresponding section.

$\mathbf{Q}_k$ (resp. $\mathbf{R}_k$) corresponds to the process (resp. measurement) noise covariance matrix. Here the measurement noise is supposed to be time-invariant, thus $\mathbf{R}_k = \mathbf{R}_0$. The filter aims at predicting the state of the system given a collection of measurements $\mathcal{Y}_k = \{\boldsymbol{y}_1, \cdots, \boldsymbol{y}_k\}$. The idea is to propagate the conditional probability density function $p(\boldsymbol{x}_k|\mathcal{Y}_k, \boldsymbol{u}_{k-1})$ to $p(\boldsymbol{x}_{k+1}|\mathcal{Y}_{k+1}, \boldsymbol{u}_k)$. For standard KF these distributions are Gaussian, that allows evaluating their first and second moments quite straightforwardly as the transformation of a normal distribution by a linear function is still normal. However, in the case of nonlinear functions the output distribution is unknown. Hence, the knowledge of the statistical moments requires to compute the entire probability density function. To avoid this computational burden the extended version of the KF proposes to linearize the system around the last state estimator using a Taylor expansion. Once the system is linearized the standard KF approach is used. One iteration of the EKF follows these different steps:

- Consider the last state estimate $\boldsymbol{x}(k|k)$
- Linearize Equation 5.30 around $\boldsymbol{x}(k|k)$
- Predict the state and covariance estimate $\boldsymbol{x}(k+1|k)$ and $\mathbf{P}(k+1|k)$
- Linearize Equation 5.31 around $\boldsymbol{x}(k+1|k)$
- Update the state and covariance estimate $\boldsymbol{x}(k+1|k+1)$ and $\mathbf{P}(k+1|k+1)$.

To perform the linearizations, the Jacobians of $g$ and $h$ are introduced as

$$\begin{aligned} \mathbf{G}(k) &= \nabla g|_{\boldsymbol{x}(k|k)} \\ \mathbf{H}(k+1) &= \nabla h|_{\boldsymbol{x}(k+1|k)} \end{aligned}. \tag{5.32}$$

The prediction and updating steps read

**Predict cycle**

$$\begin{aligned} \boldsymbol{x}(k+1|k) &= g(\boldsymbol{x}(k|k), \boldsymbol{u}_k) \\ \mathbf{Q}(k) &= \mathbf{G}(k)\mathbf{Q}_0\mathbf{G}^T(k) \\ \mathbf{P}(k+1|k) &= \mathbf{G}(k)\mathbf{P}(k|k)\mathbf{G}^T(k) + \mathbf{Q}(k) \end{aligned} \tag{5.33}$$

**Update cycle**

$$\begin{aligned} \mathbf{K}(k+1) &= \mathbf{P}(k+1|k)\mathbf{H}^T(k+1)\left[\mathbf{H}(k+1)\mathbf{P}(k+1|k)\mathbf{H}^T(k+1) + \mathbf{R}_0\right]^{-1} \\ \boldsymbol{x}(k+1|k+1) &= \boldsymbol{x}(k+1|k) + \mathbf{K}(k+1)\left[\boldsymbol{y}_{k+1} - h(\boldsymbol{x}(k+1|k))\right] \\ \mathbf{P}(k+1|k+1) &= \left[\mathbf{I} - \mathbf{K}(k+1)\mathbf{H}(k+1)\right]\mathbf{P}(k+1|k)\left[\mathbf{I} - \mathbf{K}(k+1)\mathbf{H}(k+1)\right]^T + \\ &\quad \mathbf{K}(k+1)\mathbf{R}_0\mathbf{K}(k+1)^T \end{aligned} \tag{5.34}$$

where $\mathbf{I}$ is the identity matrix and $\mathbf{Q}_0$ is the baseline process noise covariance matrix. Because the EKF is based on approximation of the system it offers no guarantee of optimality. The computed covariance estimate $\mathbf{P}$ is solely an approximation. Moreover, many wrong consecutive linearizations can lead to the divergence of the method. However, it has been proven efficient for many systems and allows fast computations when the Jacobian of the nonlinear functions is easily computable. In this chapter, we compute it analytically.

**Remark 5.4** (*Predict cycle implementation*). In the predict cycle, the update of the process noise covariance (second step in Equation 5.33) is usually not included. This matrix is usually chosen manually through a trial and error process, making its design one of the bottlenecks of the method. Valappil et al. proposed in [283] the current increment-varying formulation to adapt the process noise covariance matrix. In practice, it has been necessary to implement this update if one wants to avoid recurrent divergences.

**Remark 5.5** (*Filter cycle implementation*). In the filter cycle, the covariance measurement update (third step in Equation 5.34) is usually introduced using the formula

$$\mathbf{P}(k+1|k+1) = [\mathbf{I} - \mathbf{K}(k+1)\mathbf{H}(k+1)]\,\mathbf{P}(k+1|k)\,.$$

Here the so-called *Joseph's stabilized version* of the covariance update is used. It guarantees that $\mathbf{P}$ will always be symmetric positive definite, making the computations more robust and stable.

### 5.4.2 Extended Kalman filter for static registration in laparoscopy

**Process vector** In the EKF used for the static registration the process vector $\boldsymbol{x}$ is defined by

$$\boldsymbol{x} = (\boldsymbol{\alpha}^T, C_1, C_2, E_a, \boldsymbol{t}^T, \boldsymbol{r}^T, P)^T\,, \tag{5.35}$$

where

- $\boldsymbol{\alpha}$ are the $r$ POD's reduced degrees of freedom describing the deformation of the model,
- $C_1$ and $C_2$ are the parameters defining the Veronda-Westmann behavior of the liver,
- $E_a$ is the Young modulus of the abdominal cavity,
- $\boldsymbol{t} = (t_x, t_y, t_z)^T$ is the rigid translation of the geometry, each $t_i$ ($i \in \{x, y, z\}$) defines a translation along the axis $i$,
- $\boldsymbol{r} = (r_x, r_y, r_z)^T$ is the rigid rotation of the geometry defined w.r.t the barycenter of the mesh, each $r_i$ ($i \in \{x, y, z\}$) defines an angle of rotation around the axis $i$,
- $P$ is the input pressure.

The material parameters $E_t = 50\,\text{kPa}$ and $\nu_t = 0.43$ (from [132]) defining the tumor elastic behavior and the Poisson ratio $\nu_a = 0.49$ of the abdominal cavity are supposed to be known. They are not considered as stochastic parameters. For the tumor, this is justified by the fact that its surrounding area (i.e. the liver) is softer, hence the tumor does not deform much under the pressure. The abdominal cavity is considered as incompressible, its Poisson ratio is consequently near to 0.5.

**Process function** The model function $g$ then reads

$$g(\boldsymbol{x}) = \begin{bmatrix} \hat{\boldsymbol{\alpha}} = \arg\min_{\boldsymbol{\alpha}} \Pi(\boldsymbol{\alpha}) \\ C_1 \\ C_2 \\ E_a \\ \boldsymbol{t} \\ \boldsymbol{r} \\ P \end{bmatrix}. \tag{5.36}$$

**Process function derivative** To compute the gradient of $g$, the problematic of computing the derivative of $\hat{\boldsymbol{\alpha}}$ with respect to the other parameters must be addressed. Let introduce a generic variable $\theta \in \mathbb{R}$ such as

$$\hat{\boldsymbol{\alpha}} = \arg\min_{\boldsymbol{\alpha}} \Pi(\boldsymbol{\alpha}; \theta)\,. \tag{5.37}$$

This latter equation is equivalent to

$$\nabla_{\boldsymbol{\alpha}} \Pi(\boldsymbol{\alpha}; \theta)|_{\hat{\boldsymbol{\alpha}}} = \mathbf{0} \quad \forall \hat{\boldsymbol{\alpha}} \in \mathcal{S}_{\hat{\boldsymbol{\alpha}}}\,, \quad \forall \theta \in \mathbb{R} \tag{5.38}$$

where $\mathcal{S}_{\hat{\boldsymbol{\alpha}}}$ is the space of the solution of Equation 5.37. The infinitesimal variation of Equation 5.38 reads

$$d\mathbf{J}(\boldsymbol{\alpha};\theta) = \frac{\partial \mathbf{J}(\boldsymbol{\alpha};\theta)}{\partial \alpha_1} d\alpha_1 + \cdots + \frac{\partial \mathbf{J}(\boldsymbol{\alpha};\theta)}{\partial \alpha_r} d\alpha_r + \frac{\partial \mathbf{J}(\boldsymbol{\alpha};\theta)}{\partial \theta} d\theta \,. \tag{5.39}$$

where $\mathbf{J}(\boldsymbol{\alpha};\theta) = \boldsymbol{\nabla}_{\boldsymbol{\alpha}} \Pi(\boldsymbol{\alpha};\theta)$ is the Jacobian matrix of $\Pi$ with respect to $\boldsymbol{\alpha}$. This variation being null in the vicinity of $\hat{\boldsymbol{\alpha}}$ it arises

$$\frac{\partial \mathbf{J}(\boldsymbol{\alpha};\theta)}{\partial \hat{\alpha}_1} \frac{d\hat{\alpha}_1}{d\theta} + \cdots + \frac{\partial \mathbf{J}(\boldsymbol{\alpha};\theta)}{\partial \hat{\alpha}_r} \frac{d\hat{\alpha}_r}{d\theta} = -\frac{\partial \mathbf{J}(\boldsymbol{\alpha};\theta)}{\partial \theta} \,. \tag{5.40}$$

which can be written

$$\mathbf{B}(\boldsymbol{\alpha};\theta) \frac{d\hat{\boldsymbol{\alpha}}}{d\theta} = -\frac{\partial \mathbf{J}(\boldsymbol{\alpha};\theta)}{\partial \theta} \,, \tag{5.41}$$

where $\mathbf{B}(\boldsymbol{\alpha};\theta) = \boldsymbol{\nabla}^2_{\boldsymbol{\alpha}} \Pi(\boldsymbol{\alpha};\theta)$ is the Hessian matrix of $\Pi$ with respect to $\boldsymbol{\alpha}$. Thus

$$\frac{d\hat{\boldsymbol{\alpha}}}{d\theta} = -\mathbf{B}(\boldsymbol{\alpha};\theta)^{-1} \frac{\partial \mathbf{J}(\boldsymbol{\alpha};\theta)}{\partial \theta} \,. \tag{5.42}$$

Note that if $\hat{\boldsymbol{\alpha}}$ depends on a set of parameters $\theta_i$ but that these latter are not dependent on one another, then $\frac{d\hat{\boldsymbol{\alpha}}}{d\theta_i} = \frac{\partial \hat{\boldsymbol{\alpha}}}{\partial \theta_i}$.

**Remark 5.6** (*Implicit function theorem*). The result from Equation 5.42 could have been derived from the implicit function theorem. This latter states:

" Let consider

$$\begin{array}{rccc} f: & \mathbb{R}^{n+m} & \to \mathbb{R}^m \\ & (\boldsymbol{x},\boldsymbol{y}) & \to f(\boldsymbol{x},\boldsymbol{y}) \end{array} \tag{5.43}$$

be a continuously differentiable function and $(\boldsymbol{a},\boldsymbol{b}) = (a_1,\cdots,a_n,b_1,\cdots,b_m)$ be a point such that $f(\boldsymbol{a},\boldsymbol{b}) = 0$. If the Jacobian matrix of $f$ with respect to $\boldsymbol{y}$ in $(\boldsymbol{a},\boldsymbol{b})$, noted $\mathbf{J}_{f,\boldsymbol{y}}(\boldsymbol{a},\boldsymbol{b})$, is invertible then there exist an open set $U$ of $\mathbb{R}^n$ containing $\boldsymbol{a}$ such that there exists a unique continuously differentiable function $g: U \to \mathbb{R}^m$ such that $g(\boldsymbol{a}) = \boldsymbol{b}$ and $f(\boldsymbol{x}, g(\boldsymbol{x})) = \mathbf{0} \quad \forall \boldsymbol{x} \in U$. Moreover, the partial derivatives of $g$ in $U$ are given by

$$\frac{\partial g}{\partial x_j}(\boldsymbol{x}) = -\left[\mathbf{J}_{f,\boldsymbol{y}}(\boldsymbol{x}, g(\boldsymbol{x}))\right]^{-1} \left[\frac{\partial f}{\partial x_j}(\boldsymbol{x}, g(\boldsymbol{x}))\right] \text{ ". } \tag{5.44}$$

To apply this theorem to the presented application, one would have to take $\boldsymbol{x} = \theta$, $\boldsymbol{y} = \boldsymbol{\alpha}$ and

$$\begin{array}{ll} f: (\boldsymbol{x},\boldsymbol{y}) & \to \nabla_{\boldsymbol{y}} \Pi(\boldsymbol{y};\boldsymbol{x}) \\ g: \theta & \to \hat{\boldsymbol{\alpha}} \,. \end{array} \tag{5.45}$$

Finally, the gradient of $g$ reads

$$\mathbf{G} = \begin{bmatrix} \mathbf{0}_{r\times r} & \frac{d\hat{\boldsymbol{\alpha}}}{dC_1} & \frac{d\hat{\boldsymbol{\alpha}}}{dC_2} & \frac{d\hat{\boldsymbol{\alpha}}}{dE_a} & \mathbf{0}_{r\times 1} & \mathbf{0}_{r\times 1} & \mathbf{0}_{r\times 1} & \mathbf{0}_{r\times 1} & \mathbf{0}_{r\times 1} & \mathbf{0}_{r\times 1} & \frac{d\hat{\boldsymbol{\alpha}}}{dP} \\ \mathbf{0}_{1\times r} & 1 & 0 & 0 & 0 & 0 & 0 & 0 & 0 & 0 & 0 \\ \mathbf{0}_{1\times r} & 0 & 1 & 0 & 0 & 0 & 0 & 0 & 0 & 0 & 0 \\ \mathbf{0}_{1\times r} & 0 & 0 & 1 & 0 & 0 & 0 & 0 & 0 & 0 & 0 \\ \mathbf{0}_{1\times r} & 0 & 0 & 0 & 1 & 0 & 0 & 0 & 0 & 0 & 0 \\ \mathbf{0}_{1\times r} & 0 & 0 & 0 & 0 & 1 & 0 & 0 & 0 & 0 & 0 \\ \mathbf{0}_{1\times r} & 0 & 0 & 0 & 0 & 0 & 1 & 0 & 0 & 0 & 0 \\ \mathbf{0}_{1\times r} & 0 & 0 & 0 & 0 & 0 & 0 & 1 & 0 & 0 & 0 \\ \mathbf{0}_{1\times r} & 0 & 0 & 0 & 0 & 0 & 0 & 0 & 1 & 0 & 0 \\ \mathbf{0}_{1\times r} & 0 & 0 & 0 & 0 & 0 & 0 & 0 & 0 & 1 & 0 \\ \mathbf{0}_{1\times r} & 0 & 0 & 0 & 0 & 0 & 0 & 0 & 0 & 0 & 1 \end{bmatrix} , \tag{5.46}$$

where $\mathbf{0}_{i\times j}$ indicates a $i \times j$ matrix containing zeros. The Hessian matrix and the different derivatives of the Jacobian matrix are analytically computed.

**Measurement vector** The measurement vector contains the positions of the nodes obtained through the SLAM 3D points acquisition method and the pressure. We suppose that the acquisition is only done on the model's surface where the pressure is applied. Assuming the acquisition of $M \in \mathbb{N}^*$ nodes, the measurement vector reads

$$\boldsymbol{y}_k = \begin{bmatrix} m_{1x} \\ \vdots \\ m_{Mx} \\ m_{1y} \\ \vdots \\ m_{My} \\ m_{1z} \\ \vdots \\ m_{Mz} \\ P \end{bmatrix} \tag{5.47}$$

where $\boldsymbol{m}_i = (m_{ix}, m_{iy}, m_{iz})$ with $i \in [\![1, M]\!]$ denotes the $i$-th measured points. These nodes are considered to be static during the whole registration process. However, they are randomly chosen on the surface so as so they are not located at the node of the mesh. Moreover, at each iteration of the EKF a Gaussian noise with a $\sigma_{mp} = 0.6\,\text{mm}$ standard deviation is added to the measure of the points in each axis. The choice is made considering that 95% of the points have a maximum distance error of 2 mm, thus $2 \approx \sqrt{3(1.96 * \sigma_{mp})^2}$. Finally, the liver surface concerned by the pressure is overrepresented as this is the main area of interest. To this end, three-quarters of the measured points belong to this latter. For the pressure, a $\sigma_P = 100\,\text{Pa}$ standard deviation Gaussian noise is added.

**Measurement function** The definition of the observation function $h$ is more subtle. First, as the pressure is not computed by the model, the value of the previous iteration is returned. Next, for a given process state $\boldsymbol{x}$, the POD's degrees of freedom $\boldsymbol{\alpha}$ allow reconstructing the whole mesh following $\boldsymbol{X} = \boldsymbol{X}_0 + \boldsymbol{\Phi}_r\boldsymbol{\alpha}$, where $\boldsymbol{X}_0$ is the initial mesh position and the point cloud $\boldsymbol{X} \in \mathbb{R}^{n_v \times 3}$ corresponds to $\boldsymbol{X} = (x_1, \ldots, x_{n_v}, y_1, \ldots, y_{n_v}, z_1, \ldots, z_{n_v})^T$, and $n_v$ is the number of nodes in the mesh. But, there is no correspondence between the node of the mesh and the measured points. A naive approach is employed using a brute-force point matching. It means, for each measured point, the corresponding point on the mesh is the one with the smallest Euclidean distance. This approach is not the better one as two measured points can have the same correspondence (or the other way around) but it has the advantage to be fast, which is necessary as the correspondence is done at each iteration. Prior to the correspondence, the deformed model must be rigidly registered accordingly to the translation $\boldsymbol{t}$ and the rotation $\boldsymbol{r}$. As the rotation is defined with respect to the barycenter of the mesh, noted $\boldsymbol{X}_g$, the rigidly registered mesh $\boldsymbol{X}_r$ reads

$$\boldsymbol{X}_r = \mathbf{R}(\boldsymbol{X} - \boldsymbol{X}_g) + \boldsymbol{X}_g + \boldsymbol{T} \tag{5.48}$$

where $\mathbf{R}$ is the rotation matrix defined by $\boldsymbol{r}$ and $\boldsymbol{T}$ is the translation vector defined by $\boldsymbol{t}$. For the sake of clarity, they are detailed in the case of a unique point as

$$\mathbf{R} = \mathbf{R}_x\mathbf{R}_y\mathbf{R}_z \tag{5.49}$$

where

$$\mathbf{R}_x = \begin{bmatrix} 1 & 0 & 0 \\ 0 & cos(r_x) & -sin(r_x) \\ 0 & sin(r_x) & cos(r_x) \end{bmatrix}$$

$$\mathbf{R}_y = \begin{bmatrix} cos(r_y) & 0 & sin(r_y) \\ 0 & 1 & 0 \\ -sin(r_y) & 0 & cos(r_y) \end{bmatrix}$$

$$\mathbf{R}_z = \begin{bmatrix} cos(r_z) & -sin(r_z) & 0 \\ sin(r_z) & cos(r_z) & 0 \\ 0 & 0 & 1 \end{bmatrix}$$

and

$$\mathbf{T} = \begin{bmatrix} t_x \\ t_y \\ t_z \end{bmatrix}. \tag{5.50}$$

By introducing $\mathbf{M}_m$ the point matching matrix between the measures and $\boldsymbol{X}_r$, and, $\mathbf{M}_b$ the matrix which allows computing the barycenter such as $\boldsymbol{X}_g = \mathbf{M}_b\boldsymbol{X}$, the function $h$ reads

$$h(\boldsymbol{x}) = \begin{bmatrix} \mathbf{M}_m\left[(\mathbf{R}(\mathbf{I}-\mathbf{M}_b)+\mathbf{M}_b)(\boldsymbol{X}_0+\boldsymbol{\Phi}_r\hat{\boldsymbol{\alpha}})+\boldsymbol{T}\right] \\ P \end{bmatrix} = \begin{bmatrix} h_m(\boldsymbol{x}) \\ P \end{bmatrix}. \tag{5.51}$$

**Measurement function derivative** The derivatives of $h_m$ read

$$\frac{\partial h_m}{\partial \hat{\boldsymbol{\alpha}}} = \mathbf{M}_m(\mathbf{R}(\mathbf{I}-\mathbf{M}_b)+\mathbf{M}_b)\boldsymbol{\Phi}_r \tag{5.52}$$

then

$$\frac{\partial h_m}{\partial \boldsymbol{t}} = \mathbf{M}_m \begin{bmatrix} \mathbf{1}_{n_v\times 1} & \mathbf{0}_{n_v\times 1} & \mathbf{0}_{n_v\times 1} \\ \mathbf{0}_{n_v\times 1} & \mathbf{1}_{n_v\times 1} & \mathbf{0}_{n_v\times 1} \\ \mathbf{0}_{n_v\times 1} & \mathbf{0}_{n_v\times 1} & \mathbf{1}_{n_v\times 1} \end{bmatrix} \tag{5.53}$$

and

$$\frac{\partial h_m}{\partial \boldsymbol{r}} = \mathbf{M}_m \left[\frac{\partial \mathbf{R}}{\partial r_x}, \frac{\partial \mathbf{R}}{\partial r_y}, \frac{\partial \mathbf{R}}{\partial r_z}\right](\mathbf{I}-\mathbf{M}_b)(\boldsymbol{X}_0+\boldsymbol{\Phi}_r\hat{\boldsymbol{\alpha}}) \tag{5.54}$$

where $\frac{\partial \mathbf{R}}{\partial r_i}$ $(i \in \{x, y, z\})$ can be easily computed thanks to Equation 5.49. Hence the Jacobian of $h$ is detailed as

$$\mathbf{H} = \begin{bmatrix} \frac{\partial h_m}{\partial \hat{\boldsymbol{\alpha}}} & \mathbf{0}_{3M\times 1} & \mathbf{0}_{3M\times 1} & \mathbf{0}_{3M\times 1} & \frac{\partial h_m}{\partial \boldsymbol{t}} & \frac{\partial h_m}{\partial \boldsymbol{r}} & \mathbf{0}_{3M\times 1} \\ \mathbf{0}_{1\times r} & 0 & 0 & 0 & \mathbf{0}_{1\times 3} & \mathbf{0}_{1\times 3} & 1 \end{bmatrix}. \tag{5.55}$$

**Avoiding local minima** The registered mesh can be stuck into local minima because of bad correspondences. It happens frequently if the initial registration is not good enough. In order to make the method more robust to this kind of situation, perturbations are introduced. These latter are random rotations and translations applied when the mesh appears to be stuck within a bad local minimum. To this end the mean distance

$$d_m = \frac{1}{M}\sum_{i=1}^{M} ||\boldsymbol{m}_i - h_m(\boldsymbol{x})_i||_2 \tag{5.56}$$

is introduced, where $h_m(\boldsymbol{x})_i$ is the position of the node in the deformed model's mesh corresponding to the $i$-th measured point. If the mesh is well registered, this distance should be inferior to half the mean distance between each corresponding point and its nearest neighbor on the mesh. It reads

$$t_m = \frac{1}{2M}\sum_{i=1}^{M} ||h_m(\boldsymbol{x})_i - f_{nn}(h_m(\boldsymbol{x})_i)||_2 \tag{5.57}$$

where $f_{nn}(\boldsymbol{x})$ is the function returning the nearest neighbor of the point $\boldsymbol{x}$ on the model's mesh. The division by 2 represents the fact that if some point is moving on a surface and falls between two points belonging to this latter, its distance to the nearest one is below or equal to half the distance between these points. Hence, the registration is considered to be stuck within a local minimum when $d_m > t_m$ for 40 consecutive iterations. A perturbation consists in a random translation in $[-0.2, 0.2]$ mm and a random rotation in $[-\frac{\pi}{30}, \frac{\pi}{30}]$ in each axis $x$, $y$, and $z$. The boundaries have been chosen in order to create only a slight displacement but to allow to generate a new correspondence between the points. Even though the method is quite empirical, it has been proven to be very efficient.

**Remark 5.7** (*Additional perturbations*). When the distance $d_m$ is lower than the threshold, perturbations with smaller amplitudes can still be applied. It allows finding finer local minima and does not deteriorate the final solution. However, for the sake of clarity and simplicity, we do not employ them in this chapter.

## 5.5 Validation setup

### 5.5.1 Reduced order modeling

**Dimension reduction** The EKF is validated on synthetic data. The database of simulations used for the POD has been generated with FEBio [164]. For each simulation a pressure of $2,000$ Pa was applied linearly over time. The material parameters were taken within a cartesian grid such as $C_1 \in [72.62, 99.45]$, $C_2 \in [2.62, 6.84]$ and $E_a \in [15, 25]$ kPa. For each parameter 8 values were taken within its respective range. In the end, 512 simulations were run, each one containing 100 time steps. Consequently, $51,200$ snapshots were generated. To select the number of modes used in the reduced basis, Equation 5.11 is used. The singular values are represented in Figure 7.7. It appears clearly that the true rank of the solution is around 50. However, taking so many modes is unnecessary. Using Equation 5.11 with $h = 0.995$ - this is a common value for $h$ - only 5 modes are kept.

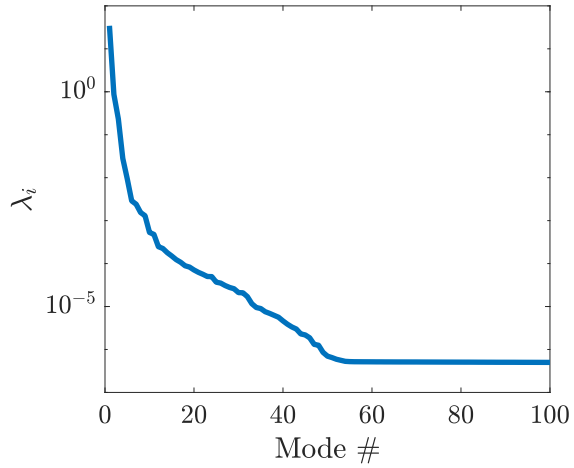


Figure 5.7: Singular values obtained with the POD applied to the database of deformations. Only the first 100 values are plotted.

**Hyperreduction** The hyperreduction is then applied. As noticed in the Remark 5.2 two RID are generated. The first is used for the computation of the strain energy and encompasses the whole set of volume elements in the mesh. After computation, only 158 quadrature points are kept over the $31,421$ points from the initial set. Among the former, 45 belong to the liver mesh,

15 to the tumor and 104 to the abdominal cavity. Figure 5.8 illustrates the reduced quadrature points position. It appears visually that the points are denser in the liver mesh. This is certainly due to the stronger nonlinearities caused by the Veronda-Westman model. Thus, more points are required to have a good approximation.

The second hyperreduction is used to compute the pressure energy and concerns only the surface element where the pressure is applied. Over $4,890$ points used for the initial quadrature only 673 are selected by the method. They are shown in Figure 5.9. Visually they seem to be uniformly distributed over the surface. This is coherent as the amplitude of the pressure is uniform over this domain and the nodes belonging to this latter have similar displacement amplitudes.

**Multistage energy minimization** The minimization procedure is not as straightforward as it seems. In Equation 5.21 it appears that the contribution of the pressure to the total potential energy functional depends on the displacement. Hence, the historic must be taken into account in order to get an accurate estimation of the pressure potential energy. To do so, the minimization process is divided into several minimizations. A simple approach is used: for a given input pressure $P$ in Pa, $n_m = \text{ceil}(\frac{P}{P_s})$ minimizations are done, where $\text{ceil}(x)$ is the function rounding $x$ to the nearest integer greater than or equal to that value and $P_s = 100\,\text{Pa}$ is the pressure step. Hence, if $P = 1.5\,\text{kPa}$, then 15 consecutive minimizations will be performed. Each minimization is initialized with the result of the previous one. The thresholds for convergence detection introduced in Section 5.3.4 are chosen such as $h_g = 10^{-10}$ and $h_s = 10^{-10}$.

### 5.5.2 Extended Kalman filter

The EKF requires the user to define several parameters, these latter are defined below. First, the ground truth used for the registration is presented.

**Ground truth** The first thing to consider is the mesh we want to register with the EKF. Here, only synthetic data are used and the ground truth is considered to be the result of a high-fidelity computation with the following parameters: $C_1 = 72.62$, $C_2 = 4.58$, $E_a = 20\,\text{kPa}$, $\boldsymbol{t} = (0, 0, 0)$, $\boldsymbol{r} = (0, 0, 0)$ and $P = 1.5\,\text{kPa}$. The Veronda-Westman parameters are taken from [63] and the Young modulus of the abdominal cavity is chosen arbitrarily.

**Initial state estimate** To initialize the EKF, the initial state guess $\boldsymbol{x}_0$ and the uncertainties about this latter, represented by its state estimate covariance matrix $\mathbf{P}_0$, must be provided. Here, the ground truth is known, thus, the uncertainty must be introduced in the initial state guess. To this end, the parameters contained in the process vector are considered bounded and their initial values are randomly chosen within their expected ranges, those representing the POD's reduced degrees of freedom excepted. These latter are always chosen to be initially null as it corresponds to the initial geometry of the model. The initial values of the material parameters are picked such as $C_{1,0} \in [50, 100]$, $C_{2,0} \in [0, 15]$ and $E_{a,0} \in [10, 30]\,\text{kPa}$. Note that these ranges are larger than the ones used to generate the training dataset, it allows to test the robustness of the model. The initial pressure is taken in $P_0 \in [1, 2]\,\text{kPa}$. The initial mesh position is supposed to be user-defined, or a least it must be located not too far from the optimal one, thus $\boldsymbol{t}_0 \in [-50, 50]^3\,\text{mm}$ and $\boldsymbol{r}_0 \in [-\frac{\pi}{3}, \frac{\pi}{3}]^3$. If the mesh is located too far from its optimal solution the risk is to fall into a wrong minimum and not to be able to correct it. Hence, in this state, the method requires a manual intervention to check the initial guess. However, as presented below the latter does not require high precision. Moreover, the task could be easily automatized using an algorithm as the iterative closest point [27]. At the end of the filter cycle of the EKF, if one of the parameters is out of its bounds its value is approximated with the nearest boundary. This approximation is useful to avoid any divergence during the first increments when the registered mesh tends to undergo large displacements and strains. Consequently, it must be ensured that the parameters' boundaries contain the ground truth solution, which is the case here. The initial state estimate covariance matrix $\mathbf{P}_0$ is arbitrarily defined as follows

$$\mathbf{P}_0 = \text{diag}(\boldsymbol{\sigma}_p^2)\,, \tag{5.58}$$

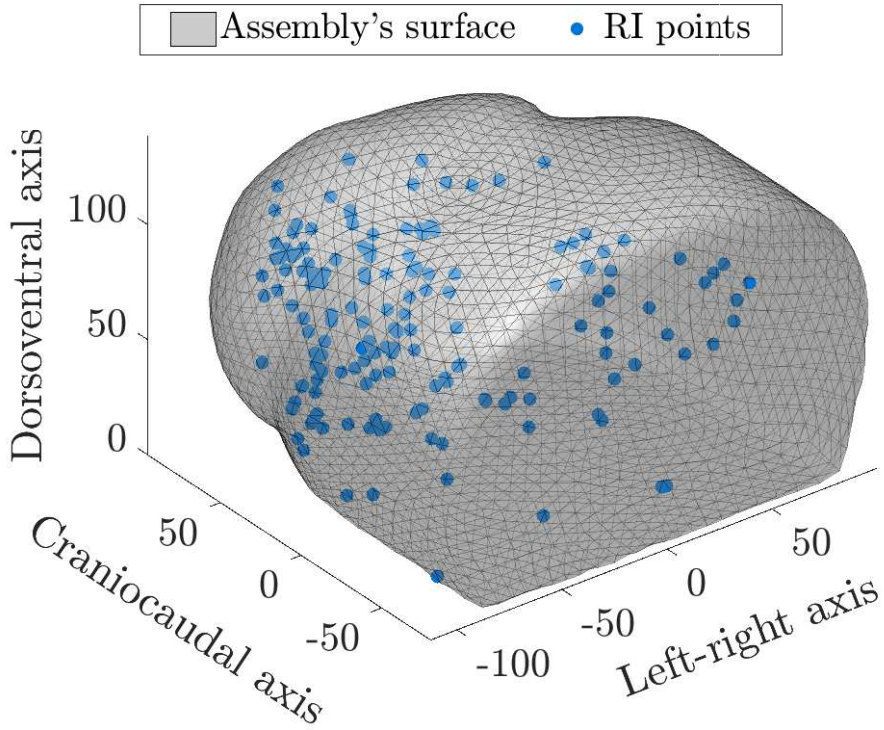


Figure 5.8: Position of the reduced integration domain's points in the assembly. It can be seen that the quadrature is more dense in the liver area.

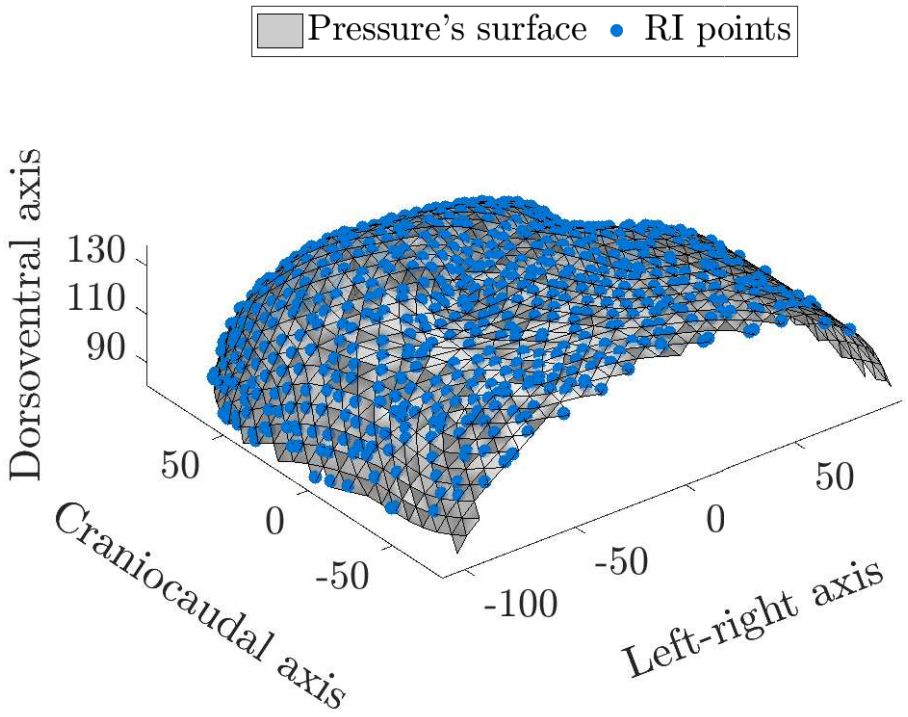


Figure 5.9: Position of the reduced integration domain's points on the pressure's surface. The quadrature points are uniformly distributed on the surface.

where diag is the diagonalization operator and

$$\boldsymbol{\sigma}_p = (5 \times \boldsymbol{\sigma}_{POD}, 1, 0.1, 5, 1, 1, 1, 0.1, 0.1, 0.1, 30)\,, \tag{5.59}$$

where the translation is expressed in millimeters, the pressure in pascal, the abdominal cavity Young modulus in kilopascal, and $\boldsymbol{\sigma}_{POD} = (\lambda_1, \cdots, \lambda_r)$ are the singular values obtained with the POD.

**Process covariance matrix** The initial process covariance matrix reads

$$\mathbf{Q}_0 = \mathrm{diag}(\boldsymbol{\sigma}_q^2)\,, \tag{5.60}$$

where diag is the diagonalization operator and

$$\boldsymbol{\sigma}_q = (\boldsymbol{\sigma}_{POD}, 0.1, 0.05, 0.1, 0.2, 0.2, 0.2, 0.2, 0.2, 0.2, 1)\,, \tag{5.61}$$

where the translation is expressed in millimeters, the pressure in pascal, and the abdominal cavity Young modulus in kilopascal. In practice, the use of the updating method (see Remark 5.4) for the process covariance matrix made the choice of these initial values less critical.

**Measurement covariance matrix** The initial measurement covariance matrix is defined as

$$\mathbf{R}_0 = \mathrm{diag}(\boldsymbol{\sigma}_r^2)\,, \tag{5.62}$$

where diag is the diagonalization operator and

$$\boldsymbol{\sigma}_r = (\sigma_{md}\mathbf{1}_{1\times 3M}, \sigma_P)\,. \tag{5.63}$$

Note that even though the measurement error is known due to the fact that synthetic data are used, $\sigma_{md} \neq \sigma_{mp}$ is employed - $\sigma_{mp}$ is the measurement noise of the position of the points in Equation 5.47. Effectively, the same standard deviation cannot be used as the correspondence between the vertices is not known. Hence, the latter must be taken into account in the measurement error of the position of the points. To do so, the distance between each measured point and its nearest neighbor is computed in the initial frame. $\sigma_{md}$ value is chosen to be the mean of this distance. The underlying idea is the following: if the correspondence between a point of the registered mesh and a measured point is bad, then the measurement error is such that there a non-negligible probability that the second nearest measured point be also a good candidate. It allows the mesh to move more freely during the registration and avoid it to be too frequently "stuck" in a local minimum caused by a bad correspondence.

**Veronda-Westman material parameters** A characteristic of the model appeared when running the first tests with the EKF: the function mapping the Veronda-Westman parameters $(C_1, C_2)$ to the POD's reduced degrees of freedom $\boldsymbol{\alpha}$ is not injective. It means two solutions with different sets of Veronda-Westman material parameters can be identical. This phenomenon is illustrated in Figure 5.10 for the first two reduced degrees of freedom. Consequently, when initializing randomly the EKF, the solution can stabilize at any couple of values $(C_1, C_2)$ satisfying the mechanical equilibrium. It means the filter cannot be used for parameter identification if both material parameters are considered as state variables or, at least, its ability to approximate the ground truth cannot be assessed. That is why the parameter $C_1$ is removed from the state vector and from its depending matrices in the rest of the chapter. Its value is fixed to the ground truth value mentioned earlier.

## 5.6 Results

### 5.6.1 Reduced order model

First of all, the ROM is validated on the ground truth case. The true pressure, materials parameters, and position of the mesh are considered known. Only the minimization detailed in Section

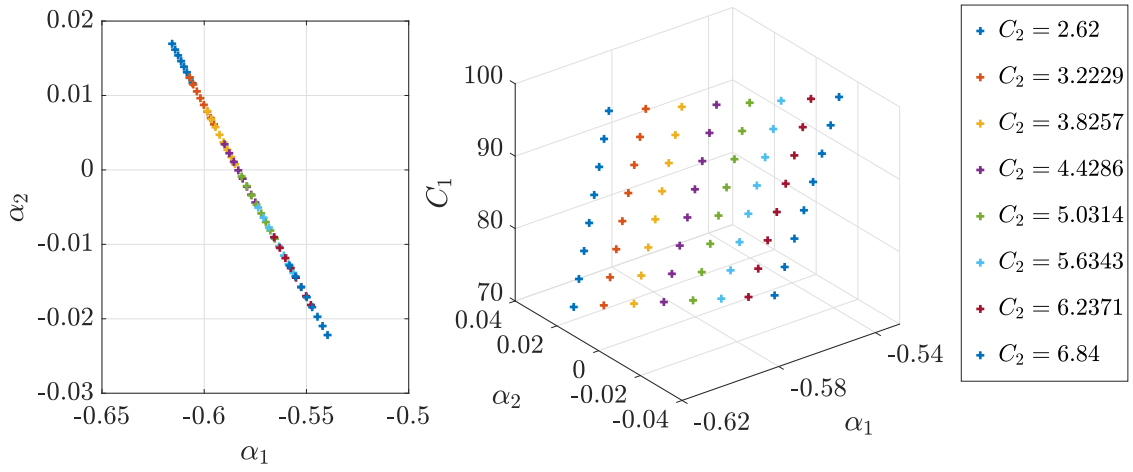


Figure 5.10: Values of the first two reduced parameters $\alpha_1$ and $\alpha_2$ computed with different Veronda-Westman material parameters under a pressure of 1.5 kPa. On the left is given a representation in the reduced parameters domain. On the right the plot relates the Veronda-Westman material parameters values with the values of the reduced parameters. It can be seen that different couples $(C_1, C_2)$ correspond to the same solution $(\alpha_1, \alpha_2)$.

5.3.4 is performed to evaluate the deformation degrees of freedom $\boldsymbol{\alpha}$. The minimization process took around 0.4 s when initialized with $\boldsymbol{\alpha} = \mathbf{0}_{r\times 1}$ against 450 s for the high fidelity computation with FEBio. To evaluate the performance of the ROM two metrics are considered, the strain energy and the volumetric overlap error (VOE). The former is written $\mathrm{SE} = \int_\Omega \Psi \, d\Omega$ (see Equations 5.1, 5.4 and 5.6), and the latter is used to evaluate the goodness of the registration of the shape. It is defined following

$$\mathrm{VOE}(A, B) = 100 \times (1 - \frac{|A \cap B|}{|A \cup B|}), \tag{5.64}$$

where $A$ and $B$ represent the compared shapes. A value of 100% means the shapes are completely dissociated and a value of 0% means they are perfectly superimposed. The pressure potential energy is not considered as FEBio cannot return it, hence there is no ground truth data to compare the results with.

The results for the strain energy are shown in Figure 5.11. The strain energy - SE - error between the ground truth and the ROM is defined as

$$100 \times \frac{|\mathrm{SE}_{\mathrm{GT}} - \mathrm{SE}_{\mathrm{ROM}}|}{|\mathrm{SE}_{\mathrm{GT}} + \epsilon|}$$

where $\epsilon = 10^{-10}$. In this case, the ROM tends to slightly overestimate the true strain energy. The relative error - as well as the absolute one - tends to increase for increasing values of $P$. Moreover, slight shifts in the error happen every 100 Pa. They are caused by the multistage minimization procedure detailed in Section 5.5.1. Without this procedure, the error would diverge for high values of $P$ because of the wrong estimation of the pressure potential energy. It is possible to improve the strain energy accuracy by reducing the pressure step. However, it would require more computations hence a compromise must be done between speed and accuracy.

The results for the VOE between the ROM solution and the ground truth are presented in Figure 5.12. A distinction is made between the VOE of the whole assembly and the one of the tumor only. Table 5.1 reports the VOE values at $P = 1.5$ kPa and also contains the VOE between the initial geometry and the ground truth in order to help the reader apprehending the extent of the deformation. These data show that the assembly is very well superimposed, with an error below 0.5%. Concerning the tumor, the error is higher but stays under 4%, which is still an accurate representation of the tumor position. The discrepancy between the two errors is due to the fact that the Veronda-Westman model involves stronger nonlinearities than the St Venant-

Kirchhoff one, hence the ROM has more difficulties to generate an accurate representation of the liver deformation.

Globally the strain energy error and the VOE are coherent and show that the ROM approximation is deteriorated with increasing pressure. More modes of deformation or more points in the RID could be used to increase the accuracy. However, it would increase the computational burden. As mentioned earlier a compromise must be done between computational speed and accuracy.

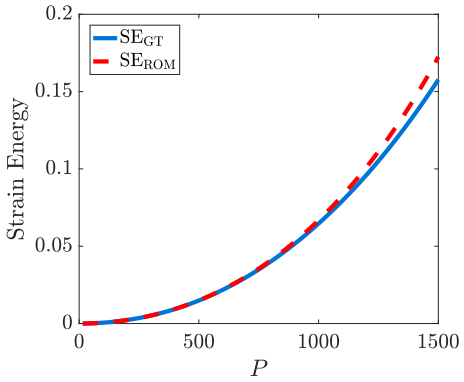


(a) Comparison of the strain energy returned by FEBio, i.e. the ground truth (GT), and the reduced order model (ROM).

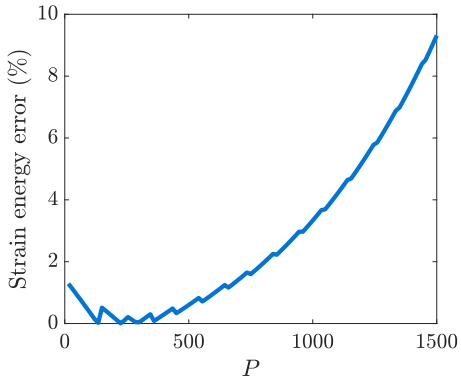


(b) Relative error in percentage between the ground truth and the ROM.

Figure 5.11: Strain energy of the model as a function of the pressure $P$.

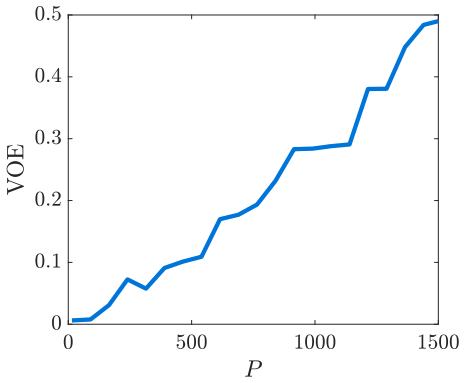


(a) VOE for the whole assembly.

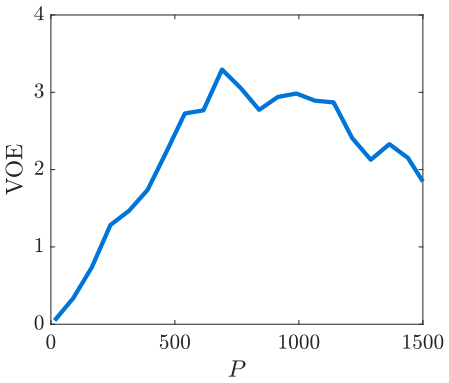


(b) VOE for the tumor only.

Figure 5.12: The VOE between the ROM solution and the ground truth is plotted. The error made on the whole assembly is very low. The one on the tumor is higher but stays acceptable.

| | Initial | Minimization |
|---|---|---|
| Assembly | 10.01% | 0.47% |
| Tumor | 79.79% | 1.87% |

Table 5.1: VOE at $P = 1.5\,\text{kPa}$ for the whole assembly and the tumor. The initial case corresponds to the undeformed geometry. It shows that without deformation of the model the tumor position would be poorly estimated, hence the necessity to use deformable models.

### 5.6.2 Extended Kalman filter

Next, the EKF results are presented over a single registration. 3,000 iterations were done. An iteration took around 0.2 s to be computed using a Matlab (The MathWorks, Inc., USA) implementation. This result can be surprising when compared to the time required to perform a minimization given in the previous section. As in the EKF the system is continuous over time, the minimization can be initialized with the values of $\boldsymbol{\alpha}$ at the previous increment. It generally offers a consequent speed-up, which is confirmed here. The initial position of the registered mesh is shown in Figure 5.13a and compared to the ground truth one. As it is shown both meshes are close to one another but are far from being ideally superimposed. The idea is to start from an initial position a user could quickly perform manually. To give an idea of the registration quality, the final position of the registered mesh is shown in Figure 5.13b.

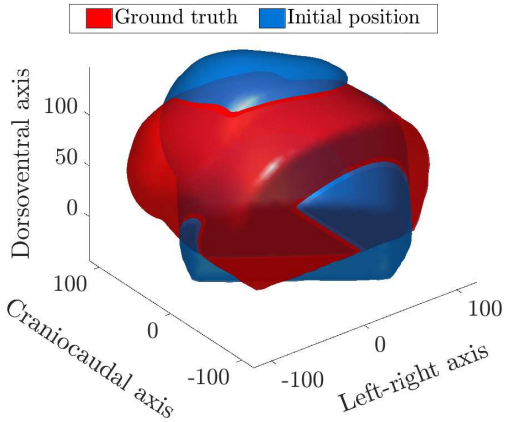


(a) Initial position of the registered mesh. Such positioning can be quickly performed manually.

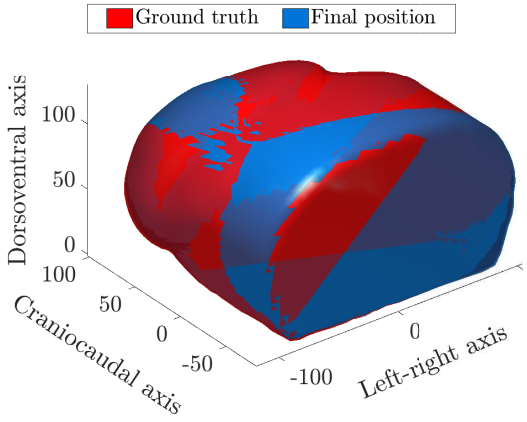


(b) Final position of the registered mesh. The difference with the ground truth is barely discernible at naked eye.

Figure 5.13: Comparison between the positions of the ground truth mesh (in blue) and the registered mesh (in red) before and after the registration.

The different variables of the process vector are plotted and commented hereafter. To begin with, the pressure is plotted in Figure 5.14. The estimated value converges near the real value after 200 iterations. Despite the strong variations of the measurements, the pressure estimation stays stable with low variance, demonstrating the robustness of this estimate.

The translation and rotation are plotted in Figure 5.15 and 5.16, respectively. Both sets of parameters follow the same trend. They undergo large variations at the beginning, followed by a stabilization near the optimal position in $\boldsymbol{t} = \mathbf{0}$ and $\boldsymbol{r} = \mathbf{0}$. The stabilization happens around 150 iterations for the rotation and 300 for the translation. The shift in the stabilizations is easily explained by the fact that the deformation caused by the pressure is more or less a translation of the upper part of the model in the dorsoventral axis. Hence, even though this deformation is badly represented, the rotation required to align the mesh is almost the same on the contrary to the translation. The estimated variances are always very low, which does not necessarily correspond to the real variations, especially at the beginning. This is probably caused by the correspondence that can be highly nonlinear, hence the EKF may have difficulties to linearize the variance accurately around these points.

The evolution of the material parameters $C_2$ and $E_a$ are plotted in Figure 5.17 and 5.18, respectively. Like the translation and rotation, they undergo important variations during the firsts iterations. They slowly stabilize between the 500-th and 1000-th increments. If the final value of the abdominal cavity's Young modulus is near from the ground truth, the Veronda-Westman parameter is quite different from the desired value. Moreover, $E_a$ has an important estimated variance and $C_2$ value is noisy even at a high number of iterations. Hence, using this EKF for parameter identification may not be pertinent. The estimation of the material parameters strongly

depends on the translation and rotation. The position of the boundary conditions depends on these latter, thus, a slight shift in the translation or the rotation can compel the material parameters to take "wrong" values. Besides, the estimation of these parameters is also dependent on the number and the position of the measured points on the surface. With a higher number of points the surface is better represented, and, with a larger surface more information can be collected. Here, as shown in Figure 5.3, only the upper part of the model is concerned by the measure. As this part mainly undergo displacements along the dorsoventral axis the information collected is not very rich. However, the visible area during laparoscopy is also limited so the model cannot be tested with too much information. Besides, adding more points during the acquisition implies computational overhead harmful to the computational speed. Once again the user must do a compromise.

The registration is evaluated by considering the position of the tumor's barycenter $\boldsymbol{d}_b$ in Figure 5.19 and the VOE of the whole assembly and of the tumor in Figure 5.20. In both figures, the convergence is reach around 200 iterations. The tumor's barycenter is registered with a precision of 2 mm, corresponding to a 17% VOE. This result is encouraging as it means that most of the tumor is well superimposed. The assembly in its totality is very well registered with a VOE around 3%.

Besides, in all the plots an important jump can be seen in the values around 50 iterations (see Figure 5.19b for example). This is caused by the procedure set up in Section 5.4.2 to avoid local minima. In this case, it also allows a faster convergence.

Finally, the EKF is run 150 times with the random initial conditions described in Section 5.5.2. As before, 3000 iterations are done in order to ensure the convergence. For each registration, the values of interest are averaged over the last 100 increments - to remove the noise - and their mean and standard deviation are reported in Table 5.2. It appears that the pressure is always estimated very precisely. The position of the mesh is most of the time correct, with a mean VOE for the tumor around 20%. Its barycenter is evaluated at approximately 2.4 mm in average. However, the material parameters are not well estimated. They tend to compensate for the positioning error and consequently converge toward wrong values. The effect is less pronounced for the abdominal cavity Young's modulus than for the Veronda-Westman parameters. The iteration number for which the tumor reaches approximately its final position, to within 1 mm, is also reported. Most of the registration converged in less than 200 iterations. By looking at the discrepancy between the median and the mean values it appears that some peculiar registrations take a lot of iterations to converge. These latter could certainly be avoided by a better initial guess.

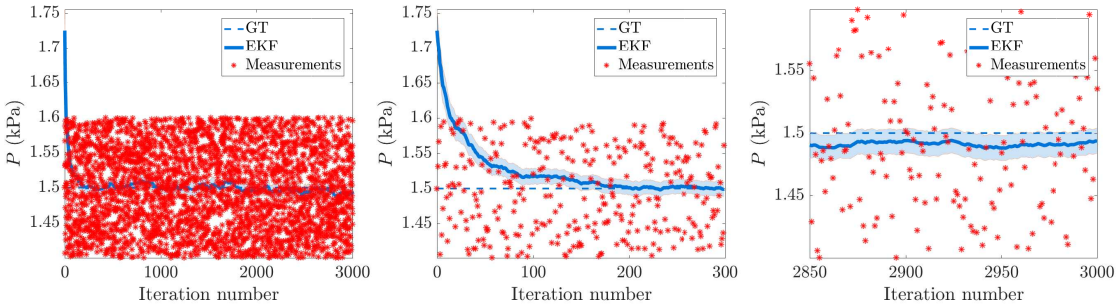


(a) All iterations. (b) Zoom over the first 300 iterations. (c) Zoom over the last 150 iterations.

Figure 5.14: Representation of the pressure during the registration process. The measured pressure at each iteration is also represented. The shading represents the estimated variance of the pressure ($\mathbf{P}_{ii}^{\frac{1}{2}}$ for the $i$-th parameter).

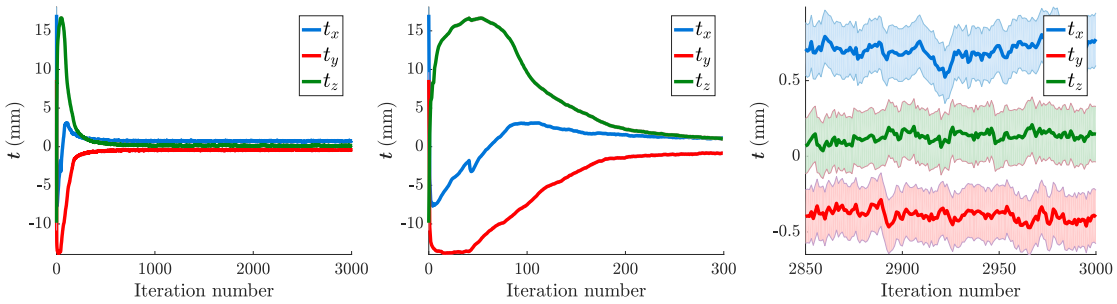


(a) All iterations. (b) Zoom over the first 300 iterations. (c) Zoom over the last 150 iterations.

Figure 5.15: Representation of the translation variables during the registration process. The shading represents the estimated variances of the corresponding process parameters ($\mathbf{P}_{ii}^{\frac{1}{2}}$ for the $i$-th parameter). $\boldsymbol{t} = \mathbf{0}_{3\times1}$ is the ground truth.

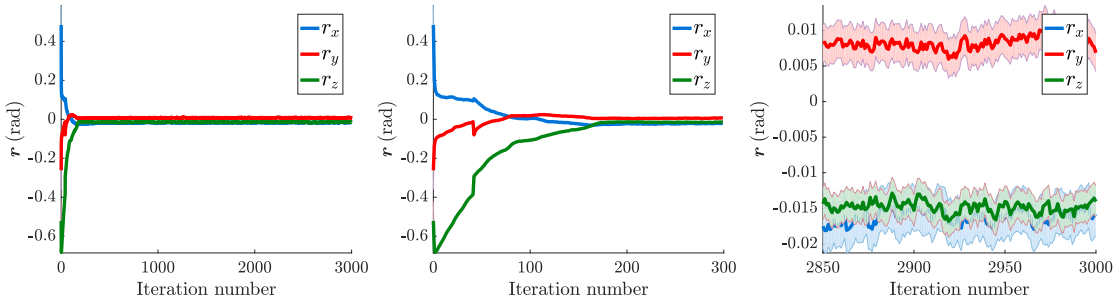


(a) All iterations. (b) Zoom over the first 300 iterations. (c) Zoom over the last 150 iterations.

Figure 5.16: Representation of the rotation variables during the registration process. The shading represents the estimated variances of the corresponding process parameters ($\mathbf{P}_{ii}^{\frac{1}{2}}$ for the $i$-th parameter). $\boldsymbol{r} = \mathbf{0}_{3\times1}$ is the ground truth.

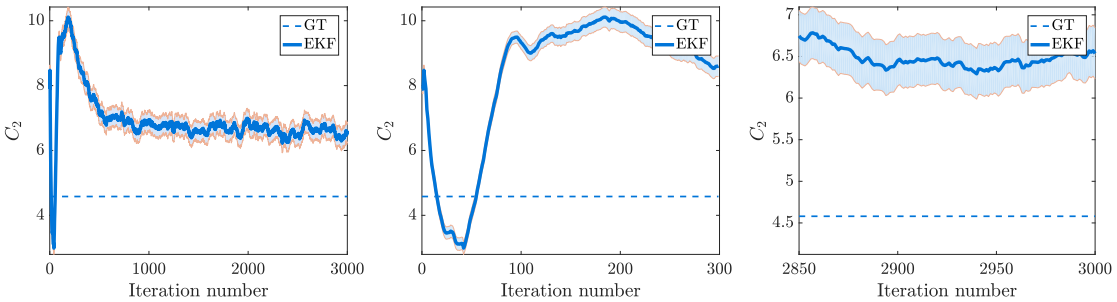


(a) All iterations. (b) Zoom over the first 300 iterations. (c) Zoom over the last 150 iterations.

Figure 5.17: Representation of the material parameter $C_2$ during the registration process. The ground truth is represented with a dotted line. The shading represents the estimated variance of $C_2$ ($\mathbf{P}_{ii}^{\frac{1}{2}}$ for the $i$-th parameter).

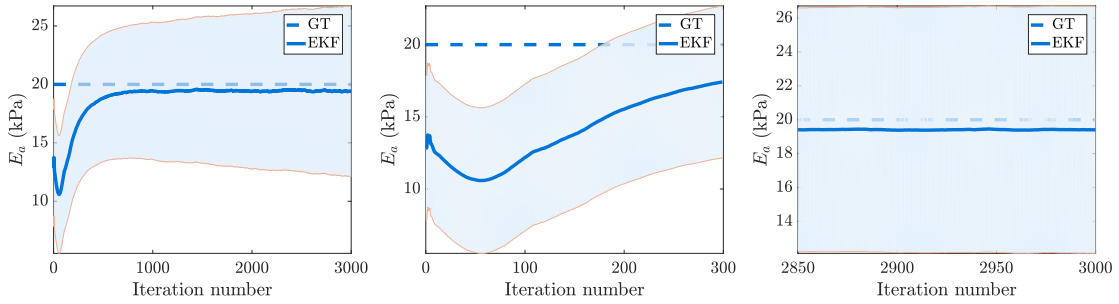


(a) All iterations. (b) Zoom over the first 300 iterations. (c) Zoom over the last 150 iterations.

Figure 5.18: Representation of the material parameter $Ea$ during the registration process. The ground truth is represented with a dotted line. The shading represents the estimated variance of $E_a$ ($\mathbf{P}_{ii}^{\frac{1}{2}}$ for the $i$-th parameter).

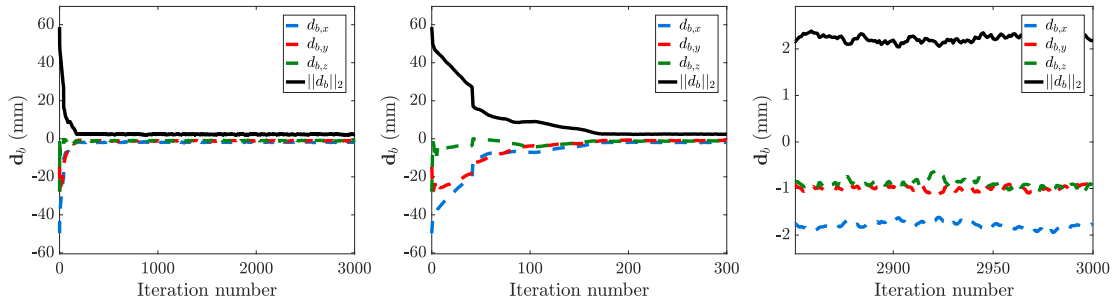


(a) All iterations. (b) Zoom over the first 300 iterations. (c) Zoom over the last 150 iterations.

Figure 5.19: Representation of the tumor's barycenter $\boldsymbol{d}_b$ during the registration process. The position along each axis is represented along with the distance to the ground truth position. The ground truth is considered to be zero for all values.

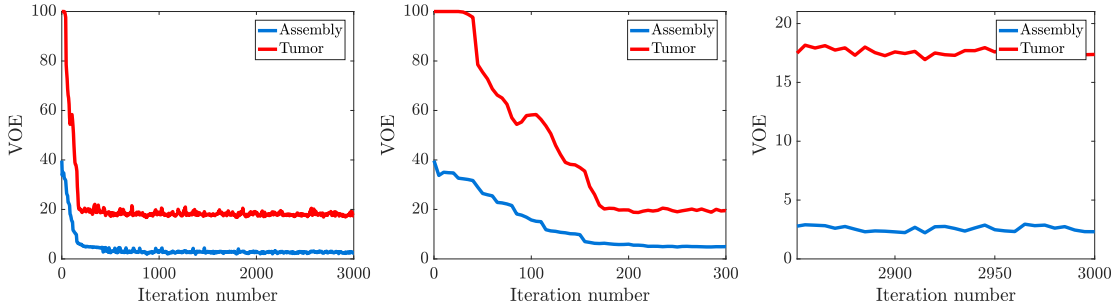


(a) All iterations. (b) Zoom over the first 300 iterations. (c) Zoom over the last 150 iterations.

Figure 5.20: Representation of the VOE of the whole assembly and of the tumor. A value of 100% means the shapes are completely dissociated and a value of 0% means they perfectly overlap. The whole assembly is very well superimposed as its error is below 4%. The tumor performs worse but the result stays acceptable, below 20% of error. This is probably due to the fact that the tumor is within the liver and that the Veronda-Westman parameter is poorly identified.

| | GT | Median | Mean | Std |
|---|---|---|---|---|
| $P$ (kPa) | 1.5 | 1.499 | 1.499 | $4 \times 10^{-3}$ |
| $C_2$ | 4.58 | 3.5 | 3.88 | 3.15 |
| $E_a$ (kPa) | 20 | 21.57 | 22.12 | 3.15 |
| $t_x$ (mm) | 0 | 0.07 | -0.12 | 1.19 |
| $t_y$ (mm) | 0 | 0.27 | 0.21 | 0.86 |
| $t_z$ (mm) | 0 | -0.52 | -0.45 | 1.10 |
| $r_x$ (rad) | 0 | $-5.8 \times 10^{-3}$ | $-6.5 \times 10^{-3}$ | $1.13 \times 10^{-2}$ |
| $r_y$ (rad) | 0 | $-2.1 \times 10^{-3}$ | $-6.7 \times 10^{-3}$ | $3.00 \times 10^{-2}$ |
| $r_z$ (rad) | 0 | $-1.1 \times 10^{-3}$ | $-2.1 \times 10^{-3}$ | $2.10 \times 10^{-2}$ |
| $\text{VOE}_{assembly}$ | 0 | 3.4 | 3.4 | 1.7 |
| $\text{VOE}_{tumor}$ | 0 | 18.0 | 18.7 | 9.8 |
| $\|\|\boldsymbol{d}_b\|\|_2$ (mm) | 0 | 2.4 | 2.5 | 1.4 |
| $\#(\|\|\boldsymbol{d}_b\|\|_2 < 1\,\text{mm})$ | / | 140 | 184 | 118 |

Table 5.2: Estimated values of interest over 150 registrations randomly initialized. The ground truth values are reported in the left column. The median, mean and standard deviation are reported in the others. The last line measures the iteration number when the value $||\boldsymbol{d}_b||_2$ converges toward its final value to within 1 mm.

## 5.7 Discussion

From the results, it arises that the presented method succeeds to register the deformable model on the ground truth quite accurately, but performs poorly when it comes to estimating the material parameters. As said earlier, the estimation of the material parameter is closely related to the estimation of the model position. Small errors can induce large discrepancies in the estimation, particularly concerning the Veronda-Westman parameter $C_2$ which appeared to be very sensitive. To improve the positioning, the most straightforward strategy would be to use landmarks detection from the operative scene. In [224] and [212] the authors use the ridge line and the falciform ligament to register semi-automatically the liver model to the intra-operative images. The methods are pinned as semi-automatic as the landmarks detection is performed manually by an operator. It would be easy to enforce the correspondence between specific points in our EKF. Such a strategy would certainly increase the robustness of the model. Indeed, if the correspondence of some points was already known then local minima could be avoided. However, the algorithm would not be unsupervised anymore. From the opposite perspective, the variability of the material parameters' estimation shows that a strong identification could be harmful to the quality of the registration. Indeed, the EKF finds the set of parameters that allows the best fit of the surfaces and, in this application, succeeds to find good results even with poor estimations of the material parameters. If these latter were predetermined, the filter may be unable to adapt the augmented scene and would stay stuck more often in local minima due to measurement or correspondence errors. It would probably be even more visible on real medical data where the correspondence's discrepancy between the model and the data would be bigger.

A second way to improve the method would be to use different boundary conditions. In [212] the gravity is also taken into account. As only synthetic data were used for our validation it had no impact, but to validate the model on a real setup it may be necessary to model the effect of gravity. This latter would require to adapt slightly the method as the gravity and the rotation variables would be dependent. Moreover, the gravity direction should be added to the measures. The dependence between the rotation and the gravity may help increase the accuracy of the registration as it would restrain the compatibility between the positioning and the deformation. However, the creation of the database would take more time as the rotation should be incorporated as a parameter. Otherwise, in [116], the contours are used as boundary conditions. Following the same idea, if the correspondence is known between some landmarks, then their movement could be imposed in the EKF. It may help gets more precision in the area of interest. But then, the detection of the contours and of their correspondence could be harmful if badly done.

Third, one of the advantages of the method presented in this chapter is that the hyperelastic material constitutive laws can be easily modified. Here the Veronda-Westman and the St Venant-Kirchhoff have been chosen but other ones, such as the Mooney-Rivlin or the Ogden laws that are commonly used to model the liver [174], could have been used. Moreover, each organ could be modeled with its proper law, allowing a complete representation of the abdomen. By doing so, finer boundary conditions could be used. For example, here we represented the back of the patient, which can be undoubtedly considered as fixed.

Finally, the computational times reported in these results enable quasi real-time performances. Even though the registration takes some iterations to be achieved - around 184 iterations if the registration is considered good when the tumor is in the vicinity of its final position -, this time does not exceed the minute, which is reasonable in the OR. Besides, Matlab is not optimal in terms of computational efficiency, hence the algorithm may be accelerated by using a lower-level language implementation. Furthermore, some modifications could be brought to the method in order to get faster registrations. First, to accelerate the ROM a rough approximation of the registration could be done using fewer modes in the POD and a smaller RID. The shape would be then badly registered but could be used as the starting point for a new registration with more modes and more quadrature points in the RID. However, the more time-consuming step is not necessarily the strain energy minimization. As said in Section 5.6.2 the temporal continuity of the deformation allows initializing the minimization with the result of the previous iteration. Therefore, only the first minimizations take time to converge. Considering the first 200 increments in the example provided in the results, around 30% of the time was spent in the predict cycle (see Equation 5.33) against almost 70% in the update one (see Equation 5.34). After investigation, the time-consuming step appears to be the matrix inversion required to compute $\mathbf{K}(k+1)$. The size of this matrix is directly linked to the number of measured points on the surface of the abdomen. By using only 100 measures instead of the 600 used in the example, the computational ratio can be reversed with 80% for the predict cycle and 20% for the update one. Thus, the computational time is divided by a factor greater than 2. As before, a strategy could be to use fewer measurements to make an initial guess and then adding more data to get a better final registration.

From this discussion, we can draw the pros and cons of the use of the presented method. The main advantage of using MOR is that it enables the use of complex mechanical behaviors with real-time performances on standard devices. With its embedding in the EKF it also permits to identify the material parameters - with different levels of accuracy as mentioned before - and make the registration procedure unsupervised. This latter feature is notably due to the fact that the ROM allows modeling the whole body. Hence, the whole abdominal cavity may be represented. By assuming that the offline stage of the ROM encompasses all possible situations occurring during the operation, the surface of the abdominal cavity should be sufficient to perform the registration, without requiring landmarks. This latter assumption is the main bottleneck of the method as it is difficult to ensure the fidelity and completeness of the model and of the training set. As discussed before, some forces have not been taken into account in the present chapter (e.g. the gravity) as well as the collision between the organs and with the table. It has been shown in [180] that this latter is a potential source of error. Moreover, modeling the whole body requires to assign different properties to each organ, which can be a cumbersome task and challenge the parameters' identification. That is why it could be preferable to directly work with landmark detection techniques and to only model the organ of interest (e.g. [224, 116]). Though, in the literature, this approach is limited by the absence of representation of the organs in contact with the organ of interest, hence, the simulation cannot take into account the interaction between them. Moreover, the complexity of the mechanical behavior is generally limited due to the real-time constraint. That is why mass-springs models [181] or co-rotational FE [224, 114, 116] are commonly employed. Hyperelastic models have been used in [212] for quasi real-time applications but were limited by the identification of the boundary conditions. Thus, in a nutshell, the route of MOR - based on a training stage - enables the use of a complete and complex model but jeopardizes the quality of the registration if the pre-trained model is not faithful enough to the in situ surgical scene. On the other hand, approaches relying on simpler mechanical behaviors and salient features identification are more versatile and can be adapted to any position of the patient, not only those

belonging to a pre-computed database, but may lack information concerning the physical behavior and/or the boundary conditions. An experimental validation would be necessary to compare both kinds of approaches and get a better understanding of the EKF behavior presented in this chapter.

## 5.8 Conclusion

In this chapter, we proposed a method with quasi real-time capabilities to perform the organ static registration in augmented-reality laparoscopy. The method uses preoperative images of the organs, a partial surface reconstruction acquired intraoperatively thanks to the SLAM method, and a measure of the pneumoperitoneum pressure. The scene is then reconstructed thanks to an EKF based on an innovative reduced order modeling approach involving hyperreduction. A new hyperreduction method, based on a non-negative sparse approximation technique coined as nnFOCUSS, has been developed in order to find RIDs. A simple test case to recover the Gauss-Legendre quadrature points has proven the superiority of our approach to finding the most compact integration domains when compared to methods from the literature. Moreover, the ROM can be qualified as semi-intrusive as it allows the use of external software to generate the data. This new MOR method can be adapted to any type of hyperelastic material to describe the behavior of the organ.

We have validated the EKF performance on synthetic data adapted to mimic the real conditions in the OR, especially by considering a limited field of view. Results showed a good ability to register the organs and to represent their deformations due to the intra-abdominal pressure. Nonetheless, material parameters identification did not give satisfactory results. More investigations should be done to conclude if such a feature could and should be included in the EKF. The results also demonstrated the quasi real-time performance of the method. This fact added to its low memory requirement enables its use in standard clinical settings.

# Part II: partial conclusion

In this part, we developed the theme of data completion based on physical priors in the medical framework. We showed that many measurements are partial and noisy and can be improved or enhanced thanks to the biophysical simulation. The choice of a proper physical modeling permits to regularize the data reconstruction through a restriction of the search space. In practice, the combination of synthetic and measured data is performed via the solving of inverse problems. They allow to adapt the boundary conditions and/or the materials parameters of the models in order to get the best compromise between the medical data and the physical priors assumed through the simulation. The model order reduction (MOR) methods are particularly adapted in this context to provide an acceleration of the computations. We restrained the discussion on the construction of the augmented reality scene in laparoscopy. It involves the solving of non-linear mechanical problems in order to adapt the preoperative images onto the intraoperative data.

We proposed a method based on an extended Kalman filter (EKF) to perform the initial static scene registration in an unsupervised manner. To reach a computational time compatible with the requirements of an in situ operation, a reduced order model (ROM) was used as the computational core of the EKF. It is based on an original semi-intrusive approach combining the proper orthogonal decomposition method with a novel hyperreduction technique. This latter consists in a non-negative version of the focal underdetermined system solver method, a sparse regression technique. Its ability to find reduced integration domains has been shown to overcome other hyperreduction methods found in the literature in the particular case of the identification of the Gauss-Legendre quadrature rule.

The semi-intrusivity of the method is to be qualified. The non-intrusive aspect comes from the use of an external solver to generate the training data set and to solve the minimization problem. Nonetheless, the user has to implement the expression of the system's strain energy. In the current state of the approach, the computation of the Jacobian and Hessian matrices requires the knowledge of the finite element structure of the model. Hence, further developments could be envisaged to free the user from this knowledge and provide a more rigorous non-intrusivity.

Anyhow, the results prove the ability of the methodology to register the augmented scene onto a three-dimensional representation of the surface of the abdominal cavity. However, the identification of the material parameters with the EKF does not provide satisfactory results as they are not correctly identified. Hence, it means the method is able to represent the geometry with bad sets of parameters. The reason is that some parameters are in "competition" for the registration. Some of them have a great influence on the identification of others. Consequently, a large error in the identification of a parameter can be compensated by an almost insignificant one on the identification of another. This poses the question of how a model should be parametrized. Ideally, each parameter should account for a specific behavior of the model and be uncorrelated with the others. In practice, that is never the case. Inverse problem methods - in particular in the Bayesian framework - are able to provide an estimation of the uncertainty. However, for a display in an augmented reality framework, it may not be convenient to interpret. A solution to the bad parameter identification would be to add more richness to the data. It does not necessarily mean a bigger quantity of data but also a better quality. In our application, it could come from the texture of the images or from the measure of salient features. Nonetheless, it often comes at the expense of the unsupervised character of the algorithm. If such data are not available, then the use of complex models can be questioned. Also, if complex models are used but the method is unable to identify the parameters, the use of simpler models could be as efficient and would not require a complex implementation. Hence, the choice of the model must be mitigated by the ability to measure pertinent and rich data.

From a different perspective, the solution to the complexity of parameter identification in the models could be not to use models. From few years the data-driven methods have gained a lot of attention in the scientific community. These methods do not rely on constitutive behaviors but use directly the measured data to solve the equations governing the physics of the system.

# Part III

# Real-time response of biophysical models under uncertainty

Chapter 6

# Real-time uncertainty propagation in mathematical models

**Abstract** This chapter is an introduction to the forward propagation of uncertainty in mathematical models for the physical simulation. First, the interest of uncertainty propagation for computational surgery is highlighted with three specific applications; the emphasis is put on the real-time constraint. Then, a short review of the main methods for forward uncertainty propagation is provided, with a focus on the probabilistic approach. In this context, model order reduction methods are highlighted as an efficient tool to satisfy the real-time constraint while preserving the underlying physics of the mathematical models. Nonetheless, their limits in the case of non-separable problems are pointed out. Such a situation is commonly encountered in the medical framework. To circumvent this issue, we propose the route of metamodeling. In dynamic processes, the creation of a metamodel involves the identification of new governing equations. In the framework of uncertainty propagation this identification is even more challenging due to the stochastic nature of the model's inputs. We propose a brief overview of the challenges encountered in the creation of metamodels for stochastic parameters and introduce the Chapter 7, in which a new approach for the identification of stochastic dynamical systems is proposed.

## Contents



## 6.1 Uncertainty propagation in computational surgery

The design and outcomes of clinical procedures often rely on assumptions that must be challenged to ensure the safety and efficiency of the treatment. Numerical modeling used in conjunction with uncertainty propagation is naturally suited to assess the pertinence and robustness of these assumptions as it enables the coverage of many situations - i.e. set of parameters - in a relatively brief lapse of time and for a moderate cost. This procedure referred to as uncertainty propagation or sensitivity analysis has been the subject of practical guides to help the decision making [29, 275]. The sensitivity analysis is more specifically the study of how the uncertainty on the outputs of a mathematical model can be divided and attributed to the inputs' variations. It is commonly used in diverse branches of computational surgery such as musculoskeletal modeling [188], hemodynamics

[252] or pharmacology [194]. Nonetheless, such analysis does not require real-time performance, even though, to be integrated into the clinical routine for patient-specific surgery they must respect short delays. The real-time performance is required in contexts where the medical staff has to monitor *in situ* the evolution of "hidden" variables, i.e. variables that cannot be directly measured. To estimate the value of such variables, *indirect indicators* are employed. Several kinds of indicators exist, it can be biological substances, visual markers, thermal or electrical measurements, or simply the position of the surgical tools. They are then integrated into the numerical simulation to infer the hidden variables. This procedure is frequently used in the framework of minimally invasive procedures as much information is not available. In this context, the real-time concept is flexible depending on the reaction speed required during the operation. It can go from the millisecond to a minute. Thus, among the many medical procedures where the propagation of uncertainty in real-time can be critical for the success of the operation, we have chosen three of them to illustrate our point. We describe them below.

**Image-guided surgery** The image-guided surgery is a surgical procedure where the surgeon uses image acquisition - preoperative and/or intraoperative - to guide its tools during the operation. It is most of the time a minimally-invasive treatment. In standard surgical navigation systems, landmarks are affixed to the patient and to the surgical tools. Optical devices then detect and compute their position into a global reference frame. The final goal is to track the position of the surgical tool-tip from the knowledge of the landmarks. When they are available, intraoperative images can be used to check the validity of the estimated position but, as they are only two-dimensional, they cannot but trusted to capture the tool-tip position. As many uncertainties due to the registration, tracking, and instrument calibration degrade the estimation of the tool-tip position, it is important to take into account the averaged position but also the estimated deviation in the final display. Indeed, the surgeon is not always aware of these sources of uncertainties and can believe that the display returned by the navigation system is the truth. This can lead to potentially dramatic errors when the operation implies a sensitive surgical act (e.g. excising a tumor near a blood vessel or inserting a screw into a spine).

**Radiation therapy** Radiation therapy uses ionizing radiation to control or kill malignant cells. The main challenge in such a procedure is to determine the quantity of radiation absorbed by the tissue. On one hand to ensure the destruction of the tumor and on the other hand to spare normal tissue from unnecessary exposure. Several setups exist to perform the medical procedure. The amount and the kind of radiation used for the dose depend on the patient state, its disease, and its medical history. Then, the delivery can be done by one or several sources with possibly different angles. Also, the total dose can be fractionated over time in order to allow healthy tissue to recover. Finally, the radiation beam undergoes a scattering due to the patient tissue and from collimation upstream in the linear accelerator. Hence, for an accurate estimation of the operation outcomes, all the uncertainties on these data must be taken into account, plus the patient-specific anatomy and positioning during each stage of the procedure. It is important to have a good estimate of the averaged absorbed dose in order to adapt the clinical setup and avoid to radiate healthy tissue already at the limit of its recovery ability.

**Surgical oncology** As seen above, non-invasive methods such as radiation therapy can be used to treat cancers. When these latter are not available the tumor removal can be done using surgery, especially with minimally invasive procedures. Several approaches exist such as laser therapy, ultrasound therapy, cryotherapy or radiofrequency ablation (RFA). All these procedures face the same bottleneck: the assessment of the ablation size is not available intraoperatively. In some cases, real-time medical imaging devices can be used to have a visual feedback. But even then, these devices can at best provide only slices of the area of interest when a full three-dimensional representation would be necessary in order to take into account the patient-specific tumor's shape. Moreover, many of the previously cited therapies are based on temperature treatments. The temperature has a certain diffusion "inertia" that is not visually accessible and that can only be simulated. Besides, in these procedures, the clinician generally wants to find a compromise between the treatment time, the size of the ablation - to avoid destroying healthy tissue - and, in the

case of thermal therapies, the quantity of heat or cold injected. Indeed, the phenomenon known as the heat sink effect, which is the propagation of the temperature through the body, can lead to damage organs located in the vicinity of the tumor. Consequently, it is important to be able to estimate the ablation area in real-time while taking into account the many uncertainties, such as the tumor shape or the material parameters, in order to allow the surgeon to stop the procedure if critical states are reached.

These three examples show that it may be necessary to assess uncertainties in real-time in order to return an averaged response of the system. The deviation of the system to this mean value can also be displayed in order to provide the clinician with a confidence interval. We introduce in the next section some methods employed to perform the uncertainty propagation, also known as *forward uncertainty propagation* in contrast with the inverse uncertainty propagation mentioned in Chapter 4.

**Remark 6.1** (*Terminology: stochastic*). In this chapter, the term stochastic is used to refer to the probabilistic nature of the model's parameters. The difference must be made between its use in the context of stochastic differential equations where an additional term is added in the governing equations to model the noise. For example, let's consider the heat equation

$$\frac{\partial T}{\partial t} = \alpha \nabla^2 T$$

where $\alpha$ is the thermal diffusivity. In our case the stochasticity lies in the determination of the parameter $\alpha$, hence the heat equation reads

$$\frac{\partial T}{\partial t} = \hat{\alpha} \nabla^2 T \,, \quad \hat{\alpha} \in \mathcal{X}$$

where $\mathcal{X}$ is an arbitrary probability distribution. On the other case, which is not considered in this chapter, the equation would read

$$\frac{\partial T}{\partial t} = \alpha \nabla^2 T + \xi$$

where $\xi$ is a noise term.

## 6.2 The forward uncertainty propagation

### 6.2.1 Overview

The forward propagation of uncertainty - shorten in this chapter as *uncertainty propagation* - is the effect of the approximation of a mathematical model's inputs on its outputs. The inputs' approximation, or variables' uncertainties, can be due to error measurements, to the inherent variability of the data or to incomplete information. A classification of uncertainty can be found in Figure 6.1. When one or several variables are uncertain or a complex mathematical model is used, the impact of the variation of a variable on the function's output is non-trivial. Several methods exist to perform uncertainty propagation. They are generally sorted based on how the uncertainty is described. The main categories are:

- **The interval analysis**. It has been introduced in the late sixties by Moore et al. [183]. The basic concept is to use intervals instead of deterministic values when these latter are consider uncertain. The simplest example is the addition, such as $[1, 2] + [3, 4] = [4, 6]$. The lower bound is determined by $1 + 3 = 4$ and the upper one by $2 + 4 = 6$. The solution is then enclosed within a lower and an upper value. The concept can be then extended to more complex functions.

- **The information gap decision theory** [23]. It is often described as a theory for "supporting decisions under severe uncertainty". It is based on three information, the goals, the options, and the info-gaps. The info-gaps are the boundaries of our knowledge and the options are the different possibilities available to reach the goals. This theory offers a decision-making structure to prioritize the choices according to these three pieces of information based on a robustness analysis. The robustness is set by estimating the deviation from a goal, ideally leading to solutions that still lie within the options' range.

- **The possibilistic theory**. It is based on the concept of non-parametric or fuzzy approaches [300]. It employs membership functions to model the uncertain input parameters. The classical probability theory introduced below is a subset of the possibility theory.

- **The probabilistic methods**. They assume that the uncertain parameters follow given probability density functions and propagate these latter to define the probability density function of the solution. These methods are parametric representations of uncertainty.

In the context of physical simulations, and especially in the finite element (FE) framework, the probabilistic methods are the most widely used. Indeed, FE analyses can easily be described by a parametrization of the problem (geometry, boundary conditions, material parameters, ...) which fit well within a probabilistic approach. That is why the main probabilistic methods are introduced below. A review can be found in [267].

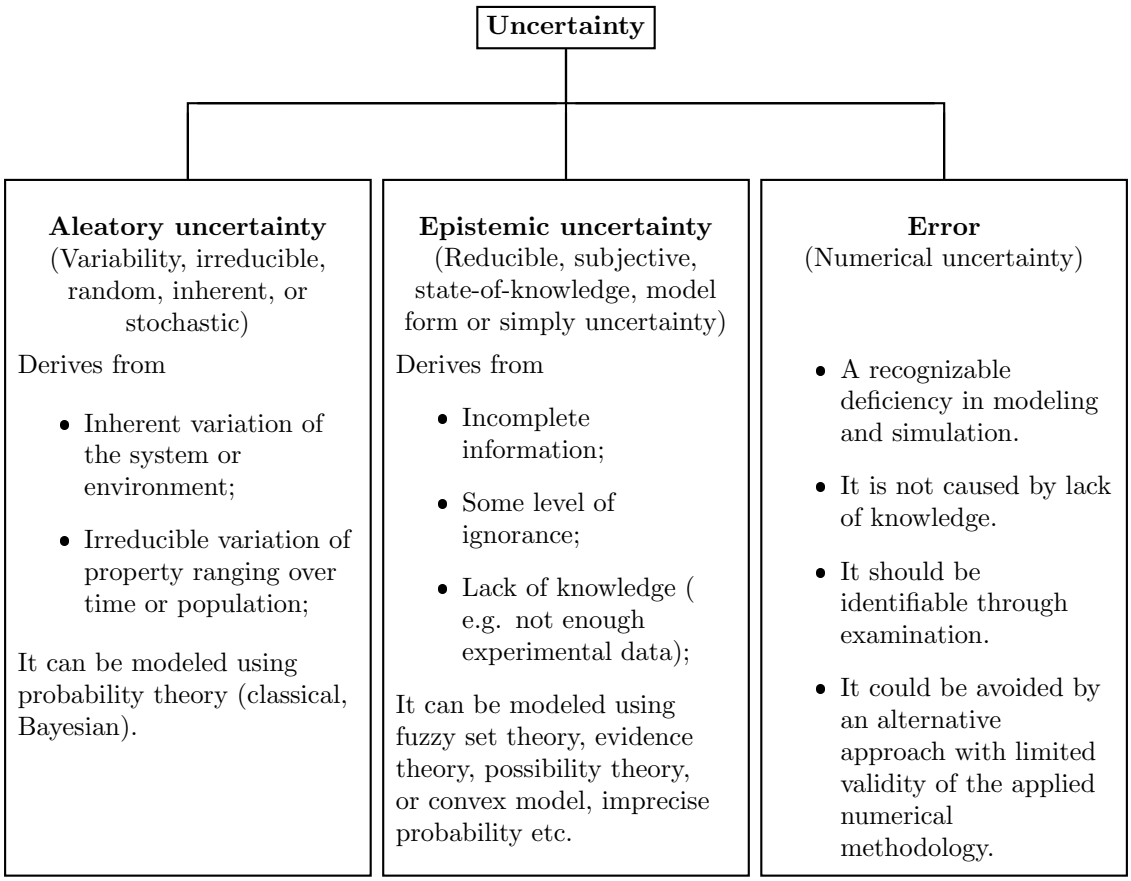


Figure 6.1: Classification of the uncertainty (from [118]).

### 6.2.2 Probabilistic methods

The typical problem in probabilistic methods for uncertainty propagation is the following:
"*Let* $\boldsymbol{X} : \Omega_{\boldsymbol{X}} \to \mathbb{R}^q$ *be a random variable in some probability space* $(\Omega_{\boldsymbol{X}}, \mathcal{F}, P_{\boldsymbol{X}})$ *and* $g$ *a mathematical function such as* $Y = g(\boldsymbol{X})$*. We want to estimate the probability measure* $P_Y$*.*"
Often, the complete probability measure $P_Y$ is not accessible, hence only its first moments are computed (expectation and variance). The expectation of $\boldsymbol{X}$ is defined in its continuous version as

$$\bar{\boldsymbol{x}} = \mathrm{E}[\boldsymbol{X}] = \int_{\mathbb{R}} x f_{\boldsymbol{X}}(x) dx \tag{6.1}$$

where $f_{\boldsymbol{X}}$ is the density probability function, and in its discrete version as

$$\bar{\boldsymbol{x}} = \mathrm{E}[\boldsymbol{X}] = \sum_{i=1}^{n} \boldsymbol{x}_i p_i = \boldsymbol{x}_1 p_1 + \boldsymbol{x}_2 p_2 + \cdots + \boldsymbol{x}_n p_n \tag{6.2}$$

where the $p_i$ are the probabilities associated with each random sample $\boldsymbol{x}_i$ ($i \in (\llbracket 1, n \rrbracket)$. The variance reads

$$\sigma^2_{\boldsymbol{X}} = \mathrm{Var}(\boldsymbol{X}) = \mathrm{E}\left[(\boldsymbol{X} - \bar{\boldsymbol{x}})^2\right] \tag{6.3}$$

where $\sigma_{\boldsymbol{X}}$ is the standard deviation. Similar notations are used for $Y$ (resp. $y = g(\boldsymbol{x})$).

#### 6.2.2.1 Monte-Carlo

The Monte-Carlo based methods [239] are probably the most simple and accurate methods to evaluate the propagation of uncertainty. Statistically independent random samples $(\boldsymbol{x}_1, \cdots, \boldsymbol{x}_n)$ are generated according to $P_{\boldsymbol{X}}$ and the values of interest $y_i = g(\boldsymbol{x}_i)$ are computed. The Monte-Carlo estimator uses the law of large numbers to build an empirical estimate of the mean such as

$$\bar{y} = \frac{1}{n} \sum_{i=1}^{n} y_i \,. \tag{6.4}$$

The precision of this estimate is evaluated through the empirical variance $\sigma^2_y$, it reads

$$\sigma^2_y = \frac{1}{n} \sum_{i=1}^{n} (\bar{y} - y_i)^2 \,. \tag{6.5}$$

The empirical estimation leads to an error in $O(n^{-\frac{1}{2}})$, hence, increasing the size of the sampling by 100 leads to improve the accuracy by 10. This observation is the principal bottleneck of the method as a very large amount of simulations must be performed to have reliable results. To circumvent this issue, variance reduction techniques have been set up in order to reduce the dispersion of the estimate or to improve the sampling strategy. According to [38], the main variance reduction techniques are the antithetic variates, the control variates, the conditional Monte-Carlo, the stratified sampling and the importance sampling. Among the sampling strategies, it is interesting to emphasize the Latin hypercube sampling (LHS) [268] as this latter will be used in Chapter 7. The idea of LHS is based on the Latin square. It is a two-dimensional square grid where there is a unique sample for each row and each column (see Figure 6.2). The LHS is the generalization of this concept to an arbitrary number of dimensions. It ensures that the hyperplane defined by each draw does not contain one of the previously defined samples. Hence, the sampling is done iteratively as the knowledge of the samples' historic is required. By doing so, the LHS ensures that the set of samples is representative of the real variability, which is not the case in purely random sampling. It allows considering smaller sets and speed-up the convergence of the Monte-Carlo method.

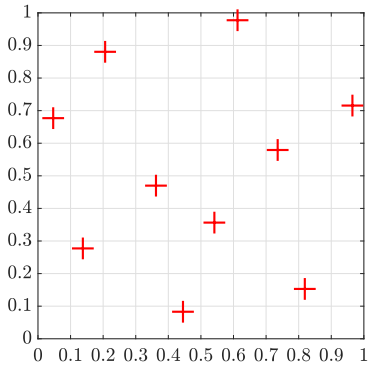


Figure 6.2: Latin hypercube sampling in two dimensions. $n = 10$ random points are chosen within $[0, 1] \times [0, 1]$. Each dimension is divided into $n$ equally spaced intervals and a unique sample belongs to each one of them.

#### 6.2.2.2 Method of moments or moment propagation

In the case of continuous variables and sufficiently differentiable functions, truncated Taylor series of the expected value of the input parameters can be used to propagate uncertainties. For example, the second-order Taylor expansion of $g$ in $\bar{\boldsymbol{x}}$ reads

$$g(\boldsymbol{X}) \approx g(\bar{\boldsymbol{x}}) + \sum_{i=1}^{q} \left.\frac{\partial g}{\partial x_i}\right|_{\bar{\boldsymbol{x}}} (X_i - \bar{x}_i) + \frac{1}{2} \sum_{i=1}^{q} \sum_{j=1}^{q} \left.\frac{\partial^2 g}{\partial x_i \partial x_j}\right|_{\bar{\boldsymbol{x}}} (X_i - \bar{x}_i)(X_j - \bar{x}_j)\,. \tag{6.6}$$

Consequently, the first moment is

$$\mathrm{E}[g(\boldsymbol{X})] \approx \mathrm{E}\left[ g(\bar{\boldsymbol{x}}) + \sum_{i=1}^{q} \left.\frac{\partial g}{\partial x_i}\right|_{\bar{\boldsymbol{x}}} (X_i - \bar{x}_i) + \frac{1}{2} \sum_{i=1}^{q} \sum_{j=1}^{q} \left.\frac{\partial^2 g}{\partial x_i \partial x_j}\right|_{\bar{\boldsymbol{x}}} (X_i - \bar{x}_i)(X_j - \bar{x}_j) \right]\,. \tag{6.7}$$

Assuming independent input variables, considering that $\mathrm{E}[(\boldsymbol{X} - \bar{\boldsymbol{x}})] = 0$ and according to the definition of the variance in Equation 6.3, it arises

$$\bar{y} = \mathrm{E}[g(\boldsymbol{X})] \approx g(\bar{\boldsymbol{x}}) + \frac{1}{2} \sum_{i=1}^{q} \left.\frac{\partial^2 g}{\partial x_i^2}\right|_{\bar{\boldsymbol{x}}} \sigma_{x_i}^2\,. \tag{6.8}$$

Similarly

$$\sigma_y^2 = \sum_{i=1}^{q} \left(\frac{\partial g}{\partial x_i}\right)^2 \sigma_{x_i}^2\,. \tag{6.9}$$

As presented, low truncation orders often offer poor estimations of the variance for highly nonlinear functions. In these cases, higher truncation orders must be considered. The main advantage of the method of moments is its computational efficiency, depending on the method used to compute the derivatives.

**Remark 6.2** (*First-order Taylor expansion*). If only the first-order Taylor expansion is used, then $\bar{y} \approx g(\bar{\boldsymbol{x}})$, which is referred to as a *deterministic* solution. If $g$ is linear, this equation is exact.

#### 6.2.2.3 Polynomial chaos expansion

The polynomial chaos (PC) expansion is based on the representation of the quantity of interest $Y$ as the linear combination of multivariate orthonormal polynomials $\Psi$ in the input vector $\boldsymbol{X}$, it reads

$$Y = \sum_{i=0}^{\infty} c_i \Psi_i(\boldsymbol{X}) \,. \tag{6.10}$$

This representation is correct if $Y$ is supposed to have a finite variance [264], which is justified when considering a physical system. To reach this expression, let consider $\boldsymbol{X}$ contains independent components. The joint probability density function can be written

$$f_{\boldsymbol{X}}(\boldsymbol{x}) = \prod_{i=1}^{q} f_{X_i}(x_i) \,. \tag{6.11}$$

The scalar product between two functionals $(\phi_1, \phi_2)$ with respect to each variable $X_i$ is then introduced such as

$$\langle \phi_1, \phi_2 \rangle_i = \int_{\Omega_{X_i}} \phi_1(x)\phi_2(x) f_{X_i}(x) dx \,. \tag{6.12}$$

This scalar product is also the expectation of $\phi_1\phi_2$ with respect to the distribution $P_{X_i}$. Two functions are said two be orthogonal when $\mathrm{E}[\phi_k(X_i)\phi_l(X_i)] = \langle \phi_k, \phi_l \rangle_i = \delta_{kl}$, where $\delta_{kl}$ is the Kronecker delta. It is then possible using the Gram-Schmidt orthogonalization to build a family of orthogonal polynomials, and, by a normalization step, to reach the expression of the polynomials $\Psi_i(\boldsymbol{X})$. In practice, the basis of the orthogonal polynomials is chosen accordingly to the nature of the distribution of $\boldsymbol{X}$ [296]; their correspondence is summarized in Table 6.1. The term "polynomial chaos" usually refers to the use of Hermite's polynomial. The generalization to other types of polynomials is pinned as "generalized polynomial chaos". Note that the distributions $P_{X_i}$ are usually not standardized, hence, an isoprobabilistic transform is usually applied to express the variables on the correct support.

| | Distribution | Orthogonal polynomial | Support |
|---|---|---|---|
| Continuous | Gaussian | Hermite | $(-\infty, \infty)$ |
| | Gamma | Laguerre | $[0, \infty)$ |
| | Beta | Jacobi | $[a, b]$ |
| | Uniform | Legendre | $[a, b]$ |
| Discrete | Poisson | Charlier | $\{0, 1, 2, \cdots\}$ |
| | Binomial | Krawtchouk | $\{0, 1, \cdots, N\}$ |
| | Negative Binomials | Meixner | $\{0, 1, 2, \cdots\}$ |
| | Hypergeometric | Hahn | $\{0, 1, \cdots, N\}$ |

Table 6.1: Correspondence between the random variables' distributions and their type of polynomial bases for PC expansion (taken from [296]).

Once the PC polynomials basis has been determined, the coefficients $c_i$ shall be computed. As Equation 6.10 is an infinite sum, the first step is to consider a truncation scheme to get a finite expression. Often the sum is reduced to 3 to 5 terms. Then, several methods exist to compute the coefficients. We present here the standard one which involves a Galerkin projection. As the PC basis is orthonormal, each coefficient can be computed by projecting Equation 6.10 on its associated polynomial, it reads

$$\langle \Psi_i(\boldsymbol{X}), Y \rangle = \int_{\Omega_{\boldsymbol{X}}} \Psi_i(\boldsymbol{x}) g(\boldsymbol{x}) f_{\boldsymbol{X}}(\boldsymbol{x}) d\boldsymbol{x} = c_i \,. \tag{6.13}$$

Hence the last difficulty is to estimate the integral defined in Equation 6.13 for each parameter. As said earlier, the scalar product defined here is equivalent to the expectation, hence, a Monte-Carlo approach can be used to estimate its value [97]. Otherwise, a numerical quadrature can be applied

[151, 26]. Once the truncated version of Equation 6.10 has been defined, the moments can be easily computed. For example, as $\Psi_0 = 1$, we have $\mathrm{E}[\Psi_i] = 0 \quad \forall\, i > 0$, thus

$$\mathrm{E}[Y] = c_0\,. \tag{6.14}$$

Similarly, the variance reads

$$\sigma_Y^2 = \mathrm{E}[(Y - c_0)^2] = \sum_{i=1}^{n_t} c_i^2 \tag{6.15}$$

where $n_t$ is the truncation order.

The PC expansion used in the context of FE is known as the spectral stochastic FE method. To get more insight into the subject the reader can refer to the review by B. Sudret [270].

#### 6.2.2.4 Stochastic collocation

The stochastic collocation method (SCM) has been introduced in [295] to circumvent two bottlenecks identified, respectively, in the Monte-Carlo and the PC expansion methods in the context of differential equations. In the case of the Monte-Carlo method, it is the high number of function evaluations required to converge to the solution. Knowing that a FE simulation can take several hours the method can rapidly become intractable. In PC expansion, the bottleneck comes from the implementation burden required to adapt each problem. Hence, the SCM offers a non-intrusive way to evaluate the parameter uncertainty, achieving fast convergence assuming sufficient smoothness of the solution in the random space. As indicated by its name, the SCM uses a collocation scheme to sample the parametric space. At each collocation point a deterministic solution is computed. The collocation points position is fixed a priori. The solutions are then interpolated over the whole subspace of the stochastic parameters using appropriate polynomials $\mathcal{P}_i$. It reads

$$Y = \sum_{i=1}^{n_c} g(\boldsymbol{x}_i)\mathcal{P}_i(\boldsymbol{x}) \tag{6.16}$$

where $n_c$ is the number of collocation points and $\boldsymbol{x}_i$ are their positions. Given Equation 6.16, the moments can be easily evaluated, e.g.

$$\mathrm{E}[Y] = \sum_{i=1}^{n_c} g(\boldsymbol{x}_i) \int_{\Omega_{\boldsymbol{X}}} \mathcal{P}_i(\boldsymbol{x}) f_{\boldsymbol{X}}(\boldsymbol{x}) d\boldsymbol{x}\,. \tag{6.17}$$

The evaluation of such expectation requires the explicit knowledge of the functions $\mathcal{P}_i$. The computation of the integral may be cumbersome but need only to be done once during a preprocessing stage.

The subtlety of the method lies in the choice of the collocation points, in order to get the minimum of computations to perform to reach an accurate estimate of $Y$. In [295] the Stroud's cubature points [269] and the Smolyak sparse grid algorithm [263] (see Figure 6.3) are considered. Further researches employed anisotropic [204] or adaptative [163] sparse grids to alleviate the computational cost.

**Remark 6.3** (*Stochastic collocation method and sparse subspace learning*). The SCM is particularly interesting as it is built on the same theoretical basis as the sparse subspace learning method used in Chapter 3. It offers interesting perspectives for the coupling of both methods.

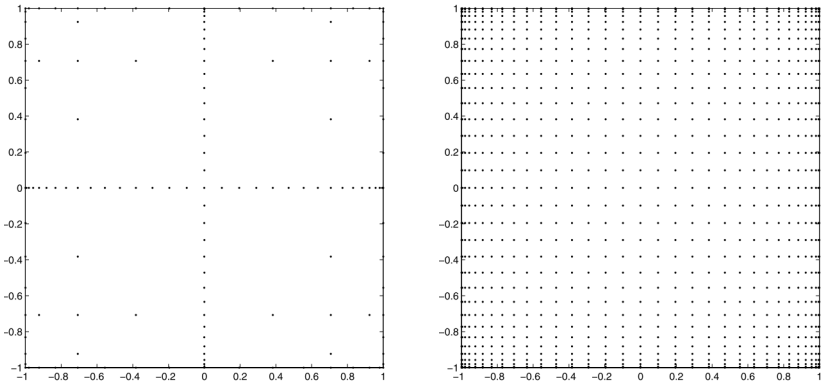

Figure 6.3: Two-dimensional interpolation collocation points based on the extrema of Chebychev polynomials. The sparse grid is represented on the left versus a representation of the full grid on the right (figure from [295]). A drastic reduction in the number of collocation points is achieved thanks to the sparse approach.

## 6.3 Potential and limits of real-time techniques for uncertainty propagation

All the methods previously presented have been successfully used in the medical framework for uncertainty estimation. Solutions for each one of the medical procedures mentioned in Section 6.1 have been proposed. For example, in the context of image-guided surgery, Simpson et al. in [261] use the method of moments to propagate in real-time the uncertainty about the tool-tip position. Otherwise, in radiotherapy, the Monte-Carlo is commonly used to estimate the dose and has become a gold standard [11]. Computational times of the order of the minute have been reached to perform the uncertainty propagation [133]. Finally, in [86], the generalized polynomial chaos method is used in the context of laser therapy for tumor ablation to provide real-time feedback to the physician to help the decision making. However, when complex models are required to reach a certain degree of accuracy, these procedures are not always suited or efficient in a real-time context.

In the framework of FE, the complexity of a model depends on the number of degrees of freedom, the number of uncertain parameters and the presence of nonlinearities. The number of uncertain parameters and the nature of the nonlinearities are generally a choice of the user and cannot be modified. On the other hand, the number of degrees of freedom is imposed by the desired accuracy of the model but can be reduced. A common approach to do so, and consequently decrease the computational time, is the use of model order reduction (MOR) techniques. Several methods exist but the most common ones are the so-called projection-based, which describe the solution in a lower-dimensional subspace. By doing so, the solution of the governing equations is often reduced to the solving of small systems, enabling real-time computations. This computational efficiency can then be exploited by uncertainty propagation methods based on direct simulations such as the Monte-Carlo or the stochastic collocation methods. Two kinds of projection-based MOR methods exist. The first is called the *a posteriori* methods. They are based on a database of solutions of the model, called *snapshots*, previously computed. The most known methods are the proper orthogonal decomposition (POD) and the reduced basis (RB). The second kind of projection-based MOR methods is the *a priori*. They construct the reduced order model (ROM) from the sole knowledge of the governing equations of the system. The most known method is the proper generalized decomposition (PGD). Both kinds of methods have proven to be pertinent for uncertainty propagation. For instance, the POD has been successfully used in the Monte-Carlo framework [79]. Several studies have also coupled ROMs and stochastic collocation approaches, in particular in the RB framework [57, 301]. Eventually, a PGD-like method has been developed in the context of uncertainty propagation under the name of generalized spectral decomposition in [206]. Nonetheless, MOR methods can fail to reduce the dimensional complexity of a problem,

especially in the case of dynamical systems when highly concentrated sources or fronts are moving (e.g. see [70]). The solution is then called *non-separable* in space and time, and can be more generally non-separable in the parametric space. This specific case arises frequently in the medical context (e.g. tumor growth or mechanical palpation modeling). Moreover, as the physical and/or biophysical states are often interdependent, the simulation error on one field is easily propagated through the whole model which leads to inaccurate and uncontrollable results. Hence, further than the real-time capability, it is the accuracy of the model that is jeopardized by the non-separability. We will show this phenomenon in Chapter 7.

An alternative to reduce the computational time is the use of surrogate models, also mentioned as metamodels. They are models of models, i.e. a simplified version of the initial model. They are built from a limited set of runs of the original model, called the experimental design - which is equivalent to the previously mentioned snapshots -, and assume some regularity of the solution. Their main strength is that only the quantities of interest are evaluated, which involves very few computations and provides quasi-instantaneous results. Standard metamodeling methods, to name a few, are the support vector machine [241], the kriging [143], and even the PC expansion [141]. The difficulty when using such an approach is then to integrate the dynamics of the response into the metamodel, this concept is known as *system identification*. In the case of MOR methods, the governing equations solved were the same as in the initial FE problem, hence dynamical systems were naturally represented. With the metamodels, the new set of governing equations is not based on physics and new dynamical relations must be set while taking into account the uncertainty of the parameters. That is what is done, for example, in [169], where the system identification is performed using a nonlinear autoregressive with exogenous input model. By using it in conjunction with the PC expansion the authors successfully generate a surrogate model for stochastic dynamical systems. Alternatively, an interesting and recent method to capture the dynamics of a system is the sparse identification of nonlinear dynamics method [44]. Using this method as a basis, we intend in the next chapter to give a new and original response to the problem of dynamical and stochastic metamodeling as an alternative to MOR methods in the context of non-separable models. Another advantage of using a sparse identification to build the metamodel is the identification of the indicators of the hidden variables mentioned in Section 6.1. The relation between the indicators and the hidden variables is a priori unknown and the choice of the indicators is in itself uncertain. Moreover, multiple indicators can be combined to generate complex representations of the variables of interest. For instance, in [130], the authors propose a general formula to estimate the lesion quality in atrial fibrillation ablation treatment based on two indicators: the measure of the contact force and of the electrical power over time. To reach such formulation the indicators discovery and the testing of their multiple combinations should be ideally automatized. As we will see in the next chapter, sparse identification enables such feature. We will consider the framework of RFA as it involves highly complex nonlinearities, the interdependence of the physical and biophysical states, and is non-separable due to the presence of moving fronts in the solution.

Chapter 7

# A metamodeling approach to study radiofrequency ablation outcomes under uncertainty of the model's parameters

**Abstract** In this chapter, we propose a method to build metamodels of dynamical systems under parameter uncertainty. We apply it in the context of the real-time monitoring of the necrosis of the tissue during radiofrequency ablation procedures. First, we try to employ a model order reduction method - the proper orthogonal decomposition - to accelerate the computations and satisfy the real-time constraint. However, it is shown that such an approach is not able to reduce the dimension of the state variables. Indeed, the radiofrequency ablation procedure involves the dynamic evolution of fronts that causes the non-separability of the model. From this statement, the alternative of metamodeling is proposed. The idea behind the concept of metamodeling is to infer a new set of governing equations by directly relating specific indicators to the outputs of interest, here the evolution of the necrosis. The sparse identification of nonlinear dynamic method has been proven to be an efficient approach in the case of deterministic and dynamic systems. We extend its application to the case of stochastic inputs and apply it in the context of radiofrequency ablation procedures. By using an appropriate sampling of the stochastic space, results show the potential of the method to propagate in a faster-than-real-time fashion the mean behavior of the system under varying boundary conditions. Moreover, the sparse identification allows the automatic identification of the indicators representing the evolution of the necrosis and their nonlinear relation to this latter. However, the difficulty to validate the results and compare them to a solid ground truth is highlighted in the discussion.

## Contents

## 7.1 Introduction

### 7.1.1 Motivations

Computer-assisted surgery is now firmly embedded within the medical framework as a means to plan, monitor and drive the evolution of quantities of interest during surgical interventions [95, 232, 156]. The simulation is at the core of the approach by allowing the representation of hidden features and the prediction of surgical outcomes. Modern imaging techniques such as magnetic resonance images (MRI) or computed tomography (CT) scans allow reconstructing reliably the anatomy of the patient and creating patient-specific models. Coupled with advanced numerical techniques, such as the finite element (FE) method, complex biophysical behaviors involving coupling and nonlinearities can be modeled. Nonetheless, the models' parameters used for the simulations are not perfectly determined due to the uncertainties related to the variability of the biological tissues and physiological phenomena. Hence, the challenge is to integrate these variations in the simulation while respecting the delay imposed by the clinical routine, and, in the case of *in situ* operations, reach real-time computations. Techniques such as the Monte-Carlo method [239] or the stochastic collocation approach [295] have been successfully used in the medical framework to propagate the models' uncertainty. Nonetheless, both methods require several evaluations of the deterministic model to estimate the mean response of the system. Or, even with powerful hardware and optimized software, running a unique patient-specific simulation in real-time is rarely possible when a complex model is involved. Hence, propagating the parameter uncertainty appears to be even more critical. Many methods have been developed to alleviate the cost of a direct simulation. Among them, two great families of methods can be highlighted: the model order reduction and the metamodeling. In this chapter, we attempt to provide an answer to the real-time simulation of complex models under uncertain parameters from the viewpoint of model order reduction and metamodeling. In this latter case, we also seek to automatically select the relevant descriptors, or *indicators*, describing the physics of the values of interest. To illustrate our approach, we use the context of radiofrequency ablation (RFA). In particular, we aim at generating a numerical tool able to assess in real-time the degree of necrosis of the tissues for a specific patient while taking into account the uncertainty of the model's parameters. The RFA is an interesting framework as it involves complex models embedding strong non-linearities and several coupling between the different biophysical fields modeled.

### 7.1.2 Medical and simulation context

RFA is a common procedure for hepatic tumor ablation when surgical resection is not possible. First, the clinician inserts a probe percutaneously - or during open surgery - in the liver parenchyma and through the tumor. Medium frequency alternating current (350-500 kHz) is then used to generate heat at the tip of the probe, leading to the necrosis of the surrounding tissues. The main drawback of the technique is that the assessment of the necrotic area cannot be done during the operation and the clinician must mainly rely on his expertise to drive the electrical pulses. In particular, the charring and dehydration of the tissue around the electrode produce an electrical impedance rise that reduces energy diffusion and the coagulation area. Consequently, the tissue's impedance has proven to be a relevant indicator to drive the pulses [131, 62]. Procedures such as the Goldberg protocol [101] have been set up in order to maximize the ablation efficiency. Also, specific electrodes are employed to spread the heat and avoid the impedance rises. Nonetheless, it does not guarantee the whole destruction of the tumor. Moreover, it does not prevent from overheating the tissue, which can lead to collateral injuries such as biliary tract damage [162]. On the contrary, tissue cooling by the neighboring blood vessels, known as the heat-sink effect, can lead to non-uniform destruction of the tissues. This phenomenon can cause an overestimation of the heated area and consequently increases the risks of recurrence [100, 308, 222]. Consequently, patient-specific numerical simulation is seen as a promising way to handle these difficulties as the necrotic area can be simulated and directly visualized while taking into account the relevant anatomical features.

In [280], Trujillo et al. propose a complete framework to model the RFA procedure for the liver using an internally-cooled electrode. They simulate the complete biophysics by integrating, thermal, electrical and physiological processes, and in particular the coagulation. Moreover, the model integrates the material parameters' nonlinearities related to the aforementioned fields. It creates a strong coupling between them and allows accounting for the impedance variations. However, material properties can vary day to day depending on the patient physical condition. Hence, it is important to take into account this variability in the patient's model. Several efforts have been done to integrate parameter uncertainties within numerical RFA procedures and many studies tried to understand what are the main parameters that influence the RFA outcomes through sensitivity analyses. In [197] it has been found that the ablation volume is mainly controlled by blood perfusion, then electrical conductivity and finally thermal conductivity. This study encompassed several kinds of tissues (bone, fat, lung, liver,...). Concerning healthy liver tissues only, Hall et al. [113] found that the most important variables in the ablation zone prediction were the blood perfusion, the electrical conductivity, and the cell death model. Similarly, Wang et al. [291] concluded that the most significant parameters were the electrical conductivity, the equivalent resistance of the tissue and its density. They also state that the thermal conductivity variability can be neglected, which is in discordance with Monsalvo et al. [182], for whom thermal and electrical conductivities are predominant parameters. The importance of thermal conductivity is also backed-up by Santos et al.'s study [81] in which it is found to be the more important parameter along with the perfusion. Thus, even if some disagreements exist, the parameters seeming to have the greatest impact on the simulations are the thermal and electrical conductivities and the perfusion coefficient. To build on this work, we propose to integrate into Trujillo's model of RFA the uncertainty on these parameters. The initial model is already complex, hence it is a real challenge to perform the uncertainty propagation in real-time. We add another level of complexity by performing the simulations on a medical image-based model of the liver, to account for the patient-specific anatomy.

### 7.1.3 Toward real-time uncertainty propagation in radiofrequency ablation simulation

Several studies have tackled the issue of real-time RFA simulation. Notably, Huang et al. [128] proposed to integrate the Monte-Carlo method into a RFA planning system in order to better predict the necrosis and limit the damages to healthy tissues while taking into account the variation of the material parameters. The simulations were two-dimensional (2D) and did not consider the dependence of certain parameters on the temperature or on the thermal damages. To run more

complex three-dimensional (3D) models in a reasonable amount of time, new approaches must be contemplated. In [13], a lattice Boltzmann solver was used to reach near real-time in patient-specific RFA of hepatic tumors integrating a computational fluid dynamics modeling of the vessels. A different approach was tackled in [35] where graphics processing unit (GPU) computing was used to accelerate the simulations up to three times the real speed. GPU is also used in [290] where a full framework for simulating RFA of the liver's tumor is presented. Within this framework, RFA planning is enabled thanks to faster-than-real-time computations, which allow integrating parameter uncertainty through an interval analysis approach and developing patient-specific models. Nonetheless, all these approaches use simple modeling of the biophysical properties; they do not integrate state-of-the-art modeling of RFA that could increase further their precision and accuracy. Bourantas et al. succeeded to run real-time simulations with nonlinear physical and thermal properties using dynamic mode decomposition [40]. Still, they did not use complex models as the Trujillo's one where an impedance rise can be observed when strong state-dependence parameters are introduced in the model. Besides, all the previously mentioned approaches can be used for prospective planning but have not been designed for the in situ prediction of the necrosis estimation under uncertain parameters.

Hence, our objective is to explore the ability of MOR methods to solve the acceleration of complex models in an uncertainty propagation framework. We show that standard MOR methods reach their limit in the case of RFA modeling due to the presence of moving fronts in the solution that cause the non-separability of the model. That is why the alternative of metamodeling is explored. We propose a novel approach to integrate parameter uncertainty in the context of system identification. This approach also enables the automation of the selection of the indicators for the representation of the values of interest.

### 7.1.4 Chapter organization

The rest of this chapter is divided into seven parts. In Section 7.2, the RFA model is presented. The geometry, the governing equations, the parameters, and the boundary conditions are described. In Section 7.3 we show the limits of standard MOR procedure based on the proper orthogonal decomposition (POD) technique. The metamodeling approach is then introduced in Section 7.4 and applied to a simple test case in Section 7.5, followed by an application to the RFA model in Section 7.6. Finally, Section 7.7 contains the results, which are discussed in Section 7.8. The conclusion is done in Section 7.9.

## 7.2 Radiofrequency ablation model

### 7.2.1 Geometry

The liver's geometry is taken from the IRCADb-01 open-source database accessible at https://www.ircad.fr/research/3d-ircadb-01/. Liver number 4 is elected for this study as it contains several small tumors and allows choosing different use cases. A tumor near the blood vessels is chosen in order to encompass the possible heat-sink effect. Its maximum length is around 19 mm for a width of 12 mm. The initial liver and tumor's surface meshes contained respectively 4,000 and 535 nodes and 8,000 and 1,066 triangles.

To perform the RFA, several choices of electrodes are available (see Figure 7.1). Here, a conventional 17G (radius 0.74 mm) internally-cooled needle-like RFA probe is inserted into the tumor. It has an active length of 10 mm with a 1 mm tip. Its position and orientation are chosen such that all the active length of the probe stays within the tumor. Figure 7.2a illustrates the whole assembly.

The computations were done using the FE method. In order to reduce the number of degrees of freedom, the area of interest is truncated using a 6 cm diameter sphere with the barycenter of the probe as its center. It encompasses the maximum area of variation of the temperature. Hence, the modeling of the tissue situated out of this volume is not relevant for the estimation of the necrotic area. The truncated domain is visible in Figure 7.2b. A 3D mesh is then generated to represent the liver tissue and the tumor. The probe is only meshed on the surface. All the operations on

the meshes were done using the open-source software PyMesh for the boolean operations on the surface meshes, Meshlab for the cleaning of these latter, and Gmsh for the creation of the 3D mesh from the surfaces. To get more accurate results, a fine mesh using 8-nodes hexahedral elements is used in the vicinity of the electrode surface, where the highest thermal and electrical gradients are expected. The rest of the model is meshed using 4-nodes tetrahedra. In the end, the mesh contains 9,054 nodes, with 29,665 tetrahedra and 3,504 hexahedra. The mesh is shown in Figure 7.3. Note that the mesh is non-conformal as pyramidal elements should have been used for the transition between hexahedral and tetrahedral elements. However, it increased significantly the computations without changing notably the results.

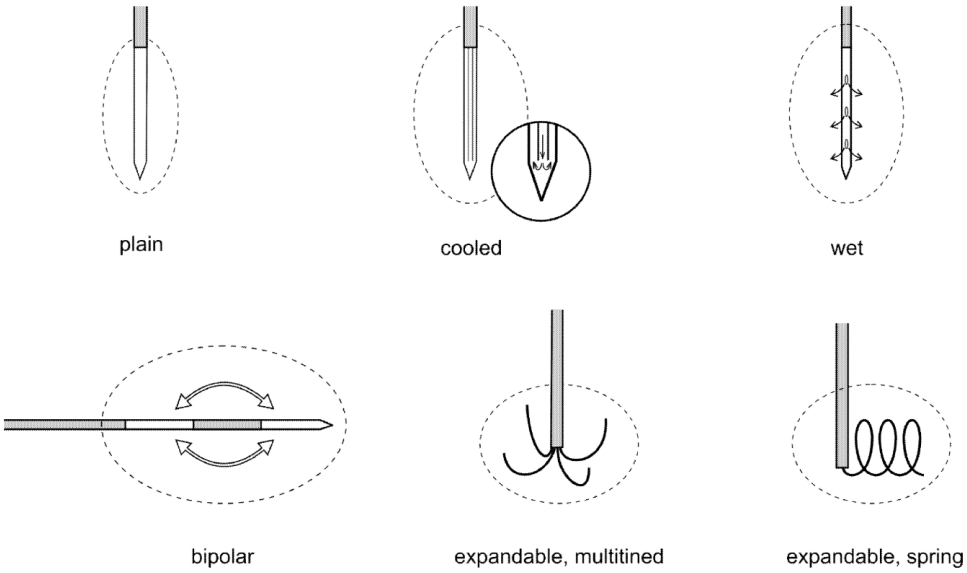


Figure 7.1: The different types of electrodes with a single shaft (from [186]). The isolated parts of the electrodes are represented in grey and the active one in white or with black lines. The plain electrode is the most simple one, it provokes a rapid rise of impedance and restrains the size of the ablation. To limit this effect, four approaches have been developed. The internal cooling (cooled electrodes), the saline perfusion through the electrode into the tissue (wet electrodes), the bipolar design (bipolar electrodes) and the distribution of the current over a larger volume of tissue (expandable electrodes).

### 7.2.2 Governing equations

**Electrical modeling** RFA involves electrical current with frequencies around 500kHz. At these frequencies the displacement currents can be neglected in soft tissues [24]. Hence, a quasi-static approximation is usually done [111, 280, 211], which allows representing the electrical potential using the Laplace equation:

$$\nabla \cdot (\sigma(T) \nabla \phi) = 0 \tag{7.1}$$

where $T$ is the tissue temperature, $\sigma$ is the temperature-dependent electrical conductivity and $\phi$ is the electrical potential.

**Thermal modeling** In applications related to living tissue it is common to use the Penne's bioheat equation [221] to represent the heat distribution. In order to encompass phase-change problems, as it is the case in RFA during vapourization, Abraham et al. [1] reformulated the equation by incorporating the enthalpy method, leading to

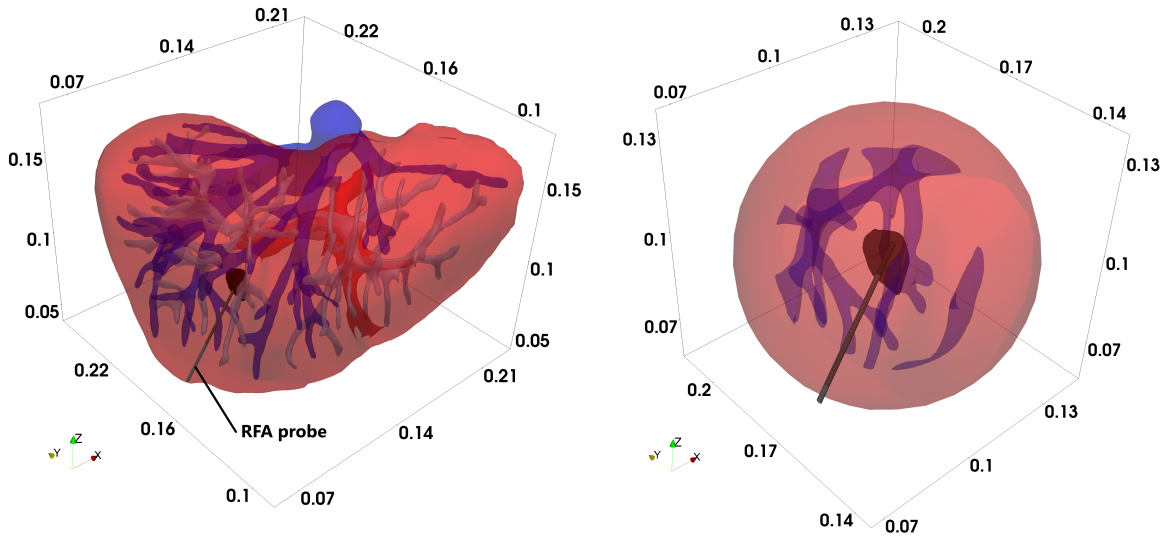


(a) Whole domain.

(b) Truncated domain.

Figure 7.2: Geometry of the model. The liver is represented in red, the tumor in black, the blood vessels in blue (dark blue for the venous system and light blue for the portal vein) and the RFA probe in dark grey. For the representation of the truncated domain, no distinction is made between the blood vessels.

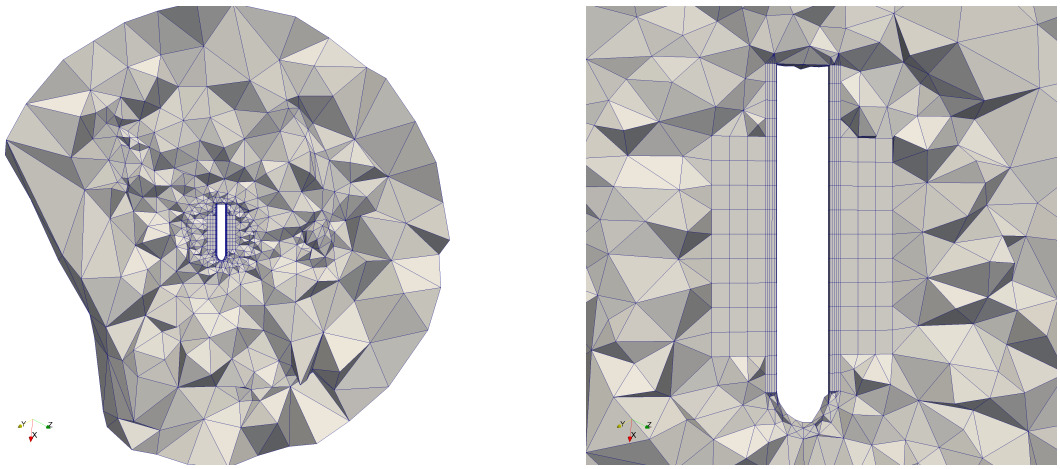

(a) Complete mesh of the truncated domain.

(b) Zoom on the needle tip.

Figure 7.3: Mesh of the truncated domain shown in Figure 7.2b. The whole mesh is represented along with a zoom on the needle area. Only the active part of the needle is represented. As shown the mesh is refined near the surface of the needle using hexahedral elements. Tetrahedra are used otherwise. The interior of the needle is not meshed. The boundary conditions on its surface are chosen so as to represent the cooling liquid circulating inside.

$$\frac{\partial(\rho h)}{\partial t} = \nabla \cdot (\kappa(T)\nabla T) + \rho_b c_b \omega_b(\Omega)\,(T_b - T) + q_h \tag{7.2}$$

where $\rho$ is the tissue density, $h$ is the enthalpy, $T$ is the tissue temperature, $T_b$ is the blood temperature (37°C), $\kappa(T)$ is the temperature-dependent thermal conductivity, $\rho_b$ is the blood density, $c_b$ is the specific heat of blood (see Table 7.1), $\omega_b(\Omega)$ is the damage-dependent blood perfusion rate and $q_h$ is the Joule heating term such as $q_h = \sigma(T)|\nabla\phi|^2$. The left-hand side relates the enthalpy variations to the temperature ones through

$$\frac{\partial(\rho h)}{\partial t} = \frac{\partial T}{\partial t} \times \begin{cases} \rho_l c_l & 0°\text{C} & < T \leq 99°\text{C} \\ h_{fg} C & 99°\text{C} & < T \leq 100°\text{C} \\ \rho_g c_g & 100°\text{C} & < T \end{cases} \tag{7.3}$$

where $\rho_l$ and $c_l$ (resp. $\rho_g$ and $c_g$) are the density and specific heat of the liquid phase (resp. the gas phase) (see Table 7.1), $h_{fg}$ is the product of latent heat of evaporation and water density at 100°C ($2.17 \times 10^9$ J.m$^{-3}$.K$^{-1}$) and $C$ is the concentration of liquid in the tissue (68%) [217].

**Thermal damage modeling** Temperature increase of the tissues above their physiological temperature for an extended period of time can lead to thermal damages, which are modeled using the Arrhenius equation [219], which is given by

$$\Omega(t) = ln\left(\frac{c(0)}{c(t)}\right) = \int_0^t A \exp\left(-\frac{\Delta E}{RT(t)}\right) dt \tag{7.4}$$

where $c(t)$ is the concentration of living cells, $c(0)$ is the initial concentration of living cells, $R$ is the universal gas constant (8.314 J.mol$^{-1}$.K$^{-1}$), $A$ is the frequency factor ($7.39 \times 10^{39}$ s$^{-1}$) and $\Delta E$ is the activation energy ($2.577 \times 10^5$ J.mol$^{-1}$) [134] for irreversible damage reaction. We consider that no damage in the blood vessels occurs and that materials properties are identical in the healthy and malignant tissues.

| Material | | $\rho_i$ (kg.m$^{-3}$) | $c_i$ (J.K$^{-1}$.kg$^{-1}$) | $\sigma_{37}$ (S.m$^{-1}$) | $\kappa_{37}$ (W.m$^{-1}$.K$^{-1}$) | $\omega_{b0}$ (s$^{-1}$) |
|---|---|---|---|---|---|---|
| Liver and tumor | $i = l$ | 1,080 | 3,455 | / | / | / |
| | $i = g$ | 370 | 2,156 | / | / | / |
| Blood | $i = b$ | 1,000 | 3,639 | 0.667 | 525 | 0.05 |

Table 7.1: Values of materials density $\rho$, specific heat $c$, electrical conductivity a 37°C $\sigma_{37}$, thermal conductivity a 37°C $\kappa_{37}$ and baseline perfusion $\omega_{b0}$ depending on the phase state [281, 7, 280]. The values replaced by a " / " are indicated in Table 7.2 as they are stochastic parameters.

### 7.2.3 State-dependent parameters

**Thermal-dependent parameters** The electrical conductivity thermal dependence is modeled as in [280], it reads

$$\sigma(T) = \begin{cases} \sigma_{37}\, e^{0.015(T-37)} & 0\,°\text{C} & \leq T < 99\,°\text{C} \\ \sigma_{37}\, 2.5345 & 99\,°\text{C} & \leq T \leq 100\,°\text{C} \\ \sigma_{37}\, (2.5345 - 0.50183(T-100)) & 100\,°\text{C} & < T < 105\,°\text{C} \\ \sigma_{37}\, 2.5345 \times 10^{-2} & 105\,°\text{C} & \leq T \end{cases} \tag{7.5}$$

where $\sigma_{37}$ is the electrical conductivity of the tissue at 37°C and $T$ is expressed in degree Celsius. In Equation 7.2, the temperature dependence of $\kappa$ is described as in [284] by the linear relation:

$$\kappa = \kappa_{37} + 1.161 \times 10^{-3}(T - 37) \tag{7.6}$$

where $\kappa_{37}$ is the thermal conductivity of the tissue assessed at 37°C and $T$ is expressed in degree Celsius.

**Damage-dependent parameter** The blood perfusion dependence to the damage has been studied in [255], where the degree of vascular stasis - also mentioned as coagulation in this chapter - is introduced as

$$DS = 1 - \frac{c(t)}{c(0)} = 1 - e^{-\Omega} \tag{7.7}$$

and is related to the blood perfusion with

$$\omega_b(DS) = \omega_{b0}(1 - DS) \tag{7.8}$$

where $\omega_{b0}$ is the baseline perfusion. Equation 7.7 is easily interpreted as the percentage of probability of cell death at a specific location, for this reason, the use of $DS$ will be preferred over $\Omega$ in the rest of the chapter.

**Stochastic variables** The baseline electrical conductivity, thermal conductivity, and perfusion are considered to be stochastic variables in the tumor and the healthy tissues. They are considered as Gaussian distributions. These values are reported in Table 7.2. In the framework of this chapter, the simulations concern only a specific patient. The values reported in the previously mentioned table cover whole cohorts. Consequently, the values used in the generation of the set of parameters for the training are not identical to those reported in Table 7.2. The mean value is kept the same but all standard deviations are divided by four by considering that the estimation of the parameters for a unique patient should be more condensed than data acquired over whole cohorts. This choice is arbitrary but allows avoiding generating too much variation of the stochastic parameters.

| Material | | $\sigma_{37}$ (S.m$^{-1}$) | $\kappa_{37}$ (W.m$^{-1}$.K$^{-1}$) | $\omega_{b0}$ (s$^{-1}$) |
|---|---|---|---|---|
| Liver | Mean | 0.25 [112] | 0.5122 [284] | 0.0208 [273] |
| | Std | 0.05 [112] | 0.11 [191] | 0.0093 [273] |
| Tumor | Mean | 0.5 [112] | 0.64 [7] | 0.0221 [273] |
| | Std | 0.2 [112] | 0.13 [7] | 0.018 [273] |

Table 7.2: Mean values and standard deviation (Std) of the state-dependent parameters. As all values are not directly available from the literature, some have been extrapolated.

### 7.2.4 Boundary conditions

**Electrical boundary conditions** The electrical pulses can be modeled either by imposing the voltage or the current on the active part of the electrode's surface as a boundary condition. In [280] both cases are studied in the framework of Goldberg et al. procedure [101]. Voltage pulses allow a better prediction of the coagulation zone when compared to experiments. However, current pulses produce a more realistic evolution of the electrical variables and are more relevant from a clinical point of view. For these reasons current pulses are used in the current model, the boundary condition reads

$$\sigma \frac{\partial \phi}{\partial n}\bigg|_{\Omega_e} = \frac{I}{S_{elec}} \tag{7.9}$$

where $\Omega_e$ is the non-isolated electrode's surface, $S_{elec}$ is the measure of this latter, $\boldsymbol{n}$ is the outward-pointing normal vector and $I$ is the imposed current. Goldberg protocol is also followed to automatically adjust the current intensity. In this latter, the impedance is monitored. When the impedance reaches a value 20 Ω superior to the baseline the pulse is stopped for 20 seconds. If the pulse duration is under 10 seconds then the next pulse's intensity is decreased by 0.1 A. An example is shown in Figure 7.4. Concerning the boundary condition on the liver's surface, a study by Ooi et al. [211] suggests that a Robin type is more suited, especially when the tumor is near the liver's surface. It reads

$$\left.\frac{\partial \phi}{\partial n}\right|_{\Omega_l} = -\frac{\boldsymbol{n} \cdot (\boldsymbol{r} - \boldsymbol{r}_0)}{|\boldsymbol{r} - \boldsymbol{r}_0|^2} \phi \tag{7.10}$$

where $\Omega_l$ is the liver's surface, $\boldsymbol{n}$ is the outward-pointing normal vector, $\boldsymbol{r}$ is the position of the vector in space and $\boldsymbol{r}_0$ is the position of the barycenter of the active part of the electrode.

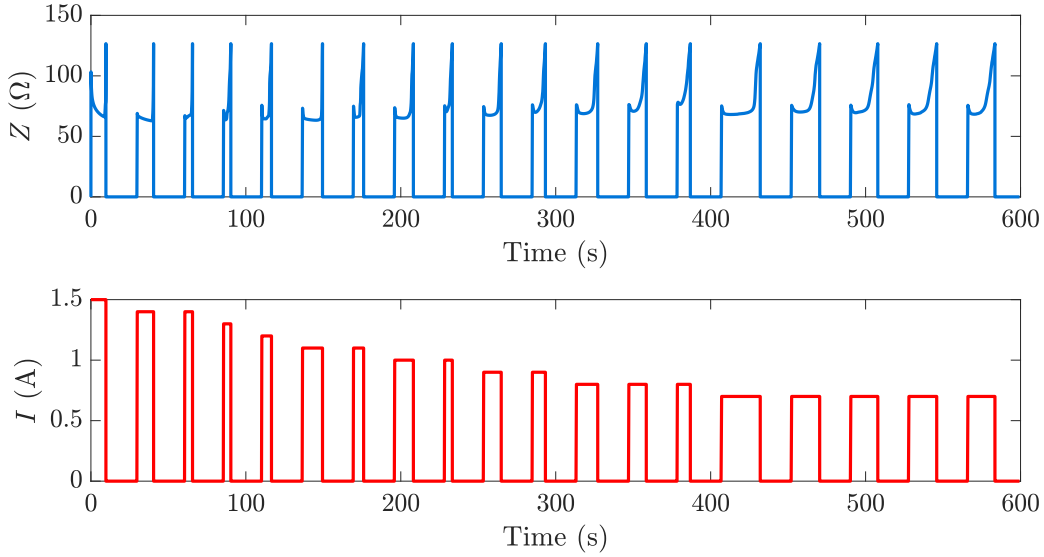


Figure 7.4: Evolution of the impedance $Z$ and current intensity $I$ over time using the Goldberg protocol. The data come from the simulation using the mean parameters presented in Table 7.2. The initial intensity is 1.5 A. The pulses are applied over a 10 minutes period.

**Thermal boundary conditions** As a cooled-tip probe is used, a Robin boundary condition is imposed on the active part of the electrode's surface $\Omega_e$. It reads

$$-\kappa \left.\frac{\partial T}{\partial n}\right|_{\Omega_e} = h_{elec}(T - T_{elec}) \tag{7.11}$$

where $h_{elec}$ is the heat transfer coefficient between the electrode and the tissue and $T_{elec}$ is the temperature of the cooling liquid circulating in the probe. The same values as in [211] are used, meaning the internally-circulating liquid is at temperature $T_{elec} = 2$°C and its flow rate is chosen to be 100 ml.min$^{-1}$, resulting in $h_{elec} = 5,646$ W.K$^{-1}$.m$^{-2}$. On the other hand, thermal insulation is imposed on the surface of the liver $\Omega_l$, such as

$$-\kappa \left.\frac{\partial T}{\partial n}\right|_{\Omega_l} = 0\,. \tag{7.12}$$

A summary of the electrical and thermal boundary conditions is shown in Figure 7.5.

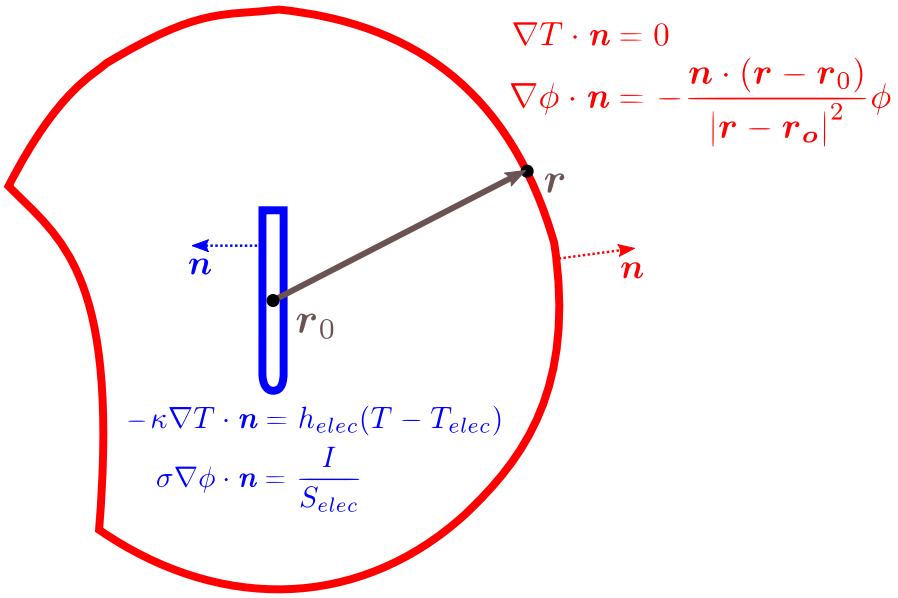


Figure 7.5: Scheme of the boundary conditions of the model on a slice. The temperature $T$ and the potential $\phi$ are represented. The electrode's surface and the associated boundary conditions are in blue. Similarly, the liver's surface and its associated boundary conditions are in red. For each surface the direction of the normal $\boldsymbol{n}$ is represented. The measurement of the electrode's surface is noted $S_{elec}$.

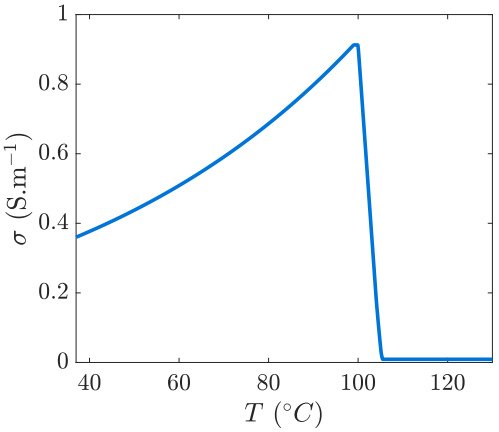


(a) Electrical conductivity (see Equation 7.5).

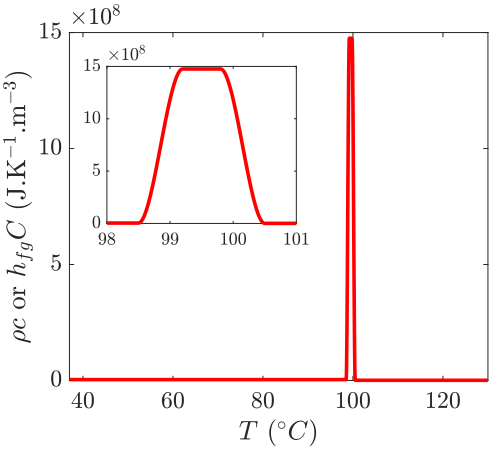


(b) Coefficient of the temporal derivative of the temperature (see Equation 7.3). A zoom is done over the range 98-101°C.

Figure 7.6: Variation of the electrical conductivity and the enthalpy coefficients over the temperature. These values vary very quickly around 99-100°C - where the water evaporation occurs -, making the equations very stiff.

### 7.2.5 Numerical solving

**FE formulation** The FE solver was implemented on Matlab (The MathWorks, Inc., USA). In this framework, the problem can be written as a differential-algebraic equation. For computational efficiency, a segregated approach is employed, hence, we solve separately the different physics of the problem. For the electrical potential, Equation 7.1 becomes

$$\left(\mathbf{K}_\sigma + \mathbf{B}_\sigma\right)\boldsymbol{\phi} = \boldsymbol{b}_I \tag{7.13}$$

where $\mathbf{K}_\sigma$ is the $\sigma$-dependent stiffness matrix, $\mathbf{B}_\sigma$ is the $\sigma$-dependent matrix representing the Robin boundary condition on the liver's surface, and $\boldsymbol{b}_I$ is the vector representing the Neumann boundary condition on the electrode's surface. Similarly, for the temperature Equation 7.2 reads

$$\mathbf{M}_{\rho c}\frac{\partial \boldsymbol{T}}{\partial t} = -\mathbf{K}_\kappa \boldsymbol{T} + \mathbf{K}_\omega(\boldsymbol{T}_b - \boldsymbol{T}) + \mathbf{B}_{h_{elec}}(\boldsymbol{T}_{elec} - \boldsymbol{T}) + \boldsymbol{b}_{q_h} \tag{7.14}$$

where $\mathbf{M}_{\rho c}$ is the $\rho c$-dependent mass matrix, $\mathbf{K}_\kappa(T)$ is the $\kappa$-dependent stiffness matrix, $\mathbf{K}_\omega$ is the $\omega$-dependent matrix representing the blood perfusion heat, $\mathbf{B}_{h_{elec}}$ is the matrix representing the Robin boundary conditions on the electrode's surface, and $\boldsymbol{b}_{q_h}$ is the $(\sigma, \phi)$-dependent vector representing the Joule heating term. Finally, for the degree of vascular stasis, Equation 7.4 combined with Equation 7.7 becomes

$$\frac{\partial \boldsymbol{DS}}{\partial t} = A\exp\left(-\frac{\Delta E}{R\boldsymbol{T}}\right) \circ (1 - \boldsymbol{DS})\,, \tag{7.15}$$

where $\circ$ denotes the Hadamard product. Note that it is more pertinent from a numerical viewpoint to consider $DS$ rather than $\Omega$ as the former has bounded values on the contrary to the latter. Hence, it increases the stability of the computations.

**Temporal discretization** To ensure the stability of the numerical scheme, we solve the set of equations using semi-implicit formulations. Let consider we know the state of the system at time $t$ and we look for a solution at time $t + dt$. The potential at time $t + dt$ is written

$$\left(\mathbf{K}_\sigma^t + \mathbf{B}_\sigma^t\right)\boldsymbol{\phi}^{t+dt} = \boldsymbol{b}_I^{t+dt}\,, \tag{7.16}$$

the temperature

$$\left(\frac{\mathbf{M}_{\rho c}^t}{dt} + \mathbf{K}_\kappa^t + \mathbf{K}_\omega^t + \mathbf{B}_{h_{elec}}\right)\boldsymbol{T}^{t+dt} = \left(\frac{\mathbf{M}_{\rho c}^t}{dt}\boldsymbol{T}^t + \mathbf{K}_\omega^t \boldsymbol{T}_b + \mathbf{B}_{h_{elec}}\boldsymbol{T}_{elec} + \boldsymbol{b}_{q_h}(\sigma^t, \phi^{t+dt})\right)\,, \tag{7.17}$$

and the degree of vascular stasis

$$\boldsymbol{DS}^{t+dt} = \boldsymbol{DS}^t + dt \times A\exp\left(-\frac{\Delta E}{R\boldsymbol{T}^{t+dt}}\right) \circ (1 - \boldsymbol{DS}^t)\,. \tag{7.18}$$

Because of the variation of the electrical conductivity $\sigma$ (see Equation 7.5) and of the enthalpy (see Equation 7.3), represented in Figure 7.6, the equations are very stiff. It means that physical phenomena appear at a different time scales. For instance, in a second the temperature can vary of only 1°C while the enthalpy coefficients are multiplied by $10^8$. Moreover, there is a strong coupling between the different physical fields of the system through the material parameters. Consequently, it is important to ensure the temporal convergence.

**Time stepping** The Richardson extrapolation [238] is used to ensure the first-order accuracy of the temporal scheme. The method is based on the fact that a quantity $f$ yielded by a numerical simulation can be written

$$f = f_{exact} + g_1 h + g_2 h^2 + g_3 h^3 + \cdots\,, \tag{7.19}$$

where $h$ is the grid spacing of a parameter on which depends the simulation and $g_i$ is a function independent from this latter. In our case, $h$ is the step of the temporal discretization. The

extrapolation uses different grids to approximate $f_{exact}$. For instance, by using the grid steps $h_1$ and $h_2 = \frac{h_1}{2}$, it arises the first order extrapolation as

$$f_{exact} = 2f_2 - f_1 + O(h_1^2) \approx 2f_2 - f_1\,, \tag{7.20}$$

where $f_i$ is the function evaluated with the step $h_i$. Hence, we evaluate the different physical fields of the problem on two distinct grids with the time steps $dt$ and $\frac{dt}{2}$. At each increment $dt$ the maximum of the absolute error between $f_{dt}$ and $f_{exact} = 2f_{\frac{dt}{2}} - f_{dt}$ is evaluated for each field. An absolute tolerance of $0.1\,\Omega$ (resp. $0.1\,°C$, resp. $0.01$) is set for the electrical potential (resp. the temperature, resp. the degree of vascular stasis). When one of these tolerances is not respected, the time step $dt$ is divided by a factor 3. Conversely, after 300 successful increments the time step is increased by a factor 3. Using this adaptive time-stepping allows automatically managing the stiffness of the equations by using small time steps when high variations occurred - i.e. the impedance rises - and larger ones otherwise. In practice, the time step varied between 100 ms and 3.7 ms.

**Solving of Equations 7.16 and 7.17** To speed-up the computations, the linear systems are solved using the preconditioned conjugate gradients method, using Matlab's `pcg` function. As the matrices are symmetric and positive definite, the incomplete Cholesky factorization is used as a preconditioner, using Matlab's `ichol` function. The preconditioning of the matrices is done every 50 time steps or when this latter is modified by the adaptive temporal scheme.

**Spatial discretization** Linear finite elements are employed. In particular, 4-nodes tetrahedra with one Gauss quadrature point and 8-nodes hexahedra with eight Gauss quadrature points are used. Note that the convergence of the results with respect to the mesh size has not been thoroughly checked because of the extensive computational time of certain simulations (several days). As explained later, we had to explore a maximum of input parameters, thus, it was not practicable to use more elements in the mesh as it would have extended the computational time. Moreover, for the application presented in this chapter, it is not necessary to ensure the mesh convergence. Nonetheless, as shown in Figure 7.3b we use finer hexahedra in the vicinity of the electrode's tip in order to get the best possible representation. Indeed, it is in this area that the greatest variations in temperature and electrical potential occur. As the behavior of the impedance is dependent on these variations and that this latter drives the pulses through the Goldberg protocol, the accuracy is required to get realistic trains of pulses.

## 7.3 Why using a metamodel?

As we have seen in the previous chapters, MOR methods are convenient to speed-up computations while preserving faithful representations of the physical phenomena. In the case of the RFA application presented in this chapter, the standard MOR methods reach their limits in terms of separability of the solution. We introduce them through the example of the POD applied to the reduction of RFA simulations. First, we briefly remind the concept behind the POD and then show its limits in the current context.

### 7.3.1 Dimensionality reduction using the proper orthogonal decomposition

The POD (which is similar to the singular value decomposition (SVD), principal component analysis or the Karhunen-Loève transform) is used to get a lower dimensional representation of a given data set $\mathbf{X} = [\boldsymbol{x}_1, \cdots, \boldsymbol{x}_{n_s}]$, where the $\boldsymbol{x}_i$ are called the *snapshots* and are the solutions for different states of a given problem. In the application presented in this chapter, the computations are done in finite dimension, meaning $\boldsymbol{x}_i \in \mathbb{R}^q$ where $q \in \mathbb{N}$. In practice, it decomposes $\mathbf{X}$ into an orthonormal basis $\boldsymbol{\Phi} = [\boldsymbol{\phi}_1, \cdots, \boldsymbol{\phi}_q]$ such as

$$\mathbf{X} = \boldsymbol{\Phi}\mathbf{A}\,, \tag{7.21}$$

where the matrix $\mathbf{A} = [\boldsymbol{\alpha}_1, \cdots, \boldsymbol{\alpha}_{n_s}]$ contains the vectors that allow reconstructing the data set from the orthogonal basis following $\boldsymbol{x}_i = \boldsymbol{\Phi}\boldsymbol{\alpha}_i$. To each vector $\boldsymbol{\phi}_i$, hereafter mentioned as a mode, is assigned a singular value $\lambda_i$. The interest of the POD decomposition is that the method returns the modes sorted such as $\lambda_1 \geq \cdots \geq \lambda_q \geq 0$. As the singular values can be interpreted as a quantification of the variability of each mode (meaning the greater the singular value, the more important the mode is in the representation of the data set), the representation of $\mathbf{X}$ can be done with a truncated basis $\boldsymbol{\Phi}_r = [\boldsymbol{\phi}_1, \cdots, \boldsymbol{\phi}_r]$ with $1 \leq r \leq q$, optimal in the least-squares sense. If the data set is chosen large and rich enough, any new solution $\tilde{\boldsymbol{x}}$ taken in a near subspace can be written as

$$\tilde{\boldsymbol{x}} = \sum_{i=1}^{r} \boldsymbol{\phi}_i \tilde{\alpha}_i. \tag{7.22}$$

The selection of the truncation order $r$ is usually done to maximize the *relative information content* (RIC) while minimizing $r$. The RIC can be defined directly on the singular values [67] or on their squared values [223], it reads

$$\hat{r} = \underset{r \in \mathbb{N}_+^*}{\arg\min} \left( \frac{\sum_{i=1}^{r} \lambda_i^k}{\sum_{j=1}^{q} \lambda_j^k} > h \right), \quad k \in \{1, 2\} \tag{7.23}$$

where $h \in (0, 1]$ is a threshold defining the percentage of variability (or energy) the ROM must encompass. Often a 99% criterion energy is chosen but values taken from the literature can vary from 75% to 99.5% [43]. Ideally, $\hat{r} \ll q$, leading to a drastic reduction in the number of degrees of freedom of the model. Usually, $\hat{r}$ takes values around a few tens.

Finally, in the context of model reduction, the computations are often accelerated using the Galerkin approach. In this latter, the equations of the problem are projected onto $\boldsymbol{\Phi}_r$ to ensure the orthogonality of the residual with respect to the reduced basis. The size of the linear systems to be solved are then reduced from $q \times q$ to $\hat{r} \times \hat{r}$. It enables a consequent speed-up if the condition $\hat{r} \ll q$ is respected.

### 7.3.2 The limits of the proper orthogonal decomposition

To illustrate the difficulties of the POD to reduce the model in the case of RFA, the method is applied to a database of 300 simulations. The Monte-Carlo procedure is used to draw the values of the stochastic parameters. For each simulation, 100 time steps per pulse's period are stored. For each time step, a snapshot is generated, i.e. the temperature, electrical potential, and coagulation fields are stored. The time steps are chosen such as the phenomenon of impedance rise is over-represented. As it drives the pulses it should be encompassed in the reduced order representation. The POD is then applied to each field. Note that the SVD is usually used to compute the modes. In our case, as the database is large, a variant of the SVD called the incremental random SVD [36] is preferred. In this method, a limit on the maximum number of modes must be specified. Here 4000 is chosen. That explains why $r \leq 4000$ in the figures mentioned hereafter. The singular values are represented in Figure 7.7. They tend to decrease rapidly for $r < 10$ then their slopes become less pronounced. The relative information content is plotted for $k = 1$ and $k = 2$ in Figure 7.8 and the number of modes $r$ required to satisfy the threshold $h$ for a given $k$ is reported in Table 7.3. There is an important difference between $k = 1$ and $k = 2$. The former is much more conservative and several hundreds of modes are required to reach a threshold of 99% in each one of the three fields represented. In the case of the temperature, this number is above two thousand. On the other hand, with $k = 2$ approximately ten modes are required to reach a RIC almost equal to 1. The comparison of the two configurations leads to thinking that the first modes contain a lot of information, but that the rest of it is diluted into the tail of the modes ($r > 10$).

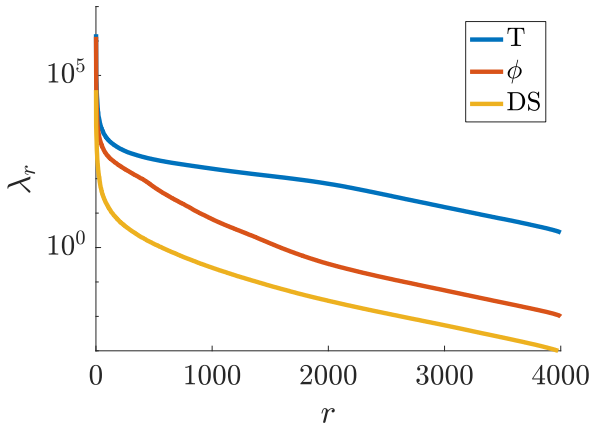


Figure 7.7: Singular values computed for the electrical potential, the temperature, and the coagulation. An important drop in their values is observed for a low number of modes ($< 10$), followed by a low decrease in their values. This trend explains the low efficiency of the proper orthogonal decomposition in this case.

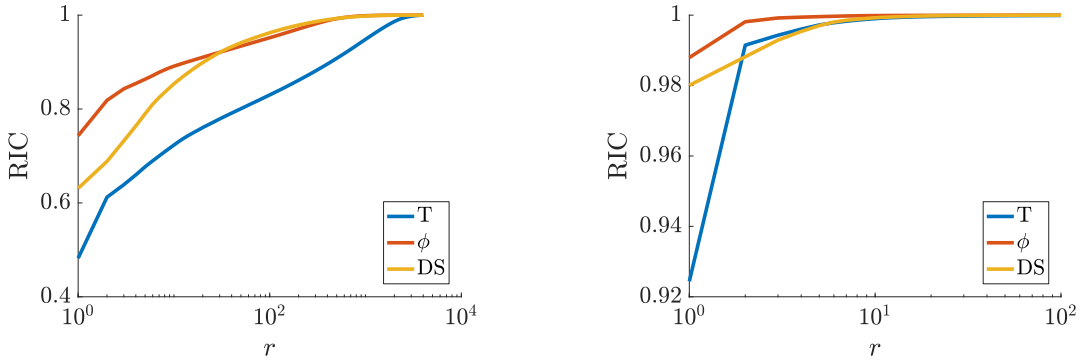


(a) $k = 1$. (b) $k = 2$.

Figure 7.8: Relative information content. For $k = 1$ several hundreds of modes are required to reach a RIC of 99%. In contrast, with $k = 2$ approximately ten modes a necessary to reach this threshold.

| | $k = 1$ | | | $k = 2$ | | |
|---|---|---|---|---|---|---|
| $h$ | 75% | 99% | 99.5% | 75% | 99% | 99.5% |
| $T$ | 17 | 2,186 | 2,585 | 1 | 2 | 4 |
| $\phi$ | 2 | 436 | 599 | 1 | 2 | 2 |
| $DS$ | 4 | 392 | 620 | 1 | 3 | 4 |

Table 7.3: Value of $\hat{r}$ depending on $k$ and $h$. The values are reported for the temperature $T$, the electrical potential $\phi$ and the degree of vascular stasis $DS$. Using $k = 1$ leads to select a greater number of modes $r$ than using $k = 2$. This highlights the importance of the thresholding method chosen to determine $\hat{r}$.

After a short investigation, the phenomenon is easily interpretable. The main bottleneck is that a temperature, a potential, and a coagulation front appear due to the expansion of the necrosed area and the changes in the temperature-dependent materials (see Figure 7.9). The main modes of the POD are related to the changes happening far from the electrode, where there are no fronts and where the dynamics is dampened by the diffusion phenomenon. On the contrary, in the vicinity of the electrode, the alternation between heat and cooling phases creates a moving front, going back and forth for the temperature and the potential. In the case of the coagulation, the front is always expanding as the phenomenon is not reversible. As these areas of the model contain valuable information they are densely meshed. Consequently, the tails in Figure 7.7 are no more than the translation of the fronts moving through each point of the mesh. Schematically, a superposition (or linear combination) of specific states of the front will not be able to represent a new one if the front is not exactly located on the same nodes of the mesh (see Remark 7.1). So, each time the front concerns a new set of nodes, a new mode must be added. The POD efficiency becomes dependent on the mesh and the modes cannot be easily truncated anymore. One could argue that as long as the number of modes of the POD is significantly lower than the number of degrees of freedom used in the FE model it could still be interesting to use the POD. This assertion must be qualified. Indeed, the POD implies the resolution of full linear systems, whereas the FE method implies sparse matrices which can be efficiently solved by any linear-system solver. To get an interesting speed-up the number of modes must be such that solving the reduced full linear system is faster than to solve the full sparse one.

Furthermore, when using projection-based MOR methods - as the POD - in the context of nonlinear equations, the use of hyperreduction is mandatory to get a real speed-up. This topic has not been addressed here as the goal was to show the limits of standard MOR methods and not to build a complete ROM.

**Remark 7.1** (*Non-separability of a front on 1D*). To illustrate the non-separability of a front, we provide a one-dimensional (1D) example. We consider a linearly spaced grid into $x = [1, 50]$ divided in 50 cells. A database of 5 positions of the front is generated, such as at each position the front moves of $\Delta x = 10$ cells toward higher values (see Figure 7.10). The POD is applied to this database and we try to reconstruct an out-of-sample front, located between the first and the second one. As shown in Figure 7.10, the reconstruction of the front is false for $x \in [10, 20]$. This is due to the fact that the separability of the solution depends on the spatial discretization and of the number of positions of the front captured in the database.

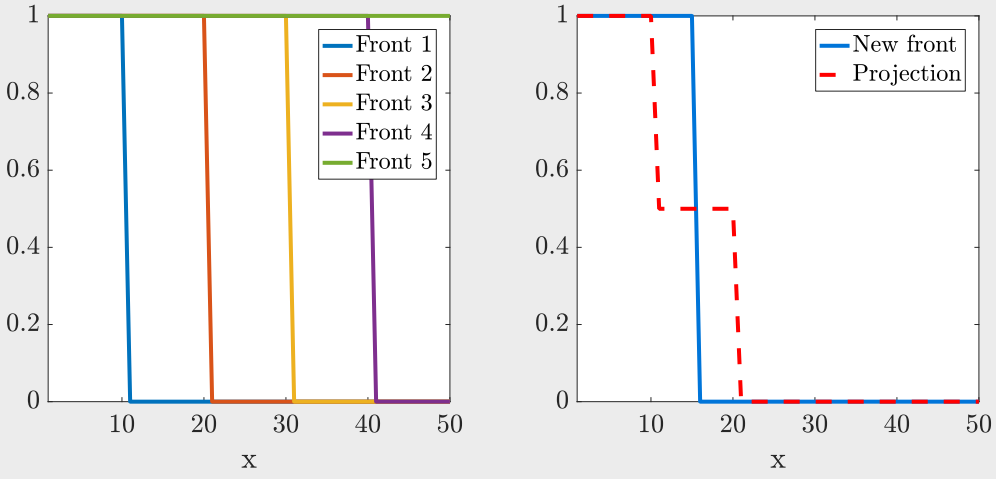


Figure 7.10: Representation of the database of 1D fronts, on the left, and the reconstruction of an out-of-sample with the POD, on the right. As the database is non-separable, the out-of-sample is poorly rebuilt.

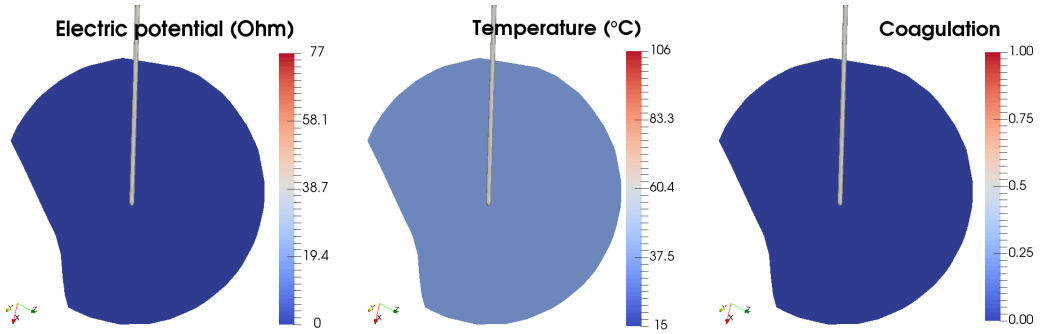


(a) $t = 0\,\mathrm{s}$.

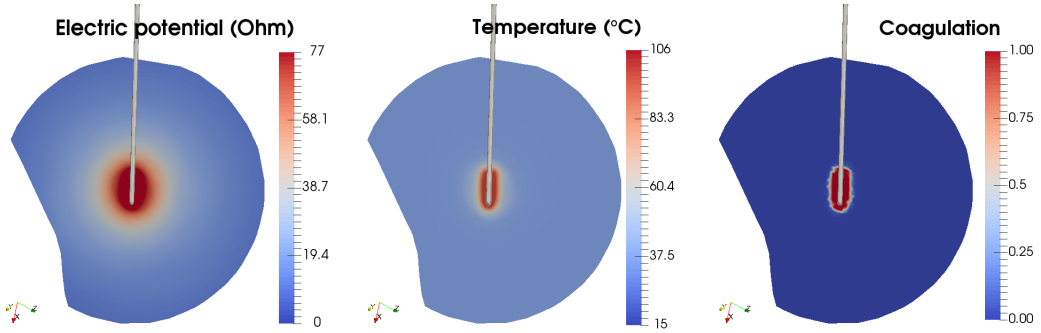


(b) $t = 2\,\mathrm{s}$.

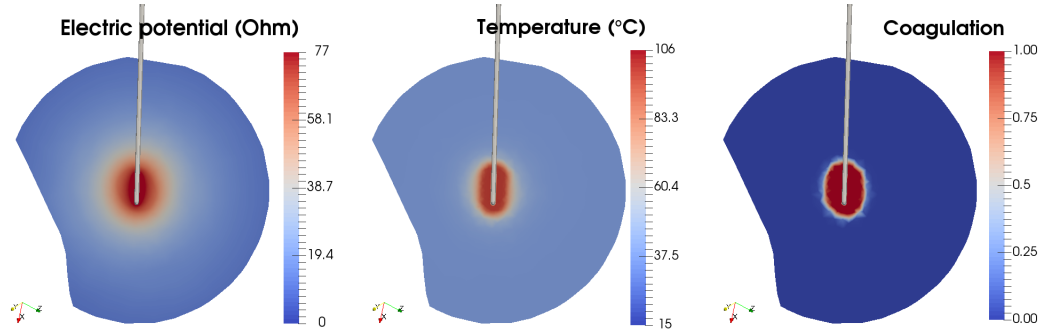


(c) $t = 7\,\mathrm{s}$.

Figure 7.9: 2D slice of the result for a high fidelity simulation with the mean stochastic parameters detailed in Table 7.2 and an initial current intensity of 1.5 A. The electrical potential, temperature, and coagulation fields are represented at different times $t$ during the first pulse. The front of each field is visible. Fronts located even closer to the electrode's tip also appear at each impedance rise but are not shown here.

### 7.3.3 Applicability of the proper orthogonal decomposition to non-separable problems

MOR methods are useful to reduce the computational complexity of a model while respecting its governing equations. If the ROM is correctly built it ensures a realistic physical behavior. For this reason, we explored in the first instance their ability to accelerate the RFA simulations. Unfortunately, as we have shown in the previous section, standard MOR methods face a major problem when it comes to reducing the dimensionality of simulations containing parameter variations, different physical regimes, or moving features such as discontinuities and fronts. The reducibility of the model is then strongly related to space discretization, which often implies a poor model reduction. Typical applications facing this issue are the representation of a fissure or the displacement of a heat source. Both imply a localized discontinuity leading to the failure of classical MOR methods. In the last decade, several authors proposed different approaches to this problem, especially using the POD. In [41] the authors represent a moving heat-source in 2D using nested-POD and hyperreduction through the discrete empirical interpolation method. A similar application is tackled in [69], also using a hyperreduction approach and a moving frame to represent the heat source. More straightforwardly, in [140] a spatial domain decomposition is proposed to solve a fracture problem using the POD. The ROM is only built on the domain far from the fracture, and consequently far from the highly nonlinear phenomenon leading to the POD failure. Consequently, some solutions exist to overcome the non-reducibility of MOR methods but they are often specific and not easily adaptable. Some have been tested without success in the case of the RFA. Besides, because of the strong coupling between the different physical fields, an error on one of them can be rapidly propagated to the others. As the system is dynamic the error is accumulated and propagated through time. Moreover, as the electrical pulses are driven by the system's state, and notably by the impedance rise appearing near the needle's tip where the model is the most difficult to reduce, for similar initial conditions the ROM and the high fidelity model will have different behaviors. This phenomenon is shown in Figure 7.11.

For these reasons, the route of metamodeling has been chosen. Metamodels are models of models. They allow evaluating only the quantities of interest. The result is then completely uncorrelated from the mesh of the model and from its reducibility. In the remainder of this chapter, we develop a new metamodeling approach to encompass parameter uncertainty during the system identification process.

## 7.4 Creation of the metamodel

### 7.4.1 System identification

In the case of dynamical systems, the metamodeling can be seen as a system identification process. System identification methods aim at building a mathematical model of a dynamical system from measured data, without taking into consideration its underlying physical behaviors. Mathematically, it can be formulated as inferring a function $f$ such as

$$\frac{d}{dt}x(t) = f(x(t), \boldsymbol{v}(t)), \tag{7.24}$$

where the scalar $x(t) \in \mathbb{R}$ represents the state of the system at time $t$, $\boldsymbol{v}(t) \in \mathbb{R}^{n_v}$ contains measurements of the system and the function $f(x(t), \boldsymbol{v}(t))$ describes its dynamic behavior. This procedure can be seen as an inverse problem as the measurements are often noisy and the model is not exact. As said in Chapter 4, regularization approaches are commonly used to solve such a problem and, according to [157], they offer interesting perspectives for estimation of dynamical systems. In particular, as pointed out in [262], the prime use of regularization is not only to fit the data but also to allow more parameters in the model structure than actually necessary, in order to select only the relevant ones. Indeed, most physical systems have only a few relevant terms that define their dynamics. However, the structure of the model cannot be known a priori and unnecessary parameters can have an adverse effect on the solution. That is why sparsity promoting techniques are an interesting approach to simultaneously select the parametric representation of

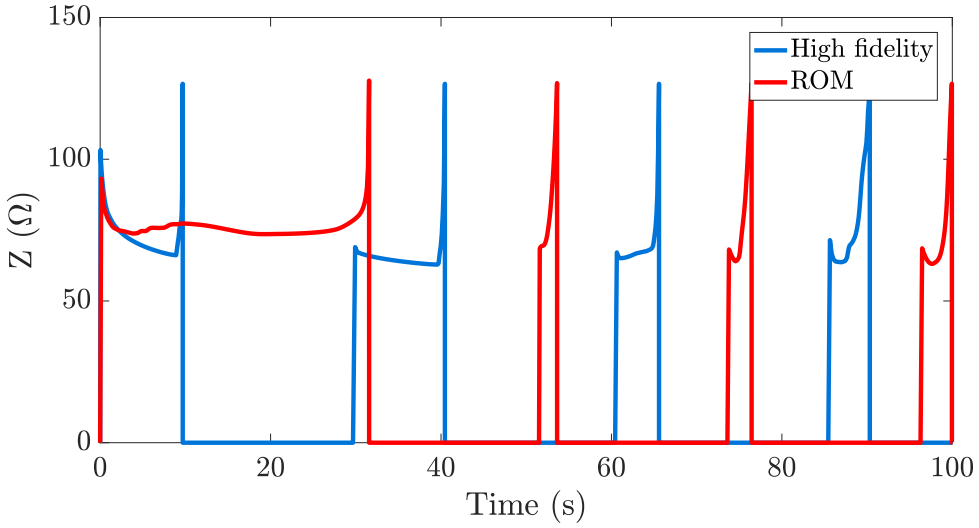


Figure 7.11: Comparison of the impedance evolution over time for the high fidelity model and the ROM. The same set of initial parameters has been used for both models, with the mean stochastic parameters detailed in Table 7.2 and an initial current intensity of 1.5 A. The Goldberg protocol is employed to drive the pulses. The ROM has been built with a RIC of 75% using $k = 1$ (see Table 7.3 for the corresponding number of modes). Note that the coagulation field is not reduced as its computation does not involve the solving of a linear system (see Equation 7.18). The number of modes is very low but, as no hyperreduction has been used, 8 minutes have been necessary to simulate a 100 seconds process with the ROM (against several hours for the high fidelity simulation). The comparison of the two results shows that the pulse trains are very different between the two simulations. It is interesting to note that around the time $t = 10\,\mathrm{s}$, at the end of the first pulse of the high fidelity model, the impedance of the ROM increases slightly before decreasing. It is due to the fact that the POD did not capture well the behavior of the physical fields near the electrode's tip, where the impedance rise happens. It creates a shift between the pulse trains of the two models and, in the long term, a different evaluation of the necrotic area.

the model while fitting the data. In this context, the sparse identification of nonlinear dynamics (SINDy) algorithm has been introduced in [44] as an efficient means to infer the governing equations of a system.

SINDy uses sparsity-promoting techniques to extract from raw data the expression of $f(x(t), \boldsymbol{v}(t))$. The first step is to collect data on the temporal evolution of the system state $x$, its derivative $\dot{x} = \frac{d}{dt}x$ and the measurements $\mathbf{v}$ and to store them into matrices, such as

$$\boldsymbol{x} = \begin{bmatrix} x(t_1) \\ x(t_2) \\ \vdots \\ x(t_m) \end{bmatrix}, \dot{\boldsymbol{x}} = \begin{bmatrix} \dot{x}(t_1) \\ \dot{x}(t_2) \\ \vdots \\ \dot{x}(t_m) \end{bmatrix}, \text{and } \mathbf{V} = \begin{bmatrix} \boldsymbol{v}^T(t_1) \\ \boldsymbol{v}^T(t_2) \\ \vdots \\ \boldsymbol{v}^T(t_m) \end{bmatrix} = \begin{bmatrix} v_1(t_1) & v_2(t_1) & \cdots & v_{n_v}(t_1) \\ v_1(t_2) & v_2(t_2) & \cdots & v_{n_v}(t_2) \\ \vdots & \vdots & \ddots & \vdots \\ v_1(t_m) & v_2(t_m) & \cdots & v_{n_v}(t_m) \end{bmatrix}. \tag{7.25}$$

where $m$ is the number of time steps considered. Note that most of the time the derivative must be numerically computed, possibly leading to noisy estimates. In [44] the authors propose to use the total variation regularization [245] to denoise the derivative [53]. Thus, we employ this method. Next, a matrix $\Theta(\boldsymbol{x}, \mathbf{V})$ is generated such as each one of its columns is the solution of a user-defined function depending on the variables $(x, v_1, \cdots, v_{n_v})$. Any function and combination of functions can be used, here the choice is restrained to polynomials of degree $d \in \mathbb{N}$ with all their possible combinations. Hence, a row of $\Theta$ will contain all the following values: $x(t_i)^{d_1} \times v_1(t_i)^{d_2} \times \ldots \times v_{n_v}(t_i)^{d_{n_v+1}} \quad \forall [d_1, \cdots, d_{n_v+1}] \in [\![0, d]\!]^{n_v+1}$, leading to $n = (d+1)^{n_v+1}$ possibilities. A user-defined function must not be repeated. Once $\Theta(\boldsymbol{x}, \mathbf{V})$ is computed, each one of its columns will represent a

candidate function for the right-hand side of Equation 7.24. To choose the active functions among all possible candidates a sparse regression is done on the linear system

$$\dot{\boldsymbol{x}} = \Theta(\boldsymbol{x}, \mathbf{V})\boldsymbol{\xi}\,. \tag{7.26}$$

$\boldsymbol{\xi}$ is a sparse vector determining the functions present in $\Theta$ used to represent the corresponding system's state derivative. Several methods exist to perform sparse regressions, in the original paper the Lasso method [277] was used. Here we consider the focal underdetermined system solver (FOCUSS) method, detailed in the next section.

**Remark 7.2** (*Standard SINDy expression*). SINDy was initially developed using a simpler of form of Equation 7.24, such as

$$\frac{d}{dt}\boldsymbol{x}(t) = f(\boldsymbol{x}(t))$$

where $\boldsymbol{x}$ is a vector of real values describing the system state. In this chapter the expression is adapted to the case where a vector of measure $\boldsymbol{v}$ is introduced as a variable of $f$. This approach is coined as SINDY with control in [45].

### 7.4.2 Sparse approximation with the focal underdetermined system solver

*The FOCUSS algorithm has already been introduced earlier in the thesis, in Chapter 5 Section 5.3.3.3. We repeat here some notions for the sake of completeness.*

**Sparse approximation** Sparse approximations, or sparse regressions, are methods designed to obtain the sparsest representation of the solution $\boldsymbol{\xi}$ to the $m \times n$ $(m < n)$ underdetermined linear system of equations described in Equation 7.26. The matrix $\Theta$ is commonly pinned as the dictionary and each one of its columns is referred to as an atom. The sparsity constraint in Equation 7.26 can be reformulated as a minimization problem

$$\begin{aligned} &\min_{\boldsymbol{\xi}\in\mathbb{R}^n} \|\boldsymbol{\xi}\|_p \\ &\text{subject to } \dot{\boldsymbol{x}} = \Theta\boldsymbol{\xi} \end{aligned} \tag{7.27}$$

where $\|\bullet\|_p$ stands for the $\ell^p$-norm. Intuitively, $p = 0$ is the simplest norm to chose. This norm can be interpreted as the number of non-zero terms in $\boldsymbol{\xi}$ and is a direct measure of the sparsity. However, solving this problem is NP-hard [192], that is why methods using $\ell^p$-norms with $p \leq 1$ have been developed. Note that for $p < 1$, $\|\bullet\|_p$ is not a true norm. Thus, this norm-like diversity measure is pinned as "$\ell_{(p\leq 1)}$ diversity measure" in [236].

**FOCUSS** The initial FOCUSS algorithm was introduced in [106] in a noise-free framework. In this context, FOCUSS gives an exact solution to the problem defined in Equation 7.27. However, it can be desirable to relax the equality in Equation 7.26 by introducing a noise vector $\boldsymbol{\nu}$ such as

$$\Theta\boldsymbol{\xi} = \dot{\boldsymbol{x}} + \boldsymbol{\nu} \tag{7.28}$$

to get sparser solutions or to encompass noise in the data. A regularized version of the algorithm was then developed [235], leading to the iterative algorithm:

$$\mathbf{W}^{k+1} = \operatorname{diag}\left(\left|\xi_i^k\right|^{1-\frac{p}{2}}\right) \tag{7.29}$$

$$\boldsymbol{q}^{k+1} = \arg\min_{\boldsymbol{q}} \left\|\Theta\mathbf{W}^{k+1}\boldsymbol{q} - \dot{\boldsymbol{x}}\right\|_2^2 + \gamma\|\boldsymbol{q}\|_2^2 \tag{7.30}$$

$$\boldsymbol{\xi}^{k+1} = \mathbf{W}^{k+1}\boldsymbol{q}^{k+1} \tag{7.31}$$

where $k \in \mathbb{N}^+$ is the iteration number and $\gamma \in \mathbb{R}^+$ is a regularization parameter. High values of $\gamma$ will promote the sparsity of $\boldsymbol{\xi}$ whereas low values will compel the equality $\Theta\boldsymbol{\xi} = \dot{\boldsymbol{x}}$.

**Finding the regularization parameter** Several methods were proposed to automatize the selection of $\gamma$, notably in [234]. In this thesis, we follow the route described in [302] using the generalized cross-validation (GCV) technique. The GCV states that the optimal value of $\gamma$ should minimize the GCV function

$$V(\gamma) = \frac{||\dot{\boldsymbol{x}} - \Theta\boldsymbol{\xi}||_2^2}{(\frac{1}{m}\,\mathrm{Tr}(\mathbf{I} - \mathbf{P}_\gamma))^2} \tag{7.32}$$

where Tr stands for the Trace and $\mathbf{P}_\gamma$ is the influence matrix derived from $\Theta\boldsymbol{\xi} = \mathbf{P}_\gamma\dot{\boldsymbol{x}}$. After some developments [302], the equation becomes for a given iteration $k$:

$$V^k(\gamma) = \frac{\sum_{i=1}^m \mu_i^2 \left(\frac{\gamma}{\sigma_i^2+\gamma}\right)^2}{\frac{1}{m}\left(\sum_{i=1}^m \frac{\gamma}{\sigma_i^2+\gamma}\right)^2} \tag{7.33}$$

where $\sigma_i = \mathbf{\Sigma}_{ii}$ and $\mu_i = \left(\mathbf{U}^T\dot{\boldsymbol{x}}\dot{\boldsymbol{x}}^T\mathbf{U}\right)_{ii}$ with $[\mathbf{U}, \mathbf{\Sigma}, \mathbf{V}] = \mathrm{svd}(\Theta\mathbf{W}_k)$ such as $\Theta\mathbf{W}_k = \mathbf{U}\mathbf{\Sigma}\mathbf{V}^T$. The function svd denotes the SVD. Hence, at each iteration, $\gamma^k$ is determined following

$$\gamma^k = \underset{\gamma_{min}<\gamma<\gamma_{max}}{\arg\min}\; V^k(\gamma)\,. \tag{7.34}$$

The golden section search method is used to determine the optimal value. The boundaries $\gamma_{min}$ and $\gamma_{max}$ can be estimated following the method proposed in [234].

**FOCUSS initialization** For any initialization of $\dot{\boldsymbol{x}}$ FOCUSS will find a solution. This latter can be either a stable, saddle or an unstable fixed point [106] and is not ensured to be optimal. Consequently several approaches can be considered, we list hereafter some possibilities:

$$\begin{aligned}
&\boldsymbol{\xi}^0 = \Theta^+\dot{\boldsymbol{x}} && \text{, where } \Theta^+ \text{ denotes the pseudoinverse}\\
&\boldsymbol{\xi}^0 = \mathrm{rand}(n,1) && \text{, where rand generates } n \text{ uniform randoms in } [0,1]\\
&\boldsymbol{\xi}^0 = \mathrm{ones}(n,1) && \text{, where ones generates a column vector of ones of size } n.
\end{aligned}$$

The first approach is equivalent to initialize with the least-squares solution of the system. The second one is a purely random initialization and the third applies the same initial weight to all atoms of the dictionary. Note that the atoms do not have the same norm, that can lead to overestimating the weights of some atoms in FOCUSS. If it is not desired the columns of $A$ must be normalized first, as discussed in Chapter 5 Section 5.3.3.3.

**FOCUSS for large atoms** When creating the dictionary $\Theta$, the condition $m < n$ on its size is not always satisfied in the case where its creation is conditioned by another method, such as SINDy. However, this does not mean that its rank $r_\theta$ is superior to $n$. In this case, the SVD can be performed a priori to reduce the number of rows. By considering $[\mathbf{U}_\Theta, \mathbf{\Sigma}_\Theta, \mathbf{V}_\Theta] = \mathrm{svd}(\Theta)$ such as $\Theta = \mathbf{U}_\Theta\mathbf{\Sigma}_\Theta\mathbf{V}_\Theta^T$ we write

$$\dot{\boldsymbol{x}}_r = \mathbf{U}_{\Theta t}^T\dot{\boldsymbol{x}} \quad \text{and} \quad \Theta_r = \mathbf{U}_{\Theta t}^T\Theta = \mathbf{\Sigma}_{\Theta t}\mathbf{V}_\Theta^T$$

where $\mathbf{U}_{\Theta t}$ is the truncation of $\mathbf{U}_\Theta$ to the $r_\theta$-th column and $\mathbf{\Sigma}_{\Theta t}$ is the truncation of $\mathbf{\Sigma}_\Theta$ to the $r_\theta$-th row. FOCUSS is then applied to solve

$$\begin{aligned}
&\min\nolimits_{\boldsymbol{\xi}\in\mathbb{R}^n} \|\boldsymbol{\xi}\|_p\\
&\text{subject to } \dot{\boldsymbol{x}}_r = \Theta_r\boldsymbol{\xi}
\end{aligned} \tag{7.35}$$

where $p \leq 1$, which is equivalent to Equation 7.27.

**Remark 7.3** (*Equivalence between Equations 7.27 and 7.35*). The projection of the dictionary $\Theta$ and the measurement vector $\boldsymbol{x}$ onto the principal modes of the SVD decomposition only impact the FOCUSS algorithm in Equation 7.30 which now reads

$$\boldsymbol{q}^{k+1} = \arg\min_{\boldsymbol{q}} \left\|\Theta_r \mathbf{W}^{k+1}\boldsymbol{q} - \dot{\boldsymbol{x}}_r\right\|_2^2 + \gamma\|\boldsymbol{q}\|_2^2 . \tag{7.36}$$

Or, knowing that $\Theta = \mathbf{U}_\Theta \boldsymbol{\Sigma}_\Theta \mathbf{V}_\Theta^T$ and that $\mathbf{U}_\Theta$ and $\mathbf{V}_\Theta$ are orthogonal:

$$\begin{aligned}\left\|\Theta\mathbf{W}^{k+1}\boldsymbol{q} - \dot{\boldsymbol{x}}\right\|_2^2 &= \|\mathbf{U}_\Theta^T\left(\boldsymbol{\Theta}\mathbf{V}_\Theta\mathbf{V}_\Theta^T\mathbf{W}^{k+1}\boldsymbol{q} - \dot{\boldsymbol{x}}\right)\|_2^2 \\ &= \|\boldsymbol{\Sigma}_\Theta \underbrace{\mathbf{V}_\Theta^T\mathbf{W}^{k+1}\boldsymbol{q}}_{=\boldsymbol{z}} - \mathbf{U}_\Theta^T\dot{\boldsymbol{x}}\|_2^2 \\ &= \underbrace{\sum_{i=1}^{r_\theta}\left(\sigma_{\Theta,i}z_i - \boldsymbol{u}_{\Theta,i}^T\dot{\boldsymbol{x}}\right)^2}_{\|\boldsymbol{\Theta}_r\mathbf{W}^{k+1}\boldsymbol{q}-\dot{\boldsymbol{x}}_r\|_2^2} + \underbrace{\sum_{i=r_\theta+1}^{m}\left(\boldsymbol{u}_{\Theta,i}^T\dot{\boldsymbol{x}}\right)^2}_{\text{constant}} .\end{aligned}$$

where $\boldsymbol{u}_{\Theta,i}$ is the $i$-th column of $\mathbf{U}_\Theta$ and $\sigma_{\Theta,i}$ is the $i$-th singular value of $\Theta$. The last equality is due to the fact that $\sigma_{\Theta,i} = 0\,\forall i > r_\theta$, as $r_\theta$ is the rank of $\Theta$. Hence solving Equation 7.30 is equivalent to solve Equation 7.36, and solving Equation 7.27 is equivalent to solve Equation 7.35.

### 7.4.3 Sparse regression for system identification under parameter uncertainty

**Problem statement** Let's consider a dynamical system depending on time-independent stochastic parameters $\boldsymbol{\theta}$ such as

$$\dot{x}(t) = f(x(t), \boldsymbol{v}(t); \boldsymbol{\theta}) . \tag{7.37}$$

One would like to estimate the average dynamical response of the system with respect to the parameters $\boldsymbol{\theta}$. Based on the SINDy method, we developed a new approach to include the variability of the parameters, coined as stochastic sparse regression (SSR) in the rest of this chapter. The first step is to collect a dataset of snapshots $\boldsymbol{x}^i$ ( $i \in [\![1, n_s]\!]$ ), i.e. solutions over time of the model for values of $\boldsymbol{\theta}$ picked from their respective probability distributions. We assume all snapshots have the same temporal sampling. The solutions are then vectorized following

$$\tilde{\boldsymbol{x}} = \text{vec}([\boldsymbol{x}^1, \cdots, \boldsymbol{x}^{n_s}]) = \begin{bmatrix} x^1(t_1) \\ \vdots \\ x^1(t_m) \\ \vdots \\ x^{n_s}(t_1) \\ \vdots \\ x^{n_s}(t_m) \end{bmatrix} . \tag{7.38}$$

The measurement vectors $\mathbf{v}^i$ are stacked similarly to build the matrix $\tilde{\mathbf{V}}$. The corresponding dictionary $\Theta(\tilde{\boldsymbol{x}}, \tilde{\mathbf{V}})$ is then built and the derivative vector $\dot{\tilde{\boldsymbol{x}}}$ is computed. The sparse regression system reads

$$\dot{\tilde{\boldsymbol{x}}} = \Theta(\tilde{\boldsymbol{x}}, \tilde{\mathbf{V}})\boldsymbol{\xi} . \tag{7.39}$$

A common way to write the sparse approximation problem defined by Equation 7.27 is

$$\hat{\boldsymbol{\xi}} = \arg\min_{\boldsymbol{\xi}} \left\|\Theta\boldsymbol{\xi} - \dot{\tilde{\boldsymbol{x}}}\right\|_2^2 + \gamma\|\boldsymbol{\xi}\|_p \quad \text{with } p \leq 1. \tag{7.40}$$

In this form, the problem appears clearly as a least-squares regression with a penalization term on the sparsity of the vector $\boldsymbol{\xi}$. Doing a sparse regression on Equation 7.39 is then equivalent to find the best subset of functions within the dictionary that averages the dataset of snapshots in the least-squares sense. Nonetheless, when looking for the average solution with respect to the parameters $\boldsymbol{\theta}$, doing a standard sparse approximation results in a biased solution. This is caused by the non-uniform distribution of the $x(t)$ and $(v_1(t), \cdots, v_{n_v}(t))$ in the dictionary $\Theta$. A standard least-squares regression on temporal data will ideally require a uniform sampling over time if the same confidence must be attributed at any instant. Equivalently, we want to put the same trust in any set of variables $\mathcal{S} = (x(t), v_1(t), \cdots, v_{n_v}(t))$ used to infer the least-squares solution. Nonetheless, the apparent distribution of $\mathcal{S}$ in $\Theta$ is dependent on the time sampling. Hence, the least-squares regression will create a model more reliable where the density of data is high but will not reflect the desired relationship between $\mathcal{S}$ and the $\dot{\tilde{x}}$. For sets of data belonging to areas where few points are available the model will not be trustworthy. To get a more robust model the apparent distribution of the $\mathcal{S}$ is "uniformized" using a weighted least-squares approach.

**Weighted least-squares for sparse regression** First, a kernel density estimation technique based on a product of Gaussian kernel functions [256] is used to find the multivariate probability density function $\Psi_{\mathbf{h}}(x, v_1, \cdots, v_{n_v})$ of $\mathcal{S}$. It reads in its general form

$$\Psi_{\mathbf{h}}(\boldsymbol{u}) = \frac{1}{N} \sum_{i=1}^{N} K_{\mathbf{H}} \left( \boldsymbol{u} - \mathcal{S}_i \right) \tag{7.41}$$

where $N = n_s m$, $\boldsymbol{u} = (u_1, \cdots, u_{n_v+1})^T$ and $\mathcal{S}_i = (x_i, v_{1i}, \cdots, v_{n_v i})^T$ is the set of parameters corresponding to the $i$-th solution drawn from the dataset of snapshots. $\mathbf{H}$ is the bandwidth symmetric positive definite $(n_v + 1) \times (n_v + 1)$ matrix. $K_{\mathbf{H}}(\boldsymbol{u}) = |\mathbf{H}|^{-1/2} K\left(\mathbf{H}^{-1/2}\boldsymbol{u}\right)$ and $K$ is the kernel function. For the sake of simplicity, a diagonal bandwidth matrix is used such as $\mathbf{H} = \mathrm{diag}(h_1^2, \cdots, h_{n_v+1}^2)$. Thus, the formulation of $\Psi_{\mathbf{h}}(\boldsymbol{u})$ can be detailed as

$$\Psi_{\mathbf{h}}(\boldsymbol{u}) = \frac{1}{N h_1 \cdots h_{n_v+1}} \sum_{i=1}^{N} \prod_{j=1}^{n_v+1} k\left( \frac{u_j - \mathcal{S}_{ij}}{h_j} \right) \tag{7.42}$$

where $k(u) = \frac{1}{\sqrt{2\pi}} e^{-\frac{1}{2}u^2}$ is the expression of the Gaussian kernel. Finally, the weight matrix $\mathbf{W} = \mathrm{diag}(w_1, \cdots, w_N)$ is created such as

$$w_i = \frac{N}{\sum_{k=1}^{N} \left(1/\Psi\left(x_i, v_{1i}, \cdots, v_{n_v i}\right)\right)} \frac{1}{\Psi\left(x_i, v_{1i}, \cdots, v_{n_v i}\right)} \,. \tag{7.43}$$

If the initial distribution of the parameters is uniform the weights will be equal to one. Otherwise, large weights will be associated with points in low-density areas and small ones to points located in high-density areas. By introducing the weighting into the sparse regression, Equation 7.40 becomes

$$\hat{\boldsymbol{\xi}} = \arg\min_{\boldsymbol{\xi}} \left\| \mathbf{W}^{\frac{1}{2}} \left( \Theta\boldsymbol{\xi} - \dot{\tilde{\boldsymbol{x}}} \right) \right\|_2^2 + \gamma \|\boldsymbol{\xi}\|_p \quad \text{with } p \leq 1. \tag{7.44}$$

In the weighted least-squares formalism, the weights are ideally equal to the reciprocal of the variance of the measurements. In our case, it means that we are going to tolerate a higher error in areas where the data is dense and a smaller one where the data is sparse. This could be harmful in the presence of outliers. Here as all our data come from simulations, we can suppose that there is no outlier.

A simple use case is given below to illustrate and give more insight into the inverse density weighting principle.

**Example 7.1** (*Least-squares fitting despite misspecification of distribution, a one dimensional empirical case*). Let consider a vector $\boldsymbol{x}_u = (x_u^1, \cdots, x_u^n)$ where each $x_u^i$ is drawn from the uniform distribution in $(0,1]$, its probability density function is noted $f_U(x_u)$. We introduce the function

$$\begin{array}{rccc} g & : (0,1] & \longrightarrow & (0,1] \\ & x & \longrightarrow & x^3 \end{array} \tag{7.45}$$

and the vector $\boldsymbol{x}_g = (x_g^1, \cdots, x_g^n)$ such as $x_g^i = g(x_u^i)$. Hence, we have two sampling of the domain $(0,1]$. The first, described by $\boldsymbol{x}_u$, is uniform and the second, described by $\boldsymbol{x}_g$, has the probability density function $f_G(x_g)$. Its expression can be computed knowing that

$$F_U(x_u) = \int_{-\infty}^{t} f_U(t)dt = P(X_u \leq x_u)$$

and

$$F_G(x_g) = P(X_g \leq x_g) = P\left(X_u^3 \leq x_g\right) = P(X_u \leq x_g^{\frac{1}{3}}) = F_U(x_g^{\frac{1}{3}})\,.$$

As $f_G(x_g) = \frac{d}{dx}F_G(x_g)$, hence

$$f_G(x_g) = \frac{d}{dx_g}F_U(x_g^{\frac{1}{3}}) = \frac{1}{3}F_U(x_g^{-\frac{2}{3}})\,.$$

Finally, since $f_U$ is the uniform distribution

$$f_G(x_g) = \frac{x_g^{-\frac{2}{3}}}{3}\,.$$

Figure 7.12 shows the distribution of $x_g$.

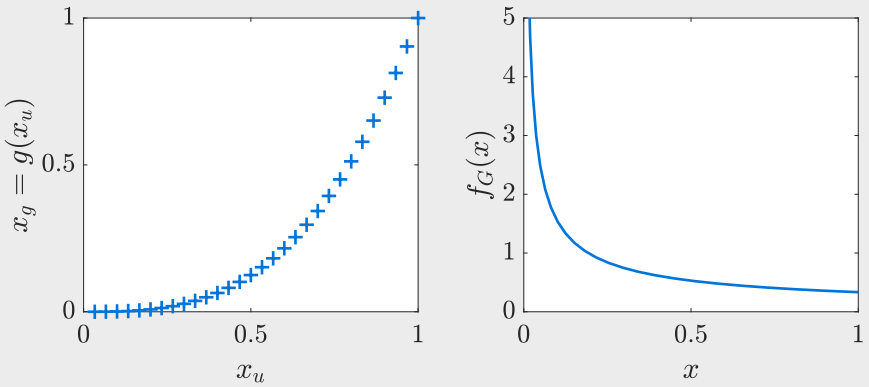


Figure 7.12: On the left: $x_g$ versus $x_u$. On the right: probability density function of $x_g$. The values of $x_g$ are more represented toward low values of $x$.

We define the function

$$\begin{array}{rccc} \mathcal{T} & : (0,1] & \longrightarrow & (-1,1) \\ & x & \longrightarrow & 1 + \tanh\left(-10 \times \mathrm{abs}\left(x - \alpha\right)\right) \end{array} \tag{7.46}$$

where $\alpha$ belongs to the normal distribution $\mathcal{N}(0.5, 0.2)$. We want to find the least-squares approximation of $\mathcal{T}$ on $(0,1]$ for different realizations $\alpha$. The goal is to show empirically that the least-squares regression is different depending on the sampling distribution of $x$, but that it is possible to approximate one least-squares regression with the other using a weighting strategy. This theme has been tackled in [195] for linear least-squares. The different sampling cases are illustrated in Figure 7.13.

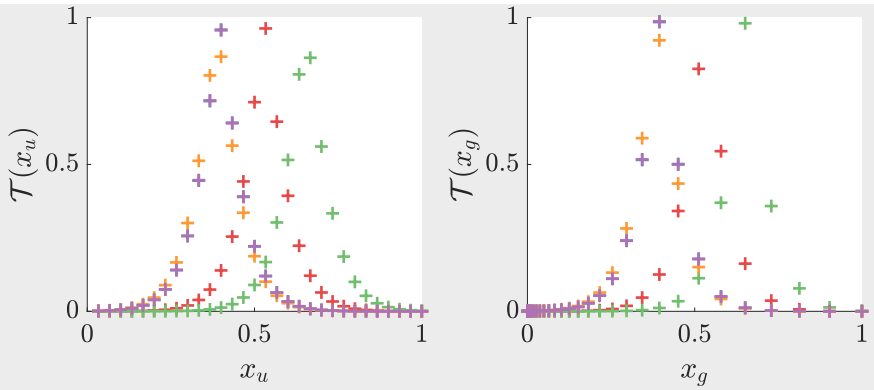


Figure 7.13: Computation of $\mathcal{T}$ for different values of $\alpha$ drawn from $\mathcal{N}(0.5, 0.2)$. On the left are represented the data computed on $\boldsymbol{x}_u$ and on the right computed on $\boldsymbol{x}_g$. For the sake of clarity, only 5 different drawings of $\alpha$ are presented with 30 data points each. A different color is used for each draw. The different samplings imply different points densities that impact the least-squares regressions.

First, a database of random vectors $\boldsymbol{x}_u^i \in \mathbb{R}^{500}$ $(i \in [\![1, 100]\!])$ drawn from $f_U(x_u)$ is generated. To each vector is associated an $\alpha_i \in \mathcal{N}(0.5, 0.2)$. Next, the following vectors are defined: $\boldsymbol{x}_g^i = g(\boldsymbol{x}_u^i)$, $\boldsymbol{y}_u^i = \mathcal{T}(\boldsymbol{x}_u^i; \alpha_i)$ and $\boldsymbol{y}_g^i = \mathcal{T}(\boldsymbol{x}_g^i; \alpha_i)$. Three least-squares approximations using polynomials of order 2 are then performed. The first one reads

$$\hat{\boldsymbol{\beta}}_u = \underset{\boldsymbol{\beta}_u}{\arg\min} ||\mathbf{Y}_u - \mathbf{X}_u \boldsymbol{\beta}_u||_2^2 \tag{7.47}$$

where $\mathbf{Y}_u = \text{vec}([\mathbf{y}_u^1, \cdots, \mathbf{y}_u^{100}])$ and $\mathbf{X}_u = \big((1, \cdots, 1)^T, \text{vec}([\boldsymbol{x}_u^1, \cdots, \boldsymbol{x}_u^{100}]), \text{vec}([\boldsymbol{x}_u^1, \cdots, \boldsymbol{x}_u^{100}]) \circ \text{vec}([\boldsymbol{x}_u^1, \cdots, \boldsymbol{x}_u^{100}])\big)$ , $\circ$ denotes the Hadamard product. This solution is considered as the ground truth. The second is written

$$\hat{\boldsymbol{\beta}}_g = \underset{\boldsymbol{\beta}_g}{\arg\min} ||\mathbf{Y}_g - \mathbf{X}_g \boldsymbol{\beta}_g||_2^2 \tag{7.48}$$

where $\mathbf{Y}_g$ and where $\mathbf{X}_g$ are defined similarly than $\mathbf{Y}_u$ and $\mathbf{X}_u$. The last one is the weighted version of Equation 7.48:

$$\hat{\boldsymbol{\beta}}_w = \underset{\boldsymbol{\beta}_w}{\arg\min} ||\mathbf{W}^{\frac{1}{2}}(\mathbf{Y}_g - \mathbf{X}_g \boldsymbol{\beta}_w)||_2^2 \tag{7.49}$$

where $\mathbf{W}$ is defined as explained in Equation 7.43 using the probability density function $f_G$. Note that in this example the probability density function is known analytically. In the cases where this function is unknown a kernel density estimation method must be used. Each solution $\hat{\boldsymbol{\beta}}_j$ $(j \in \{u, g, w\})$ defines a function $\mathcal{L}_j$, that is

$$\mathcal{L}_j(x) = \hat{\boldsymbol{\beta}}_j[1] + \hat{\boldsymbol{\beta}}_j[2]x + \hat{\boldsymbol{\beta}}_j[3]x^2 \,. \tag{7.50}$$

The solutions are plotted in Figure 7.14. It is clear that $\mathcal{L}_u$ and $\mathcal{L}_w$ are almost equal even though their variables have different distributions. Hence, for non-uniform distributions of $x$, using Equation 7.49 is equivalent to approximate Equation 7.47.

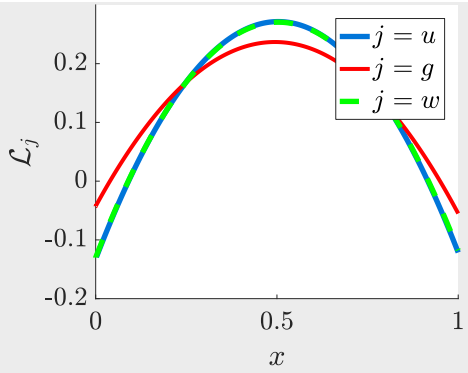


Figure 7.14: Least-squares regressions of $\mathcal{T}$ for different realizations of the stochastic variable $\alpha$. A polynomial of order 2 is used to perform the regression. Three regressions are represented. The first, labeled $u$, uses a uniform distribution of $x$, i.e. $\boldsymbol{x}_u$, and is used as a ground truth. The last two, labeled $n$ and $w$, are done using the vector $\boldsymbol{x}_n$. The third is done using a weighted least-squares regression.

## 7.5 Application of stochastic sparse regression to a simple test case

In this section we propose to test the ability of the SSR to find a known dynamic behavior using synthetic data and fixed boundary conditions, i.e. the measurements are independent of the system's state.

To this end, we consider two functions

$$v_1(t) = \cos\left(\frac{\pi t}{5}\right) \quad \text{and} \quad v_2(t) = \tanh\left(\frac{t-50}{10}\right)$$

representing the measurement vector $\boldsymbol{v}(t) = (v_1(t), v_2(t))$ (see Figure 7.15a). The function $f$ representing the dynamic behavior of this system is defined as

$$\dot{x}(t) = f(x(t), \boldsymbol{v}(t); \boldsymbol{\theta}) = \theta_1 x(t) v_1(t) + \theta_2 v_1(t)^2 v_2(t)\,, \tag{7.51}$$

where $\boldsymbol{\theta} = (\theta_1, \theta_2)$ are the stochastic parameters such as $\theta_1 \in \mathcal{N}(0.2, 0.05)$ and $\theta_2 \in \mathcal{N}(0.4, 0.1)$, and $\mathcal{N}$ denotes the normal distribution. This ordinary differential equation is solved for $t \in [0, 100]$ sampled at a frequency of 10 Hz. A database of 50 solutions is computed. They are initialized with $x = 0$ at $t = 0$ and values of $(\theta_1, \theta_2)$ chosen from their respective distributions. The mean parameters $(\theta_1^m, \theta_2^m)$ shown in Table 7.4 are computed using a standard least-squares regression (see Figure 7.15b) such as

$$(\theta_1^m, \theta_2^m) = \arg\min_{\boldsymbol{\theta}} ||\dot{\tilde{\boldsymbol{x}}} - f(\tilde{\boldsymbol{x}}, \tilde{\boldsymbol{v}}; \boldsymbol{\theta})||_2^2\,. \tag{7.52}$$

where the notation $\tilde{\bullet}$ represents the vectorization of the elements of the database. Thus, the aim is to rediscover this ground truth values thanks to the SSR, without knowing the formulation of $f$ a priori.

The parameters of the SSR algorithm are arbitrarily chosen such as $p = 0.5$ for the $\ell^p$-norm in FOCUSS, $[\gamma_{min}, \gamma_{max}] = [10^{-2}, 10^4]$ for the GCV technique used to determine $\gamma$, the atoms of the dictionary $\Theta$ are normalized and the vector $\boldsymbol{\xi}^0$ is randomly initialized. We do not use the weighted least-squares as we compare the results with a standard least-squares regression. Polynomials of degree $d = 2$ are used to build the dictionary $\Theta$, consequently, it contains the candidate functions $xv_1$ and $v_1^2 v_2$ among 26 others. As the SSR is randomly initialized, the method is run 100 times to maximize the probability of finding the sparsest solution. The sparsity for each run is reported in the histogram in Figure 7.16a. By choosing the sparsest solution, we find the same formulation

of $f$ than in Equation 7.51 with the coefficients reported in Table 7.4. The solution obtained with the SSR is compared to the ground truth in Figure 7.16b, it attests to the good quality of the SSR's solution.

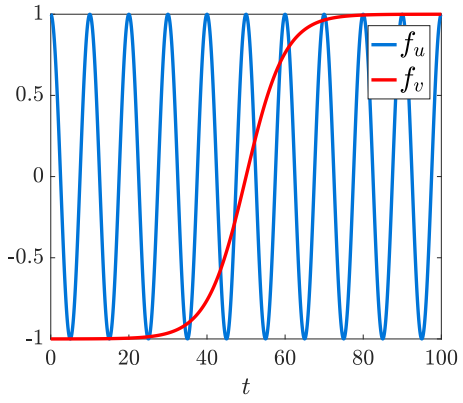


(a) Functions $v_1$ and $v_2$ over time $t$.

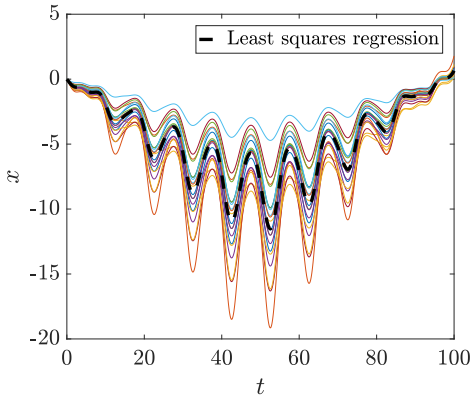


(b) Database of the 50 solutions. The least-squares approximation is also represented with a black dotted line.

Figure 7.15: Representation of the measurement functions (on the left) and of the behavior of $x$ for different values of the parameters $(\theta_1, \theta_2)$ (on the right).

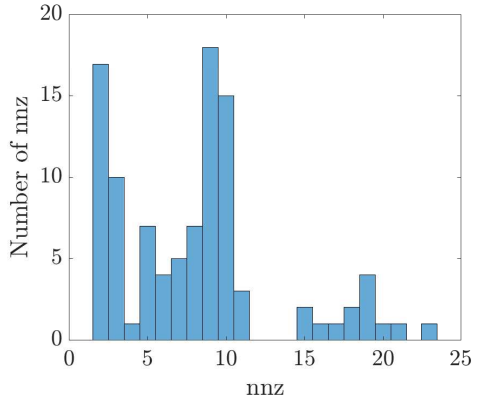


(a) Histogram of the number of non-zero values contained in the solution of each run of the SSR.

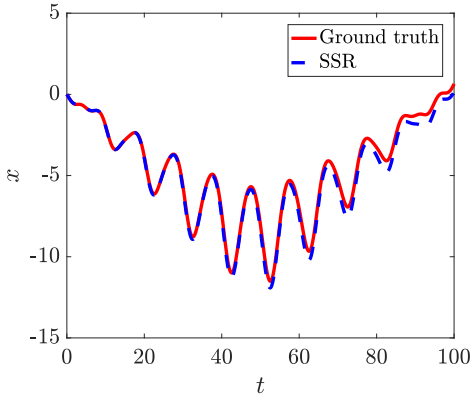


(b) Comparison between the ground truth solution computed with the least-squares regression and the SSR's solution. For this latter the sparsest solution has been considered as the best.

Figure 7.16: Representation of the number of non-zero values in the different runs of the SSR (on the left) and of the comparison between the ground truth and the SSR's solution for nnz = 2 (on the right). A slight shift appears between the ground truth and the SSR's solution for high values of $t$. As the system is dynamic, this is due to the accumulation of the error over $t$.

| | $\theta_1^m$ | $\theta_2^m$ |
|---|---|---|
| Ground truth | 0.222,806 | 0.387,531 |
| SSR | 0.222,804 | 0.387,508 |

Table 7.4: Comparison between the ground truth solution computed with the least-squares regression and the SSR's solution. For this latter, the sparsest solution has been considered as the best.

## 7.6 Application of stochastic sparse regression to the radiofrequency ablation model

### 7.6.1 Database creation

A total of $n_s = 300$ RFA simulations were run following the Monte-Carlo method. A simulation took between a few minutes and several days depending on the boundary conditions, their distribution is represented in Figure 7.17. Indeed, as the electrical pulse train depends on the impedance, each simulation has a specific set of boundary conditions that evolve dynamically with the system. For each simulation, the stochastic parameters were drawn from their distributions described in Table 7.2 using a Latin hypercube sampling [268]. For each set of stochastic parameters an initial current intensity was chosen in $[0.5, 1.5]$ A from a uniform distribution. The pulses were then applied for 10 minutes followed by 2 minutes without pulse. To introduce more variability in the database, the Goldberg protocol was respected in only a quarter of the simulations. In the rest, an "approximate" protocol was considered. The pulses were stopped when the impedance reached a value superior to a random value between 20 and 30 Ω above the baseline. The pulses were then paused for a random time between 10 and 20 seconds. Finally, the new pulses' intensity was chosen to be random between 0 and $\pm 0.1$ A their previous values. The underlying idea is that to extract a better physics of the problem more richness must be added to the data. By using simulations going out of the frame imposed by the Goldberg protocol, the inferred model has more chances to be robust when encountering peculiar situations.

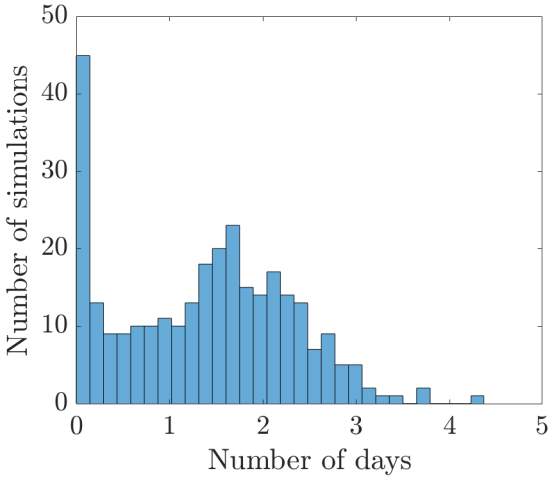


Figure 7.17: Histogram of the computational time of the 300 RFA simulations. The majority of the simulations took around a day and a half. Some simulations were very fast as no impedance rise was detected, which is the more computationally demanding step to simulate. The simulations were performed in parallel by using the high-performance computing resources of the Centrale Nantes Supercomputing Centre on the cluster Liger.

### 7.6.2 Values of interest

In the current RFA application, the system's state $x$ describes the percentage of vascular stasis (see Equation 7.7) above a specific threshold in a specified volume. Two thresholds are considered for the vascular stasis: $DS = 0.90$ and $DS = 0.99$. They correspond to the 90% and 99% probabilities of cell death. Two volumes are also considered, the first contains the tumor and all the healthy tissue within a distance of 5 mm from the tumor surface, and the second contains the tumor plus the healthy tissue within a distance of 10 mm. This allows evaluating the percentage of cell death with two distinct safety margins. Each case is numbered from 1 to 4 (see Table 7.5). The evolution

of the percentage of vascular stasis in the four cases is represented over the whole database in Figure 7.18.

| Case # | Safety margin (mm) | Vascular stasis threshold |
|---|---|---|
| 1 | 5 | 0.90 |
| 2 | 5 | 0.99 |
| 3 | 10 | 0.90 |
| 4 | 10 | 0.99 |

Table 7.5: Numbering of the four quantities of interest depending on the safety margin and the threshold on the degree of vascular stasis.

The measurement vector $\mathbf{v}(t)$ contains the electrical energy $Q(t)$ and the average power $P(t)$ such as $\mathbf{v}(t) = (P(t), Q(t))$. There are computed using

$$Q(t) = \int_{u=0}^{t} Z(u)I(u)^2 du \quad \text{and} \quad P(t) = \frac{Q(t)}{t} \tag{7.53}$$

where $Z$ is the impedance and $I$ the intensity of the pulse. Note that these values are easily available during an operation. Furthermore, the derivative $\dot{x}$ is always positive as the necrosed volume cannot decrease. To enforce the positivity condition Equation 7.24 is particularized as

$$\dot{x} = f(x, Q, P)^2 \Leftrightarrow \sqrt{\dot{x}} = f(x, Q, P)\,, \tag{7.54}$$

where $x$ is the percentage of coagulation above a given vascular stasis threshold in a specific volume encompassing the tumor. Figure 7.19 illustrates the behavior of $x$, $\dot{x}$, $Q$ and $P$ for a specific simulation in the first case of study.

Polynomials of degree $d = 4$ are used to build the dictionary $\Theta$. To enforce the nullity at $t = 0$ the constant is removed. As three variables are used, the dictionary contains 124 atoms.

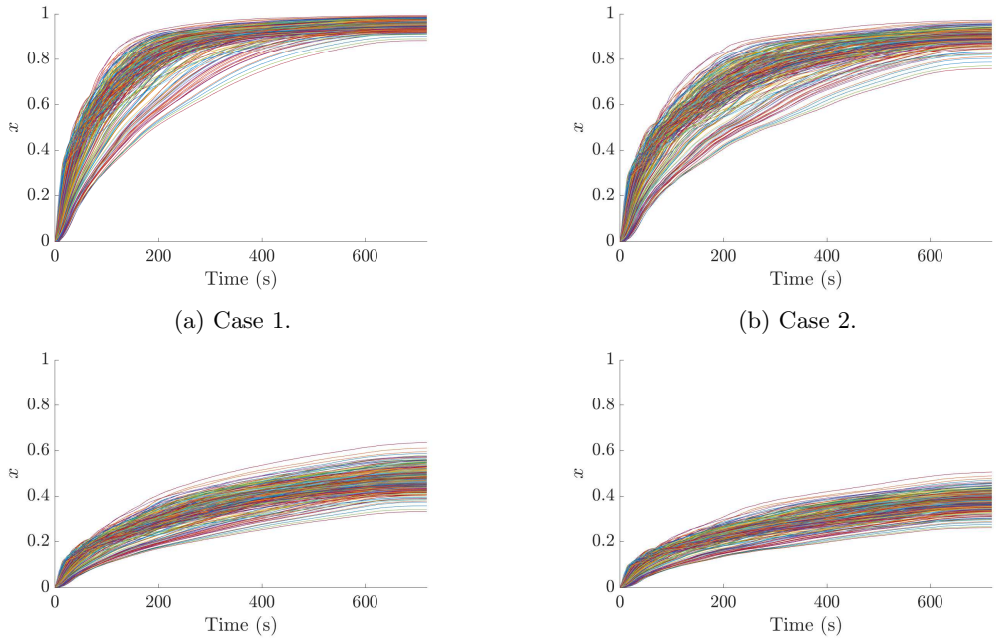


(a) Case 1.

(b) Case 2.

(c) Case 3.

(d) Case 4.

Figure 7.18: Databases of the evolution of the percentage of necrosis for the four cases.

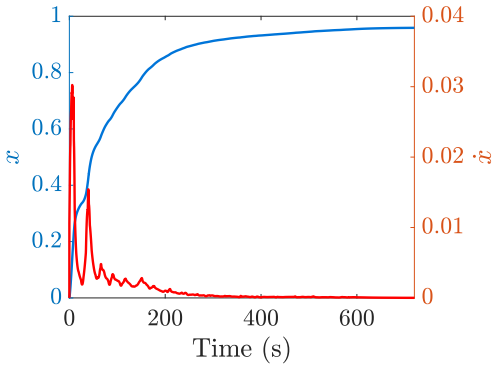


(a) Representation of the percentage of coagulation $x$ and its derivative $\dot{x}$ over time (case #1).

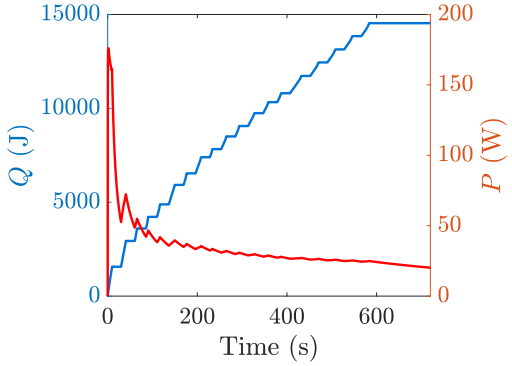


(b) Representation of the electrical energy $Q$ and the average power $P$ over time.

Figure 7.19: Values of interest used in the SSR representation. They are extracted from the simulation using the mean stochastic parameters detailed in Table 7.2, an initial current intensity of 1.5 A and following the Goldberg protocol. The pulses are applied for 10 minutes followed by 2 minutes of rest. The percentage of coagulation and its derivative are shown in the first case of study (see Table 7.5).

### 7.6.3 Error estimation

To evaluate the performance of the method proposed in this chapter, the procedure was applied to a set of $n_{in} = 250$ simulations and the remaining set of $n_{out} = 50$ simulations was used for validation. As explained in Section 7.4.2, FOCUSS solution is not unique and depends on the initialization. Moreover, the solution will depend on the $\ell^p$-norm chosen by the user. To find the best solution, different values of $p \in [0.5, 1]$ were tested. For each $p$, $n_r$ sparse approximations were done using a uniform random initialization. The dictionary was normalized in order to avoid favoring some atoms. The boundaries for the $\gamma$ parameter used in the GCV method were $\gamma_{min} = 10^{-7}$ and $\gamma_{max} = 10^{7}$ (see Equation 7.34). Note that this approach does not ensure to find the global minima. Also, a common bandwidth of $h = 0.2$ was arbitrarily used for the creation of the weights (see Equations 7.42 and 7.43). To evaluate the output of each sparse regression, the error was estimated over the whole left-out set of simulations using

$$E = \frac{1}{n_{out}} \sum_{i=1}^{n_{out}} e_i \quad \text{with} \quad e_i = \frac{||x_i - \hat{x}_i||_1}{t_f} = \int_{t=0}^{t_f} \frac{|x_i(t) - \hat{x}_i(t)|}{t_f} dt \tag{7.55}$$

where $x_i(t)$ is the ground truth solution of the $i$-th simulation, $\hat{x}_i(t) = \int_{u=0}^{t} f(x(u), Q(u), P(u))^2 du$ is the solution computed with the SSR approximation and $t_f = 12\,\text{min}$ is the final time of the simulations. The SSR approximation corresponds to the result obtained with the metamodel by using as inputs the values of $Q$ and $P$ computed with the high fidelity simulation.

We chose this error estimate because it represents the average absolute error at any given time. To get an accurate numerical integration the data were all sampled in time at 5Hz.

## 7.7 Results

The results were generated with a Matlab (The MathWorks, Inc., USA) implementation.

### 7.7.1 Choice of the stochastic sparse regression's function

To choose the optimal solution, $n_r = 50$ random FOCUSS regressions were computed for 50 values of $p$ equally spaced in $[0.5, 1]$. For each sparse approximation the error $E$ (see Equation 7.55) was computed over the whole left-out set of data. Figure 7.20 shows the relation between the error and

the value of $p$ for each case study. In Figure 7.21 is plotted the corresponding average number of non-zero values obtained with FOCUSS. We see that the mean error decreases when $p$ increases, so as its variability. On the contrary, the number of non-zero values and its variability increase with $p$. This is coherent as more non-zero values means that more functions are used to fit the data, thus a better representation. Hence, by using high or low values for $p$ the user can foster its confidence in the sparsity or in the error $E$. Here, the sparsity is fostered and $1,000$ new random FOCUSS were applied using $p = 0.5$. For each case, the sparsity of the sparse approximation is compared to the error $E$. It generates a Pareto front as can be seen in Figure 7.22. The best solution among all the realization was chosen as the one with the lowest error $E$ for a number of non-zero values below or equal to 10. For each case $i$ ($i = 1, \cdots, 4$) the function $f_i$ obtained with SSR is:

- $f_1(x,Q,P) = a_{1,1}QP + a_{1,2}Q^4(1-x)^2 + a_{1,3}Q^2P(1-x)^2 + a_{1,4}P^2(1-x)^2 + a_{1,5}QP^2(1-x)^2 + a_{1,6}Q(1-x)^4 + a_{1,7}Q^2(1-x)^4 + a_{1,8}P(1-x)^4 + a_{1,9}QP(1-x)^4 + a_{1,10}Q^2P^2(1-x)^4\,,$
- $f_2(x,Q,P) = a_{2,1}QP(1-x) + a_{2,2}Q^2P^2(1-x) + a_{2,3}Q^4P^2(1-x) + a_{2,4}Q(1-x)^2 + a_{2,5}P(1-x)^2 + a_{2,6}Q^2(1-x)^4 + a_{2,7}QP(1-x)^4 + a_{2,8}P^2(1-x)^4 + a_{2,9}Q^2P^4(1-x)^4\,,$
- $f_3(x,Q,P) = a_{3,1}Q + a_{3,2}P^2 + a_{3,3}(1-x)^2 + a_{3,4}Q^4(1-x)^4 + a_{3,5}P(1-x)^4 + a_{3,6}QP(1-x)^4 + a_{3,7}Q^2P^2(1-x)^4 + a_{3,8}Q^4P^3(1-x)^4 + a_{3,9}QP^4(1-x)^4\,,$
- $f_4(x,Q,P) = a_{4,1}P + a_{4,2}(1-x)^3 + a_{4,3}(1-x)^4 + a_{4,4}P(1-x)^4 + a_{4,5}QP(1-x)^4\,,$

where $x$ is the quantity of interest, $Q$ is the measured energy integrated over time, $P$ is the averaged power and the $a_{i,j}$ ($j \in [\![1, 10]\!]$) are the coefficients associated with each polynomial. From Figure 7.22 we can also state that all cases tend to reach the same minimum error, around $E = 0.02$, but the third and fourth cases present a lower number of non-zero values.

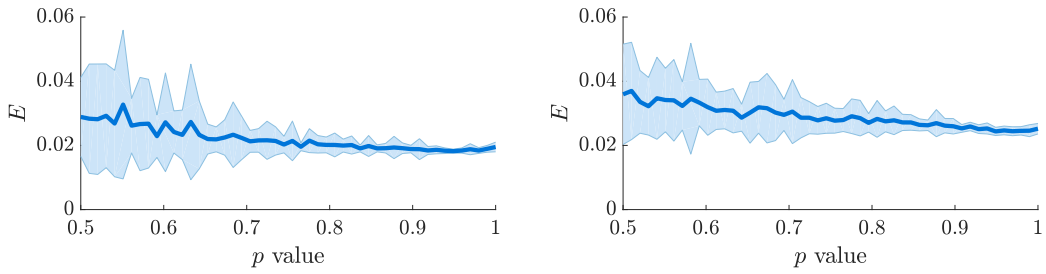


(a) Case 1.




(b) Case 2.

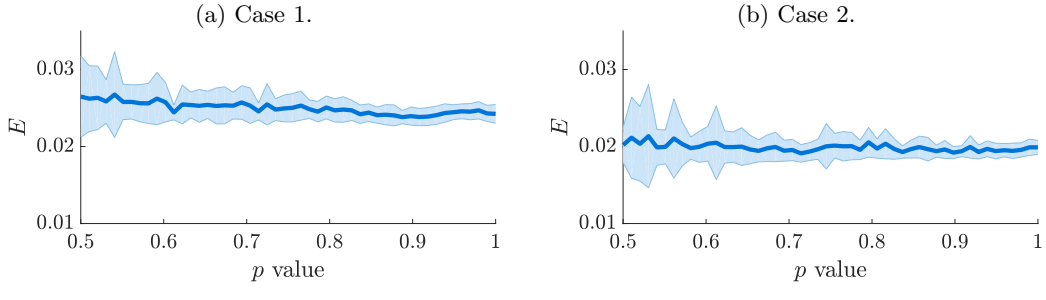


(c) Case 3.




(d) Case 4.

Figure 7.20: Reconstruction error as a function of the $\ell^p$-norm used in FOCUSS. For each $p$ $n_r = 50$ simulations are done. The blue line represents the mean and the shaded area represents one standard deviation.

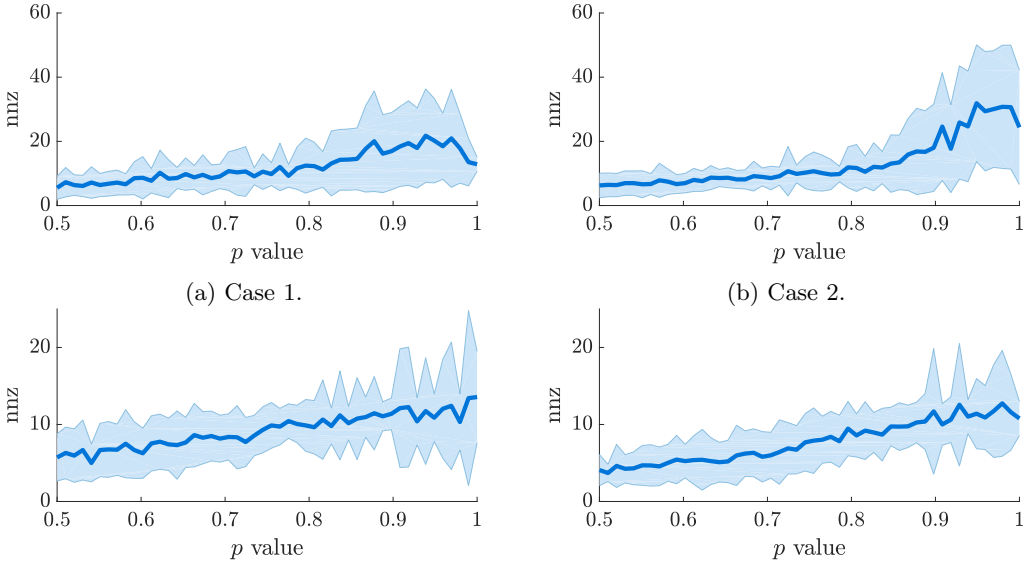


(a) Case 1. (b) Case 2.

(c) Case 3. (d) Case 4.

Figure 7.21: Number of non-zero values returned by the sparse approximation as a function of the $\ell^p$-norm used in FOCUSS. For each $p$ $n_r = 50$ simulations are done. The blue line represents the mean and the shaded area represents one standard deviation.

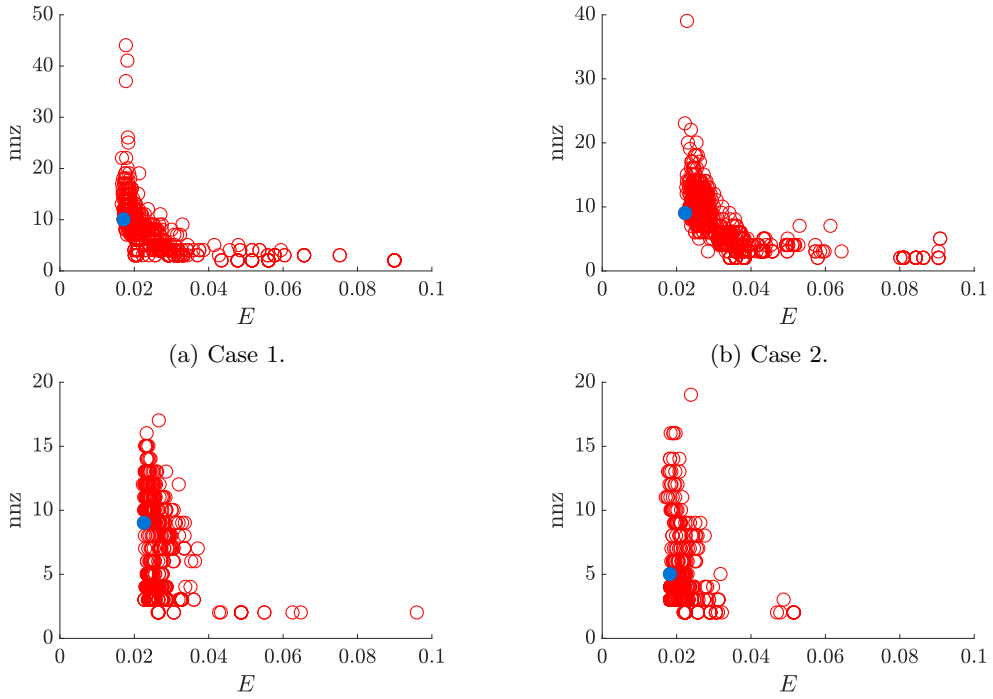


(a) Case 1. (b) Case 2.

(c) Case 3. (d) Case 4.

Figure 7.22: Number of non-zero values returned by the sparse approximation as a function of the error. $p = 0.5$ is used in FOCUSS and 1000 random initializations are run. The red circles represent the outcome of each run. The blue dot corresponds to the run picked to define the function used to represent the dynamics of each case.

### 7.7.2 Coagulation's representation

To give the reader more insight into the behavior of the metamodel, the percentage of coagulation and its derivative over time are shown in Figure 7.23 in the case of the simulation described in Figure 7.19. In this case, the SSR's functions seem to follow the same trend that the high fidelity simulation. Some discrepancies can be seen when the derivative increases quickly but it does not deteriorate significantly the representation of the coagulation percentage. Note that this figure only attests to the good general behavior of the metamodel. It cannot be seen as a rigorous evaluation of its accuracy as the SSR returns an averaged behavior. Hence, by comparing a deterministic simulation with the metamodel one must not expect a perfect fit. Also, an averaged value of all the high fidelity simulations cannot be used to be compared with the SSR's result; indeed, all the simulations have different boundary conditions hence they cannot be averaged over time. Concerning the computational time a consequent speed-up is achieved as only a few seconds are required to compute the solutions with the SSR approach, against several hours for the high fidelity simulation.

To get a better understanding of the influence of the Goldberg protocol on the results, Figure 7.24 shows a comparison of the error between the simulations following the Goldberg protocol and those that do not. It appears that the error is smaller in the simulations where the Goldberg protocol is applied. The simulations that do not follow the protocol are submitted to randomized pulses, consequently, they tend to present more variability and are more difficult to represent. They are used to create a more robust model and help to extract its underlying physics. Whatsoever, as the final goal is to be able to represent pulses following the Goldberg protocol this result is comforting.

Next, the error is linked to the distance of the value of the stochastic parameters with respect to the mean value of these latter in Figure 7.25. For each simulation, the distance is computed as

$$d_m(\sigma^t, \kappa^t, \omega^t, \sigma^l, \kappa^l, \omega^l) = \sqrt{(\sigma^t - \sigma_0^t)^2 + (\kappa^t - \kappa_0^t)^2 + (\omega^t - \omega_0^t)^2 + (\sigma^l - \sigma_0^l)^2 + (\kappa^l - \kappa_0^l)^2 + (\omega^l - \omega_0^l)^2} \quad (7.56)$$

where the index 0 indicates the mean value (see Table 7.2) and the indices $l$ and $t$ relate to the liver and the tumor, respectively. The error is lower when the parameters are near from their mean values. This result is expected as the parameters are drawn from normal distributions. As the SSR's functions are tailored to represent the mean behavior - in the least-squares sense - over these specific parameter distributions, the error should be smaller for small values of $d_m$. However, note that there is no reason that the error should be smaller in the cases where the parameters are equal to their mean values. Indeed, when using nonlinear functions the mean result does not correspond to the result of the function when using the mean parameters. Here, we can only attest that the more probable are the sets of parameters, the better they will be fitted.

In Figure 7.26 is shown the influence of the initial current intensity over the fitting. It appears that it does not have a great influence on the fitting error. This was also expected as the initial current intensity is drawn from a uniform distribution.

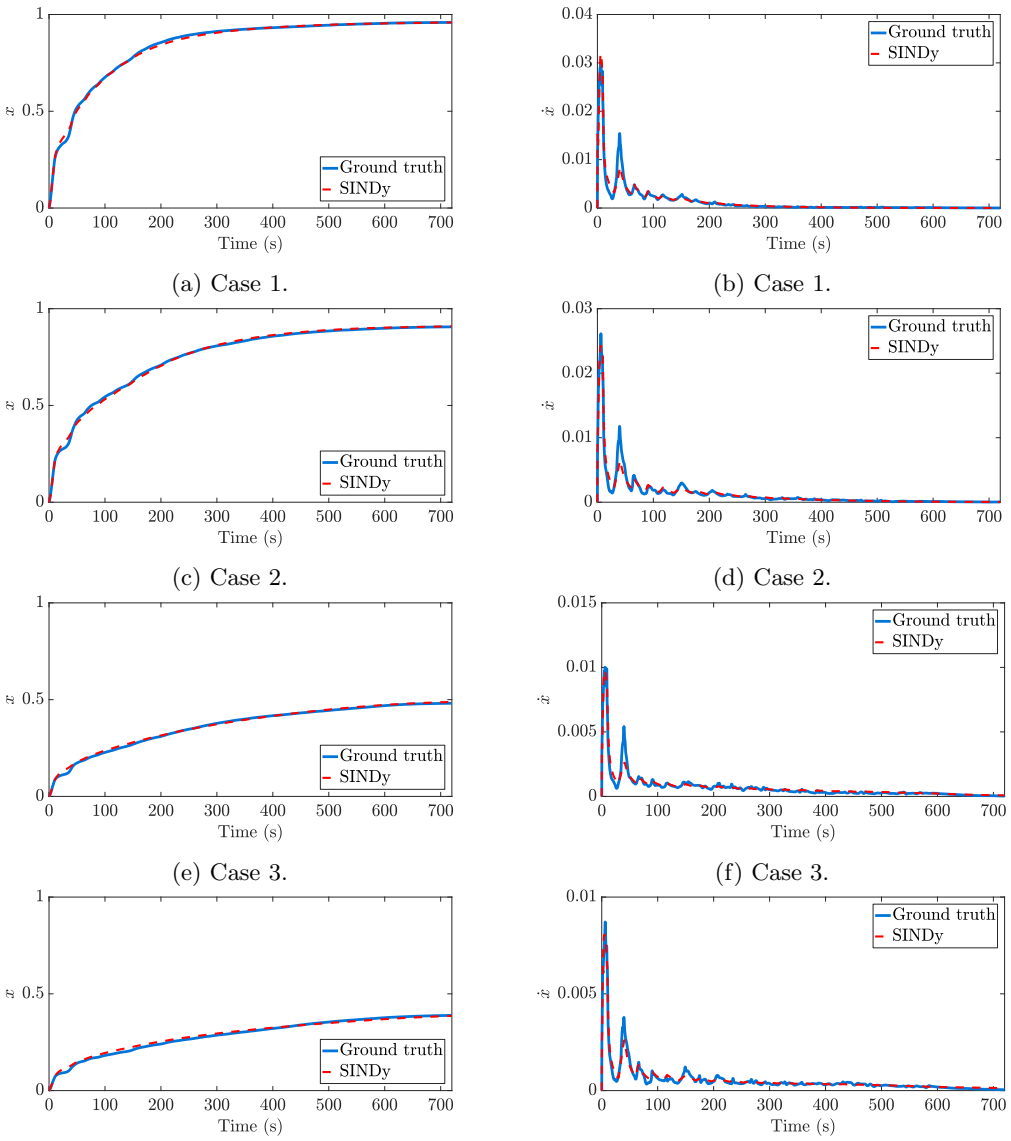


(a) Case 1. (b) Case 1.

(c) Case 2. (d) Case 2.

(e) Case 3. (f) Case 3.

(g) Case 4. (h) Case 4.

Figure 7.23: Comparison of the ground truth solutions obtained with the high fidelity FE simulation and their reconstructions with the SSR. A reconstruction means that the values of $Q$ and $P$ obtained with the high fidelity simulation were used as inputs in the SSR's metamodels. The FE simulation is done using the mean parameters from Table 7.2 and using the Goldberg protocol. On the left is represented the evolution of the percentage of coagulation for the four cases and on the right are represented their respective derivatives. The error $E$ for each case is, in the order, $5 \times 10^{-3}$, $6.2 \times 10^{-3}$, $5 \times 10^{-3}$ and $8 \times 10^{-3}$.

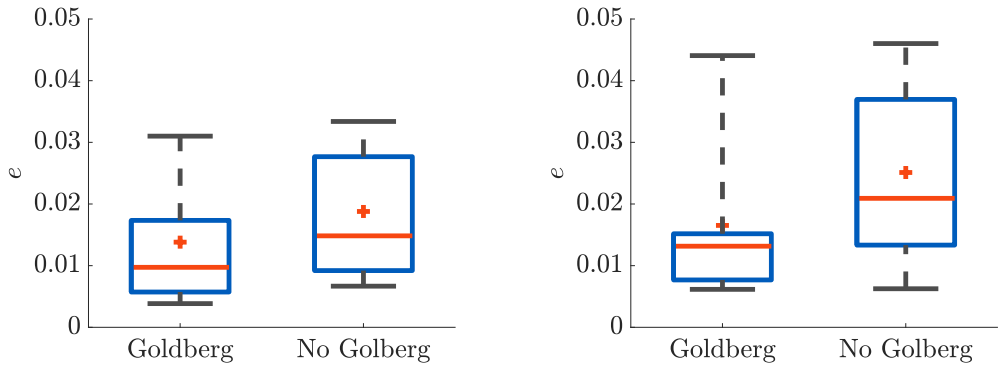


(a) Case 1.




(b) Case 2.

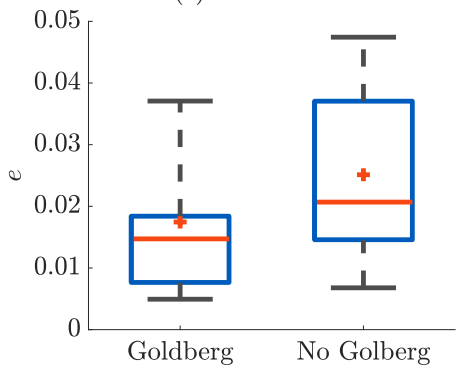


(c) Case 3.

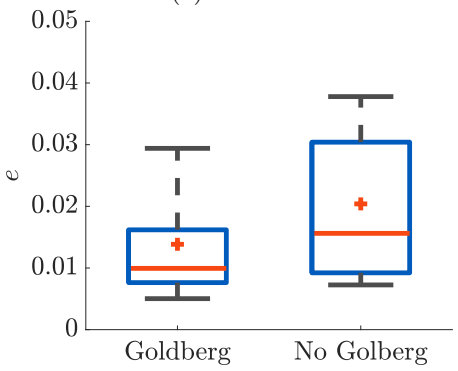


(d) Case 4.

Figure 7.24: Comparison of the error for the left-out simulations depending if they follow the Goldberg protocol or not. The mean is represented by a red dot and the median by a red line. The borders of the box represent the 25%-75% range and the whiskers the 9%-91% one. In the $n_{out} = 50$ left-out simulations 16 followed the Goldberg protocol. It is clear that the results are more reliable when the pulses follow the Goldberg protocol.

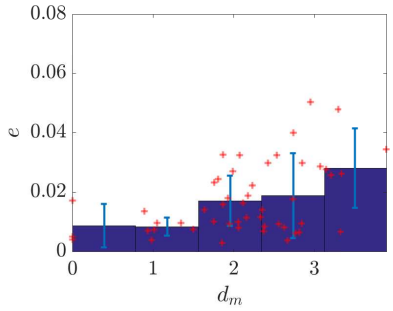


(a) Case 1.

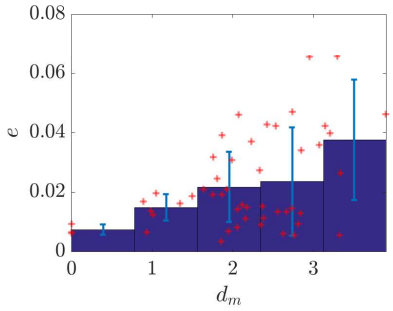


(b) Case 2.

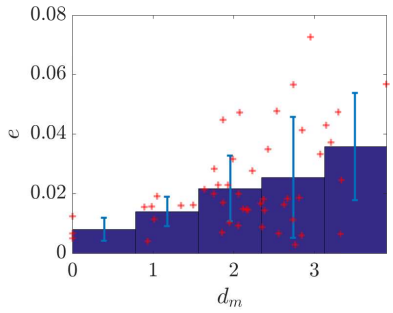


(c) Case 3.

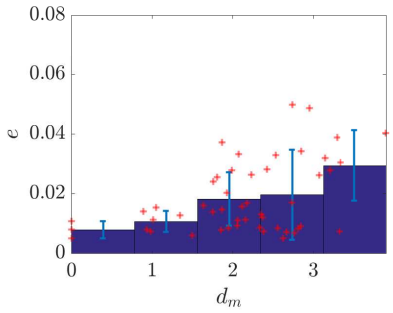


(d) Case 4.

Figure 7.25: The error is represented with bars as a function of the distance of its parameters to the mean ones (see Equation 7.56). A bar corresponds to the mean value of $E$ over the corresponding domain. For each bar is represented the standard deviation and the values of the error for each simulation are shown with transparent red crosses.

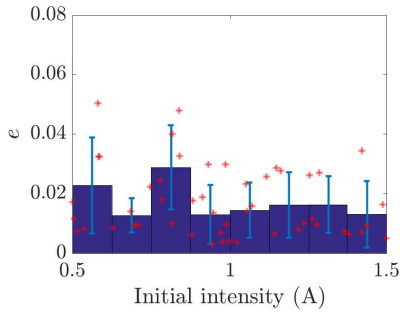


(a) Case 1.

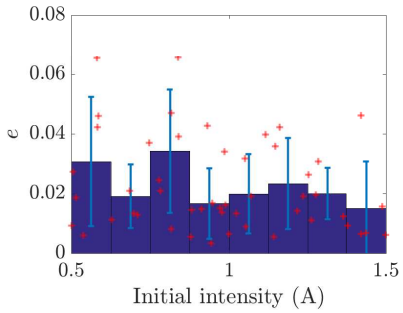


(b) Case 2.

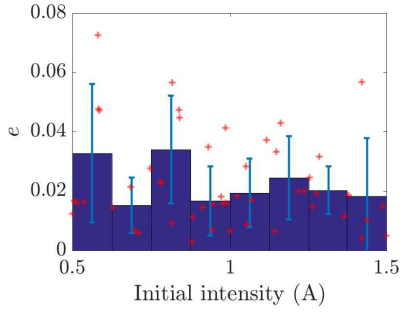


(c) Case 3.

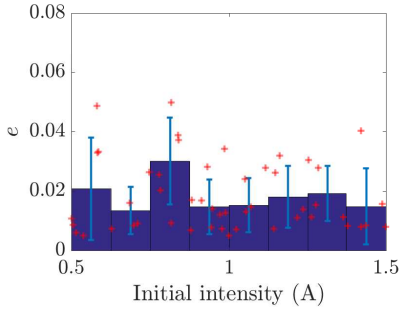


(d) Case 4.

Figure 7.26: The error is represented as bars as a function of the initial intensity. A bar corresponds to the mean value of $E$ over the corresponding domain. For each bar is represented the standard deviation and the values of the error for each simulation are shown with transparent red crosses.

### 7.7.3 Comparison with non-weighted data

The relevance of the use of weighted least-squares in the SSR (see Section 7.4.3) is addressed in Figure 7.27. The error is represented using box plots. The same methodology is applied to chose the SSR's functions for the non-weighted data than for the weighted ones. The results show similar mean and median errors. Their dispersions are slightly different. The weighted data tend to have a bigger 25%-75% range of error but a smaller 9%-91% one. The fact that the weighting reduces the maximal amplitude of the error can be interpreted as more robustness in the model when facing use cases badly represented by the training data. Whatsoever, the differences are so small that it is difficult to draw a clear conclusion. At least, the weighting does not deteriorate the solutions.

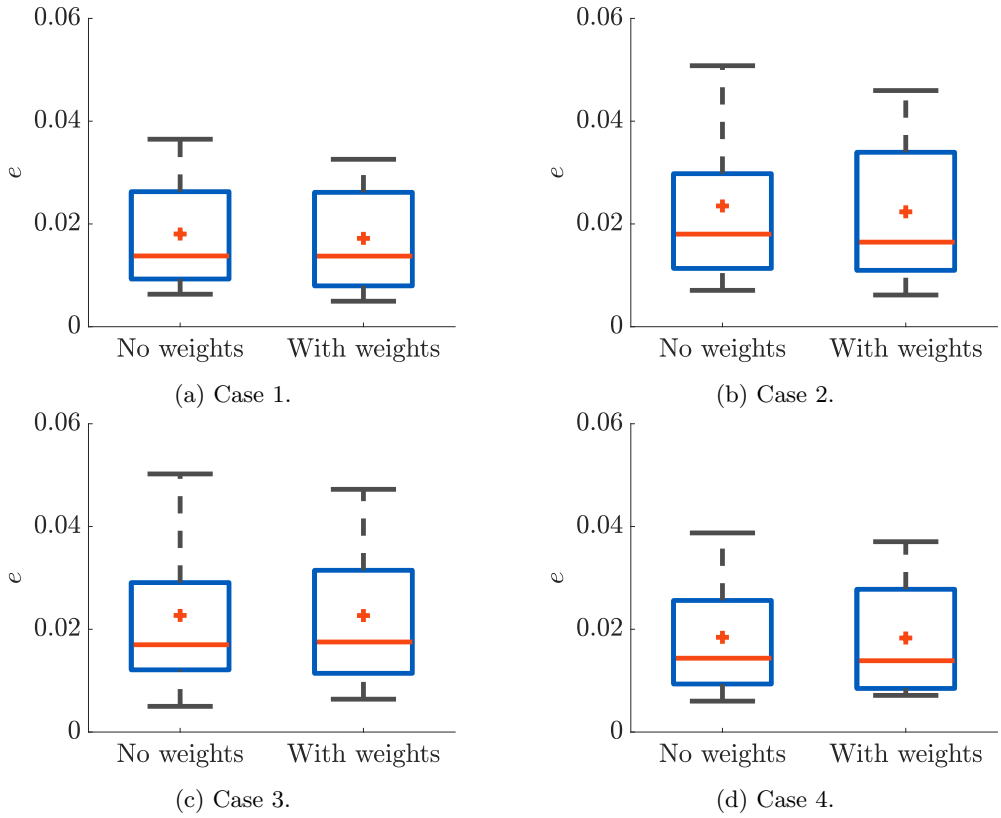


(a) Case 1. (b) Case 2.

(c) Case 3. (d) Case 4.

Figure 7.27: Comparison between the results with the weighting of the data explained in Section 7.4.3 and without weighting. The mean is represented by a red dot and the median by a red line. The borders of the box represent the 25%-75% range and the whiskers the 9%-91% one.

## 7.8 Discussion

The RFA model used in this chapter takes into account the real geometry of the organ and uses fine representations of the physical and biophysical phenomena. The complexity of these latter makes impossible the real-time computations. Moreover, when taking into account the variability of the parameters the required number of computations tends to increase dramatically, e.g using the Monte-Carlo method.To complexify the problem further, the pulses are dependent on the system state and are unique for each simulation, or, in the case of use in the operating room, for each patient. Hence, the computations cannot be done offline as the boundary conditions are not known beforehand: the dynamics of the system must be taken into account. To make the problem practicable, the standard approach implies to accelerate the computations and do the stochastic computations on the fly while acquiring the pulses' states. Here, the route of model order reduction was explored but was shown to be unsuitable. That is why we developed a metamodeling technique.

This latter has two main advantages. The first is the rapidity of execution. With the metamodel the state of the system over a 12 minutes period can be evaluated in few seconds. Moreover, it does not require any heavy computational hardware. The second advantage is that the variability of the parameters is embedded in the model. The output is directly the representation of an averaged behavior and does not require multiple simulations.

Nonetheless, the proposed technique has its limits. The SSR has been applied successfully on the representation of the coagulation volume in four distinct cases. These latter have been chosen arbitrarily and may be adapted to the preference of the user straightforwardly. However, the success in these cases does not ensure the replicability in other use cases. In this chapter, the SSR's functions have been built using the measurement vector containing the electrical energy and the average power. These indicators of the necrosis have been determined after several trials and errors. If one wants to represent a value of interest other than the coagulation this trial and error process must be repeated and is not guaranteed to reach a good result. A promising development would be to automatize the selection of the indicators of the values of interest from the available data. Indeed, as mentioned in the introduction the SSR method can be used as a selector of the indicators of the value of interest we seek to represent. However, the more indicators are tested simultaneously, the greater the size of the dictionary will be in the sparse regression process. It can rapidly reach the limits of a standard computer. Hence, several approaches could be contemplated, such as using high-performance computing or treating sequentially several smaller dictionaries. Apart from the choice of the indicators, the functions used to generate the atoms of the dictionary could also benefit from further developments. In particular, it would be interesting to employ other nonlinear functions than polynomials. Nonetheless, it would not be straightforward as the constants inside the nonlinear functions would not be adaptable by the sparse regression.

Besides, the required size of the initial database used to create the metamodel is hard to estimate. Cross-validation techniques could be envisaged to test on the fly the validity of the model. A metric should be determined to assess the convergence of the method and stop the Monte-Carlo method. In this chapter, instead of generating more simulations we have brought more variability in the data by injecting randomness through an approximated Goldberg protocol. Even though the impact of this approach is not easily quantifiable, it allows avoiding overfitting the simulations where the Goldberg protocol is applied.

Furthermore, the user may want to apply conditions on the derivative of the system state fitted by the SSR to impose some physical constraint. The sparse regression does not easily allow doing that. Nonetheless, in Section 7.6.2 we show a "trick" to impose the positivity of the derivative by applying the SSR to the square root of this latter. The derivative is then equal to the squared value of the output returned by the SSR's function. In practice, it allowed generating more stable functions and get better results. Moreover, the physics of the problem is better respected as the coagulation volume cannot decrease.

Next, the approach of metamodeling allowed to represent the mean response - in the least-squares sense - of the system under variable boundary conditions for stochastic parameters, but, it lacks an estimator of confidence over the computed values. It would be valuable to know the variance of the data in order to be able to know if the model is trustable. A possible solution could be to redo a metamodel but this time for the error. The user would dispose of a metamodel to represent the mean and another one to represent the confidence he can have in the first metamodel.

Finally, in Section 7.4.3 is explained how the SSR is applied to a set of data including parameters variations. In particular, a weighting is done to counterbalance the non-uniform sampling of the variables - more insight on this subject can be found in [195], where the concept of inverse density weighting is developed in the framework of linear least-squares. In the application presented in this thesis, the bandwidths of the kernel density function were chosen empirically. Hence, the weighting is probably not performed optimally. Nonetheless, several methods exist to determine these parameters [119]. Some fully automatic bandwidth selections have been tested [39, 147] but they tend to produce bandwidths too small. Unfortunately, if larger bandwidths than the optimum are acceptable - it will at worst approximate the uniform distribution - smaller ones can produce very large weights that will mislead the least-squares approximation. This motivated the empirical choice of the bandwidths. Besides, if the weighting is straightforward in the case of a unique simulation, when we apply it to a collection of simulations another consideration must be taken

into account. Indeed, for each simulation, the parameters do not belong to the same domain. For example, in a simulation the percentage of coagulation $x$ will reach a maximum of 0.5 whereas in another it will reach 1. When doing a least-squares regression, if a majority of simulations only reach a value of 0.5 it could be desirable that the response value - which depends on $x$ - be more represented for $x < 0.5$ as this data are statistically more likely to happen. By doing the weighting on all the collection of data simultaneously some isolated values associated with a peculiar simulation may be given too high importance. However, giving important weights to these values may also improve the robustness of the model when extreme situations are encountered. Hence, the weighting can be applied from different manners. Unfortunately, it is difficult to evaluate its benefits. As shown in Section 7.7.3 the error is not significantly different with or without weighting. Because there is no ground truth to compare the result with, no reliable conclusion can be drawn from the utility of the weighting. Nonetheless, from a theoretical point of view, its use is justified.

## 7.9 Conclusion

We presented and tested a procedure to create a metamodel including variable parameters using a sparse regression algorithm. The technique has been developed in the framework of RFA with an internally-cooled electrode. A complex RFA model able to represent the impedance rise due to the charring and dehydration of the tissues has been used. The geometry of the model was extracted from an MRI in order to test the method in near-reality conditions. The RFA pulses followed the Goldberg protocol, i.e. they were dependent on the measured impedance. Uncertainties were introduced on several material parameters. By using a Latin hypercube sampling, the metamodel has been able to represent the average dynamical evolution of the coagulation for different cases of use with faster-than-real-time capabilities. Consequently, this approach offers a new way to monitor the coagulation evolution in the case of RFA procedures while taking into account the variability of the parameters. Several points were discussed to improve the method, paving the way for future research.

# Part III: partial conclusion

This part has been the opportunity to explore the uncertainty propagation in the medical framework. We focused in particular on the propagation of uncertainty in quasi real-time. This need essentially occurs during *in situ* operations where the clinicians must assess the evolution of some values of interest but do not have direct access to them. The simulation is a relevant solution to this lack of data as it can be used to infer unknown physical behaviors from the knowledge of the boundary conditions. By using a finite element (FE) approach, the uncertainty on the parameters - such as the material parameters or the boundary conditions - can be efficiently embedded within the simulation framework. These techniques are generally coined as the stochastic FE methods. Nonetheless, these latter enable the accurate simulation of the uncertainty propagation in complex biophysical models but at the cost of expensive computational times. To alleviate this cost and satisfy the real-time constraint, model order reduction (MOR) methods have been considered. Such an approach allows accelerating the simulations while preserving the physics of the model through an *offline/online* approach. However, we have shown that MOR methods are somewhat limited when the simulations involve moving discontinuities such as highly concentrated sources or fronts, the solution is then said to be *non-separable* in space and time. In particular, we illustrated this phenomenon in the case of the radiofrequency ablation (RFA) procedure. In this latter, a needle-like electrode is used to heat the tissue through electrical pulses. This heat provokes the necrosis of the surrounding cells and allows the ablation of tumors, for example. Nonetheless, the size of the necrotic area cannot be directly assessed as this is a minimally invasive procedure. Moreover, the different material parameters of the healthy tissue and of the tumors cannot be exactly determined. Finally, the clinician should have real-time access to the necrosis assessment in order to stop the pulses if the whole tumor is destroyed and avoid to harm healthy tissue. For these reasons, the RFA context is perfectly suited to illustrate the need for real-time uncertainty propagation through the simulation. As the MOR methods are unable to significantly accelerate the computations in this framework, we have employed the route of metamodeling. A metamodel is the model of a model, it only connects some user-defined inputs, or *indicators*, to the outputs of interest, with no considerations for the physics of the problem. We have developed a new framework for the metamodeling of stochastic and dynamics simulations, based on a sparse regression approach and the Monte-Carlo method. One advantage of this approach is that it allows automatically selecting the relevant indicators for the representation of the outputs of interest, by picking candidate functions from a user-defined dictionary. To validate the method, we have applied it to a RFA model based on a patient-specific anatomical representation. It has shown promising results as we were able to monitor the dynamic evolution of the necrosis for different use cases. Nonetheless, as we discussed the robustness of the method is problematic because of the lack of ground truth to compare the results with.

Consequently, further developments of the stochastic sparse regression would involve a rigorous approach to validate the results but also a better automation of the selection of the indicators. To better validate the results, the sampling of the Monte-Carlo method should be done simultaneously with the construction of the metamodel in order to certify the completeness of the database. Also, cross-validation techniques could be integrated in order to ensure the convergence of the metamodel. Concerning the choice of the indicators, the choice of the relevant measures have been done manually in the previous chapter through a trial and error process. This task is cumbersome and, in the end, it does not guarantee an optimal choice. The main limitation is the computational burden associated with the sparse regression. Hence, high-performance computing techniques could be employed to perform it. Otherwise, several sparse regressions employing different dictionaries could be used. A metric should be defined in order to rate the best candidate functions among all

the regressions and in the end select a reduced set that will be employed to build the metamodel. For the applications in a medical context, the discovery of these indicators would have a double interest as it may permit to correlate the evolution of some values of interest to measured inputs. Hence, it would unveil the hidden relationships between variables and allow a better understanding of some physiological behaviors.

# Conclusion and perspectives

This thesis has been devoted to the application of model order reduction (MOR) methods in the context of computational surgery and, we hope, will contribute to the development of organ digital twins. In particular, sparsity-related techniques have been exploited to propose innovative solutions. Three principal axes of development have been tackled:

- the incorporation of the patient-specific anatomy in parametric reduced order models (ROMs),
- the use of ROMs to complete partial or noisy medical data based on physical priors,
- the ability of MOR methods to perform the uncertainty propagation in a medical context and the introduction of the metamodeling alternative.

Each one of these axes corresponds to a specific need of the organ digital twin. First, this latter must be adaptable to the anatomy of each new patient. Then, it must be able to integrate medical data, even if they are partial or noisy. Finally, the twin cannot be perfectly determined and must be able to encompass the uncertainty describing it. A part of the thesis has been dedicated to each subject.

In Part I, we proposed a whole framework for the construction of shape-parametric ROMs. It ranges from the shape parametrization to the MOR along with a morphing procedure. At each level, new solutions have been proposed to ensure the viability of the ROM. A particularity of the approach is, that thanks to the sparse subspace learning (SSL) method employed to reduce the model, the procedure is non-intrusive. It means that external software can be used to perform the computations and the MOR method can be employed as a black-box. This latter has proven its efficiency in a simple linear case adapted to represent the deformation of the liver during a breathing cycle. However, we have shown the limits of the approach when confronted with the high dimensionality of the shape parametrization. We proposed several leads to solve this issue, either by reducing the shape's dimensionality, by clustering the data, by adapting the SSL or by modeling only a portion of the shape.

In Part II, we tackled the issue of medical data completion thanks to models based on physical priors. In particular, we focused the discussion on the scene reconstruction in the framework of augmented reality in laparoscopy. We developed a new approach for the initial static scene reconstruction based on an extended Kalman filter (EKF) accelerated through the use of a ROM. This latter is composed of a projection-based approach coupled with an innovative hyperreduction method based on sparse regression. It permitted to embed nonlinear behaviors into the model while reaching near real-time computational speeds. In the end, the ROM shown its efficiency and the EKF succeeded to perform the registration. However, the results are somewhat mitigated by the poor material parameter identification. It led to a discussion on the role of the model and its relation to the data in the context of parameter identification.

Finally, in Part III, we addressed the challenge of real-time propagation of uncertainties in biophysical models. In particular, the context of the radiofrequency ablation (RFA) procedure was chosen as a use case. This latter revealed to be very complex as it involves strong nonlinearities and coupling. Hence, it is a real challenge to accelerate the computations. Also, the presence of moving fronts in the RFA simulations permitted to evidence one limitation of standard MOR methods: the non-separability in space and time. To bypass this bottleneck, we employed the alternative of metamodeling. A metamodel is the model of a model, and do not have the constraint to respect the physics of the problem as in MOR methods. Nonetheless, encompassing the uncertainty of the parameters in the metamodel is not straightforward. To this end, we proposed a novel approach to perform the identification of a stochastic system through the use of a sparse

regression approach. This stochastic sparse regression allowed in the context of the RFA to monitor the mean and dynamic evolution of the necrosis of the tissue using the sole knowledge of the measured impedance and of the imposed pulses' intensity. As we discussed, it could also be used for the identification of the indicators of the values of interest. However, we also pointed out the lack of validation of our results and encouraged the need for a more rigorous estimation of the error.

Through these three contributions, we have covered many aspects of the MOR methods. In particular, we did not restrain our approaches to one type of method but tried to make the best use of the different kinds of techniques: projection-based methods, interpolation-based methods, and even the metamodeling. In each situation, sparsity-related techniques have been at the core of the approach. They have been used either to sample the parametric space in the SSL method or to perform the sparse regression in the hyperreduction and in the stochastic metamodel.

Notably, in the methods developed in this thesis, the accent has been put on the non-intrusivity of the techniques. As a matter of fact, the integration of MOR methods will be better accepted in the medical routine if they only require small adjustments of the old practices. A common critic addressed to MOR methods is that they require to modify the source code of the numerical solvers. Hence, their use is difficult as the users do not always have access to it, especially if they use commercial software. Moreover, the solutions proposed by model reduction are often specific, and, for each new problem an implementation effort is required.

Thanks to the approaches presented in this manuscript, we have shown that ROMs can be built without requiring too much intrusivity. For instance, with the SSL the model reduction becomes completely non-intrusive. The method can be straightforwardly applied as an add-on to standard/commercial finite element solvers. Then, with the approach proposed in the second part, we introduced a so-called semi-intrusive method. This method is partially intrusive as it requires the implementation of the expression of the system's energy we seek to minimize. Note that for some systems this method could not be applied directly as the solution is not always a minimum of energy. Anyhow, in the current state of the method, external solvers can be used to generate the solutions of the training database and perform the reduced order energy minimization. This is a promising first step towards actual non intrusive model order reduction. Finally, with the metamodeling approach proposed in the last part, the approach is obviously non-intrusive as we only considered the evolution of specific values of interest to build our solution, without taking into consideration the physics of the problem. Nonetheless, as we indicated in the discussion of Chapter 7, the selection of the values of interest used as inputs of the metamodel is not automatized yet. To get an unsupervised metamodeling approach, this step could certainly benefit from further research.

Thus, we have shown the potential of MOR technologies to answer some of the challenges encountered in the computational surgery framework and proposed some solutions in specific use cases. It is reasonable to think that such technology could integrate the medical routine in a medium-term perspective. A first concrete step has been done in the thesis of M. Kugler [148], in relation to the work presented in this manuscript and in the context of the project 3D-Surg. An approach for the real-time and nonlinear representation of the liver's deformation during the free-breathing is presented and integrated within a complete medical framework. The method is based on the SSL and exploits the novel sampling strategy introduced in Chapter 3. The preliminary results on synthetic data prove the ability of the SSL to integrate complex models into the existent hardware and software without downgrading the computational speed, nor the accuracy. Hence, with this thesis, we hope to set the foundations for future researches such as this one, leading to the integration of MOR solutions into medical procedures, but also to encourage the identification and solving of the other bottlenecks of MOR methods in computational surgery.

# Bibliography


[1] J. Abraham and E. Sparrow. A thermal-ablation bioheat model including liquid-to-vapor phase change, pressure-and necrosis-dependent perfusion, and moisture-dependent properties. *International Journal of Heat and Mass Transfer*, 50(13-14):2537–2544, 2007.

[2] Y. Adagolodjo, R. Trivisonne, N. Haouchine, S. Cotin, and H. Courtecuisse. Silhouette-based pose estimation for deformable organs application to surgical augmented reality. In *2017 IEEE/RSJ International Conference on Intelligent Robots and Systems (IROS)*, pages 539–544. IEEE, 2017.

[3] A. Agudo, B. Calvo, and J. Montiel. Fem models to code non-rigid ekf monocular slam. In *2011 IEEE International Conference on Computer Vision Workshops (ICCV Workshops)*, pages 1586–1593. IEEE, 2011.

[4] A. Agudo, B. Calvo, and J. Montiel. Finite element based sequential bayesian non-rigid structure from motion. In *2012 IEEE Conference on Computer Vision and Pattern Recognition*, pages 1418–1425. IEEE, 2012.

[5] P. Alliez, D. Cohen-Steiner, M. Yvinec, and M. Desbrun. Variational tetrahedral meshing. In *ACM Transactions on Graphics (TOG)*, volume 24, pages 617–625. ACM, 2005.

[6] N. Alpert, J. Bradshaw, D. Kennedy, and J. Correia. The principal axes transformation—a method for image registration. *Journal of nuclear medicine*, 31(10):1717–1722, 1990.

[7] I. Altrogge, T. Preusser, T. Kroger, S. Haase, T. Patz, and M. Kirby. Sensitivity analysis for the optimization of radiofrequency ablation in the presence of material parameter uncertainty. *International Journal for Uncertainty Quantification*, 2(3):295–321, 2012.

[8] A. Ammar, A. Huerta, F. Chinesta, E. Cueto, and A. Leygue. Parametric solutions involving geometry: a step towards efficient shape optimization. *Computer Methods in Applied Mechanics and Engineering*, 268:178–193, 2014.

[9] D. Amsallem, M. Zahr, Y. Choi, and C. Farhat. Design optimization using hyper-reduced-order models. *Structural and Multidisciplinary Optimization*, 51(4):919–940, 2015.

[10] S. S. An, T. Kim, and D. L. James. Optimizing cubature for efficient integration of subspace deformations. In *ACM transactions on graphics (TOG)*, volume 27, page 165. ACM, 2008.

[11] P. Andreo. Monte carlo simulations in radiotherapy dosimetry. *Radiation Oncology*, 13(1):121, 2018.

[12] P. Argoul. Overview of Inverse Problems. Lecture, Sept. 2012.

[13] C. Audigier, T. Mansi, H. Delingette, S. Rapaka, V. Mihalef, D. Carnegie, E. Boctor, M. Choti, A. Kamen, N. Ayache, et al. Efficient lattice boltzmann solver for patient-specific radiofrequency ablation of hepatic tumors. *IEEE Transactions on Medical Imaging*, 34(7):1576–1589, 2015.

[14] A. Badías, I. Alfaro, D. González, F. Chinesta, and E. Cueto. Reduced order modeling for physically-based augmented reality. *Computer Methods in Applied Mechanics and Engineering*, 341:53–70, 2018.

[15] T. J. Baker. Mesh movement and metamorphosis. *Engineering with Computers*, 18(3):188–198, 2002.

[16] J. Bano, A. Hostettler, S. Nicolau, S. Cotin, C. Doignon, H. Wu, M. Huang, L. Soler, and J. Marescaux. Simulation of pneumoperitoneum for laparoscopic surgery planning. In *International Conference on Medical Image Computing and Computer-Assisted Intervention*, pages 91–98. Springer, 2012.

[17] M. Barrault, Y. Maday, N. C. Nguyen, and A. T. Patera. An 'empirical interpolation'method: application to efficient reduced-basis discretization of partial differential equations. *Comptes Rendus Mathematique*, 339(9):667–672, 2004.

[18] D. Bartz and B. Preim. Visualization and exploration of segmented anatomic structures. In *Biomedical Image Processing*, pages 379–401. Springer, 2010.

[19] S. Behdadfar, L. Navarro, J. Sundnes, M. Maleckar, S. Ross, H. H. Odland, and S. Avril. A centerline-based model morphing algorithm for patient-specific finite element modeling of the left ventricle. *IEEE Transactions on Biomedical Engineering*, 65(6):1391–1398, 2017.

[20] P. Beillas and F. Berthet. An investigation of human body model morphing for the assessment of abdomen responses to impact against a population of test subjects. *Traffic Injury Prevention*, 18(sup1):142–147, mar 2017.

[21] J. Belinha. Meshless methods: the future of computational biomechanical simulation. *Journal of Biometrics & Biostatistics*, 7(4):1–3, 2016.

[22] S. Belongie, J. Malik, and J. Puzicha. Shape matching and object recognition using shape contexts. *IEEE transactions on pattern analysis and machine intelligence*, 24(4):509–522, 2002.

[23] Y. Ben-Haim. *Info-gap decision theory: decisions under severe uncertainty*. Elsevier, 2006.

[24] E. J. Berjano. Theoretical modeling for radiofrequency ablation: state-of-the-art and challenges for the future. *Biomedical engineering online*, 5(1):24, 2006.

[25] S. Bernhardt, S. A. Nicolau, L. Soler, and C. Doignon. The status of augmented reality in laparoscopic surgery as of 2016. *Medical image analysis*, 37:66–90, 2017.

[26] M. Berveiller, B. Sudret, and M. Lemaire. Comparison of methods for computing the response coefficients in stochastic finite element analysis. volume 2, 2004.

[27] P. J. Besl, N. D. McKay, et al. A method for registration of 3-d shapes. *IEEE Transactions on pattern analysis and machine intelligence*, 14(2):239–256, 1992.

[28] D. Bielser and M. H. Gross. Interactive simulation of surgical cuts. In *Proceedings the Eighth Pacific Conference on Computer Graphics and Applications*, pages 116–442. IEEE, 2000.

[29] J. Bilcke, P. Beutels, M. Brisson, and M. Jit. Accounting for methodological, structural, and parameter uncertainty in decision-analytic models: a practical guide. *Medical decision making*, 31(4):675–692, 2011.

[30] D. Boltcheva, D. Bechmann, and S. Thery. Discrete delaunay: Boundary extraction from voxel objects. In *Sixth International Conference on 3-D Digital Imaging and Modeling (3DIM 2007)*, pages 209–216. IEEE, aug 2007.

[31] J. Bonet and R. D. Wood. *Nonlinear Continuum Mechanics for Finite Element Analysis*, volume 24. Cambridge University Press, 03 2008.

[32] F. L. Bookstein. Principal warps: Thin-plate splines and the decomposition of deformations. *IEEE Transactions on pattern analysis and machine intelligence*, 11(6):567–585, 1989.

[33] F. L. Bookstein. *Morphometric tools for landmark data: geometry and biology*. Cambridge University Press, 1997.

[34] F. Bordeu. Pxdmf : A file format for separated variables problems. Technical report, Ecole Centrale de Nantes, 2013.

[35] A. Borsic, E. Hoffer, and E. A. Attardo. Gpu-accelerated real time simulation of radio frequency ablation thermal dose. In *2014 40th Annual Northeast Bioengineering Conference (NEBEC)*, pages 1–2. IEEE, 2014.

[36] D. Borzacchiello, J. V. Aguado, and F. Chinesta. Non-intrusive sparse subspace learning for parametrized problems. *Archives of Computational Methods in Engineering*, 26(2):303–326, 2019.

[37] Z. Botev. The normal law under linear restrictions: simulation and estimation via minimax tilting. *Journal of the Royal Statistical Society: Series B (Statistical Methodology)*, 79(1):125–148, 2017.

[38] Z. Botev and A. Ridder. Variance reduction. *Wiley StatsRef: Statistics Reference Online*, pages 1–6, 2014.

[39] Z. I. Botev, J. F. Grotowski, D. P. Kroese, et al. Kernel density estimation via diffusion. *The Annals of Statistics*, 38(5):2916–2957, 2010.

[40] G. C. Bourantas, M. Ghommem, G. C. Kagadis, K. Katsanos, V. C. Loukopoulos, V. N. Burganos, and G. C. Nikiforidis. Real-time tumor ablation simulation based on the dynamic mode decomposition method. *Medical physics*, 41(5), 2014.

[41] B. Brands, J. Mergheim, and P. Steinmann. Reduced-order modelling for linear heat conduction with parametrised moving heat sources. *GAMM-Mitteilungen*, 39(2):170–188, 2016.

[42] T. L. Bredbenner, T. D. Eliason, W. L. Francis, J. M. McFarland, A. C. Merkle, and D. P. Nicolella. Development and validation of a statistical shape modeling-based finite element model of the cervical spine under low-level multiple direction loading conditions. *Frontiers in bioengineering and biotechnology*, 2:58, 2014.

[43] M. C. Brindise and P. P. Vlachos. Proper orthogonal decomposition truncation method for data denoising and order reduction. *Experiments in Fluids*, 58(4):28, 2017.

[44] S. L. Brunton, J. L. Proctor, and J. N. Kutz. Discovering governing equations from data by sparse identification of nonlinear dynamical systems. *Proceedings of the National Academy of Sciences*, 113(15):3932–3937, 2016.

[45] S. L. Brunton, J. L. Proctor, and J. N. Kutz. Sparse identification of nonlinear dynamics with control (sindyc). *IFAC-PapersOnLine*, 49(18):710–715, 2016.

[46] M. Bucki, C. Lobos, and Y. Payan. A fast and robust patient specific finite element mesh registration technique: application to 60 clinical cases. *Medical image analysis*, 14(3):303–317, 2010.

[47] M. Bucki, C. Lobos, Y. Payan, and N. Hitschfeld. Jacobian-based repair method for finite element meshes after registration. *Engineering with Computers*, 27(3):285–297, 2011.

[48] M. D. Buhmann. *Radial basis functions: theory and implementations*, volume 12. Cambridge university press, 2003.

[49] H.-J. Bungartz and M. Griebel. Sparse grids. *Acta numerica*, 13:147–269, 2004.

[50] P. M. Carter, C. A. Flannagan, M. P. Reed, R. M. Cunningham, and J. D. Rupp. Comparing the effects of age, bmi and gender on severe injury (ais 3+) in motor-vehicle crashes. *Accident Analysis & Prevention*, 72:146–160, 2014.

[51] A. D. Castellano-Smith, T. Hartkens, J. Schnabel, D. R. Hose, H. Liu, W. A. Hall, C. L. Truwit, D. J. Hawkes, and D. L. Hill. Constructing patient specific models for correcting intraoperative brain deformation. In *International Conference on Medical Image Computing and Computer-Assisted Intervention*, pages 1091–1098. Springer, 2001.

[52] T. Chapman, P. Avery, P. Collins, and C. Farhat. Accelerated mesh sampling for the hyper reduction of nonlinear computational models. *International Journal for Numerical Methods in Engineering*, 109(12):1623–1654, 2017.

[53] R. Chartrand. Numerical differentiation of noisy, nonsmooth data. *ISRN Applied Mathematics*, 2011, 2011.

[54] A. Chatterjee. An introduction to the proper orthogonal decomposition. *Current science*, pages 808–817, 2000.

[55] S. Chaturantabut and D. C. Sorensen. Nonlinear model reduction via discrete empirical interpolation. *SIAM Journal on Scientific Computing*, 32(5):2737–2764, 2010.

[56] J.-S. Chen, M. Hillman, and S.-W. Chi. Meshfree methods: progress made after 20 years. *Journal of Engineering Mechanics*, 143(4):04017001, 2017.

[57] P. Chen and A. Quarteroni. Weighted reduced basis method for stochastic optimal control problems with elliptic pde constraint. *SIAM/ASA Journal on Uncertainty Quantification*, 2(1):364–396, 2014.

[58] Y. Chen and G. Medioni. Object modelling by registration of multiple range images. *Image and vision computing*, 10(3):145–155, 1992.

[59] Y. Chi, J. Liu, S. K. Venkatesh, S. Huang, J. Zhou, Q. Tian, and W. L. Nowinski. Segmentation of liver vasculature from contrast enhanced ct images using context-based voting. *IEEE Transactions on Biomedical Engineering*, 58(8):2144–2153, 2011.

[60] F. Chinesta, R. Keunings, and A. Leygue. *The proper generalized decomposition for advanced numerical simulations: a primer*. Springer Science & Business Media, 2013.

[61] F. Chinesta, A. Leygue, F. Bordeu, J. V. Aguado, E. Cueto, D. González, I. Alfaro, A. Ammar, and A. Huerta. Pgd-based computational vademecum for efficient design, optimization and control. *Archives of Computational Methods in Engineering*, 20(1):31–59, 2013.

[62] J. Chinitz, G. Michaud, and K. Stephenson. Impedance-guided radiofrequency ablation: Using impedance to improve ablation outcomes. *The Journal of Innovations in Cardiac Rhythm Management*, 8:2868–2873, 10 2017.

[63] C. Chui, E. Kobayashi, X. Chen, T. Hisada, and I. Sakuma. Combined compression and elongation experiments and non-linear modelling of liver tissue for surgical simulation. *Medical and Biological Engineering and Computing*, 42(6):787–798, 2004.

[64] H. Chui and A. Rangarajan. A new point matching algorithm for non-rigid registration. *Computer Vision and Image Understanding*, 89(2):114–141, 2003.

[65] T. F. Cootes, C. J. Taylor, D. H. Cooper, and J. Graham. Training models of shape from sets of examples. In *BMVC92*, pages 9–18. Springer, 1992.

[66] T. F. Cootes, C. J. Taylor, et al. Statistical models of appearance for computer vision. Technical report, 2004.

[67] L. Cordier and M. Bergmann. Proper Orthogonal Decomposition: an overview. In *Lecture series 2002-04, 2003-04 on post-processing of experimental and numerical data*, page 46. VKI, 2008.

[68] J. M. Cormier. The influence of body mass index on thoracic injuries in frontal impacts. *Accident Analysis & Prevention*, 40(2):610–615, 2008.

[69] A. Cosimo, A. Cardona, and S. Idelsohn. Improving the k-compressibility of hyper reduced order models with moving sources: applications to welding and phase change problems. *Computer Methods in Applied Mechanics and Engineering*, 274:237–263, 2014.

[70] A. Cosimo, A. Cardona, and S. Idelsohn. Global–local rom for the solution of parabolic problems with highly concentrated moving sources. *Computer Methods in Applied Mechanics and Engineering*, 326:739–756, 2017.

[71] S. Cotin, H. Delingette, and N. Ayache. A hybrid elastic model for real-time cutting, deformations, and force feedback for surgery training and simulation. *The Visual Computer*, 16(8):437–452, 2000.

[72] B. Couteau, Y. Payan, and S. Lavallée. The mesh-matching algorithm: an automatic 3d mesh generator for finite element structures. *Journal of biomechanics*, 33(8):1005–1009, 2000.

[73] E. Cueto and F. Chinesta. Real time simulation for computational surgery: a review. *Advanced Modeling and Simulation in Engineering Sciences*, 1(1):11, 2014.

[74] B. Dagon, C. Baur, and V. Bettschart. A framework for intraoperative update of 3d deformable models in liver surgery. In *2008 30th Annual International Conference of the IEEE Engineering in Medicine and Biology Society*, pages 3235–3238. IEEE, 2008.

[75] P. Dalal, B. C. Munsell, S. Wang, J. Tang, K. Oliver, H. Ninomiya, X. Zhou, and H. Fujita. A fast 3d correspondence method for statistical shape modeling. In *Computer Vision and Pattern Recognition, 2007. CVPR'07. IEEE Conference on*, pages 1–8. IEEE, 2007.

[76] R. H. Davies. *Learning shape: optimal models for analysing natural variability*. PhD thesis, 2002.

[77] G. Davis, S. Mallat, and M. Avellaneda. Adaptive greedy approximations. *Constructive approximation*, 13(1):57–98, 1997.

[78] A. J. Davison. Real-time simultaneous localisation and mapping with a single camera. *Proceedings Ninth IEEE International Conference on Computer Vision*, pages 1403–1410 vol.2, 2003.

[79] C. Ding, R. R. Deokar, Y. Ding, G. Li, X. Cui, K. K. Tamma, and S. P. Bordas. Model order reduction accelerated monte carlo stochastic isogeometric method for the analysis of structures with high-dimensional and independent material uncertainties. *Computer Methods in Applied Mechanics and Engineering*, 349:266–284, 2019.

[80] P. Dokládal, C. Lohou, L. Perroton, and G. Bertrand. Liver blood vessels extraction by a 3-d topological approach. In *Medical Image Computing and Computer-Assisted Intervention–MICCAI'99*, pages 98–105. Springer, 1999.

[81] I. Dos Santos, D. Haemmerich, D. Schutt, A. F. da Rocha, and L. R. Menezes. Probabilistic finite element analysis of radiofrequency liver ablation using the unscented transform. *Physics in Medicine & Biology*, 54(3):627, 2009.

[82] T. R. dos Santos, A. Seitel, T. Kilgus, S. Suwelack, A.-L. Wekerle, H. Kenngott, S. Speidel, H.-P. Schlemmer, H.-P. Meinzer, T. Heimann, et al. Pose-independent surface matching for intra-operative soft-tissue marker-less registration. *Medical image analysis*, 18(7):1101–1114, 2014.

[83] A. Erdemir, T. M. Guess, J. Halloran, S. C. Tadepalli, and T. M. Morrison. Considerations for reporting finite element analysis studies in biomechanics. *Journal of biomechanics*, 45(4):625–633, 2012.

[84] O. G. Ernst, B. Sprungk, and H.-J. Starkloff. Bayesian inverse problems and kalman filters. In *Extraction of Quantifiable Information from Complex Systems*, pages 133–159. Springer, 2014.

[85] G. Evensen. The ensemble kalman filter: Theoretical formulation and practical implementation. *Ocean dynamics*, 53(4):343–367, 2003.

[86] S. J. Fahrenholtz, R. J. Stafford, F. Maier, J. D. Hazle, and D. Fuentes. Generalised polynomial chaos-based uncertainty quantification for planning mrglitt procedures. *International Journal of Hyperthermia*, 29(4):324–335, 2013.

[87] C. Farhat, P. Avery, T. Chapman, and J. Cortial. Dimensional reduction of nonlinear finite element dynamic models with finite rotations and energy-based mesh sampling and weighting for computational efficiency. *International Journal for Numerical Methods in Engineering*, 98(9):625–662, 2014.

[88] C. Farhat, T. Chapman, and P. Avery. Structure-preserving, stability, and accuracy properties of the energy-conserving sampling and weighting method for the hyper reduction of nonlinear finite element dynamic models. *International Journal for Numerical Methods in Engineering*, 102(5):1077–1110, 2015.

[89] B. F. Farrell and P. J. Ioannou. State estimation using a reduced-order kalman filter. *Journal of the Atmospheric Sciences*, 58(23):3666–3680, 2001.

[90] S. Farzaneh, O. Trabelsi, and S. Avril. Inverse identification of local stiffness across ascending thoracic aortic aneurysms. *Biomechanics and modeling in mechanobiology*, 18(1):137–153, 2019.

[91] J. Fernandez and P. Hunter. An anatomically based patient-specific finite element model of patella articulation: towards a diagnostic tool. *Biomechanics and modeling in mechanobiology*, 4(1):20–38, 2005.

[92] V. Ferrari, R. M. Viglialoro, P. Nicoli, F. Cutolo, S. Condino, M. Carbone, M. Siesto, and M. Ferrari. Augmented reality visualization of deformable tubular structures for surgical simulation. *The International Journal of Medical Robotics and Computer Assisted Surgery*, 12(2):231–240, 2016.

[93] D. Forti and G. Rozza. Efficient geometrical parametrisation techniques of interfaces for reduced-order modelling: application to fluid–structure interaction coupling problems. *International Journal of Computational Fluid Dynamics*, 28(3-4):158–169, 2014.

[94] B. B. Frericks, F. C. Caldarone, B. Nashan, D. H. Savellano, G. Stamm, T. D. Kirchhoff, H.-O. Shin, A. Schenk, D. Selle, W. Spindler, et al. 3d ct modeling of hepatic vessel architecture and volume calculation in living donated liver transplantation. *European radiology*, 14(2):326–333, 2004.

[95] F. T. Gebhard, M. D. Kraus, E. Schneider, U. C. Liener, L. Kinzl, and M. Arand. Does computer-assisted spine surgery reduce intraoperative radiation doses? *Spine*, 31(17):2024–2027, 2006.

[96] C. Geuzaine and J.-F. Remacle. Gmsh: A 3-d finite element mesh generator with built-in pre- and post-processing facilities. *International journal for numerical methods in engineering*, 79(11):1309–1331, 2009.

[97] D. M. Ghiocel and R. G. Ghanem. Stochastic finite-element analysis of seismic soil–structure interaction. *Journal of Engineering Mechanics*, 128(1):66–77, 2002.

[98] S. F. Gibson. 3d chainmail: A fast algorithm for deforming volumetric objects. *SI3D*, 97:149, 1997.

[99] S. Gold, A. Rangarajan, C.-P. Lu, S. Pappu, and E. Mjolsness. New algorithms for 2d and 3d point matching: Pose estimation and correspondence. *Pattern recognition*, 31(8):1019–1031, 1998.

[100] S. Goldberg, P. F. Hahn, K. Tanabe, P. R. Mueller, W. Schima, C. A. Athanasoulis, C. Compton, L. Solbiati, and G. Scott Gazelle. Percutaneous radiofrequency tissue ablation: Does perfusion-mediated tissue cooling limit coagulation necrosis? *Journal of vascular and interventional radiology : JVIR*, 9:101–11, 01 1998.

[101] S. N. Goldberg, M. C. Stein, G. S. Gazelle, R. G. Sheiman, J. B. Kruskal, and M. E. Clouse. Percutaneous radiofrequency tissue ablation: optimization of pulsed-radiofrequency technique to increase coagulation necrosis. *Journal of vascular and interventional radiology*, 10(7):907–916, 1999.

[102] K. Golec. *Hybrid 3D Mass Spring System for Soft Tissue Simulation.* PhD thesis, Université de Lyon, 2018.

[103] D. González, A. Badías, I. Alfaro, F. Chinesta, and E. Cueto. Model order reduction for real-time data assimilation through extended kalman filters. *Computer Methods in Applied Mechanics and Engineering*, 326:679–693, 2017.

[104] D. González, E. Cueto, and F. Chinesta. Computational patient avatars for surgery planning. *Annals of biomedical engineering*, 44(1):35–45, 2016.

[105] A. Gooya, K. Lekadir, I. Castro-Mateos, J. M. Pozo, and A. F. Frangi. Mixture of probabilistic principal component analyzers for shapes from point sets. *IEEE transactions on pattern analysis and machine intelligence*, 40(4):891–904, 2017.

[106] I. F. Gorodnitsky and B. D. Rao. Sparse signal reconstruction from limited data using focuss: A re-weighted minimum norm algorithm. *IEEE Transactions on signal processing*, 45(3):600–616, 1997.

[107] O. G. Grasa, E. Bernal, S. Casado, I. Gil, and J. Montiel. Visual slam for handheld monocular endoscope. *IEEE transactions on medical imaging*, 33(1):135–146, 2013.

[108] O. G. Grasa, J. Civera, A. Guemes, V. Munoz, and J. Montiel. Ekf monocular slam 3d modeling, measuring and augmented reality from endoscope image sequences. In *Medical image computing and computer-assisted intervention (MICCAI)*, volume 2, 2009.

[109] L. Grassi, N. Hraiech, E. Schileo, M. Ansaloni, M. Rochette, and M. Viceconti. Evaluation of the generality and accuracy of a new mesh morphing procedure for the human femur. *Medical engineering & physics*, 33(1):112–120, 2011.

[110] N. M. Grosland, R. Bafna, and V. A. Magnotta. Automated hexahedral meshing of anatomic structures using deformable registration. *Computer methods in biomechanics and biomedical engineering*, 12(1):35–43, 2009.

[111] D. Haemmerich. Mathematical modeling of impedance controlled radiofrequency tumor ablation and ex-vivo validation. In *2010 Annual International Conference of the IEEE Engineering in Medicine and Biology*, pages 1605–1608. IEEE, 2010.

[112] D. Haemmerich, D. J. Schutt, A. S. Wright, J. G. Webster, and D. M. Mahvi. Electrical conductivity measurement of excised human metastatic liver tumours before and after thermal ablation. *Physiological measurement*, 30(5):459, 2009.

[113] S. K. Hall, E. H. Ooi, and S. J. Payne. Cell death, perfusion and electrical parameters are critical in models of hepatic radiofrequency ablation. *International Journal of Hyperthermia*, 31(5):538–550, 2015.

[114] N. Haouchine, J. Dequidt, I. Peterlik, E. Kerrien, M.-O. Berger, and S. Cotin. Image-guided simulation of heterogeneous tissue deformation for augmented reality during hepatic surgery. In *2013 IEEE International Symposium on Mixed and Augmented Reality (ISMAR)*, pages 199–208. IEEE, 2013.

[115] N. Haouchine, J. Dequidt, I. Peterlik, E. Kerrien, M.-O. Berger, and S. Cotin. Towards an accurate tracking of liver tumors for augmented reality in robotic assisted surgery. In *2014 IEEE International Conference on Robotics and Automation (ICRA)*, pages 4121–4126. IEEE, 2014.

[116] N. Haouchine, F. Roy, L. Untereiner, and S. Cotin. Using contours as boundary conditions for elastic registration during minimally invasive hepatic surgery. In *2016 IEEE/RSJ International Conference on Intelligent Robots and Systems (IROS)*, pages 495–500. IEEE, 2016.

[117] J. Hazrati-Marangalou. Database of femur samples. https://data.4tu.nl/repository/uuid:4ae59365-92f0-480b-a899-ade34bc84a00, 2013. Accessed: 2017-09-01.

[118] L.-P. He, H.-Z. Huang, L. Du, X.-D. Zhang, and Q. Miao. A review of possibilistic approaches to reliability analysis and optimization in engineering design. In *International Conference on Human-Computer Interaction*, pages 1075–1084. Springer, 2007.

[119] N.-B. Heidenreich, A. Schindler, and S. Sperlich. Bandwidth selection for kernel density estimation: a review of fully automatic selectors. *AStA Advances in Statistical Analysis*, 97(4):403–433, 2013.

[120] T. Heimann and H.-P. Meinzer. Statistical shape models for 3d medical image segmentation: a review. *Medical image analysis*, 13(4):543–563, 2009.

[121] T. Heimann, B. Van Ginneken, M. A. Styner, Y. Arzhaeva, V. Aurich, C. Bauer, A. Beck, C. Becker, R. Beichel, G. Bekes, et al. Comparison and evaluation of methods for liver segmentation from ct datasets. *IEEE transactions on medical imaging*, 28(8):1251–1265, 2009.

[122] N. Henze and B. Zirkler. A class of invariant consistent tests for multivariate normality. *Communications in Statistics-Theory and Methods*, 19(10):3595–3617, 1990.

[123] J. A. Hernández, M. A. Caicedo, and A. Ferrer. Dimensional hyper-reduction of nonlinear finite element models via empirical cubature. *Computer methods in applied mechanics and engineering*, 313:687–722, 2017.

[124] T. Hoshi, Y. Kobayashi, K. Kawamura, and M. G. Fujie. Developing an intraoperative methodology using the finite element method and the extended kalman filter to identify the material parameters of an organ model. In *2007 29th Annual International Conference of the IEEE Engineering in Medicine and Biology Society*, pages 469–474. IEEE, 2007.

[125] A. Hostettler, D. George, Y. Rémond, S. A. Nicolau, L. Soler, and J. Marescaux. Bulk modulus and volume variation measurement of the liver and the kidneys in vivo using abdominal kinetics during free breathing. *Computer methods and programs in biomedicine*, 100(2):149–157, 2010.

[126] A. Hostettler, S. Nicolau, Y. Rémond, J. Marescaux, and L. Soler. A real-time predictive simulation of abdominal viscera positions during quiet free breathing. *Progress in biophysics and molecular biology*, 103(2-3):169–184, 2010.

[127] J. Hu. Parametric human modeling. In *Basic Finite Element Method as Applied to Injury Biomechanics*, pages 417–445. Elsevier, 2018.

[128] W.-H. Huang and C.-K. Chui. A radio-frequency ablation planning system using stochastic finite element method. In *2012 IEEE/SICE International Symposium on System Integration (SII)*, pages 603–608. IEEE, 2012.

[129] J. Hummel, M. Figl, M. Bax, H. Bergmann, and W. Birkfellner. 2d/3d registration of endoscopic ultrasound to ct volume data. *Physics in Medicine & Biology*, 53(16):4303, 2008.

[130] A. Hussein, M. Das, S. Riva, M. Morgan, C. Ronayne, A. Sahni, M. Shaw, D. Todd, M. Hall, S. Modi, et al. Use of ablation index-guided ablation results in high rates of durable pulmonary vein isolation and freedom from arrhythmia in persistent atrial fibrillation patients: the praise study results. *Circulation: Arrhythmia and Electrophysiology*, 11(9):e006576, 2018.

[131] H. Iida, T. Aihara, S. Ikuta, and N. Yamanaka. Effectiveness of impedance monitoring during radiofrequency ablation for predicting popping. *World Journal of Gastroenterology: WJG*, 18(41):5870–5878, 2012.

[132] M. T. Islam, S. Tang, C. Liverani, E. Tasciotti, and R. Righetti. Non-invasive imaging of young's modulus and poisson's ratio in cancers in vivo, 2018.

[133] K. Jabbari. Review of fast monte carlo codes for dose calculation in radiation therapy treatment planning. *Journal of medical signals and sensors*, 1(1):73, 2011.

[134] S. Jacques, S. Rastegar, S. Thomsen, and M. Motamedi. The role of dynamic changes in blood perfusion and optical properties in laser coagulation of tissue. *IEEE J Sel Top Quantum Electron*, 2:922–33, 1996.

[135] M. Jamil and E. Ng. Quantification of the effect of electrical and thermal parameters on radiofrequency ablation for concentric tumour model of different sizes. *Journal of thermal biology*, 51:23–32, 2015.

[136] G. R. Joldes, A. Wittek, and K. Miller. Real-time nonlinear finite element computations on gpu–application to neurosurgical simulation. *Computer methods in applied mechanics and engineering*, 199(49-52):3305–3314, 2010.

[137] I. T. Jolliffe. *Principal Component Analysis, second ed.* Springer, 2002.

[138] S. J. Julier and J. K. Uhlmann. Unscented filtering and nonlinear estimation. *Proceedings of the IEEE*, 92(3):401–422, 2004.

[139] R. Kent, M. Trowbridge, F. J. Lopez-Valdes, R. H. Ordoyo, and M. Segui-Gomez. How many people are injured and killed as a result of aging? frailty, fragility, and the elderly risk-exposure tradeoff assessed via a risk saturation model. In *Annals of Advances in Automotive Medicine/Annual Scientific Conference*, volume 53, page 41. Association for the Advancement of Automotive Medicine, 2009.

[140] P. Kerfriden, J.-C. Passieux, and S. P.-A. Bordas. Local/global model order reduction strategy for the simulation of quasi-brittle fracture. *International Journal for Numerical Methods in Engineering*, 89(2):154–179, 2012.

[141] P. Kersaudy, B. Sudret, N. Varsier, O. Picon, and J. Wiart. A new surrogate modeling technique combining kriging and polynomial chaos expansions–application to uncertainty analysis in computational dosimetry. *Journal of Computational Physics*, 286:103–117, 2015.

[142] H. M. Kjer and J. Wilm. *Evaluation of surface registration algorithms for PET motion correction*. PhD thesis, Technical University of Denmark, DTU, DK-2800 Kgs. Lyngby, Denmark, 2010.

[143] J. P. Kleijnen. Kriging metamodeling in simulation: A review. *European journal of operational research*, 192(3):707–716, 2009.

[144] G. Klein and D. Murray. Parallel tracking and mapping for small ar workspaces. In *Proceedings of the 2007 6th IEEE and ACM International Symposium on Mixed and Augmented Reality*, pages 1–10. IEEE Computer Society, 2007.

[145] B. Koo, E. Özgür, B. Le Roy, E. Buc, and A. Bartoli. Deformable registration of a preoperative 3d liver volume to a laparoscopy image using contour and shading cues. In *International Conference on Medical Image Computing and Computer-Assisted Intervention*, pages 326–334. Springer, 2017.

[146] A. Koshakji, A. Quarteroni, and G. Rozza. Free form deformation techniques applied to 3d shape optimization problems. Technical report, jan 2013.

[147] M. Kristan, A. Leonardis, and D. Skočaj. Multivariate online kernel density estimation with gaussian kernels. *Pattern Recognition*, 44(10-11):2630–2642, 2011.

[148] M. Kugler. *Simulation du mouvement des organes de l'abdomen: application aux déformations du foie et de ses vascularisations en vue de d'une reconstitution en temps réel lors d'une chirurgie mini-invasive*. PhD thesis, 2018.

[149] M. Kugler, A. Hostettler, L. Soler, Y. Remond, and D. George. A new algorithm for volume mesh refinement on merging geometries: Application to liver and vascularisation. *Journal of Computational and Applied Mathematics*, 330:429–440, 2018.

[150] T. Lassila and G. Rozza. Parametric free-form shape design with pde models and reduced basis method. *Computer Methods in Applied Mechanics and Engineering*, 199(23-24):1583–1592, 2010.

[151] O. P. Le Maıtre, M. T. Reagan, H. N. Najm, R. G. Ghanem, and O. M. Knio. A stochastic projection method for fluid flow: Ii. random process. *Journal of computational Physics*, 181(1):9–44, 2002.

[152] Z. Li, X. Han, H. Ge, and C. Ma. A semi-automatic method of generating subject-specific pediatric head finite element models for impact dynamic responses to head injury. *Journal of the mechanical behavior of biomedical materials*, 60:557–567, 2016.

[153] Z. Li, J. Hu, M. P. Reed, J. D. Rupp, C. N. Hoff, J. Zhang, and B. Cheng. Development, validation, and application of a parametric pediatric head finite element model for impact simulations. *Annals of biomedical engineering*, 39(12):2984–2997, 2011.

[154] B. Lin, A. Johnson, X. Qian, J. Sanchez, and Y. Sun. Simultaneous tracking, 3d reconstruction and deforming point detection for stereoscope guided surgery. In *Augmented Reality Environments for Medical Imaging and Computer-Assisted Interventions*, pages 35–44. Springer, 2013.

[155] B. Lin, Y. Sun, X. Qian, D. Goldgof, R. Gitlin, and Y. You. Video-based 3d reconstruction, laparoscope localization and deformation recovery for abdominal minimally invasive surgery: a survey. *The International Journal of Medical Robotics and Computer Assisted Surgery*, 12(2):158–178, 2016.

[156] H.-H. Lin and L.-J. Lo. Three-dimensional computer-assisted surgical simulation and intraoperative navigation in orthognathic surgery: a literature review. *Journal of the Formosan Medical Association*, 114(4):300–307, 2015.

[157] L. Ljung and T. Chen. What can regularization offer for estimation of dynamical systems? In *11th IFAC International Workshop on Adaptation and Learning in Control and Signal Processing (ALCOSP13), 3-5 July 2013, Caen, France*, pages 1–8. IFAC, 2013.

[158] D. Lorente, F. Martínez-Martínez, M. J. Rupérez, M. Lago, M. Martínez-Sober, P. Escandell-Montero, J. M. Martínez-Martínez, S. Martínez-Sanchis, A. J. Serrano-López, C. Monserrat, et al. A framework for modelling the biomechanical behaviour of the human liver during breathing in real time using machine learning. *Expert Systems with Applications*, 71:342–357, 2017.

[159] Y.-C. Lu, A. R. Kemper, S. Gayzik, C. D. Untaroiu, and P. Beillas. Statistical modeling of human liver incorporating the variations in shape, size, and material properties. *Stapp car crash journal*, 57:285–311, 2013.

[160] Y.-C. Lu and C. D. Untaroiu. Statistical shape analysis of clavicular cortical bone with applications to the development of mean and boundary shape models. *Computer methods and programs in biomedicine*, 111(3):613–628, 2013.

[161] Y.-C. Lu and C. D. Untaroiu. A statistical geometrical description of the human liver for probabilistic occupant models. *Journal of biomechanics*, 47(15):3681–3688, 2014.

[162] B. M Kunzli, P. Abitabile, and C. Maurer. Radiofrequency ablation of liver tumors: Actual limitations and potential solutions in the future. *World journal of hepatology*, 3:8–14, 01 2011.

[163] X. Ma and N. Zabaras. An adaptive hierarchical sparse grid collocation algorithm for the solution of stochastic differential equations. *Journal of Computational Physics*, 228(8):3084–3113, 2009.

[164] S. A. Maas, B. J. Ellis, G. A. Ateshian, and J. A. Weiss. Febio: finite elements for biomechanics. *Journal of biomechanical engineering*, 134(1):011005, 2012.

[165] Y. Maday, N. Nguyen, A. Patera, and G. S. H. Pau. A general multipurpose interpolation procedure: The magic points. *Communications on Pure and Applied Analysis*, 8:383–404, 2009.

[166] N. Mahmoud, I. Cirauqui, A. Hostettler, C. Doignon, L. Soler, J. Marescaux, and J. Montiel. Orbslam-based endoscope tracking and 3d reconstruction. In *International workshop on computer-assisted and robotic endoscopy*, pages 72–83. Springer, 2016.

[167] N. Mahmoud, A. Hostettler, T. Collins, L. Soler, C. Doignon, and J. Montiel. Slam based quasi dense reconstruction for minimally invasive surgery scenes. *arXiv e-prints*, abs/1705.09107, 2017.

[168] N. Mahmud, J. Cohen, K. Tsourides, and T. M. Berzin. Computer vision and augmented reality in gastrointestinal endoscopy. *Gastroenterology report*, 3(3):179–184, 2015.

[169] C. V. Mai, M. D. Spiridonakos, E. N. Chatzi, and B. Sudret. Surrogate modeling for stochastic dynamical systems by combining nonlinear autoregressive with exogenous input models and polynomial chaos expansions. *International Journal for Uncertainty Quantification*, 6(4):313–339, 2016.

[170] G. Malandain, G. Bertrand, and N. Ayache. Topological segmentation of discrete surfaces. *International journal of computer vision*, 10(2):183–197, 1993.

[171] A. Manzoni, A. Quarteroni, and G. Rozza. Model reduction techniques for fast blood flow simulation in parametrized geometries. *International journal for numerical methods in biomedical engineering*, 28(6-7):604–625, 2012.

[172] A. Manzoni, A. Quarteroni, and G. Rozza. Shape optimization for viscous flows by reduced basis methods and free-form deformation. *International Journal for Numerical Methods in Fluids*, 70(5):646–670, 2012.

[173] B. Marchand, L. Chamoin, and C. Rey. Real-time updating of structural mechanics models using kalman filtering, modified constitutive relation error, and proper generalized decomposition. *International Journal for Numerical Methods in Engineering*, 107(9):786–810, 2016.

[174] S. Marchesseau, S. Chatelin, and H. Delingette. Nonlinear biomechanical model of the liver. In *Biomechanics of Living Organs*, pages 243–265. Elsevier, 2017.

[175] J. Marescaux, J.-M. Clément, V. Tassetti, C. Koehl, S. Cotin, Y. Russier, D. Mutter, H. Delingette, and N. Ayache. Virtual reality applied to hepatic surgery simulation: the next revolution. *Annals of surgery*, 228(5):627–634, 1998.

[176] F. Martínez-Martínez, M. J. Rupérez, J. D. Martín-Guerrero, C. Monserrat, M. Lago, E. Pareja, S. Brugger, and R. López-Andújar. Estimation of the elastic parameters of human liver biomechanical models by means of medical images and evolutionary computation. *Computer methods and programs in biomedicine*, 111(3):537–549, 2013.

[177] F. Martínez-Martínez, M. J. Rupérez-Moreno, M. Martínez-Sober, J. Solves-Llorens, D. Lorente, A. Serrano-López, S. Martínez-Sanchis, C. Monserrat, and J. D. Martín-Guerrero. A finite element-based machine learning approach for modeling the mechanical behavior of the breast tissues under compression in real-time. *Computers in biology and medicine*, 90:116–124, 2017.

[178] S. Martínez-Sanchis, M. Rupérez, E. Nadal, E. Pareja, S. Brugger, D. Borzacchiello, R. López-Andújar, and C. Monserrat. Estimating the relative stiffness between a hepatic lesion and the liver parenchyma through biomechanical simulations of the breathing process. *Mathematical Problems in Engineering*, 2018, 2018.

[179] C. R. Maurer and J. M. Fitzpatrick. A review of medical image registration. *Interactive image-guided neurosurgery*, pages 17–44, 1993.

[180] R. Modrzejewski, T. Collins, A. Bartoli, A. Hostettler, and J. Marescaux. Soft-body registration of pre-operative 3d models to intra-operative rgbd partial body scans. In *International Conference on Medical Image Computing and Computer-Assisted Intervention*, pages 39–46. Springer, 2018.

[181] R. Modrzejewski, T. Collins, B. Seeliger, A. Bartoli, A. Hostettler, and J. Marescaux. An in vivo porcine dataset and evaluation methodology to measure soft-body laparoscopic liver registration accuracy with an extended algorithm that handles collisions. *International journal of computer assisted radiology and surgery*, pages 1–9, 2019.

[182] J. F. Monsalvo, M. J. García, H. Millwater, and Y. Feng. Sensitivity analysis for radiofrequency induced thermal therapies using the complex finite element method. *Finite Elements in Analysis and Design*, 135:11–21, 2017.

[183] R. E. Moore. *Interval analysis*, volume 4. Prentice-Hall Englewood Cliffs, NJ, 1966.

[184] N. Moshtagh et al. Minimum volume enclosing ellipsoid. *Convex Optimization*, 111:112, 2005.

[185] P. Mountney, D. Stoyanov, A. Davison, and G.-Z. Yang. Simultaneous stereoscope localization and soft-tissue mapping for minimal invasive surgery. In *International Conference on Medical Image Computing and Computer-Assisted Intervention*, pages 347–354. Springer, 2006.

[186] S. Mulier, Y. Miao, P. Mulier, B. Dupas, P. Pereira, T. de Baere, R. Lencioni, R. Leveillee, G. Marchal, L. Michel, et al. Electrodes and multiple electrode systems for radiofrequency ablation: a proposal for updated terminology. *European radiology*, 15(4):798–808, 2005.

[187] R. Mur-Artal, J. M. M. Montiel, and J. D. Tardos. Orb-slam: a versatile and accurate monocular slam system. *IEEE transactions on robotics*, 31(5):1147–1163, 2015.

[188] C. A. Myers, P. J. Laz, K. B. Shelburne, and B. S. Davidson. A probabilistic approach to quantify the impact of uncertainty propagation in musculoskeletal simulations. *Annals of biomedical engineering*, 43(5):1098–1111, 2015.

[189] E. Nadal, F. Chinesta, P. Díez, F. Fuenmayor, and F. Denia. Real time parameter identification and solution reconstruction from experimental data using the proper generalized decomposition. *Computer Methods in Applied Mechanics and Engineering*, 296:113–128, 2015.

[190] F. Naets, F. Cosco, and W. Desmet. An extended kalman filter approach for augmented strain/stress visualization in mechanical systems. In *2014 IEEE/ASME 10th International Conference on Mechatronic and Embedded Systems and Applications (MESA)*, pages 1–6. IEEE, 2014.

[191] V. M. Nahirnyak, S. W. Yoon, and C. K. Holland. Acousto-mechanical and thermal properties of clotted blood. *The Journal of the Acoustical Society of America*, 119(6):3766–3772, 2006.

[192] B. K. Natarajan. Sparse approximate solutions to linear systems. *SIAM journal on computing*, 24(2):227–234, 1995.

[193] M. Nesme, Y. Payan, and F. Faure. *Efficient, Physically Plausible Finite Elements*. The Eurographics Association, 2005.

[194] I. Nestorov. Modelling and simulation of variability and uncertainty in toxicokinetics and pharmacokinetics. *Toxicology Letters*, 120(1-3):411–420, 2001.

[195] W. K. Newey and P. A. Ruud. Density weighted linear least squares. Department of economics, working paper series, Department of Economics, Institute for Business and Economic Research, UC Berkeley, 1994.

[196] C. D. Newgard and K. J. McConnell. Differences in the effectiveness of frontal air bags by body size among adults involved in motor vehicle crashes. *Traffic injury prevention*, 9(5):432–439, 2008.

[197] E. Ng and M. Jamil. Parametric sensitivity analysis of radiofrequency ablation with efficient experimental design. *International Journal of Thermal Sciences*, 80:41–47, 2014.

[198] S. Nicolau, L. Soler, D. Mutter, and J. Marescaux. Augmented reality in laparoscopic surgical oncology. *Surgical oncology*, 20(3):189–201, 2011.

[199] D. P. Nicolella and T. L. Bredbenner. Development of a parametric finite element model of the proximal femur using statistical shape and density modelling. *Computer methods in biomechanics and biomedical engineering*, 15(2):101–110, 2012.

[200] S. Niroomandi, I. Alfaro, E. Cueto, and F. Chinesta. Real-time deformable models of non-linear tissues by model reduction techniques. *Computer methods and programs in biomedicine*, 91(3):223–231, 2008.

[201] S. Niroomandi, I. Alfaro, E. Cueto, and F. Chinesta. Accounting for large deformations in real-time simulations of soft tissues based on reduced-order models. *Computer Methods and Programs in Biomedicine*, 105(1):1–12, 2012.

[202] S. Niroomandi, I. Alfaro, D. Gonzalez, E. Cueto, and F. Chinesta. Real-time simulation of surgery by reduced-order modeling and x-fem techniques. *International journal for numerical methods in biomedical engineering*, 28(5):574–588, 2012.

[203] S. Niroomandi, D. González, I. Alfaro, F. Bordeu, A. Leygue, E. Cueto, and F. Chinesta. Real-time simulation of biological soft tissues: a pgd approach. *International journal for numerical methods in biomedical engineering*, 29(5):586–600, 2013.

[204] F. Nobile, R. Tempone, and C. G. Webster. An anisotropic sparse grid stochastic collocation method for partial differential equations with random input data. *SIAM Journal on Numerical Analysis*, 46(5):2411–2442, 2008.

[205] J. Nocedal and S. Wright. *Numerical optimization*. Springer Science & Business Media, 2006.

[206] A. Nouy. A generalized spectral decomposition technique to solve a class of linear stochastic partial differential equations. *Computer Methods in Applied Mechanics and Engineering*, 196(45-48):4521–4537, 2007.

[207] J. M. Oakes, A. L. Marsden, C. Grandmont, S. C. Shadden, C. Darquenne, and I. E. Vignon-Clementel. Airflow and particle deposition simulations in health and emphysema: from in vivo to in silico animal experiments. *Annals of biomedical engineering*, 42(4):899–914, 2014.

[208] B. J. Odelson, M. R. Rajamani, and J. B. Rawlings. A new autocovariance least-squares method for estimating noise covariances. *Automatica*, 42(2):303–308, 2006.

[209] A. M. Okamura. Haptic feedback in robot-assisted minimally invasive surgery. *Current opinion in urology*, 19(1):102, 2009.

[210] O. Oktay, L. Zhang, T. Mansi, P. Mountney, P. Mewes, S. Nicolau, L. Soler, and C. Chefd'hotel. Biomechanically driven registration of pre-to intra-operative 3d images for laparoscopic surgery. In *International Conference on Medical Image Computing and Computer-Assisted Intervention*, pages 1–9. Springer, 2013.

[211] E. H. Ooi, K. W. Lee, S. Yap, M. A. Khattab, I. Y. Liao, E. T. Ooi, J. J. Foo, S. R. Nair, and A. F. M. Ali. The effects of electrical and thermal boundary condition on the simulation of radiofrequency ablation of liver cancer for tumours located near to the liver boundary. *Computers in biology and medicine*, 106:12–23, 2019.

[212] E. Özgür, B. Koo, B. Le Roy, E. Buc, and A. Bartoli. Preoperative liver registration for augmented monocular laparoscopy using backward–forward biomechanical simulation. *International journal of computer assisted radiology and surgery*, 13(10):1629–1640, 2018.

[213] L. Panait, E. Akkary, R. L. Bell, K. E. Roberts, S. J. Dudrick, and A. J. Duffy. The role of haptic feedback in laparoscopic simulation training. *Journal of Surgical Research*, 156(2):312–316, 2009.

[214] S. Pant, C. Corsini, C. Baker, T.-Y. Hsia, G. Pennati, and I. E. Vignon-Clementel. Inverse problems in reduced order models of cardiovascular haemodynamics: aspects of data assimilation and heart rate variability. *Journal of The Royal Society Interface*, 14(126):20160513, 2017.

[215] A. T. Patera and M. Yano. An lp empirical quadrature procedure for parametrized functions. *Comptes Rendus Mathematique*, 355(11):1161–1167, 2017.

[216] Y. C. Pati, R. Rezaiifar, and P. S. Krishnaprasad. Orthogonal matching pursuit: Recursive function approximation with applications to wavelet decomposition. In *Proceedings of 27th Asilomar conference on signals, systems and computers*, pages 40–44. IEEE, 1993.

[217] T. Pätz, T. Kröger, and T. Preusser. Simulation of radiofrequency ablation including water evaporation. In *World Congress on Medical Physics and Biomedical Engineering, September 7-12, 2009, Munich, Germany*, pages 1287–1290. Springer, 2009.

[218] C. J. Paulus, N. Haouchine, D. Cazier, and S. Cotin. Surgical augmented reality with topological changes. In *International conference on medical image computing and computer-assisted intervention*, pages 413–420. Springer, 2015.

[219] J. A. Pearce. Models for thermal damage in tissues: processes and applications. *Critical Reviews™ in Biomedical Engineering*, 38(1):1–20, 2010.

[220] B. Peherstorfer, D. Butnaru, K. Willcox, and H.-J. Bungartz. Localized discrete empirical interpolation method. *SIAM Journal on Scientific Computing*, 36(1):168–192, 2014.

[221] H. H. Pennes. Analysis of tissue and arterial blood temperatures in the resting human forearm. *Journal of applied physiology*, 1(2):93–122, 1948.

[222] K. Pillai, J. Akhter, T. C Chua, M. Shehata, N. Alzahrani, I. Al-Alem, and D. Morris. Heat sink effect on tumor ablation characteristics as observed in monopolar radiofrequency, bipolar radiofrequency, and microwave, using ex vivo calf liver model. *Medicine*, 94:e580, 03 2015.

[223] R. Pinnau. Model reduction via proper orthogonal decomposition. In *Model order reduction: theory, research aspects and applications*, pages 95–109. Springer, 2008.

[224] R. Plantefeve, N. Haouchine, J.-P. Radoux, and S. Cotin. Automatic alignment of pre and intraoperative data using anatomical landmarks for augmented laparoscopic liver surgery. In *International Symposium on Biomedical Simulation*, pages 58–66. Springer, 2014.

[225] R. Plantefeve, I. Peterlik, H. Courtecuisse, R. Trivisonne, J.-P. Radoux, and S. Cotin. Atlas-based transfer of boundary conditions for biomechanical simulation. In *International Conference on Medical Image Computing and Computer-Assisted Intervention*, pages 33–40. Springer, 2014.

[226] R. Plantefève, I. Peterlik, N. Haouchine, and S. Cotin. Patient-specific biomechanical modeling for guidance during minimally-invasive hepatic surgery. *Annals of biomedical engineering*, 44(1):139–153, 2016.

[227] N. Pozin, S. Montesantos, I. Katz, M. Pichelin, I. Vignon-Clementel, and C. Grandmont. Predicted airway obstruction distribution based on dynamical lung ventilation data: A coupled modeling-machine learning methodology. *International journal for numerical methods in biomedical engineering*, 34(9):e3108, 2018.

[228] A. J. Pullan, L. K. Cheng, M. P. Nash, A. Ghodrati, R. MacLeod, and D. H. Brooks. *The Inverse Problem of Electrocardiography*, pages 299–344. Springer London, London, 2010.

[229] A. Quarteroni, A. Manzoni, and F. Negri. *Reduced basis methods for partial differential equations: an introduction*, volume 92. Springer, 2015.

[230] A. Quarteroni and G. Rozza. Optimal control and shape optimization of aorto-coronaric bypass anastomoses. *Mathematical Models and Methods in Applied Sciences*, 13(12):1801–1823, 2003.

[231] C. Quesada, D. González, I. Alfaro, E. Cueto, and F. Chinesta. Computational vademecums for real-time simulation of surgical cutting in haptic environments. *International Journal for Numerical Methods in Engineering*, 108(10):1230–1247, 2016.

[232] A. Radtke, G. C. Sotiropoulos, E. P. Molmenti, T. Schroeder, H. O. Peitgen, A. Frilling, D. C. Broering, C. E. Broelsch, and M. Malagó. Computer-assisted surgery planning for complex liver resections: when is it helpful? a single-center experience over an 8-year period. *Annals of surgery*, 252(5):876–883, 2010.

[233] R. Rangayyan, A. P. Dhawan, and R. Gordon. Algorithms for limited-view computed tomography: an annotated bibliography and a challenge. *Applied optics*, 24(23):4000–4012, 1985.

[234] B. D. Rao, K. Engan, S. F. Cotter, J. Palmer, and K. Kreutz-Delgado. Subset selection in noise based on diversity measure minimization. *IEEE transactions on Signal processing*, 51(3):760–770, 2003.

[235] B. D. Rao and K. Kreutz-Delgado. Basis selection in the presence of noise. In *Conference Record of Thirty-Second Asilomar Conference on Signals, Systems and Computers (Cat. No. 98CH36284)*, volume 1, pages 752–756. IEEE, 1998.

[236] B. D. Rao and K. Kreutz-Delgado. An affine scaling methodology for best basis selection. *IEEE Transactions on signal processing*, 47(1):187–200, 1999.

[237] M. I. Ribeiro. Kalman and extended kalman filters: Concept, derivation and properties. Technical report, 2004.

[238] L. F. Richardson and J. A. Gaunt. The deferred approach to the limit. *Philosophical Transactions of the Royal Society of London. Series A, containing papers of a mathematical or physical character*, 226(636-646):299–361, 1927.

[239] C. Robert and G. Casella. *Monte Carlo statistical methods*. Springer Science & Business Media, 2013.

[240] M. R. Robu, J. Ramalhinho, S. Thompson, K. Gurusamy, B. Davidson, D. Hawkes, D. Stoyanov, and M. J. Clarkson. Global rigid registration of ct to video in laparoscopic liver surgery. *International journal of computer assisted radiology and surgery*, 13(6):947–956, 2018.

[241] A. Roy, R. Manna, and S. Chakraborty. Support vector regression based metamodeling for structural reliability analysis. *Probabilistic Engineering Mechanics*, 55:78–89, 2019.

[242] G. Rozza. Real time reduced basis techniques for arterial bypass geometries. In *Computational Fluid and Solid Mechanics-Third MIT Conference on Computational Fluid and Solid Mechanics*, pages 1283–1287. 2005.

[243] G. Rozza and K. Veroy. On the stability of the reduced basis method for stokes equations in parametrized domains. *Computer methods in applied mechanics and engineering*, 196(7):1244–1260, 2007.

[244] P.-B. Rubio, F. Louf, and L. Chamoin. Fast model updating coupling bayesian inference and pgd model reduction. *Computational Mechanics*, 62(6):1485–1509, 2018.

[245] L. I. Rudin, S. Osher, and E. Fatemi. Nonlinear total variation based noise removal algorithms. *Physica D: nonlinear phenomena*, 60(1-4):259–268, 1992.

[246] G. E. Ryb and P. C. Dischinger. Injury severity and outcome of overweight and obese patients after vehicular trauma: a crash injury research and engineering network (ciren) study. *Journal of Trauma and Acute Care Surgery*, 64(2):406–411, 2008.

[247] D. Ryckelynck. A priori hyperreduction method: an adaptive approach. *Journal of computational physics*, 202(1):346–366, 2005.

[248] D. Ryckelynck. Hyper-reduction of mechanical models involving internal variables. *International Journal for Numerical Methods in Engineering*, 77(1):75–89, 2009.

[249] F. Salmoiraghi, A. Scardigli, H. Telib, and G. Rozza. Free-form deformation, mesh morphing and reduced-order methods: enablers for efficient aerodynamic shape optimisation. *International Journal of Computational Fluid Dynamics*, 32(4-5):233–247, 2018.

[250] Z. Salo, M. Beek, D. Wright, and C. M. Whyne. Computed tomography landmark-based semi-automated mesh morphing and mapping techniques: generation of patient specific models of the human pelvis without segmentation. *Journal of biomechanics*, 48(6):1125–1132, 2015.

[251] F. Sánchez-Margallo, J. Moyano-Cuevas, R. Latorre, J. Maestre, L. Correa, J. Pagador, L. Sánchez-Peralta, J. Sánchez-Margallo, and J. Usón-Gargallo. Anatomical changes due to pneumoperitoneum analyzed by mri: an experimental study in pigs. *Surgical and radiologic anatomy*, 33(5):389–396, 2011.

[252] S. Sankaran, H. J. Kim, G. Choi, and C. A. Taylor. Uncertainty quantification in coronary blood flow simulations: impact of geometry, boundary conditions and blood viscosity. *Journal of biomechanics*, 49(12):2540–2547, 2016.

[253] R. Schneider and C. Georgakis. How to not make the extended kalman filter fail. *Industrial & Engineering Chemistry Research*, 52(9):3354–3362, 2013.

[254] P. H. Schönemann. A generalized solution of the orthogonal procrustes problem. *Psychometrika*, 31(1):1–10, 1966.

[255] D. J. Schutt and D. Haemmerich. Effects of variation in perfusion rates and of perfusion models in computational models of radio frequency tumor ablation. *Medical physics*, 35(8):3462–3470, 2008.

[256] D. W. Scott. *Multivariate density estimation: theory, practice, and visualization*. John Wiley & Sons, 2015.

[257] S. M. Shontz and S. A. Vavasis. A mesh warping algorithm based on weighted laplacian smoothing. In *Proceedings of 12th International Meshing Roundtable*, pages 147–158, Sept. 2003.

[258] S. M. Shontz and S. A. Vavasis. Analysis of and workarounds for element reversal for a finite element-based algorithm for warping triangular and tetrahedral meshes. *BIT Numerical Mathematics*, 50(4):863–884, 2010.

[259] S. M. Shontz and S. A. Vavasis. A robust solution procedure for hyperelastic solids with large boundary deformation. *Engineering with Computers*, 28(2):135–147, 2012.

[260] I. A. Sigal, M. R. Hardisty, and C. M. Whyne. Mesh-morphing algorithms for specimen-specific finite element modeling. *Journal of biomechanics*, 41(7):1381–1389, 2008.

[261] A. Simpson, B. Ma, R. Ellis, A. Stewart, and M. Miga. Uncertainty propagation and analysis of image-guided surgery. volume 7964, mar 2011.

[262] J. Sjöberg, T. McKelvey, and L. Ljung. On the use of regularization in system identification. *IFAC Proceedings Volumes*, 26(2):75–80, 1993.

[263] S. A. Smolyak. Quadrature and interpolation formulas for tensor products of certain classes of functions. In *Doklady Akademii Nauk*, volume 148, pages 1042–1045. Russian Academy of Sciences, 1963.

[264] C. Soize and R. Ghanem. Physical systems with random uncertainties: chaos representations with arbitrary probability measure. *SIAM Journal on Scientific Computing*, 26(2):395–410, 2004.

[265] L. Soler, S. Nicolau, P. Pessaux, D. Mutter, and J. Marescaux. Real-time 3d image reconstruction guidance in liver resection surgery. *Hepatobiliary surgery and nutrition*, 3(2):73, 2014.

[266] Y. Song, J. Totz, S. Thompson, S. Johnsen, D. Barratt, C. Schneider, K. Gurusamy, B. Davidson, S. Ourselin, D. Hawkes, et al. Locally rigid, vessel-based registration for laparoscopic liver surgery. *International journal of computer assisted radiology and surgery*, 10(12):1951–1961, 2015.

[267] G. Stefanou. The stochastic finite element method: past, present and future. *Computer methods in applied mechanics and engineering*, 198(9-12):1031–1051, 2009.

[268] M. Stein. Large sample properties of simulations using latin hypercube sampling. *Technometrics*, 29(2):143–151, 1987.

[269] A. H. Stroud. Remarks on the disposition of points in numerical integration formulas. *Mathematical Tables and Other Aids to Computation*, 11(60):257–261, 1957.

[270] B. Sudret. Polynomial chaos expansions and stochastic finite element methods. *Risk and reliability in geotechnical engineering*, pages 265–300, 2014.

[271] S. Suwelack, S. Röhl, S. Bodenstedt, D. Reichard, R. Dillmann, T. dos Santos, L. Maier-Hein, M. Wagner, J. Wünscher, H. Kenngott, et al. Physics-based shape matching for intraoperative image guidance. *Medical physics*, 41(11):111901, 2014.

[272] R. Szeliski and S. Lavallée. Matching 3-d anatomical surfaces with non-rigid deformations using octree-splines. *International journal of computer vision*, 18(2):171–186, 1996.

[273] B. Taouli, R. S. Johnson, C. H. Hajdu, M. T. Oei, M. Merad, H. Yee, and H. Rusinek. Hepatocellular carcinoma: perfusion quantification with dynamic contrast-enhanced mri. *American Journal of Roentgenology*, 201(4):795–800, 2013.

[274] A. Tarantola. *Inverse problem theory and methods for model parameter estimation*, volume 89. SIAM, 2005.

[275] L. Thabane, L. Mbuagbaw, S. Zhang, Z. Samaan, M. Marcucci, C. Ye, M. Thabane, L. Giangregorio, B. Dennis, D. Kosa, et al. A tutorial on sensitivity analyses in clinical trials: the what, why, when and how. *BMC medical research methodology*, 13(1):92, 2013.

[276] D. W. Thompson. *On Growth and Form*. Cambridge University Press, 1942.

[277] R. Tibshirani. Regression shrinkage and selection via the lasso. *Journal of the Royal Statistical Society: Series B (Methodological)*, 58(1):267–288, 1996.

[278] A. N. Tikhonov and V. I. Arsenin. *Solutions of ill-posed problems*, volume 14. Winston, 1977.

[279] P. Tiso and D. J. Rixen. Discrete empirical interpolation method for finite element structural dynamics. In *Topics in Nonlinear Dynamics, Volume 1*, pages 203–212. Springer, 2013.

[280] M. Trujillo, J. Bon, M. José Rivera, F. Burdío, and E. Berjano. Computer modelling of an impedance-controlled pulsing protocol for rf tumour ablation with a cooled electrode. *International Journal of Hyperthermia*, 32(8):931–939, 2016.

[281] S. Tungjitkusolmun, S. T. Staelin, D. Haemmerich, J.-Z. Tsai, H. Cao, J. G. Webster, F. T. Lee, D. M. Mahvi, and V. R. Vorperian. Three-dimensional finite-element analyses for radiofrequency hepatic tumor ablation. *IEEE transactions on biomedical engineering*, 49(1):3–9, 2002.

[282] G. U. Unnikrishnan, V. Unnikrishnan, J. N. Reddy, and C. Lim. Review on the constitutive models of tumor tissue for computational analysis. *Applied Mechanics Reviews*, 63, jul 2010.

[283] J. Valappil and C. Georgakis. Systematic estimation of state noise statistics for extended kalman filters. *AIChE Journal*, 46(2):292–308, 2000.

[284] J. Valvano, J. Cochran, and K. Diller. Thermal conductivity and diffusivity of biomaterials measured with self-heated thermistors. *International Journal of Thermophysics*, 6(3):301–311, 1985.

[285] M. van de Giessen, M. Foumani, G. J. Streekstra, S. D. Strackee, M. Maas, L. J. van Vliet, K. A. Grimbergen, and F. M. Vos. Statistical descriptions of scaphoid and lunate bone shapes. *Journal of biomechanics*, 43(8):1463–1469, 2010.

[286] M. Van De Giessen, N. Smitsman, S. D. Strackee, L. J. Van Vliet, K. A. Grimbergen, G. J. Streekstra, and F. M. Vos. A statistical description of the articulating ulna surface for prosthesis design. In *Biomedical Imaging: From Nano to Macro, 2009. ISBI'09. IEEE International Symposium on*, pages 678–681. IEEE, 2009.

[287] O. Van der Meijden and M. Schijven. The value of haptic feedback in conventional and robot-assisted minimal invasive surgery and virtual reality training: a current review. *Surgical endoscopy*, 23(6):1180–1190, 2009.

[288] P. Vávra, J. Roman, P. Zonča, P. Ihnát, M. Němec, J. Kumar, N. Habib, and A. El-Gendi. Recent development of augmented reality in surgery: a review. *Journal of healthcare engineering*, 2017, 2017.

[289] D. Veronda and R. Westmann. Mechanical characterization of skin—finite deformations. *Journal of Biomechanics*, 3(1):111 – 124, 1970.

[290] P. Voglreiter, P. Mariappan, M. Pollari, R. Flanagan, R. B. Sequeiros, R. H. Portugaller, J. Fütterer, D. Schmalstieg, M. Kolesnik, and M. Moche. Rfa guardian: comprehensive simulation of radiofrequency ablation treatment of liver tumors. *Scientific reports*, 8(1):787, 2018.

[291] X. Wang, H. Gao, S. Wu, Y. Bai, and Z. Zhou. Rf ablation thermal simulation model: Parameter sensitivity analysis. *Technology and Health Care*, (Preprint):1–13, 2018.

[292] Y. Wang, L. Cao, Z. Bai, M. P. Reed, J. D. Rupp, C. N. Hoff, and J. Hu. A parametric ribcage geometry model accounting for variations among the adult population. *Journal of biomechanics*, 49(13):2791–2798, 2016.

[293] A. A. Weaver, S. L. Schoell, and J. D. Stitzel. Morphometric analysis of variation in the ribs with age and sex. *Journal of anatomy*, 225(2):246–261, 2014.

[294] G. Welch, G. Bishop, et al. An introduction to the kalman filter. Technical report, 2006.

[295] D. Xiu and J. S. Hesthaven. High-order collocation methods for differential equations with random inputs. *SIAM Journal on Scientific Computing*, 27(3):1118–1139, 2005.

[296] D. Xiu and G. E. Karniadakis. The wiener–askey polynomial chaos for stochastic differential equations. *SIAM journal on scientific computing*, 24(2):619–644, 2002.

[297] R. Xu, X. Zhou, Y. Hirano, R. Tachibana, T. Hara, S. Kido, and H. Fujita. Particle system based adaptive sampling on spherical parameter space to improve the mdl method for construction of statistical shape models. *Computational and mathematical methods in medicine*, 2013, 2013.

[298] M. Yano and A. T. Patera. An lp empirical quadrature procedure for reduced basis treatment of parametrized nonlinear pdes. *Computer Methods in Applied Mechanics and Engineering*, 344:1104–1123, 2019.

[299] H. Yin, L. Sun, G. Wang, and M. W. Vannier. Modeling of elastic modulus evolution of cirrhotic human liver. *IEEE Transactions on biomedical engineering*, 51(10):1854–1857, 2004.

[300] L. A. Zadeh. Fuzzy sets. *Information and control*, 8(3):338–353, 1965.

[301] M. J. Zahr, K. T. Carlberg, and D. P. Kouri. An efficient, globally convergent method for optimization under uncertainty using adaptive model reduction and sparse grids. *SIAM/ASA Journal on Uncertainty Quantification*, 7(3):877–912, 2019.

[302] R. Zdunek and A. Cichocki. Improved m-focuss algorithm with overlapping blocks for locally smooth sparse signals. *IEEE Transactions on Signal Processing*, 56(10):4752–4761, 2008.

[303] G. L. Zeng. *Medical image reconstruction: a conceptual tutorial.* Springer, 2010.

[304] J. Zhang, Y. Zhong, and C. Gu. Deformable models for surgical simulation: a survey. *IEEE reviews in biomedical engineering*, 11:143–164, 2017.

[305] K. Zhang, L. Cao, A. Fanta, M. P. Reed, M. Neal, J.-T. Wang, C.-H. Lin, and J. Hu. An automated method to morph finite element whole-body human models with a wide range of stature and body shape for both men and women. *Journal of biomechanics*, 60:253–260, 2017.

[306] J.-X. Zhao, T. Coupez, E. Decencière, D. Jeulin, D. Cárdenas-Peña, and L. Silva. Direct multiphase mesh generation from 3d images using anisotropic mesh adaptation and a redistancing equation. *Computer Methods in Applied Mechanics and Engineering*, 309:288–306, 2016.

[307] O. C. Zienkiewicz, R. L. Taylor, and J. Z. Zhu. *The finite element method: its basis and fundamentals.* Elsevier, 2005.

[308] G. Zorbas and T. Samaras. A study of the sink effect by blood vessels in radiofrequency ablation. *Computers in Biology and Medicine*, 57, 12 2014.

Titre : Représentations d'ordre réduit et parcimonieuses pour la modélisation personnalisée des patients dans le cadre de la chirurgie computationnelle

**Mots clés :** modèle d'ordre réduit, modélisation personnalisée des patients, modélisation fondée sur des données, temps réel, données médicales

**Résumé :** Cette thèse a pour but d'évaluer l'utilisation des méthodes de réduction de modèles fondées sur des approches parcimonieuses pour atteindre des performances en temps réel dans la cadre de la chirurgie computationnelle. Elle se concentre notamment sur l'intégration de la simulation biophysique dans des modèles personnalisés de tissus et d'organes afin d'augmenter les images médicales et ainsi éclairer le clinicien dans sa prise de décision. Dans ce contexte, trois enjeux fondamentaux sont mis en évidence. Le premier réside dans l'intégration de la paramétrisation de la forme au sein du modèle réduit afin de représenter fidèlement l'anatomie du patient. Une approche non intrusive reposant sur un échantillonnage parcimonieux de l'espace des caractéristiques anatomiques est introduite et validée. Ensuite, nous abordons le problème de la complétion des données et de la reconstruction des images à partir de données partielles ou incomplètes via des à priori physiques. Nous explorons le potentiel de la solution proposée dans le cadre du recalage d'images pour la réalité augmentée en laparoscopie. Des performances proches du temps réel sont obtenues grâce à une nouvelle approche d'hyper-réduction fondée sur une technique de représentation parcimonieuse. Enfin, le troisième défi concerne la propagation des incertitudes dans le cadre de systèmes biophysiques. Il est démontré que les approches de réduction de modèles traditionnelles ne réussissent pas toujours à produire une représentation de faible rang, et ce, en particulier dans le cas de la simulation électrochirurgicale. Une alternative est alors proposée via la métamodélisation. Pour ce faire, nous étendons avec succès l'utilisation de méthodes de régression parcimonieuses aux cas des systèmes à paramètres stochastiques.

Title: Reduced order and sparse representations for patient-specific modeling in computational surgery

**Keywords:** model order reduction, patient-specific modeling, data-based modeling, real-time, medical data

**Abstract:** This thesis investigates the use of model order reduction methods based on sparsity-related techniques for the development of real-time biophysical modeling. In particular, it focuses on the embedding of interactive biophysical simulation into patient-specific models of tissues and organs to enhance medical images and assist the clinician in the process of informed decision making. In this context, three fundamental bottlenecks arise. The first lies in the embedding of the shape parametrization into the parametric reduced order model to faithfully represent the patient's anatomy. A non-intrusive approach relying on a sparse sampling of the space of anatomical features is introduced and validated. Then, we tackle the problem of data completion and image reconstruction from partial or incomplete datasets based on physical priors. The proposed solution has the potential to perform scene registration in the context of augmented reality for laparoscopy. Quasi-real-time computations are reached by using a new hyperreduction approach based on a sparsity promoting technique. Finally, the third challenge concerns the representation of biophysical systems under uncertainty of the underlying parameters. It is shown that traditional model order reduction approaches are not always successful in producing a low dimensional representation of a model, in particular in the case of electrosurgery simulation. An alternative is proposed using a metamodeling approach. To this end, we successfully extend the use of sparse regression methods to the case of systems with stochastic parameters.